

# The cosmic 21-cm revolution: charting the first billion years of our Universe

Andrei Mesinger

July 31, 2019

# Contents

<b>1</b>	<b>Theoretical Framework: The Fundamentals of the 21-cm Line</b>	<b>1</b>
1.1	Radiative Transfer of the 21-cm Line . . . . .	1
1.2	The Spin Temperature . . . . .	3
1.2.1	Collisional Coupling . . . . .	4
1.2.2	The Wouthuysen-Field Effect . . . . .	5
1.3	Heating of the Intergalactic Medium . . . . .	13
1.3.1	The Lyman- $\alpha$ Background . . . . .	13
1.3.2	The Cosmic Microwave Background . . . . .	14
1.3.3	The X-ray Background . . . . .	14
<b>2</b>	<b>Astrophysics from the 21-cm background</b>	<b>19</b>
2.1	Properties of the High- $z$ Intergalactic Medium . . . . .	19
2.1.1	The brightness temperature . . . . .	19
2.1.2	Basics of Non-Equilibrium Ionization Chemistry . . . . .	20
2.1.3	Ionization and Heating Around Point Sources . . . . .	22
2.1.4	Ionization and Heating on Large Scales . . . . .	24
2.2	Techniques for Modeling the IGM . . . . .	25
2.2.1	The Density Field . . . . .	25
2.2.2	The Ionization Field . . . . .	26
2.2.3	The (Kinetic) Temperature Field . . . . .	29
2.2.4	The Ly- $\alpha$ Background . . . . .	30
2.3	Sources of the UV and X-ray Background . . . . .	31
2.3.1	Star Formation . . . . .	32
2.3.2	UV Emission from Stars . . . . .	33
2.3.3	Escape of UV Photons from Galaxies . . . . .	35
2.3.4	X-rays from Black Holes . . . . .	35
2.3.5	X-rays from Shocks and Hot Gas . . . . .	36
2.3.6	Escape of X-rays from Galaxies . . . . .	37
2.3.7	Cosmic Rays from Supernovae . . . . .	38
2.4	Predictions for the 21-cm Background . . . . .	38
2.4.1	Generic Series of Events . . . . .	38
2.4.2	Sensitivity to Model Parameters . . . . .	39
2.4.3	Modeling Tools . . . . .	40

<b>3 Physical cosmology from the 21-cm line</b>	<b>44</b>
3.1 Physical cosmology through the 21-cm epoch . . . . .	44
3.1.1 Dark matter . . . . .	44
3.1.2 PMBH . . . . .	44
3.2 Unique signatures of cosmology . . . . .	44
3.2.1 Non-Gaussianity . . . . .	45
3.2.2 IGM Heating . . . . .	45
3.3 Separating cosmology from astrophysics . . . . .	45
3.3.1 Redshift space distortions . . . . .	45
3.3.2 Time evolution . . . . .	45
3.4 Summary . . . . .	45
<b>4 Inference from the 21cm signal</b>	<b>48</b>
4.1 What do we actually measure? . . . . .	49
4.2 Optimal methods for characterising the 21-cm signal . . . . .	49
4.2.1 Global signal . . . . .	49
4.2.2 Power spectrum . . . . .	51
4.2.3 Bispectrum . . . . .	55
4.2.4 Trispectrum . . . . .	56
4.2.5 One-point statistics . . . . .	56
4.2.6 Wavelets . . . . .	58
4.2.7 Topological measurements of the 21-cm signal . . . . .	58
4.2.8 Bubble size distributions . . . . .	63
4.2.9 Individual bubbles . . . . .	64
4.2.10 Stacked images . . . . .	64
4.2.11 Other statistics . . . . .	64
4.3 Efficient methods to model/simulate the 21cm signal . . . . .	64
4.3.1 Numerical simulations . . . . .	65
4.3.2 Semi-numerical/analytic models of the 21cm signal . . . . .	65
4.3.3 Intelligent sampling of the parameter space . . . . .	65
4.3.4 Emulators . . . . .	65
4.3.5 Characterising our ignorance . . . . .	66
4.4 Inference methods for 21cm . . . . .	66
4.4.1 Fisher Matrices . . . . .	66
4.4.2 Bayesian MCMC . . . . .	66
4.4.3 Nested sampling and model inference . . . . .	67
4.4.4 Neural Networks . . . . .	67
<b>5 Observational strategies: power spectra and images</b>	<b>72</b>
5.1 Interferometry overview . . . . .	72
5.2 21 cm observables: power spectra and images . . . . .	74
5.3 Interferometric calibration and 21 cm observations . . . . .	75
5.3.1 Direction dependent calibration . . . . .	83
5.3.2 Redundant calibration . . . . .	83
5.4 Array design and observing strategies . . . . .	84

<b>6 Foregrounds</b>	<b>95</b>
6.1 A Section	95
6.2 Foreground Mitigation	96
6.2.1 Foreground Mitigation in the Data Analysis Pipeline	97
6.2.2 Foreground Avoidance and Suppression	99
6.2.3 Foreground Subtraction	104
6.2.4 Residual Error Subtraction	109
6.3 Conclusions	109
<b>7 Chapter title</b>	<b>118</b>
7.1 A Section	118
<b>8 Status of 21 cm interferometric experiments</b>	<b>122</b>
8.1 Introduction	122
8.2 Early work	123
8.3 Experimental methodologies and current experiments	124
8.3.1 Giant Metrewave Radio Telescope - GMRT	125
8.3.2 Murchison Widefield Array - MWA	127
8.3.3 Low Frequency Array - LOFAR	131
8.3.4 Precision Array for Probing the Epoch of Reionization - PAPER	134
8.4 Published results	137
8.5 Current challenges	137
8.6 Prospects for the future	140
8.6.1 Current instruments	140
8.6.2 Future instruments	140
8.6.3 Future analyses	141
<b>9 Future prospects</b>	<b>156</b>
9.1 Forthcoming interferometric ground based instruments and upgrades	156
9.1.1 The Hydrogen Epoch of Reionization Array	156
9.1.2 The Large aperture Experiment to detect the Dark Ages	157
9.2 A Section	157

# Preface

This set of files can be used to create your typescript in L<sup>A</sup>T<sub>E</sub>X. You can add packages as necessary.

Remember that references need to be at the chapter level and you may find the package **chapterbib** useful for this.

# About the Author



Remember to include a brief biography of the Authors or Editors, including a photo.

# Contributors

## **Gianni Bernardi**

INAF - Istituto di Radio Astronomia  
via Gobetti 101, 40129, Bologna, Italy &  
Department of Physics and Electronics  
Rhodes University  
PO Box 94, Grahamstown, 6140, South Africa

## **Bradley Greig**

School of Physics  
The University of Melbourne  
Parkville, Melbourne VIC, Australia

## **Vibor Jelić**

Ruđer Bošković Institute  
Zagreb, Croatia

## **Peter Jones**

Department of Physics  
University of New England  
Acadia, Maine, USA

## **Jonathan Pritchard**

Blackett Laboratory  
Imperial College  
London, UK

## **Simon Smith**

Department of Electrical Engineering  
University of Oxbridge, Cambridge, USA

## **Cathryn M. Trott**

International Centre for Radio Astronomy Research  
Curtin University, Bentley WA, Australia



# Chapter 1

## Theoretical Framework: The Fundamentals of the 21-cm Line

Steven R. Furlanetto

### Abstract

We review some of the fundamental physics necessary for computing the highly-redshifted spin-flip background. We first discuss the radiative transfer of the 21-cm line and define the crucial quantities of interest. We then review the processes that set the spin temperature of the transition, with a particular focus on Wouthuysen-Field coupling, which is likely to be the most important process during and after the Cosmic Dawn. Finally, we discuss processes that heat the intergalactic medium during the Cosmic Dawn, including the scattering of Lyman- $\alpha$ , cosmic microwave background, and X-ray photons.

### 1.1 Radiative Transfer of the 21-cm Line

Consider a spectral line labeled by 0 (the lower level) and 1 (the upper level). The radiative transfer equation for the specific intensity  $I_\nu$  of photons at the relevant frequency is

$$\frac{dI_\nu}{d\ell} = \frac{\phi(\nu)h\nu}{4\pi} [n_1 A_{10} - (n_0 B_{01} - n_1 B_{10}) I_\nu], \quad (1.1)$$

where  $d\ell$  is a proper path length element,  $\phi(\nu)$  is the line profile function,  $n_i$  denotes the number density of atoms at the different levels, and  $A_{ij}$  and  $B_{ij}$  are the Einstein coefficients for the relevant transition (here  $i$  and  $j$  the initial and final states, respectively). For the 21-cm line, the line frequency is  $\nu_{21} = 1420.4057$  MHz. The Einstein relations associate the radiative transition rates via  $B_{10} = (g_0/g_1)B_{01}$  and  $B_{10} = A_{10}(c^2/2h\nu^3)$ , where  $g$  is the spin degeneracy factor of each state. For the 21-cm transition,  $A_{10} = 2.85 \times 10^{-15}$  s $^{-1}$  and  $g_1/g_0 = 3$ .

The relative populations of hydrogen atoms in the two spin states determine the **spin**

**temperature**,  $T_S$ , through the relation

$$\left(\frac{n_1}{n_0}\right) = \left(\frac{g_1}{g_0}\right) \exp\left\{\frac{-T_*}{T_S}\right\}, \quad (1.2)$$

where  $T_* \equiv E_{10}/k_B = 68$  mK is equivalent to the transition energy  $E_{10}$ . In almost all physically plausible situations,  $T_*$  is much smaller than any other temperature, including  $T_S$ , so all the exponentials in temperature can be Taylor expanded to leading order with high accuracy. Note, however, that  $T_S$  implicitly assumes that the level populations can be described by a single temperature – independent of each atom’s velocity. In detail, velocity-dependent effects must be considered in certain circumstances [13].

It is conventional to replace  $I_\nu$  by the equivalent **brightness temperature**,  $T_b(\nu)$ , required of a blackbody radiator (with spectrum  $B_\nu$ ) such that  $I_\nu = B_\nu(T_b)$ . In the low frequency regime relevant to the 21 cm line, the Rayleigh-Jeans formula is an excellent approximation to the Planck curve, so  $T_b(\nu) \approx I_\nu c^2/2k_B\nu^2$ .

In this limit, the equation of radiative transfer along a line of sight through a cloud of uniform excitation temperature  $T_S$  becomes

$$T'_b(\nu) = T_S(1 - e^{-\tau_\nu}) + T'_R(\nu)e^{-\tau_\nu} \quad (1.3)$$

where  $T'_b(\nu)$  is the emergent brightness measured at the cloud and at redshift  $z$ , the **optical depth**  $\tau_\nu \equiv \int ds \alpha_\nu$  is the integral of the absorption coefficient ( $\alpha_\nu$ ) along the ray through the cloud,  $T'_R$  is the brightness of the background radiation field incident on the cloud along the ray, and  $s$  is the proper distance. Because of the cosmological redshift, for the 21-cm transition an observer will measure an apparent brightness at the Earth of  $T_b(\nu) = T'_b(\nu_{21})/(1+z)$ , where the observed frequency is  $\nu = \nu_{21}/(1+z)$ . Henceforth we will work in terms of these observed quantities.

The absorption coefficient is related to the Einstein coefficients via

$$\alpha = \phi(\nu) \frac{h\nu}{4\pi} (n_0 B_{01} - n_1 B_{10}). \quad (1.4)$$

Because all astrophysical applications have  $T_S \gg T_*$ , approximately three of four atoms find themselves in the excited state ( $n_0 \approx n_1/3$ ). As a result, the stimulated emission correction represented by the first term is significant.

The fundamental observable quantity is the change in brightness temperature induced by the 21-cm line by a patch of the intergalactic medium (IGM), relative to the incident radiation field. In most models that incident field is simply the cosmic microwave background, although if other sources create a low-frequency radio background at very high redshifts, or if there is a particular source behind the IGM patch along the line of sight from the observer, a larger radio background may exist.

Consider photons incident on the patch from this background. If any redshift into resonance with the 21-cm line, they can interact with the cloud – but only for a short time, as they will redshift out of resonance as the Universe continues to expand. Thus the Hubble expansion rate sets an effective path length through the cloud, simply equal to the distance the photon travels while it remains within the line profile. The total absorption can be calculated

by integrating the IGM density across this interval, in an exactly analogous procedure to the calculation of the Gunn-Peterson Lyman- $\alpha$  optical depth [4, 11, 19]. The result is

$$\tau_{10} = \frac{3}{32\pi} \frac{hc^3 A_{10}}{k_B T_S v_{10}^2} \frac{x_{\text{HI}} n_H}{(1+z) (dv_{\parallel}/dr_{\parallel})} \quad (1.5)$$

$$\approx 0.0092 (1+\delta) (1+z)^{3/2} \frac{x_{\text{HI}}}{T_S} \left[ \frac{H(z)/(1+z)}{dv_{\parallel}/dr_{\parallel}} \right], \quad (1.6)$$

where  $n_H$  is the hydrogen number density,  $x_{\text{HI}}$  is the neutral fraction,  $dv_{\parallel}/dr_{\parallel}$  is the velocity gradient along the line of sight (here scaled to the Hubble flow). In the second part,  $T_S$  is in Kelvins, and we have scaled the density to the mean value by writing  $n_H = \bar{n}_H^0 (1+z)^3 (1+\delta)$ , where  $\bar{n}_H^0$  is the mean comoving density today.

In most circumstances, the CMB provides the background radiation source, for which with temperature  $T_\gamma(z)$ . Then  $T'_R = T_\gamma(z)$ , so that we are observing the contrast between high-redshift hydrogen clouds and the CMB. Because the optical depth is so small, we can then expand the exponentials in equation (1.3), and

$$T_b(v) \approx \frac{T_S - T_\gamma(z)}{1+z} \tau_{v_0} \quad (1.7)$$

$$\approx 9 x_{\text{HI}} (1+\delta) (1+z)^{1/2} \left[ 1 - \frac{T_\gamma(z)}{T_S} \right] \left[ \frac{H(z)/(1+z)}{dv_{\parallel}/dr_{\parallel}} \right] \text{ mK}. \quad (1.8)$$

Thus  $T_b < 0$  if  $T_S < T_\gamma$ , yielding an absorption signal; otherwise it appears in emission relative to the CMB. Both regimes are likely important for the high- $z$  Universe. Note that  $T_b$  saturates if  $T_S \gg T_\gamma$ , but the absorption can become arbitrarily large if  $T_S \ll T_\gamma$ . The observability of the 21 cm transition therefore hinges on the spin temperature; we will next describe the mechanisms that control that factor.

## 1.2 The Spin Temperature

Three competing processes determine  $T_S$ : (i) absorption of CMB photons (as well as stimulated emission); (ii) collisions with other particles; and (iii) scattering of UV photons. In the presence of the CMB alone, the spin states reach thermal equilibrium ( $T_S = T_\gamma$ ) on a time-scale of  $\sim T_*/(T_\gamma A_{10}) = 3 \times 10^5 (1+z)^{-1}$  yr – much shorter than the age of the Universe at all redshifts after cosmological recombination, indicating that CMB coupling establishes itself rapidly. Indeed all the relevant processes adjust on very short timescales (compared to the Hubble time) so equilibrium is an excellent approximation.

However, the other two processes break this coupling. We let  $C_{10}$  and  $P_{10}$  be the de-excitation rates (per atom) from collisions and UV scattering, respectively. We also let  $C_{01}$  and  $P_{01}$  be the corresponding excitation rates. In equilibrium, the spin temperature is then determined by

$$n_1 (C_{10} + P_{10} + A_{10} + B_{10} I_{\text{CMB}}) = n_0 (C_{01} + P_{01} + B_{01} I_{\text{CMB}}), \quad (1.9)$$

where  $I_{\text{CMB}}$  is the specific intensity of CMB photons at  $\nu_{21}$ . With the Rayleigh-Jeans approximation, equation (1.9) can be rewritten as

$$T_S^{-1} = \frac{T_\gamma^{-1} + x_c T_K^{-1} + x_\alpha T_c^{-1}}{1 + x_c + x_\alpha}, \quad (1.10)$$

where  $x_c$  and  $x_\alpha$  are coupling coefficients for collisions and UV scattering, respectively, and  $T_K$  is the gas kinetic temperature. Here we have used the principle of detailed balance through the relation

$$\frac{C_{01}}{C_{10}} = \frac{g_1}{g_0} e^{-T_\star/T_K} \approx 3 \left(1 - \frac{T_\star}{T_K}\right). \quad (1.11)$$

We have also *defined* the effective color temperature of the UV radiation field  $T_c$  via

$$\frac{P_{01}}{P_{10}} \equiv 3 \left(1 - \frac{T_\star}{T_c}\right). \quad (1.12)$$

In the limit in which  $T_c \rightarrow T_K$  (usually a good approximation), equation (1.10) may be written

$$1 - \frac{T_\gamma}{T_S} = \frac{x_c + x_\alpha}{1 + x_c + x_\alpha} \left(1 - \frac{T_\gamma}{T_K}\right). \quad (1.13)$$

We must now calculate  $x_c$ ,  $x_\alpha$ , and  $T_c$ , which we shall do in the next subsections.

### 1.2.1 Collisional Coupling

We will first consider collisional excitation and de-excitation of the hyperfine levels, which become important in dense gas. The coupling coefficient for collisions with species  $i$  is

$$x_c^i \equiv \frac{C_{10}^i}{A_{10}} \frac{T_\star}{T_\gamma} = \frac{n_i \kappa_{10}^i}{A_{10}} \frac{T_\star}{T_\gamma}, \quad (1.14)$$

where  $\kappa_{10}^i$  is the rate coefficient for collisional spin de-excitation in collisions (with units of  $\text{cm}^3 \text{ s}^{-1}$ ). The total  $x_c$  is the sum over all relevant species  $i$ , including collisions with (1) neutral hydrogen atoms, (2) free electrons, and (3) protons.

These rate coefficients can be calculated by the quantum mechanical cross sections of the relevant processes [25, 7, 8]. We will not list them in detail but show the rates in Figure 1.1. Although the atomic cross-section is small, in the unperturbed IGM collisions between neutral hydrogen atoms nearly always dominate these rates because the ionized fraction is small. Free electrons can be important in partially ionized gas; collisions with protons are only important at the lowest temperatures.

Given the densities relevant to the IGM, collisional coupling is quite weak in a nearly neutral, cold medium. Thus, the local density must be large in order for this process to effectively fix  $T_S$ . A convenient estimate of their importance is the critical overdensity,  $\delta_{\text{coll}}$ , at which  $x_c = 1$  for H–H collisions:

$$1 + \delta_{\text{coll}} = 0.99 \left[ \frac{\kappa_{10}(88 \text{ K})}{\kappa_{10}(T_K)} \right] \left( \frac{0.023}{\Omega_b h^2} \right) \left( \frac{70}{1+z} \right)^2, \quad (1.15)$$

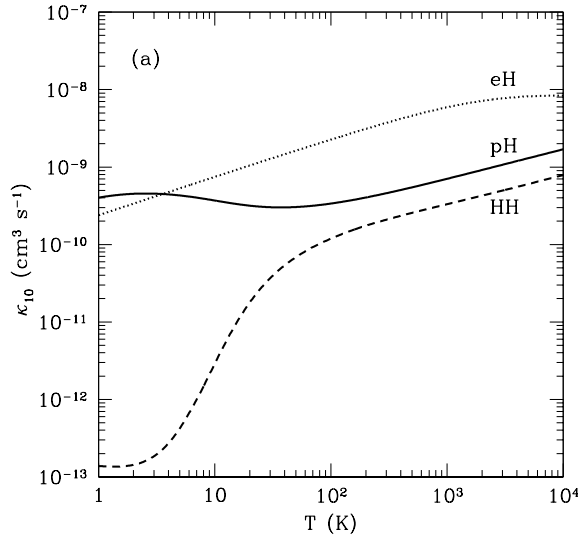


Figure 1.1: De-excitation rate coefficients for H-H collisions (dashed line), H-e<sup>-</sup> collisions (dotted line), and H-p collisions (solid line). Note that the net rates are also proportional to the densities of the individual species, so H-H collisions still dominate in a weakly-ionized medium. From [8].

where 88 K is the expected IGM temperature at  $1+z = 70$ .<sup>1</sup> In the standard picture, at redshifts  $z < 70$ ,  $x_c \ll 1$  and  $T_S \rightarrow T_\gamma$ ; by  $z \sim 30$  the IGM essentially becomes invisible. However,  $\kappa_{10}$  is extremely sensitive to  $T_K$  in this low-temperature regime. If the Universe is somehow heated above the fiducial value, the threshold density can remain modest:  $\delta_{\text{coll}} \approx 1$  at  $z = 40$  if  $T_K = 300$  K.

### 1.2.2 The Wouthuysen-Field Effect

We must therefore appeal to a different mechanism to render the 21-cm transition visible during the era of the first galaxies. This is known as the **Wouthuysen-Field mechanism** (named after the Dutch physicist Siegfried Wouthuysen and Harvard astrophysicist George Field who first explored it [24, 3]). Figure 1.2 illustrates the effect. This shows the hyperfine sub-levels of the  $1S$  and  $2P$  states of HI and the permitted transitions between them. Suppose a hydrogen atom in the hyperfine singlet state absorbs a Lyman- $\alpha$  photon. The electric dipole selection rules allow  $\Delta F = 0, 1$  except that  $F = 0 \rightarrow 0$  is prohibited (here  $F$  is the total angular momentum of the atom). Thus the atom must jump to either of the central  $2P$  states. However, these same rules now allow electrons in either of these excited states to decay to the  $1S_{1/2}$  triplet level.<sup>2</sup> Thus, atoms can change hyperfine states through the absorption and spontaneous re-emission of a Lyman- $\alpha$  photon (or indeed any Lyman-series photon; see

<sup>1</sup>Note that this is *smaller* than the CMB temperature at this time, because the IGM gas cools faster (due to adiabatic expansion) once Compton scattering becomes inefficient at  $z \sim 150$ .

<sup>2</sup>Here we use the notation  ${}_F L_J$ , where  $L$  and  $J$  are the orbital and total angular momentum of the electron.

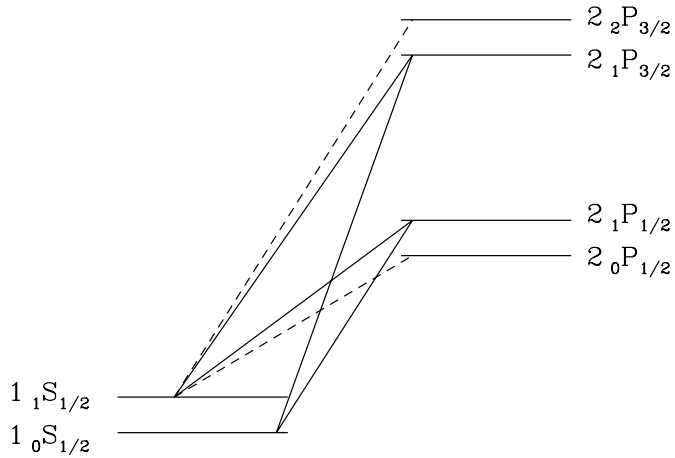


Figure 1.2: Level diagram illustrating the Wouthuysen-Field effect. We show the hyperfine splittings of the  $1S$  and  $2P$  levels. The solid lines label transitions that can mix the ground state hyperfine levels, while the dashed lines label complementary allowed transitions that do not participate in mixing. From [17].

below).

The Wouthuysen-Field coupling rate depends ultimately on the total rate (per atom) at which Lyman- $\alpha$  photons scattered through the gas,

$$P_\alpha = 4\pi\sigma_0 \int d\nu J_\nu(\nu)\phi_\alpha(\nu), \quad (1.16)$$

where  $\sigma_\nu \equiv \sigma_0\phi_\alpha(\nu)$  is the local Lyman- $\alpha$  absorption cross section,  $\sigma_0 \equiv (\pi e^2/m_e c)f_\alpha$ ,  $f_\alpha = 0.4162$  is the oscillator strength of the Lyman- $\alpha$  transition,  $\phi_\alpha(\nu)$  is the Lyman- $\alpha$  absorption profile, and  $J_\nu$  is the angle-averaged specific intensity of the background radiation field.<sup>3</sup>

Transitions to higher Lyman- $n$  levels have similar effects [12, 17]. Suppose that a UV photon redshifts into the Lyman- $n$  resonance as it travels through the IGM. After absorption, it can either scatter (by the electron decaying directly to the ground state) or cascade through a series of intermediate levels and produce a sequence of photons. The direct decay probability for any level is  $\sim 0.8$ , so a Lyman- $n$  photon will typically scatter  $N_{\text{scatt}} \approx (1 - P_{nP \rightarrow 1S})^{-1} \sim 5$  times before instead initiating a decay cascade. In contrast,

---

<sup>3</sup>By convention, we use the specific intensity in units of photons  $\text{cm}^{-2} \text{ Hz}^{-1} \text{ s}^{-1} \text{ sr}^{-1}$  here, which is conserved during the expansion of the Universe (whereas a definition in terms of energy instead of photon number is subject to redshifting).

Lyman- $\alpha$  photons scatter hundreds of thousands of times before being destroyed, usually by redshifting all the way across the (very wide) Lyman- $\alpha$  profile. As a result, coupling from the direct scattering of Lyman- $n$  photons is suppressed compared to Lyman- $\alpha$  by a large factor.

However, Lyman- $n$  photons can still be important because of their cascade products, as shown in Figure 1.3. Following Lyman- $\beta$  absorption, the only permitted decays are to the ground state (regenerating a Lyman- $\beta$  photon and starting the process again) or to the 2S level. The H $\alpha$  photon produced in the  $3P \rightarrow 2S$  transition (and indeed any photon produced in a decay to an excited state) escapes to infinity. Thus the atom will eventually find itself in the 2S state, which decays to the ground state via a forbidden two photon process with  $A_{2S \rightarrow 1S} = 8.2 \text{ s}^{-1}$ . These photons will also escape to infinity, so coupling from Lyman- $\beta$  photons can be completely neglected.<sup>4</sup>

But now consider excitation by Lyman- $\gamma$ , also shown in Figure 1.3. This can cascade (through 3S or 3D) to the 2P level, in which case the original Lyman- $n$  photon is “recycled” into a Lyman- $\alpha$  photon, which then scatters many times through the IGM. Thus, the key quantity for determining the coupling induced by Lyman- $n$  photons is the fraction  $f_{\text{rec}}(n)$  of cascades that terminate in Lyman- $\alpha$  photons. Our discussion in the previous paragraph shows that  $f_{\text{rec}}(n=3)$  vanishes, but detailed quantum mechanical calculations show that the higher states all have  $f_{\text{rec}} \sim 1/3$  [12, 17].

Focusing again on the Lyman- $\alpha$  photons themselves, we must relate the total scattering rate  $P_\alpha$  to the indirect de-excitation rate  $P_{10}$  [3, 15]. Let us first label the 1S and 2P hyperfine levels a–f, in order of increasing energy, and let  $A_{ij}$  and  $B_{ij}$  be the spontaneous emission and absorption coefficients for transitions between these levels. We write the background intensity at the frequency corresponding to the  $i \rightarrow j$  transition as  $J_{ij}$ . Then

$$P_{01} \propto B_{\text{ad}} J_{\text{ad}} \frac{A_{\text{db}}}{A_{\text{da}} + A_{\text{db}}} + B_{\text{ae}} J_{\text{ae}} \frac{A_{\text{eb}}}{A_{\text{ea}} + A_{\text{eb}}}. \quad (1.17)$$

The first term contains the probability for an a→d transition ( $B_{\text{ad}} J_{\text{ad}}$ ), together with the probability for the subsequent decay to terminate in state b; the second term is the same for transitions to and from state e (see Figure 1.2). Next we need to relate each  $A_{ij}$  to the total spontaneous decay rate from the 2P level,  $A_\alpha = 6.25 \times 10^8 \text{ Hz}$ , the total Lyman- $\alpha$  spontaneous emission rate. This can be accomplished using a sum rule stating that the sum of decay intensities ( $g_i A_{ij}$ ) for transitions from a given  $nFJ$  to all the  $n'J'$  levels (summed over  $F'$ ) is proportional to  $2F + 1$ , which implies that the relative strengths of the permitted transitions are then (1, 1, 2, 2, 1, 5), where we have ordered the lines by (initial, final) states (bc, ad, bd, ae, be, bf). With our assumption that the background radiation field is constant across the individual hyperfine lines, we find  $P_{10} = (4/27)P_\alpha$  [15].

The coupling coefficient  $x_\alpha$  is then

$$x_\alpha = \frac{4P_\alpha}{27A_{10}} \frac{T_\star}{T_\gamma} \equiv S_\alpha \frac{J_\alpha}{J_v^c}. \quad (1.18)$$

The second part evaluates  $J_v$  “near” line center and sets  $J_v^c \equiv 1.165 \times 10^{-10}[(1+z)/20]$  photons  $\text{cm}^{-2} \text{ sr}^{-1} \text{ Hz}^{-1} \text{ s}^{-1}$ .  $S_\alpha$  is a correction factor that accounts for (complicated) radiative

---

<sup>4</sup>In a medium with very high number density, atomic collisions can mix the two angular momentum states, but that process is unimportant in the IGM.

transfer effects in the intensity near the line center (see below). The coupling threshold  $J_v^c$  for  $x_\alpha = S_\alpha$  can also be written in terms of the number of Lyman- $\alpha$  photons per hydrogen atom in the Universe, which we denote  $\tilde{J}_v^c = 0.0767[(1+z)/20]^{-2}$ . This threshold is relatively easy to achieve in practice.

To complete the coupling calculation, we must determine  $T_c$  and the correction factor  $S_\alpha$ . The former is the effective temperature of the UV radiation field, defined in equation (1.12), and is determined by the shape of the photon spectrum at the Lyman- $\alpha$  resonance. The effective temperature of the radiation field *must* matter, because the energy deficit between the different hyperfine splittings of the Lyman- $\alpha$  transition (labeled bc, ad, etc. above) implies that the mixing process is sensitive to the gradient of the radiation spectrum near the Lyman- $\alpha$  resonance. More precisely, the procedure described after equation (1.17) yields

$$\frac{P_{01}}{P_{10}} = \frac{g_1}{g_0} \frac{n_{\text{ad}} + n_{\text{ae}}}{n_{\text{bd}} + n_{\text{be}}} \approx 3 \left( 1 + v_0 \frac{d \ln n_v}{d v} \right), \quad (1.19)$$

where  $n_v = c^2 J_v / 2v^2$  is the photon occupation number. Thus, by comparison to equation (1.12) we find

$$\frac{h}{k_B T_c} = - \frac{d \ln n_v}{d v}. \quad (1.20)$$

A simple argument shows that  $T_c \approx T_K$  [5]: so long as the medium is extremely optically thick, the enormous number of Lyman- $\alpha$  scatterings forces the Lyman- $\alpha$  profile to be a blackbody of temperature  $T_K$  near the line center. This condition is easily fulfilled in the high-redshift IGM, where  $\tau_\alpha \gg 1$ . In detail, atomic recoils during scattering tilt the spectrum to the red and are primarily responsible for establishing this equilibrium [6].

The physics of the Wouthuysen-Field effect are actually much more complicated than naively expected because scattering itself modifies the shape of  $J_v$  near the Lyman- $\alpha$  resonance [2]. In essence, the spectrum must develop an absorption feature because of the increased scattering rate near the Lyman- $\alpha$  resonance. Photons lose energy at a fixed rate by redshifting, but each time they scatter they also lose a small amount of energy through recoil. Momentum conservation during each scattering slightly decreases the frequency of the photon. The strongly enhanced scattering rate near line center means that photons “flow” through that region more rapidly than elsewhere (where only the cosmological redshift applies), so the amplitude of the spectrum must be smaller. Meanwhile, the scattering in such an optically thick medium also causes photons to diffuse away from line center, broadening the feature well beyond the nominal line width.

If the fractional frequency drift rate is denoted by  $\mathcal{A}$ , continuity requires  $n_v \mathcal{A} = \text{constant}$ . Because  $\mathcal{A}$  increases near resonance, the number density must fall. On average, the energy loss (or gain) per scattering is [2]

$$\frac{\Delta E_{\text{recoil}}}{E} = \frac{h v}{m_p c^2} \left( 1 - \frac{T_K}{T_c} \right), \quad (1.21)$$

where the first factor comes from recoil off an isolated atom and the second factor corrects for the distribution of initial photon energies; the energy loss vanishes when  $T_c = T_K$ , and when  $T_c < T_K$ , the gas is heated by the scattering process.

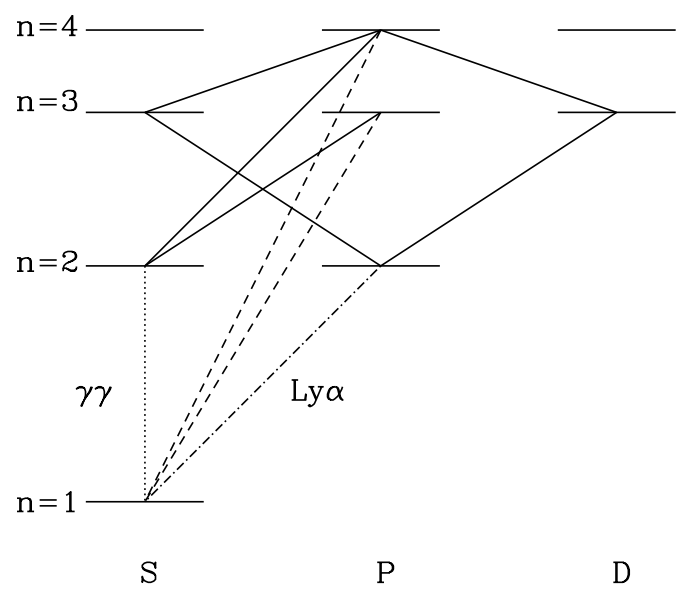


Figure 1.3: Decay chains for Lyman- $\beta$  and Lyman- $\gamma$  excitations. We show Lyman- $n$  transitions by dashed curves, Lyman- $\alpha$  by the dot-dashed curve, cascades by solid curves, and the forbidden  $2S \rightarrow 1S$  transition by the dotted curve. From [17].

To compute  $S_\alpha$ , we must calculate the photon spectrum near Lyman- $\alpha$ . We begin with the radiative transfer equation in an expanding universe (written in comoving coordinates, and again using units of photons cm $^{-2}$  sr $^{-1}$  Hz $^{-1}$  s $^{-1}$  for  $J_\nu$ ):

$$\frac{1}{cn_H\sigma_0} \frac{\partial J_\nu}{\partial t} = -\phi_\alpha(\nu) J_\nu + H\nu_\alpha \frac{\partial J_\nu}{\partial \nu} + \int d\nu' R(\nu, \nu') J_{\nu'} + C(t)\psi(\nu). \quad (1.22)$$

The first term on the right-hand side describes absorption, the second describes redshifting due to the Hubble flow, and the third accounts for re-emission following absorption.  $R(\nu, \nu')$  is the “redistribution function” that specifies the frequency of an emitted photon, which depends on the relative momenta of the absorbed and emitted photons as well as the absorbing atom. The last term accounts for the injection of new photons (via, e.g., radiative cascades that result in Lyman- $\alpha$  photons):  $C$  is the rate at which they are produced and  $\psi(\nu)$  is their frequency distribution.

The redistribution function  $R$  is the difficult aspect of the problem, but it can be simplified if the frequency change per scattering (typically of order the absorption line width) is “small.” In that case, we can expand  $J_{\nu'}$  to second order in  $(\nu - \nu')$  and rewrite equation (1.22) as a diffusion problem in frequency. The steady-state version of equation (1.22) becomes, in this so-called *Fokker-Planck* approximation, [2]

$$\frac{d}{dx} \left( -\mathcal{A}J + \mathcal{D} \frac{dJ}{dx} \right) + C\psi(x) = 0, \quad (1.23)$$

where  $x \equiv (\nu - \nu_\alpha)/\Delta\nu_D$ ,  $\Delta\nu_D$  is the Doppler width of the absorption profile,  $\mathcal{A}$  is the frequency drift rate, and  $\mathcal{D}$  is the diffusivity. The Fokker-Planck approximation is valid so long as (i) the frequency change per scattering ( $\sim \Delta\nu_D$ ) is smaller than the width of any spectral features, and either (iia) the photons are outside the line core where the Lyman- $\alpha$  line profile is slowly changing, or (iib) the atoms are in equilibrium with  $T_c \approx T_K$ .

Solving for the spectrum including scattering thus reduces to specifying  $\mathcal{A}$  and  $\mathcal{D}$ . The drift involves the Hubble flow, which sets  $\mathcal{A}_H = -\tau_\alpha^{-1}$ , where  $\tau_\alpha$  is the Gunn-Peterson optical depth for the Lyman- $\alpha$  line [11, 19]:

$$\tau_\alpha = \frac{\chi_\alpha n_{\text{HI}}(z)c}{H(z)\nu_\alpha} \approx 3 \times 10^5 x_{\text{HI}} \left( \frac{1+z}{7} \right)^{3/2}. \quad (1.24)$$

Because it is uniform, the Hubble flow does not introduce any diffusion. The remaining terms come from  $R$  and incorporate all the physical processes relevant to energy exchange in scattering. The drift from recoil causes [12]

$$\mathcal{D}_{\text{scatt}} = \phi_\alpha(x)/2, \quad (1.25)$$

$$\mathcal{A}_{\text{scatt}} = -(\eta - x_0^{-1})\phi_\alpha(x), \quad (1.26)$$

where  $x_0 \equiv \nu_\alpha/\Delta\nu_D$  and  $\eta \equiv (hv_\alpha^2)/(m_p c^2 \Delta\nu_D)$ . The latter is the recoil parameter measuring the average loss per scattering in units of the Doppler width. The small energy defect between the hyperfine levels provides another source of slow energy exchange [12] and can be incorporated into the scattering in nearly the same way as recoil.

We can now solve equation (1.23) once we choose the boundary conditions, which essentially correspond to the input photon spectrum (ignoring scattering) and the source function.

Because the frequency range of interest is so narrow, two cases suffice: a flat input spectrum (which approximately describes photons that redshift through the Lyman- $\alpha$  resonance, regardless of the initial source spectrum) and a step function, where photons are “injected” at line center (through cascades or recombinations) and redshift away. In either case, the first integral over  $x$  in equation (1.23) is trivial. At high temperatures where spin flips are unimportant to the overall energy exchange, we can write

$$\phi \frac{dJ}{dx} + 2\{[\eta - (x+x_0)^{-1}]\phi + \tau_\alpha^{-1}\}J = 2K/\tau_\alpha. \quad (1.27)$$

The integration constant  $K$  equals  $J_\infty$ , the flux far from resonance, both for photons that redshift into the line and for injected photons at  $x < 0$  (i.e., redward of line center); it is zero for injected photons at  $x > 0$ .

The formal analytic solution, when  $K \neq 0$ , is most compactly written in terms of  $\delta_J \equiv (J_\infty - J)/J_\infty$  [2]:<sup>5</sup>

$$\delta_J(x) = 2\eta \int_0^\infty dy \exp \left[ -2\{\eta - (x+x_0)^{-1}\}y - \frac{2}{\tau_\alpha} \int_{x-y}^x \frac{dx'}{\phi_\alpha(x')} \right]. \quad (1.28)$$

(An analogous form also exists for photons injected at line center.) The full problem, including the intrinsic Voigt profile of the Lyman- $\alpha$  line, must be solved numerically, but including only the Lorentzian wings from natural broadening allows a simpler solution [10]. Fortunately, this assumption is quite accurate in the most interesting regime of  $T_K < 1000$  K.

The crucial aspect of equation (1.28) is that (as expected from the qualitative argument) an absorption feature appears near the line center, with its depth roughly proportional to  $\eta$ , our recoil parameter. The feature is more significant when  $T_K$  is small (because in that case the average effect of recoil is large). Figure 1.4 shows some example spectra (both for a continuous background and for photons injected at line center).

Usually, the most important consequence is the suppression of the radiation spectrum at line center compared to the assumed initial condition. This decreases the total scattering rate of Lyman- $\alpha$  photons (and hence the Wouthuysen-Field coupling), with the suppression factor (defined in equation 2.3) as [2]

$$S_\alpha = \int_{-\infty}^\infty dx \phi_\alpha(x) J(x) \approx [1 - \delta_J(0)] \leq 1, \quad (1.29)$$

where the second equality follows from the narrowness of the line profile. Again, the Lorentzian wing approximation turns out to be an excellent one; when  $T_K \gg T_*$ , the suppression is [10]

$$S_\alpha \sim \exp \left[ -0.803 \left( \frac{T_K}{1 \text{ K}} \right)^{-2/3} \left( \frac{\tau_\alpha}{10^6} \right)^{1/3} \right]. \quad (1.30)$$

Note that this form applies to both photons injected at line center as well as those that redshift in from infinity. As we can see in Figure 1.4, the suppression is most significant in cool gas.

---

<sup>5</sup>Here we assume the gas has a sufficiently high temperature that the different hyperfine sub-transitions can be treated as one [12].

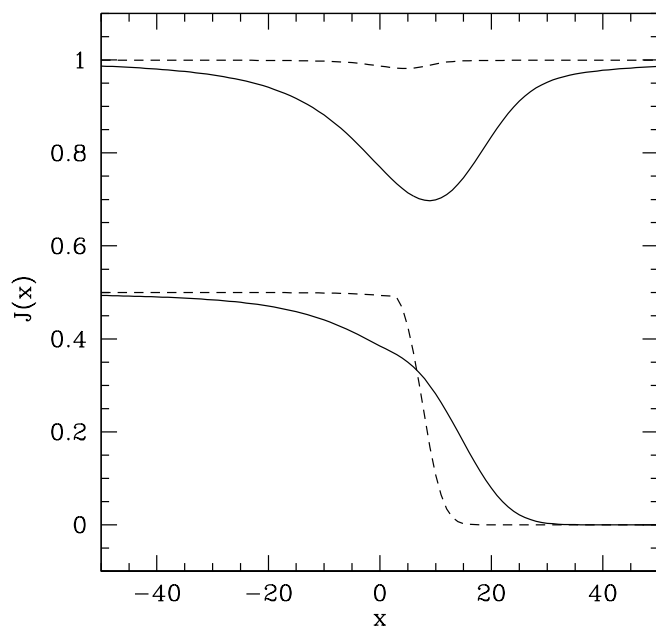


Figure 1.4: Background radiation field near the Lyman- $\alpha$  resonance at  $z = 10$ ;  $x \equiv (v - v_\alpha)/\Delta v_D$  is the normalized deviation from line center, in units of the Doppler width. The upper and lower sets are for continuous photons and photons injected at line center, respectively. (The former are normalized to  $J_\infty$ ; the latter have arbitrary normalization.) The solid and dashed curves take  $T_K = 10$  and 1000 K, respectively. From [10].

## 1.3 Heating of the Intergalactic Medium

We have seen that both collisions and the Wouthuysen-Field effect couple the spin temperature to the kinetic temperature of the gas. The 21-cm brightness temperature therefore depends on processes that heat the IGM. We will review several such mechanisms in this section.

### 1.3.1 The Lyman- $\alpha$ Background

The photons that trigger Lyman- $\alpha$  coupling exchange energy with the IGM, through the recoil in each scattering event. The typical energy exchange per scattering is small (see eq. 1.21), but the scattering rate is extremely large. If the net heating rate per atom followed the naive expectation,  $\sim P_\alpha \times (h\nu_\alpha)^2/m_p c^2$ , the kinetic temperature would surpass  $T_\gamma$  soon after Wouthuysen-Field coupling becomes efficient.

However, the details of radiative transfer radically change these expectations [2]. In a static medium, the energy exchange *must* vanish in equilibrium even though scattering continues at nearly the same rate. Scattering induces an asymmetric absorption feature near  $\nu_\alpha$  (Figure 1.4) whose shape depends on the combined effects of atomic recoils and the scattering diffusivity. In equilibrium, the latter exactly counterbalances the former.

If we removed scattering, the absorption feature would redshift away as the Universe expands. Thus, the energy exchange rate from scattering must simply be that required to maintain the feature in place. For photons redshifting into resonance, the absorption trough has total energy

$$\Delta u_\alpha = (4\pi/c) \int (J_\infty - J_v) h\nu dv, \quad (1.31)$$

where  $J_\infty$  is the input spectrum, and we note that the  $h\nu$  factor converts from our definition of specific intensity (which counts photons) to energy. The radiation background loses  $\varepsilon_\alpha = H\Delta u_\alpha$  per unit time through redshifting; this energy goes into heating the gas. Relative to adiabatic cooling by the Hubble expansion, the fractional heating amplitude is

$$\frac{2}{3} \frac{\varepsilon_\alpha}{k_B T_K n_H H(z)} = \frac{8\pi}{3} \frac{h\nu_\alpha}{k_B T_K} \frac{J_\infty \Delta v_D}{c n_H} \int_{-\infty}^{\infty} dx \delta_J(x) \quad (1.32)$$

$$\approx \frac{0.80}{T_K^{4/3}} \frac{x_\alpha}{S_\alpha} \left( \frac{10}{1+z} \right), \quad (1.33)$$

Here we have evaluated the integral for the continuum photons that redshift into the Lyman- $\alpha$  resonance; the “injected” photons actually cool the gas slightly. The net energy exchange when Wouthuysen-Field coupling becomes important (at  $x_\alpha \sim S_\alpha$ ) is therefore just a fraction of a degree, and in practice gas heating through Lyman- $\alpha$  scattering is generally unimportant [2, 10].

Fundamentally, Lyman- $\alpha$  heating is inefficient because scattering diffusivity cancels the effects of recoil. From Figure 1.4, we see that the background spectrum is weaker on the blue side of the line than on the red. The scattering process tends to move the photon toward line center, with the extra energy deposited in or extracted from the gas. Because more scattering occurs on the red side, this tends to transfer energy from the gas back to the photons, mostly canceling the energy obtained through recoil.

### 1.3.2 The Cosmic Microwave Background

The previous section shows that, when considered as a two-level process that acts in isolation, Lyman- $\alpha$  scattering has only a slight effect on the gas temperature. However, in reality this Lyman- $\alpha$  scattering always occurs in conjunction with scattering of CMB photons within the 21-cm transition. The combination leads to an enhanced heating rate [22].

In essence, the process works as follows. The CMB photons scatter through the hyperfine levels of HI to heat those atoms above their expected temperature (determined in this simple case by adiabatic cooling). Meanwhile, Lyman- $\alpha$  photons scatter through the gas as well. As they do so, they mix the hyperfine levels of the HI ground state, as depicted in Figure 1.2 – this is the Wouthuysen-Field effect. CMB scattering continues to heat the hyperfine level populations during the Lyman- $\alpha$  scattering, which then sweeps up this extra energy and ultimately deposits it as thermal energy through the net recoil effect.

We can estimate the energy available to this heating mechanism by considering the CMB energy reservoir [22]. The CMB energy density at the 21-cm transition is  $u_\nu = (4\pi/c)B_\nu \approx 8\pi(v_{21}^2/c^3)k_B T_\gamma$ . Over a redshift interval  $\Delta z = 1$ , the total energy that redshifts through the line is  $u_\nu \Delta\nu \approx 8\pi(v_{21}/c)^3 k_B T_\gamma / (1+z)^2$ . However, only a fraction  $\tau_{10}$  actually interacts with the line. If all of this energy is used for heating, the temperature change per H atom would be

$$\Delta T_{\text{CMB-Ly}\alpha} \approx \tau_{10} \frac{u_\nu \Delta\nu}{(3/2)n_H} \approx 5x_{\text{HI}} \left( \frac{1+z}{20} \right)^{-1/2} \left( \frac{10 \text{ K}}{T_S} \right) \text{ K.} \quad (1.34)$$

A more detailed calculation of the heating rate shows that it is somewhat slower, but it does amplify the effect of the Lyman- $\alpha$  heating alone by a factor of several [22]. In standard models of the early radiation backgrounds, the correction is still relatively modest, but it is not negligible. For example, in the fiducial model considered by [22], the Lyman- $\alpha$  heating on its own modifies  $T_K$  by  $\sim 1\text{--}5\%$ , but with the CMB scattering included the effect is  $\sim 9\text{--}15\%$ . Additionally, the CMB scattering can be enhanced in some exotic physics models that decrease the spin temperature substantially.

### 1.3.3 The X-ray Background

Because they have relatively long mean free paths, X-rays from galaxies and quasars are likely to be the most important heating agent for the low-density IGM [14]. In particular, photons with  $E > 1.5x_{\text{HI}}^{1/3}[(1+z)/10]^{1/2}$  keV have mean free paths exceeding the Hubble length [16]. Lower-energy X-rays will be absorbed in the IGM, depositing much of their energy as heat, as will a fraction of higher-energy X-rays.

X-rays heat the IGM gas by first photoionizing a hydrogen or helium atom. The resulting “primary” electron retains most of the photon energy (aside from that required to ionize it) as kinetic energy, which it must then distribute to the general IGM through three main channels: (1) collisional ionizations, which produce more secondary electrons that themselves scatter through the IGM, (2) collisional excitations of HeI (which produce photons capable of ionizing HI) and HI (which produces a Lyman- $\alpha$  background), and (3) Coulomb collisions with free electrons (which distributes the kinetic energy). The relative cross-sections of these processes determines what fraction of the X-ray energy goes to heating ( $f_{\text{heat}}$ ), ionization ( $f_{\text{ion}}$ ), and excitation ( $f_{\text{excite}}$ ); clearly it depends on both the ionized fraction  $x_i$  and the input photon

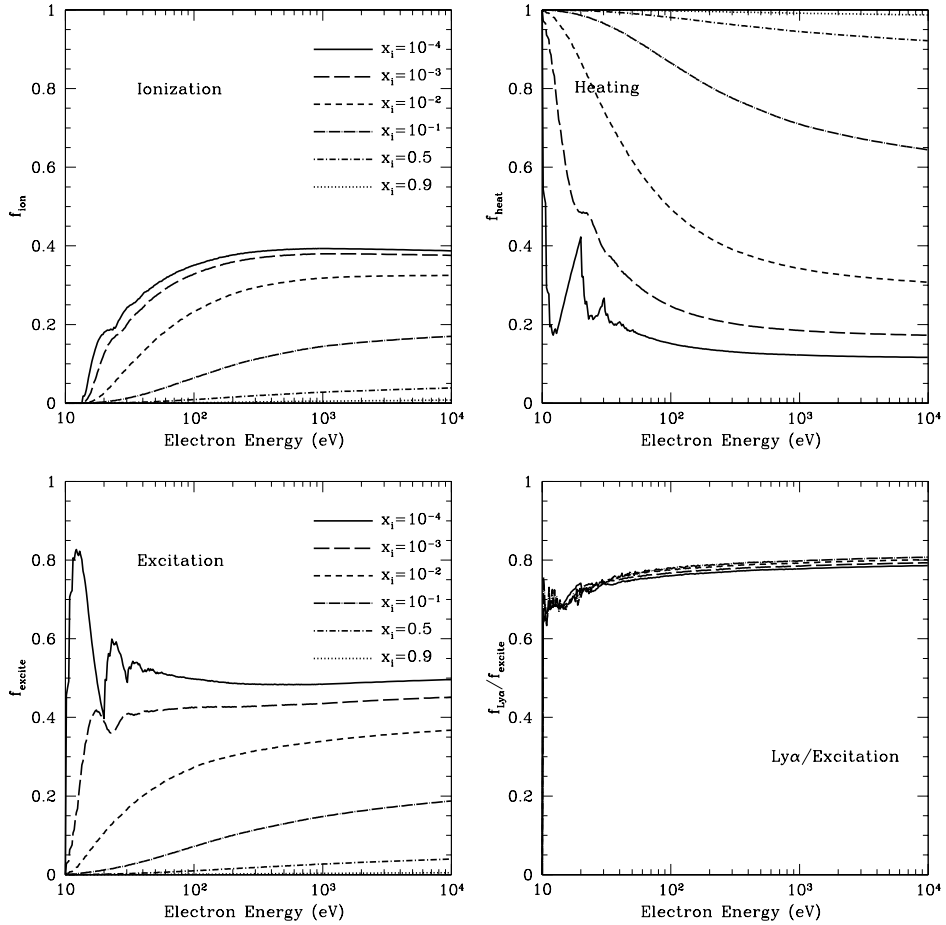


Figure 1.5: Energy deposition from fast electrons. We show the fraction of the initial energy deposited in ionization (upper left), heating (upper right), and collisional excitation (lower left), as a function of electron energy and for several different ionized fractions  $x_i$ . The lower right shows the fraction of the collisional excitation energy deposited in the HI Lyman- $\alpha$  transition,  $f_{\text{Ly}\alpha}$ . From [9].

energy. Through these scatterings, the primary photoelectrons, with  $T \sim 10^6$  K, rapidly cool to energies just below the Lyman- $\alpha$  threshold,  $< 10$  eV, and thus equilibrate with the other IGM electrons. After that, the electrons and neutrals equilibrate through elastic scattering on a timescale  $t_{\text{eq}} \sim 5[10/(1+z)]^3$  Myr. Because  $t_{\text{eq}} \ll H(z)^{-1}$ , the assumption of a single temperature fluid is an excellent one.

The details of this process have been examined numerically [20, 21, 9], and Figure 1.5 shows some example results. Note that the deposition fractions are smooth functions at high electron energies but, at low energies – where the atomic energy levels become relevant – can be quite complex. A number of approximate fits have been presented for the high-energy regime [18, 23], but they are not accurate over the full energy range. A crude but

useful approximation to the high-energy limit often suffices [1]:

$$\begin{aligned} f_{\text{heat}} &\sim (1 + 2x_i)/3 \\ f_{\text{ion}} \sim f_{\text{excite}} &\sim (1 - x_i)/3, \end{aligned} \quad (1.35)$$

where  $x_i$  is the ionized fraction. In highly ionized gas, collisions with free electrons dominate and  $f_{\text{heat}} \rightarrow 1$ ; in the opposite limit, the energy is split roughly equally between these three processes. However, the complexity of the behavior at low electron energies – together with the increasing optical thickness of the IGM in that regime, and the fact that most sources are brighter in this soft X-ray regime – suggest that a more careful treatment is needed for accurate work. [9] recommend interpolating the exact results.

# Bibliography

- [1] X. Chen and M. Kamionkowski. Particle decays during the cosmic dark ages. *PRD*, 70(4):043502, August 2004.
- [2] X. Chen and J. Miralda-Escudé. The Spin-Kinetic Temperature Coupling and the Heating Rate due to Ly $\alpha$  Scattering before Reionization: Predictions for 21 Centimeter Emission and Absorption. *ApJ*, 602:1–11, February 2004.
- [3] G. B. Field. Excitation of the Hydrogen 21-centimeter Line. *Proceedings of the Institute of Radio Engineers*, 46:240, 1958.
- [4] G. B. Field. An Attempt to Observe Neutral Hydrogen Between the Galaxies. *ApJ*, 129:525, May 1959.
- [5] G. B. Field. The Spin Temperature of Intergalactic Neutral Hydrogen. *ApJ*, 129:536, May 1959.
- [6] G. B. Field. The Time Relaxation of a Resonance-Line Profile. *ApJ*, 129:551, May 1959.
- [7] S. R. Furlanetto and M. R. Furlanetto. Spin-exchange rates in electron-hydrogen collisions. *MNRAS*, 374:547–555, January 2007.
- [8] S. R. Furlanetto and M. R. Furlanetto. Spin exchange rates in proton-hydrogen collisions. *MNRAS*, 379:130–134, July 2007.
- [9] S. R. Furlanetto and S. Johnson Stoever. Secondary ionization and heating by fast electrons. *MNRAS*, 404:1869–1878, June 2010.
- [10] S. R. Furlanetto and J. R. Pritchard. The scattering of Lyman-series photons in the intergalactic medium. *MNRAS*, 372:1093–1103, November 2006.
- [11] J. E. Gunn and B. A. Peterson. On the Density of Neutral Hydrogen in Intergalactic Space. *ApJ*, 142:1633–1636, November 1965.
- [12] C. M. Hirata. Wouthuysen-Field coupling strength and application to high-redshift 21-cm radiation. *MNRAS*, 367:259–274, March 2006.
- [13] Christopher M. Hirata and Kris Sigurdson. The spin-resolved atomic velocity distribution and 21-cm line profile of dark-age gas. *MNRAS*, 375(4):1241–1264, Mar 2007.

- [14] P. Madau, A. Meiksin, and M. J. Rees. 21 Centimeter Tomography of the Intergalactic Medium at High Redshift. *ApJ*, 475:429, February 1997.
- [15] A. Meiksin. Detecting the Epoch of First Light in 21-CM Radiation. In *Perspectives on Radio Astronomy: Science with Large Antenna Arrays*, e. M. P. van Haarlem, page 37, 2000.
- [16] S. P. Oh. Reionization by Hard Photons. I. X-Rays from the First Star Clusters. *ApJ*, 553:499–512, June 2001.
- [17] J. R. Pritchard and S. R. Furlanetto. Descending from on high: Lyman-series cascades and spin-kinetic temperature coupling in the 21-cm line. *MNRAS*, 367:1057–1066, April 2006.
- [18] M. Ricotti, N. Y. Gnedin, and J. M. Shull. The Fate of the First Galaxies. II. Effects of Radiative Feedback. *ApJ*, 575:49–67, August 2002.
- [19] P. A. G. Scheuer. A Sensitive Test for the Presence of Atomic Hydrogen in Intergalactic Space. *Nature*, 207:963, August 1965.
- [20] J. M. Shull and M. E. van Steenberg. X-ray secondary heating and ionization in quasar emission-line clouds. *ApJ*, 298:268–274, November 1985.
- [21] M. Valdés and A. Ferrara. The energy cascade from warm dark matter decays. *MNRAS*, 387:L8–L12, June 2008.
- [22] Tejaswi Venumadhav, Liang Dai, Alexander Kaurov, and Matias Zaldarriaga. Heating of the intergalactic medium by the cosmic microwave background during cosmic dawn. *PRD*, 98(10):103513, Nov 2018.
- [23] M. Volonteri and N. Y. Gnedin. Relative Role of Stars and Quasars in Cosmic Reionization. *ApJ*, 703:2113–2117, October 2009.
- [24] S. A. Wouthuysen. On the excitation mechanism of the 21-cm (radio-frequency) interstellar hydrogen emission line. *AJ*, 57:31, 1952.
- [25] B. Zygelman. Hyperfine Level-changing Collisions of Hydrogen Atoms and Tomography of the Dark Age Universe. *ApJ*, 622:1356–1362, April 2005.

# Chapter 2

## Astrophysics from the 21-cm background

**Jordan Mirocha**

The goal of this chapter is to describe the astrophysics encoded by the 21-cm background. We will begin in §2.1 with a general introduction to radiative transfer and ionization chemistry in gas of primordial composition. Then, in §2.2, we will introduce techniques used to model the UV and X-ray backgrounds that drive re-ionization and re-heating of the intergalactic medium (IGM). In §2.3, we will provide a review of the most plausible sources of ionization and heating in the early Universe, and in §2.4, we will summarize the status of current 21-cm predictions, build some intuition for how different model parameters affect the observable signals, and highlight the modeling tools available today.

### 2.1 Properties of the High- $z$ Intergalactic Medium

In this section we provide a general introduction to the intergalactic medium (IGM) and how its properties are expected to evolve with time. We will start with a brief recap of the 21-cm brightness temperature (2.1.1), then turn our attention to its primary dependencies, the ionization state and temperature of the IGM, and the radiative processes relevant to their evolution on scales large and small (§2.1.2). Readers familiar with the basic physics may skip ahead to §2.2, in which we focus specifically on how this physics is modeled in 21-cm modeling codes.

#### 2.1.1 The brightness temperature

The differential brightness temperature<sup>1</sup> of a patch of the IGM at redshift  $z$  and position  $\mathbf{x}$  is given by<sup>2</sup>

$$\delta T_b(z, \mathbf{x}) \simeq 27(1 + \delta)(1 - x_i) \left( \frac{\Omega_{b,0} h^2}{0.023} \right) \left( \frac{0.15}{\Omega_{m,0} h^2} \frac{1+z}{10} \right)^{1/2} \left( 1 - \frac{T_R}{T_S} \right), \quad (2.1)$$

---

<sup>1</sup>Can replace this first sub-section with pointers to Chapter 1 to avoid redundancy.

<sup>2</sup>Refer back to Chapter 1 for a more detailed introduction.

where  $\delta$  is the baryonic overdensity relative to the cosmic mean,  $x_i$  is the ionized fraction,  $T_R$  is the radiation background temperature (generally the CMB,  $T_R = T_\gamma$ ), and

$$T_S^{-1} \approx \frac{T_R^{-1} + x_c T_K^{-1} + x_\alpha T_\alpha^{-1}}{1 + x_c + x_\alpha}. \quad (2.2)$$

is the spin temperature, which quantifies the level populations in the ground state of the hydrogen atom, and itself depends on the kinetic temperature,  $T_K$ , and “colour temperature” of the Lyman- $\alpha$  radiation background,  $T_\alpha$ . Because the IGM is optically thick to Ly- $\alpha$  photons, the approximation  $T_K \approx T_\alpha$  is generally very accurate.

The collisional coupling coefficients,  $x_c$ , themselves depend on the gas density, ionization state, and temperature, and were computed as a function of temperature in [38]. The radiative coupling coefficient,  $x_\alpha$ , depends on the Ly- $\alpha$  intensity,  $J_\alpha$ , via

$$x_\alpha = \frac{S_\alpha}{1+z} \frac{\hat{J}_\alpha}{J_{\alpha,0}} \quad (2.3)$$

where

$$J_{\alpha,0} \equiv \frac{16\pi^2 T_\star e^2 f_\alpha}{27A_{10} T_{\gamma,0} m_e c}. \quad (2.4)$$

$\hat{J}_\alpha$  is the angle-averaged intensity of Ly- $\alpha$  photons in units of  $\text{s}^{-1} \text{cm}^{-2} \text{Hz}^{-1} \text{sr}^{-1}$ ,  $S_\alpha$  is a correction factor that accounts for variations in the background intensity near line-center [5, 12, 17],  $m_e$  and  $e$  are the electron mass and charge, respectively,  $f_\alpha$  is the Ly- $\alpha$  oscillator strength,  $T_{\gamma,0}$  is the CMB temperature today, and  $A_{10}$  is the Einstein A coefficient for the 21-cm transition.

A more detailed introduction to collisional and radiative coupling can be found in Chapter 1. For the purposes of this chapter, the key takeaway from Equations 2.1-2.3 is simply that the 21-cm background probes the ionization field, kinetic temperature field, and Ly- $\alpha$  background intensity. We quickly review the basics of non-equilibrium ionization chemistry in the next sub-section (§2.1.2) before moving on to techniques used to model these properties of the IGM in §2.2.

### 2.1.2 Basics of Non-Equilibrium Ionization Chemistry

As described in the previous section, the 21-cm brightness temperature of a patch of the IGM depends on the ionization and thermal state of the gas, as well as the incident Ly- $\alpha$  intensity<sup>3</sup>. The evolution of the ionization and temperature are coupled and so must be evolved self-consistently. The number density of hydrogen and helium ions in a static medium can be

---

<sup>3</sup>Note that Ly- $\alpha$  photons can transfer energy to the gas though we omit this dependence from the current discussion (see §1).

written as the following set of coupled differential equations<sup>4</sup>:

$$\frac{dn_{\text{H II}}}{dt} = (\Gamma_{\text{H I}} + \gamma_{\text{H I}} + \beta_{\text{H I}} n_e) n_{\text{H I}} - \alpha_{\text{H II}} n_e n_{\text{H II}} \quad (2.5)$$

$$\begin{aligned} \frac{dn_{\text{He II}}}{dt} &= (\Gamma_{\text{He I}} + \gamma_{\text{He I}} + \beta_{\text{He I}} n_e) n_{\text{He I}} + \alpha_{\text{He III}} n_e n_{\text{He III}} - (\beta_{\text{He II}} + \alpha_{\text{He II}} + \xi_{\text{He II}}) n_e n_{\text{He II}} \\ &\quad - (\Gamma_{\text{He II}} + \gamma_{\text{He II}}) n_{\text{He II}} \end{aligned} \quad (2.6)$$

$$\frac{dn_{\text{He III}}}{dt} = (\Gamma_{\text{He II}} + \gamma_{\text{He II}} + \beta_{\text{He II}} n_e) n_{\text{He II}} - \alpha_{\text{He III}} n_e n_{\text{He III}}. \quad (2.7)$$

Each of these equations represents the balance between ionizations of species H I, He I, and He II, and recombinations of H II, He II, and He III. Associating the index  $i$  with absorbing species,  $i = \text{H I}, \text{He I}, \text{He II}$ , and the index  $i'$  with ions,  $i' = \text{H II}, \text{He II}, \text{He III}$ , we define  $\Gamma_i$  as the photo-ionization rate coefficient,  $\gamma_i$  as the rate coefficient for ionization by photo-electrons [31, 15],  $\alpha_{i'}(\xi_{i'})$  as the case-B (dielectric) recombination rate coefficients,  $\beta_i$  as the collisional ionization rate coefficients, and  $n_e = n_{\text{H II}} + n_{\text{He II}} + 2n_{\text{He III}}$  as the number density of electrons.

While the coefficients  $\alpha$ ,  $\beta$ , and  $\xi$  only depend on the gas temperature, the photo- and secondary-ionization coefficients,  $\Gamma$  and  $\gamma$ , depend on input from astrophysical sources and thus constitute the bulk of the challenge for theoretical models. We will revisit these coefficients in more detail momentarily.

The final equation necessary in a primordial chemical network is that governing the kinetic temperature evolution, which we can write as a sum of various heating and cooling processes, i.e.,

$$\begin{aligned} \frac{3}{2} \frac{d}{dt} \left( \frac{k_B T_k n_{\text{tot}}}{\mu} \right) &= f^{\text{heat}} \sum_i n_i \Lambda_i - \sum_i \zeta_i n_e n_i - \sum_{i'} \eta_{i'} n_e n_{i'} \\ &\quad - \sum_i \psi_i n_e n_i - \omega_{\text{He II}} n_e n_{\text{He II}}. \end{aligned} \quad (2.8)$$

Here,  $\Lambda_i$  is the photo-electric heating rate coefficient (due to electrons previously bound to species  $i$ ),  $\omega_{\text{He II}}$  is the dielectric recombination cooling coefficient, and  $\zeta_i$ ,  $\eta_{i'}$ , and  $\psi_i$  are the collisional ionization, recombination, and collisional excitation cooling coefficients, respectively, where primed indices  $i'$  indicate ions HII, HeII, and HeIII, while unprimed indices  $i$  indicate neutrals HI, HeI, and HeII. The constants in Equation (2.8) are the total number density of baryons,  $n_{\text{tot}} = n_{\text{H}} + n_{\text{He}} + n_e$ , the mean molecular weight,  $\mu$ , Boltzmann's constant,  $k_B$ , and the fraction of photo-electron energy deposited as heat,  $f^{\text{heat}}$  [31, 15]. Formulae to compute the values of  $\alpha_i$ ,  $\beta_i$ ,  $\xi_i$ ,  $\zeta_i$ ,  $\eta_{i'}$ ,  $\psi_i$ , and  $\omega_{\text{He II}}$ , are compiled in numerous sources [11].

These equations do not yet explicitly take into account the cosmic expansion, which dilutes the density and adds an adiabatic cooling term to Eq. 2.8, however these generalizations are straightforward to implement in practice, as we will show in the next section. For the duration of this chapter we will operate within this simple chemical network, ignoring, e.g., molecular species like H<sub>2</sub> and HD whose cooling channels are important in primordial gases. Though an interesting topic in their own right, molecular processes reside in the “subgrid”

---

<sup>4</sup>Gabriel Altay pointed out a typo in my He equations many years ago...make sure that's fixed.

component of most 21-cm models, given that they influence how, when, and where stars are able to form (see §2.3), but do not directly affect the bulk properties of the IGM on large scales to which 21-cm measurements are sensitive.

### 2.1.3 Ionization and Heating Around Point Sources

In order to build intuition for the progression of ionization and heating in the IGM it is instructive to consider the impact of a single point source of UV and X-ray photons on its surroundings. Many early works focused on such 1-D radiative transfer problems, and many have subsequently been implemented in full cosmological calculations ([citations](#)). In principle, this is the ideal way to simulate reionization – iterating over all sources in a cosmological volume and for each one applying 1-D radiative transfer techniques over the surrounding  $4\pi$  steradians. In practice, such approaches are computationally expensive, and while they provide detailed predictions ([citations](#)), more approximate techniques are required to survey the parameter space and perform inference ([citations](#); see Brad’s chapter).

In 1-D, the change in the intensity of a ray of photons,  $I_\nu$ , is a function of the path length,  $s$ , the emissivity of sources along the path,  $j_\nu$ , and the absorption coefficient,  $\alpha_\nu$ ,

$$dI_\nu = j_\nu - \alpha_\nu I_\nu. \quad (2.9)$$

If considering a point source,  $j_\nu = 0$ , we can integrate to obtain

$$I_\nu(s) = I_{\nu,0} \exp \left[ - \int_0^s \alpha_\nu(s') ds' \right], \quad (2.10)$$

i.e., the intensity of photons declines exponentially along the ray. It is customary to define the optical depth,  $\tau_\nu$ , as

$$d\tau_\nu = \alpha_\nu ds, \quad (2.11)$$

in which case we can write

$$I_\nu(s) = I_{\nu,0} e^{-\tau_\nu}. \quad (2.12)$$

In the reionization context, the optical depth of interest is that of the IGM, which is composed of (almost) entirely hydrogen and helium<sup>5</sup>, in which case the optical depth is

$$\tau_\nu = \sum_i \sigma_{\nu,i} N_i \quad (2.13)$$

where  $i = \text{H}\text{I}, \text{He}\text{I}, \text{He}\text{II}$ , and  $N_i = \int_0^s ds' n_i(s')$  is the column density of each species along the ray.

With a solution for  $I_\nu(s)$  in hand, one can determine the photoionization and heating rates by integrating over all photon frequencies and weighting by the bound-free absorption cross section for each species. For example, the photoionization rate coefficient for hydrogen is given by

$$\Gamma_{\text{H}\text{I}}(s) = \int_{v_{\text{H}\text{I}}}^{\infty} \sigma_{\text{H}\text{I}} I_\nu(s) \frac{dv}{hv} \quad (2.14)$$

---

<sup>5</sup>Note that metals on small scales will also contribute some opacity, though in most models it is galaxies themselves that are the point sources of radiation from which we solve the RTE, rather than individual sources within galaxies. As a result, one’s choice of source spectrum should encode any intrinsic attenuation from metals (or H and He) in the interstellar medium. See §2.3 for more details.

where  $v_{\text{HI}}$  is the frequency of the hydrogen ionization threshold,  $h\nu = 13.6 \text{ eV}$ .

Note that in practice the RTE is solved on a grid, in which case it may be difficult to achieve high enough spatial resolution to ensure photon conservation. For example, a discretized version of Eq. 2.14 uses the intensity of radiation incident upon the face of a resolution element to calculate the photoionization rate within that element, but the radiation incident on the subsequent resolution element is not guaranteed correctly reflect the attenuation within the preceding element. As a result, in order to guarantee photon conservation, it is common to slightly reframe the calculation as follows [2]:

$$\Gamma_i = A_i \int_{v_i}^{\infty} I_v e^{-\tau_v} \left(1 - e^{-\Delta\tau_{i,v}}\right) \frac{dv}{hv} \quad (2.15)$$

$$\gamma_{ij} = A_j \int_{v_j}^{\infty} \left(\frac{v - v_j}{v_i}\right) I_v e^{-\tau_v} \left(1 - e^{-\Delta\tau_{j,v}}\right) \frac{dv}{hv} \quad (2.16)$$

$$\Lambda_i = A_i \int_{v_i}^{\infty} (v - v_i) I_v e^{-\tau_v} \left(1 - e^{-\Delta\tau_{i,v}}\right) \frac{dv}{v}, \quad (2.17)$$

The normalization constant in each expression is defined as  $A_i \equiv L_{\text{bol}}/n_i V_{\text{sh}}(r)$ , where  $V_{\text{sh}}$  is the volume of a shell in this 1-D grid of concentric spherical shells, each having thickness  $\Delta r$  and volume  $V_{\text{sh}}(r) = 4\pi[(r + \Delta r)^3 - r^3]/3$ , where  $r$  is the distance between the origin and the inner interface of each shell. We denote the ionization threshold energy for species  $i$  as  $h\nu_i$ .  $I_v$  represents the SED of radiation sources, and satisfies  $\int_v I_v dv = 1$ , such that  $L_{\text{bol}}I_v = L_v$ . Note that the total secondary ionization rate for a given species is the sum of ionizations due to the secondary electrons from all species, i.e.,  $\gamma_i = f_{\text{ion}} \sum_j \gamma_{ij} n_j / n_i$ .

These expressions preserve photon number by inferring the number of photo-ionizations of species  $i$  in a shell from the radiation incident upon it and its optical depth [2],

$$\Delta\tau_{i,v} = n_i \sigma_{i,v} \Delta r. \quad (2.18)$$

This quantity is not to be confused with the total optical depth between source and shell,  $\tau_v = \tau_v(r)$ , which sets the incident radiation field upon each shell, i.e.,

$$\begin{aligned} \tau_v(r) &= \sum_i \int_0^r \sigma_{i,v} n_i(r') dr' \\ &= \sum_i \sigma_{i,v} N_i(r) \end{aligned} \quad (2.19)$$

where  $N_i$  is the column density of species  $i$  at distance  $r$  from the source.

In words, Equations 2.15-2.17 are propagating photons from a source at the origin, with bolometric luminosity  $L_{\text{bol}}$ , and tracking the attenuation suffered between the source and some volume element of interest at radius  $r$ ,  $e^{-\tau}$ , and the attenuation within that volume element,  $\Delta\tau$ , which results in ionization and heating. In each case, we integrate over the contribution from photons at all frequencies above the ionization threshold, additionally modifying the integrands for  $\gamma_{ij}$  and  $\Lambda_i$  with  $(v - v_i)$ -like factors to account for the fact that both the number of photo-electrons (proportional to  $(v - v_j)/v_i$ ) and their energy (proportional to  $v - v_i$ ) that determine the extent of secondary ionization and photo-electric heating. **Forgot to put the factors  $f_{\text{heat}}$  and  $f_{\text{ion}}$  in above equations.**

Equations 2.15-2.17 can be solved once a source luminosity,  $L_{\text{bol}}$ , spectral shape,  $I_{\nu}$ , and density profile of the surrounding medium,  $n(r)$ , have been specified. In practice, to avoid performing these integrals on each step of an ODE solver (for Eqs. 2.5-2.8), the results can be tabulated as a function of  $\tau$  or column density,  $N_i$ , where  $\tau_{i,\nu} = \sigma_{i,\nu} N_i$  [35, 25].

Show some example results from, e.g., Thomas et al. 2008.

## 2.1.4 Ionization and Heating on Large Scales

While the procedure outlined in the previous section is relevant to small-scale ionization and heating, i.e., that which is driven by a single (or perhaps a few) source(s) close to a volume element of interest, it is also instructive to consider the ionization and heating caused by a *population* of sources separated by great distances. In this limit, rather than considering the luminosity of a single source at the origin of a 1-D grid, we treat the volume-averaged emissivity of sources in a large “chunk” of the Universe, and solve for the evolution of the mean intensity in this volume.

The transfer equation now takes its cosmological form, i.e.,

$$\left( \frac{\partial}{\partial t} - v H(z) \frac{\partial}{\partial v} \right) J_{\nu}(z) + 3H(z) J_{\nu}(z) = \frac{c}{4\pi} \varepsilon_{\nu}(z) (1+z)^3 - c \alpha_{\nu} J_{\nu}(z) \quad (2.20)$$

where  $J_{\nu}$  is the mean intensity in units of  $\text{erg s}^{-1} \text{cm}^{-2} \text{Hz}^{-1} \text{sr}^{-1}$ ,  $v$  is the observed frequency of a photon at redshift  $z$ , related to the emission frequency,  $v'$ , of a photon emitted at redshift  $z'$  as

$$v' = v \left( \frac{1+z'}{1+z} \right), \quad (2.21)$$

$\alpha_{\nu} = n \sigma_{\nu}$  is the absorption coefficient, not to be confused with recombination rate coefficient,  $\alpha_{\text{HII}}$ , and  $\varepsilon_{\nu}$  is the co-moving emissivity of sources.

The optical depth,  $d\tau = \alpha_{\nu} ds$ , experienced by a photon at redshift  $z$  and emitted at  $z'$  is a sum over absorbing species,

$$\bar{\tau}_{\nu}(z, z') = \sum_j \int_z^{z'} n_j(z'') \sigma_{j,\nu''} \frac{dl}{dz''} dz'' \quad (2.22)$$

To be fully general, one must iteratively solve this and  $J_{\nu}$ . In practice, you can tabulate  $\tau$  and it works pretty good.

The solution to Equation 2.20 assuming X, Y, and Z is

$$\hat{J}_{\nu}(z) = \frac{c}{4\pi} (1+z)^2 \int_z^{z_f} \frac{\varepsilon'_{\nu}(z')}{H(z')} e^{-\bar{\tau}_{\nu}} dz'. \quad (2.23)$$

where  $z_f$  is the “first light redshift” when astrophysical sources first turn on,  $H$  is the Hubble parameter, and the other variables take on their usual meaning. Talk briefly about how this can be solved efficiently.

With the background intensity in hand, one can solve for the rate coefficients for ionization and heating, and evolve the ionization state and temperature of the gas. These coefficients are equivalent to those for the 1-D problem (Eqs. 2.15-2.17), though the intensity

of radiation at some distance  $R$  from the source has been replaced by the mean background intensity. They are:

$$\Gamma_{\text{HI}}(z) = 4\pi n_{\text{H}}(z) \int_{v_{\min}}^{v_{\max}} \hat{J}_v \sigma_{v,\text{HI}} dv \quad (2.24)$$

$$\gamma_{\text{HI}}(z) = 4\pi \sum_j n_j \int_{v_{\min}}^{v_{\max}} f_{\text{ion}} \hat{J}_v \sigma_{v,j} (hv - hv_j) \frac{dv}{hv} \quad (2.25)$$

$$\epsilon_X(z) = 4\pi \sum_j n_j \int_{v_{\min}}^{v_{\max}} f^{\text{heat}} \hat{J}_v \sigma_{v,j} (hv - hv_j) dv \quad (2.26)$$

Note similarities between these equations and the 1-D example in previous section.

## 2.2 Techniques for Modeling the IGM

In the previous section we introduced the basics of ionization chemistry and radiative transfer in a primordial medium, and explored extreme limits on very small and very large scales. These limits bracket the range of possibilities for volume elements, which “see” radiation from a single (or few) source(s) nearby or the combined radiative output of many sources at cosmological distances. **Reality is often somewhere between.** The mean free path of photons in a hydrogen-only medium is [21]

$$\lambda_{\text{HI}} \approx 7x_{\text{H I}}^{-1} \left( \frac{hv}{200 \text{ eV}} \right)^{2.6} \left( \frac{1+z}{10} \right)^{-2} \text{ cMpc}, \quad (2.27)$$

i.e., mean-free paths for UV photons with  $hv < 0.1 \text{ keV}$  (or so) are very short. Because the mean free paths of UV photons are short, the IGM is divided roughly into two different phases: (i) a fully-ionized phase composed of “bubbles,” which grow around UV sources, and (ii) a “bulk IGM” phase outside bubbles in which ionization and heating is dominated by X-rays. The boundaries between these two phases can become fuzzy if reionization is driven by sources with hard spectra. However, even in such cases, the two-phase picture is a useful conceptual framework for understanding evolution in the 21-cm background, and provides a basis for approximations to the radiative transfer that have enabled the development of more efficient approaches to modeling the 21-cm background.

In this section, we describe the evolution of the ionization and temperature fields in this two-zone framework, in each case focusing first on the volume-averaged evolution relevant to the global 21-cm signal, and then the spatial structure relevant for 21-cm fluctuations. We will revisit extensions of the two-phase approximation in later sections.

Note that for now, we will not specify the properties of UV and X-ray sources, but instead fold their properties into a single time-, frequency-, and position-dependent emissivity,  $\epsilon = \epsilon_v(z, R)$ . Models for  $\epsilon$  will be put forth in §2.3, from which 21-cm predictions will follow in §2.4.

### 2.2.1 The Density Field

**Do we want to delve into this here?**

## 2.2.2 The Ionization Field

### Global Evolution

In the two phase approximation of the IGM, the volume-averaged ionized fraction is a weighted average between the fully-ionized phase, with volume filling fraction  $Q_{\text{HII}}$ , and the (likely) low-level ionization in the bulk IGM phase, characterized by its electron fraction,  $x_e$ , i.e.<sup>6</sup>,

$$\bar{x}_i = Q_{\text{HII}} + (1 - Q_{\text{HII}})x_e \quad (2.28)$$

In the limit of negligible ionization in the bulk IGM phase,  $\bar{x}_i \approx Q_{\text{HII}}$ , we recover the standard ionization balance equation for reionization (e.g., Madau et al., others),

$$\frac{dQ_{\text{HII}}}{dt} = n_{\text{H I}}\Gamma_{\text{HI}} - n_e n_{\text{H II}}\alpha_{\text{HII}} \quad (2.29)$$

where we have written the rate coefficient for photo-ionization generically as **the ionization photon production rate**...We have also neglected collisional ionization and ionization by hot photo-electrons, though such effects could be absorbed into  $\Gamma_{\text{HI}}$ <sup>7</sup>.

The mean ionization history is currently only crudely constrained. High- $z$  quasar spectra suggest that reionization ended at  $z \sim 6$  but provide no information on the detailed history. The CMB optical depth provides an integral constraint on reionization, i.e.,

$$\tau_e = \int_0^{R_{\text{ls}}} ds n_e(s) \sigma_T \quad (2.30)$$

where  $\sigma_T = 6.65 \times 10^{-25} \text{ cm}^{-2}$  is the Thomson cross section, and  $R_{\text{ls}}$  is the distance to the last scattering surface, and thus only roughly constrains the timing and duration of reionization.

In principle there is much more information in the spatial fluctuations in the ionization field, simple models for which we discuss in the next section.

Show predictions for  $Q_{\text{HII}}$  compared to constraints from CMB, quasars, LAEs.

### Spatial Structure

While the evolution of the average ionized fraction contains a wealth of information about the properties of UV (and perhaps X-ray) sources in the early Universe, fluctuations in the ionization field contain much more information. Indeed, the patchy “swiss cheese” structure generic to UV-driven reionization scenarios provided the initial impetus to study reionization via 21-cm interferometry [20].

If computational resources were no issue, radiative transfer simulations would be the ideal tool to approach this problem for reasons that will be apparent momentarily. However, once again, the two-phase approximation opens the door to a simple statistical treatment of

---

<sup>6</sup>Note that we should be more careful about  $x_e$  and  $x_{\text{H II}}$ . the former is important for collisional coupling, the latter for  $\bar{x}_i$

<sup>7</sup>Secondary ionization is generally unimportant in HII regions since stars do not emit much above 1 Rydberg. As a result, photo-electrons are incapable of causing further ionization, and instead deposit most of their energy in heat or collisional excitation.

fluctuations in the ionization field. Given that 21-cm fluctuation efforts are geared largely toward measuring the 21-cm power spectrum, here we restrict our discussion to the ionization power spectrum, which forms a part of the 21-cm power spectrum that we will describe in more detail in §2.4. We will follow closely the early work of [13] in what follows.

The power spectrum of the ionization field is simply the Fourier transform of its two-point correlation function, which we can write as

$$\xi \equiv \langle x_i x'_i \rangle - \langle x_i \rangle^2, \quad (2.31)$$

where  $x_i$  is the ionized fraction at a point  $\mathbf{p}$ , while  $x'_i$  is the ionized fraction at a point  $\mathbf{p}' = \mathbf{p} + \mathbf{R}$ , i.e., a different point a distance  $\mathbf{R}$  from the first point. The expectation value is related to the joint probability, i.e.,

$$\langle x_i x'_i \rangle = \int dx_i \int dx'_i x_i x'_i f(x_i, x'_i). \quad (2.32)$$

If we now assume that ionization in the “bulk” IGM is negligible,  $x_i$  is a binary field, taking on values of 0 or 1 exclusively. In this limit, the expectation value is simply

$$\langle x_i x'_i \rangle = f(x_i = 1, x'_i = 1) \equiv P_{ii}, \quad (2.33)$$

i.e.,  $\langle x_i x'_i \rangle$  is equivalent to the probability that both points are ionized.

Now, to model the probability of ionization we first assume that the ionizatoin field is composed of discrete, spherical bubbles, with size distribution  $dn/dR$ . Then, taking inspiration from the halo model [6], we can write  $P_{ii}$  as the sum of two terms,

$$P_{ii} = P_{ii,1b} + P_{ii,2b} \quad (2.34)$$

where the first term encodes the probability that both points are within a single bubble (hence the “1b” subscript), while the second term is the probability that points are in two different bubbles.

Two points separated by  $r_{12}$  can be ionized by the same bubble so long as the diameter of the bubble is the distance between the points or greater. For bubbles bigger than the absolute minimum ( $r_{12}$ ), there is an “overlap region,” with volume  $\mathcal{V}$ , in which a bubble of mass  $m$  can ionize both points.

If  $p_1$  is ionized, then the probability that  $p_2$  is ionized by the same source will be equal to the probability that a sufficiently large source, with mass  $m$ , resides within the overlap region of  $p_1$  and  $p_2$ , whose volume depends on their separation. The overlap region,  $V_o$ , is thus given by the area of intersection between two spheres, assumed here to have the same radius  $R$ , placed a distance  $r_{12}$  apart,

$$\mathcal{V} = \begin{cases} \frac{4}{3}\pi R(m)^2 - \pi r_{12} \left[ R(m)^2 - \frac{r_{12}^2}{12} \right] & r_{12} \leq 2R(m) \\ 0 & r_{12} > 2R(m) \end{cases} \quad (2.35)$$

We will denote the probability that two points are ionized by a source of mass  $m$  as  $P[m, \mathcal{V}(m, r_{12})]$ .

This argument results in an infinite sum over probabilities, with each successive terms corresponding to the probability that a point is ionized by increasingly large bubbles (accounting for the probability that smaller bubbles could *not* ionize both points, i.e., the product of the negation of all previous terms), i.e.,

$$\begin{aligned} P_{ii,1}(r_{12}) &= P[m_1, \mathcal{V}(m_1, r_{12})] \\ &\quad + (1 - P[m_1, \mathcal{V}(m_1, r_{12})])P[m_2, \mathcal{V}(m_2, r_{12})] + \dots \\ &= 1 - \exp \left[ \sum_i \log(1 - P_i) \right] \end{aligned} \quad (2.36)$$

To compute the probabilities, we need only the abundance of sources as a function of their mass, which we will leave as a general quantity,  $n(m)$ , for now, and the overlap volume, i.e.,

$$P[m_1, \mathcal{V}(m_1, r_{12})] = n(m_1) \mathcal{V}(m_1, r_{12}) \quad (2.37)$$

The final step is to realize that  $P_i = 1 - \exp[-n_i V_i]$ , which follows from a Poissonian argument, i.e., assuming that

$$P_i = \frac{\lambda^N e^{-\lambda}}{N!}. \quad (2.38)$$

However, we are uninterested in exactly how many sources ionize a point – we care only about whether the point is ionized – so we need only compute the probability that there's *not* a source in the volume, and subtract that from unity to obtain the probability that there's *any kind of* source in the volume. We know the mean number of bubbles, so we can make a Poissonian argument with  $N = 0$  to determine this probability, i.e.,

$$P(N \geq 1) = 1 - P(N = 0) = 1 - e^{-\lambda} \quad (2.39)$$

So, the probability that two points like in a single ionized bubble is

$$P_{ii,1}(r_{12}) = 1 - \exp \left[ - \sum_i n(m_i) \mathcal{V}(m_i, r_{12}) \right] \quad (2.40)$$

The other possibility is that two points are members of two different bubbles, which we denote with the probability  $P_{ii,2}$ . The probability of this occurring is the probability that a single source *cannot* ionize both points, times the probability that a source of mass  $m$  is able to ionize the first point but not the second. If we visualize the overlap of two spheres, we need the second source *not* to reside in the overlap region. So, we can simply replace  $\mathcal{V} \rightarrow V(m) - \mathcal{V}$  in Equation 2.39, and square it (to obtain probability of two sources). The total probability is then

$$\begin{aligned} \langle xx' \rangle &= P_{ii,1} + P_{ii,2} \\ &= 1 - \exp \left[ - \int n(m) \mathcal{V}(m, r_{12}) dm \right] \\ &\quad + \exp \left[ - \int n(m) \mathcal{V}(m, r_{12}) dm \right] \times \left\{ 1 - \exp \left[ - \int n(m) (V(m) - \mathcal{V}(m, r_{12})) dm \right] \right\}^2 \end{aligned} \quad (2.41)$$

This is only valid if we neglect clustering of sources. In reality, if we're in the neighborhood of a bubble, there's a good chance there's another bubble nearby. So, we can replace one of the terms in curly braces with  $n(m) \rightarrow n(m)(1 + \xi_{bb}(m, r_{12}))$ , where  $\xi_{bb}$  is the excess probability of finding a bubble of mass  $m$  a distance  $r_{12}$  away from another bubble.

At this point, it is clear that the “bubble size distribution”, or equivalent bubble mass distribution,  $n(m)$ , of sources will determine the nature of the ionization field. **Very quickly summarize the results of the excursion set approach and defer to references here.** Point to §2.4.3 for a discussion of how codes do this in practice.

Things to mention here:

- Photon conservation can be a problem.
- Dealing with overlap is a problem.

Show ionization power spectra and maybe cross spectra with density field.

### Recombinations

Will need to describe the challenge here in some detail, defer to §2.4 for how one deals with this in semi-numeric and numerical simulations.

### 2.2.3 The (Kinetic) Temperature Field

Energetic X-ray photons with  $E > 100$  eV will be able to travel large distances due to the strong energy dependence of the bound-free cross section (see Eq. 2.27). As a result, the ionization state and temperature of gas in the “bulk IGM” spans a continuum of values and must be evolved in detail.

This section needs quite a bit more work!

### Global Evolution

The largely binary nature of the ionization field results in models designed to describe the fractional volume of ionized gas and the size distribution of individual ionized regions. This binarity will be reflected in the temperature field as well given that ionized regions will be  $\sim 10^4$  K, while the rest of the bulk IGM will generally be much cooler. However, given that the 21-cm background is insensitive to the temperature within ionized regions, in what follows the mean kinetic temperature will *not* refer to a volume-averaged temperature, but rather the average temperature of gas outside fully-ionized regions.

Modeling the temperature in the bulk of the IGM in a general case is best handled by radiative transfer simulations. However, such simulations can be even more challenging than those targeting the ionization field given that (i) the mean-free paths of relevant photons are longer, (ii) the frequency-dependence of the ionization and heating rates is important, which means multi-frequency calculations are necessary, and (iii) heating generally precedes reionization, meaning smaller halos must be resolved at earlier times.

It is useful to consider first a case in which heating of the IGM is spatially uniform, which could occur if the sources of heating have very hard spectra. In this limit, we can consider the evolution of the average background intensity,

Show simple models a la Pritchard & Loeb.

## Spatial Structure

Talk about Jonathan's 2007 approach, Janakee's stuff, 21CMFAST approach, progress in RT sims (hard because X-ray mfp long). Ross et al. simulations.

Show example temperature power spectrum from, e.g., Pritchard & Furlanetto, and/or pictures from Andrei's 2013 paper. Point out dependence on normalization and spectral slope.

### 2.2.4 The Ly- $\alpha$ Background

This section needs quite a bit more work! Will discuss early Barkana stuff, Holzbauer & Furlanetto approach, semi-numeric treatments, Ahn et al.

#### Global Evolution

The Ly- $\alpha$  background intensity, which determines the strength of Wouthuysen-Field coupling [37, 10], requires a special solution to the cosmological radiative transfer equation (see Eq. 2.20). Two effects separate this problem from the generic transfer problem outlined in the previous section: (i) the Lyman series forms a series of horizons for photons in the  $10.2 < h\nu/\text{eV} < 13.6$  interval, and (ii) the Ly- $\alpha$  background is sourced both by photons redshifting into the line resonance as well as those produced in cascades downward from higher  $n$  transitions.

It is customary to solve the RTE in small chunks in frequency space. Within each chunk, the optical depth of the IGM is small<sup>8</sup>, while the edges are semi-permeable. For illustrative purposes, let us isolate the Ly- $\alpha$  background intensity sourced by photons redshifting into resonance from frequencies redward of Ly- $\beta$ .

is computed analogously via

$$\hat{J}_\alpha(z) = \frac{c}{4\pi} (1+z)^2 \sum_{n=2}^{n_{\max}} f_{\text{rec}}^n \int_z^{z_{\max}^{(n)}} \frac{\mathcal{E}'_V(z')}{H(z')} dz' \quad (2.42)$$

where  $f_{\text{rec}}^n$  is the “recycling fraction,” that is, the fraction of photons that redshift into a Ly- $n$  resonance that ultimately cascade through the Ly- $\alpha$  resonance [27]. We truncate the sum over Ly- $n$  levels at  $n_{\max} = 23$  as in [3], and neglect absorption by intergalactic  $H_2$ . The upper bound of the definite integral,

$$1 + z_{\max}^{(n)} = (1+z) \frac{[1 - (n+1)^{-2}]}{1 - n^{-2}}, \quad (2.43)$$

is set by the horizon of Ly- $n$  photons – a photon redshifting through the Ly- $n$  resonance at  $z$  could only have been emitted at  $z' < z_{\max}^{(n)}$ , since emission at slightly higher redshift would mean the photon redshifted through the Ly( $n+1$ ) resonance.

Talk about excitation of Lyman alpha by photo-electrons.

---

<sup>8</sup>But for a small  $H_2$  contribution, which here we neglect.

### Spatial Fluctuations in the Ly- $\alpha$ background

Show a figure or two from Barkana & Loeb or Holzbauer & Furlanetto.

### Ly- $\alpha$ Heating

Talk briefly about initial papers about Ly- $\alpha$  heating, the subsequent revisions, and the revival of this concept in the last year or so.

### Excitation of Ly- $\alpha$ via fast photo-electrons

Brief discussion.

## 2.3 Sources of the UV and X-ray Background

In the previous section we outlined a procedure for evolving the ionization and temperature field without actually specifying the sources of ionization and heating. Instead, we used a generic emissivity,  $\varepsilon_v$ , to encode the integrated emissions of sources at frequency  $v$  within some region  $R$ , which we will now write as an integral over the differential luminosity function of sources, i.e.,

$$\varepsilon_v(z, R) = \int_0^\infty dL_v \frac{dn}{dL_v}. \quad (2.44)$$

Given the success of models which link the evolution of galaxies to the evolution of their host dark matter halos (citations), it is common to rewrite the emissivity as an integral over the DM halo mass function (HMF),  $dn/dm$ , multiplied by a conversion factor between halo mass and galaxy light,  $dm/dL_v$ , i.e.,

$$\varepsilon_v(z, R) = \int_{m_{\min}}^\infty dm \frac{dn}{dm} \frac{dm}{dL_v}, \quad (2.45)$$

where  $m_{\min}$  is the minimum mass of DM halos capable of hosting galaxies. Because  $dn/dm$  is reasonably well-determined from large N-body simulations of structure formation (citations), much of the modeling focus is on the mass-to-light ratio,  $dm/dL_v$ , which encodes the efficiency with which galaxies form in halos and the relative luminosities of different kinds of sources within galaxies (e.g., stars, compact objects, diffuse gas) that emit at different frequencies<sup>9</sup>.

The main strength of the 21-cm background as a probe of high- $z$  galaxies is now apparent: though 21-cm measurements cannot constrain the properties of individual galaxies, they can constrain the properties of *all* galaxies, in aggregate, *even those too faint to be detected directly*. As a result, it is common to forego detailed modeling of the mass-to-light ratio and instead relate the emissivity to the fraction of mass in the Universe in collapsed objects,

$$\varepsilon_v(z, R) = \rho_b f_{\text{coll}}(z, R) \zeta_v, \quad (2.46)$$

---

<sup>9</sup>Most models consider regions  $R$  that are sufficiently large that one can assume a well-populated HMF, though at very early times this approximation may break down, rendering stochasticity due to poor HMF sampling an important effect.

where the collapsed fraction is an integral over the HMF,

$$f_{\text{coll}} = \rho_m^{-1} \int_{m_{\text{min}}}^{\infty} dm m \frac{dn}{dm} \quad (2.47)$$

and  $\zeta_v$  is an efficiency factor that quantifies the number of photons emitted at frequency  $v$  per baryon of collapsed mass in the Universe. It is generally modeled as

$$\zeta_v = f_* N_v f_{\text{esc},v}, \quad (2.48)$$

where  $f_*$  is the star formation efficiency (SFE),  $N_v$  is the number of photons emitted per stellar baryon at some frequency  $v$ , and  $f_{\text{esc}}$  is the fraction of those photons that escape into the IGM. One could define additional  $\zeta$  factors to represent, e.g., emission from black holes or exotic particles, in which case  $f_*$  and  $N_v$  would be replaced by some black hole or exotic particle production efficiencies. In practice, three  $\zeta$  factors are defined:  $\zeta$ ,  $\zeta_X$ , and  $\zeta_\alpha$ , i.e., one efficiency factor for each radiation background of interest. A minimal model for the 21-cm background thus contains four parameters:  $m_{\text{min}}$ ,  $\zeta$ ,  $\zeta_X$ , and  $\zeta_\alpha$ .

Because the factors within  $\zeta$  are degenerate with each other, at least as far as 21-cm measurements are concerned, they generally are not treated separately as free parameters. However, it is still useful to consider each individually in order to determine a fiducial value of  $\zeta$  and explore deviations from that fiducial model. In addition, inclusion of ancillary measurements may eventually allow  $\zeta$  to be decomposed into its constituent parts. For the remainder of this section, we focus on plausible values of  $f_*$ ,  $N_v$  and  $f_{\text{esc}}$ .

### 2.3.1 Star Formation

Current high- $z$  measurements support a relatively simple picture of star formation in early galaxies. The basic idea is that star formation is fueled by the inflow of gas from the IGM, but the overall rate of star formation in galaxies is self-limiting because winds and supernovae explosions expell gas that would otherwise form stars ([many many references](#)). Qualitatively, the need for some kind of feedback is apparent simply from the mismatch in shapes between the halo mass function and galaxy luminosity function, the latter of which is steeper at both the very bright and very faint ends.

[Introduce MAR-driven models, semi-empirical constraints, etc.](#)

[Show example SFE recovered from UVLF fits. Variations in expectations at very high- \$z\$ .](#)

#### Pop III Star Formation

The very first generations of stars to form in the Universe did so under very different conditions than stars today, and it is not clear that the arguments outlined in the previous section apply. The first stars, by definition, formed from chemically-pristine material, since no previous generations of stars had existed to enrich the medium with heavy elements. This has long been recognized as a reason that the first stars are likely different than stars today ([references](#)). Without the energetically low-lying electronic transitions common in heavy elements, hydrogen-only gas clouds cannot cool efficiently, as collisions energetic enough to excite atoms from  $n = 1$  to  $n = 2$  (which subsequently cool via spontaneous emission of

$\text{Ly}-\alpha$  photons) imply temperatures of  $\sim 10^4$  K. Halos with such virial temperatures are very rare at redshifts greater than  $z \sim 10$ .

However, other cooling channels may be available even in halos too small to support atomic (hydrogen) line cooling. Hydrogen molecules,  $\text{H}_2$ , can form using free electrons as a catalyst<sup>10</sup>,



These reactions are limited by the availability of free electrons<sup>11</sup> and the survivability of  $\text{H}^-$  ions. Even in the absence of astrophysical backgrounds, the formation of  $\text{H}_2$  is limited by the CMB, which at the high redshifts of interest can dissociate the  $\text{H}^-$  ion. [34] found that the molecular hydrogen fraction in high- $z$  halos scales with the virial temperature as

$$f_{\text{H}_2} \approx 3.5 \times 10^{-4} \left( \frac{T_{\text{vir}}}{10^3 \text{ K}} \right)^{1.52}. \quad (2.51)$$

Once the first stars form, the situation grows considerably more complicated. As will be detailed in the following section (§2.3.2), massive stars are prodigious sources of UV photons. Some of these photons originate in the Lyman-Werner band ( $\sim 11.2\text{-}13.6$  eV), and are thus capable of dissociating molecular hydrogen. This processs is expected to quickly surpass  $\text{H}^-$  dissociation by the CMB as the most important mechanism capable of regulating star formation in chemically pristine halos.

A substantial literature has emerged in the last  $\sim 20$  years aimed at understanding the critical LW background intensity,  $J_{\text{LW}}$ , required to prevent star formation in high- $z$  minihaloes.

$$M_{\min} = 2.5 \times 10^5 \left( \frac{1+z}{26} \right)^{-3/2} (1 + 6.96(4\pi J_{\text{LW}})^{0.47}) M_\odot \quad (2.52)$$

#### Brief discussion of self-shielding complication.

Talk about metal enrichment and how this is (probably) the cause of the demise of PopIII.

Draw attention to how 21-cm background can contribute here: Ly- $\alpha$  and LW backgrounds are closely related. Note that there are very few studies of PopIII in the 21-cm background. Can point to Anastasia's stuff, my stuff, maybe Rick's stuff will be done soon...

Bottom line:  $m_{\min}$  sort of understood,  $f_*$  unknown.

Show some models for the PopIII SFRD and compare to PopII SFRD extrapolated from observations and/or predictions from models.

### 2.3.2 UV Emission from Stars

Stellar photons are likely the dominant drivers of reionization<sup>12</sup> and the initial “activation” of the 21-cm background via Wouthuysen-Field coupling at  $z \sim 30$ . The 21-cm background

---

<sup>10</sup>Dust is the primary catalyst of  $\text{H}_2$  formation in the local Universe, but of course is does not exist in the first collapsing clouds.

<sup>11</sup>Exotic models in which an X-ray background emerges before the formation of the first stars may similarly affect early star formation by boosting the electron fraction.

<sup>12</sup>There is still some room for a contribution from quasars [?, see, e.g.,] Madau2018.

is thus sensitive to the spectral characteristics of stars in the Lyman continuum and Lyman Werner bands<sup>13</sup>. It is also in principle sensitive to the spectrum of even harder He-ionizing photons, since photo-electrons generated from helium ionization can heat and ionize the gas, while HeII recombinations can result in H-ionizing photons. The 21-cm signal could in principle even constrain the rest-frame infrared spectrum of stars in the early Universe, since IR photons can feedback on star-formation at very early times through  $H^-$  photo-detachment [36]. In this section, we focus only on the soft UV spectrum ( $E < 54.4$  eV) to which the 21-cm background is most sensitive.

The most detailed predictions for stellar spectra come from stellar population synthesis (SPS) models, which take the following approach:

- Assume a model for the stellar initial mass function (IMF),  $\xi(m)$ , i.e., the number of relative number of stars formed in different mass bins. Commonly-adopted IMFs include Salpeter [29], Chabrier [4], Kroupa [18], and Scalo [30] which are all generally power-laws with indices  $\sim -2.3$ , but differing in shape at the low mass end of the distribution ( $M_* < 0.5 M_\odot$  ).
- Assume a model for stellar evolution, i.e., how stars of different masses traverse the Hertzprung-Russell (HR) diagram over time.
- Assume a model for stellar atmospheres, i.e., as a function of stellar mass, age, and composition, determine the output spectrum.

With all these ingredients, one can synthesize a spectrum from a population of stars with a given age,

$$L_v(t) = \int_0^t dt' \int_{m_{\min}}^{\infty} dm \xi(m) l_v(m, t') \quad (2.53)$$

where  $l_v(m, t)$  is the specific luminosity of a star of mass  $m$  and age  $t$ , and we have assumed that  $\xi$  is normalized to the mass of the star cluster,  $\int dm \xi(m) = M_*$ . Equation 2.53 can be generalized to determine the spectrum of a galaxy with an arbitrary star formation history (SFH) composed of discrete bursts. mention poor IMF sampling? Widely used stellar synthesis codes include STARBURST99 [19], BPASS [8], FSPS, Bruzual & Charlot...

Generally, 21-cm models do not operate at level of SPS models because the 21-cm background is insensitive to the detailed spectra and SFHs of individual galaxies. Instead, because 21-cm measurements probe the relatively narrow intervals  $10.2 < h\nu/\text{eV} < 13.6$  via Wouthuysen-Field coupling and  $h\nu > 13.6$  eV through the ionization field, it is common to distill the predictions of SPS models into just two numbers,  $N_{\text{ion}}$  and  $N_\alpha$ , which integrate over age and the details of the stellar SED, i.e.,

$$N_{\text{ion}} = m_*^{-1} \int_0^\infty dt' \int_{v_{\text{LL}}}^\infty \frac{dv}{h\nu} L_v(t') \quad (2.54)$$

$$N_\alpha = m_*^{-1} \int_0^\infty dt' \int_{v_\alpha}^{v_{\text{LL}}} \frac{dv}{h\nu} L_v(t') \quad (2.55)$$

---

<sup>13</sup>We use this definition here loosely. Technically, the LW band is  $\sim 11.2 - 13.6$  eV, a range which bounds photons capable of photo-dissociating molecular hydrogen,  $H_2$ . The Ly- $\alpha$  background is sourced by photons in a slightly broader interval,  $\sim 10.2 - 13.6$  eV, but it is tedious to continually indicate this distinction, and as a result, we use “LW band” to mean all photons capable of eventually generating Ly- $\alpha$  photons.

where  $v_{LL}$  is the frequency of the Lyman limit (13.6 eV) and  $v_\alpha$  is the Ly- $\alpha$  frequency. UV emission is dominated by massive, short-lived stars, hence the integration from  $t = 0$  to  $t = \infty$ .

Assuming a Scalo IMF, stellar metallicity of  $Z = Z_\odot/20$ , using STARBURST99 SPS model, [3] report  $N_\alpha = 9690$ , further broken down into sub-intervals between each Ly- $n$  resonance, an oft-used reference value even today. The canonical value of  $N_{ion} = 4000$  (I think) makes the same assumptions but I can't find where this first appeared. The general expectation is for  $N_{ion}$  and  $N_\alpha$  increase for more top-heavy IMF and lower metallicity, meaning these values are likely to increase for Pop III stars (citations). Similarly, binary evolution can effectively increase the lifetimes of massive stars, leading to a net gain in UV photon production [32].

Note that detailed SPS may be needed to if jointly fitting 21-cm measurements and galaxy population.

Show PopII and PopIII spectra?

### 2.3.3 Escape of UV Photons from Galaxies

Summarize briefly the status of  $f_{esc}$ .

### 2.3.4 X-rays from Black Holes

Though stars themselves emit few photons at energies above the HeII-ionizing edge ( $\sim 54.4$  eV), their remnants can be strong X-ray sources. While solitary remnants will be unlikely to accrete much gas from the diffuse ISM, remnants in binary systems may accrete gas from their companions, either via Roche-lobe overflow or stellar winds. Such systems are known as X-ray binaries (XRBs), further categorized by the mass of the donor star: “low-mass X-ray binaries” (LMXBs) are those fueled by Roche-lobe overflow from a low-mass companion, while “high-mass X-ray binaries” (HMXBs) are fed by the winds of massive companions. XRBs exhibit a rich phenomenology of time- and frequency-dependent behavior and are thus interesting in their own right. For a review see, e.g., [28].

In nearby star-forming galaxies, the X-ray luminosity is generally dominated by the HMXBs [16, 9, 1]. Furthermore, the total luminosity in HMXBs scales with the star formation rate, as expected given that the donor stars in these systems are massive, short-lived stars. An oft-used result in the 21-cm literature stems from the work of [1] (update of Gil-fanov), who find

$$L_X = 2.6 \times 10^{39} \left( \frac{\dot{M}_*}{M_\odot \text{ yr}^{-1}} \right) \text{ erg s}^{-1} \quad (2.56)$$

where  $L_X$  refers to the 0.5-8 keV band. This relation provides an initial guess for many 21-cm models, which add an extra factor  $f_X$  to parameterize our ignorance of how this relation evolves with cosmic time. For example, [14] write

$$L_X = 3 \times 10^{40} f_X \left( \frac{\dot{M}_*}{M_\odot \text{ yr}^{-1}} \right) \text{ erg s}^{-1}, \quad (2.57)$$

which is simply Equation 2.56 re-normalized to a broader energy range,  $0.2 < h\nu/\text{keV} < 3 \times 10^4$ , assuming a power-law spectrum with spectral index  $\alpha_X = -1.5$ , where  $\alpha_X$  is defined by  $L_E \propto E^{\alpha_X}$ , with  $L_E$  in energy units.

The normalization of these empirical  $L_X$ -SFR relations are not entirely unexpected, at least at the order-of-magnitude level. For example, if one considers a galaxy forming stars at a constant rate, a fraction  $f_\bullet \simeq 10^{-3}$  of stars will be massive enough ( $M_* > 20 M_\odot$ ) to form a black hole assuming a Chabrier IMF. Of those, a fraction  $f_{\text{bin}}$  will have binary companions, with a fraction  $f_{\text{surv}}$  surviving the explosion of the first star for a time  $\tau$ . If accretion onto these black holes occurs in an optically thin, geometrically-thin disk with radiative efficiency  $\epsilon_\bullet = 0.1$  which obeys the Eddington limit, then a multi-color disk spectrum is appropriate and a fraction  $f_{0.5-8} = 0.84$  of the bolometric luminosity will originate in the 0.5-8 keV band. Finally, assuming these BHs are “active” for a fraction  $f_{\text{act}}$  of the time, we can write [23, 24]

$$L_X \sim 2 \times 10^{39} \text{ erg s}^{-1} \left( \frac{\dot{M}_*}{M_\odot \text{ s}^{-1}} \right) \left( \frac{\epsilon_\bullet}{0.1} \right) \left( \frac{f_\bullet}{10^{-3}} \right) \left( \frac{f_{\text{bin}}}{0.5} \right) \left( \frac{f_{\text{surv}}}{0.2} \right) \left( \frac{\tau}{20 \text{ Myr}} \right) \left( \frac{f_{\text{act}}}{0.1} \right) \left( \frac{f_{0.5-8}}{0.84} \right). \quad (2.58)$$

While several of these factors are uncertain, particularly  $f_{\text{surv}}$  and  $f_{\text{act}}$ , this expression provides useful guidance in setting expectations for high redshift. For example, it has long been predicted that the first generations of stars were more massive on average than stars today owing to inefficient cooling in their birth clouds. This would boost  $f_\bullet$ , and thus  $L_X/\dot{M}_*$ , so long as most stars are not in the pair-instability supernova (PISN) mass range, in which no remnants are expected.

There are of course additional arguments not present in Eq. 2.58. For example, the MCD spectrum is only a good representation of HMXB spectra in the “high soft” state. At other times, in the so-called “low hard” state, HMXB spectra are well fit by a power-law. The relative amount of time spent in each of these states is unknown.

In addition, physical models for the  $L_X$ -SFR relation may invoke the metallicity as a driver of changes in the relation with time and/or galaxy (stellar) mass. As the metallicity declines, one might expect the stellar IMF to change (as outlined above), however, the winds of massive stars responsible for transferring material to BHs will also grow weaker as the opacity of their atmospheres decline. As a result, increases in  $L_X/\text{SFR}$  likely saturate below some critical metallicity. Observations of nearby, metal-poor dwarf galaxies support this picture, with  $L_X/\text{SFR}$  reaching a maximum of  $\sim 10$  times the canonical relation quoted in Eq. 2.56 [1].

Show different spectra often adopted in models and discuss.

### Super-Massive Black Holes

Say a few words about plausibility, reference [33].

#### 2.3.5 X-rays from Shocks and Hot Gas

While compact remnants of massive stars are likely the leading producer of X-rays in high- $z$  star-forming galaxies (see previous sub-section), the supernovae events in which these objects are formed may not be far behind. Supernovae inject a tremendous amount of energy

into the surrounding medium, which then cools either via inverse Compton emission (in supernova remnants; [26]) or eventually via bremsstrahlung radiation (in the hot interstellar medium; ISM). Because these sources are related to the deaths of massive stars their luminosity is expected to scale with SFR, as in the case of HMXBs. Indeed, [22] find that diffuse X-ray emission in nearby sources follows the following relation in the 0.5-2 keV band:

$$L_X = 8.3 \times 10^{38} \left( \frac{\dot{M}_*}{M_\odot \text{ yr}^{-1}} \right) \text{ erg s}^{-1} \quad (2.59)$$

This luminosity is that from all unresolved emission, and as a result, is not expected to trace emission from the hot ISM alone. Emission from supernova remnants will also contribute to this luminosity, as will fainter, unresolved HMXBs and LMXBs. [22] estimate that  $\sim 30 - 40\%$  of this emission may be due to unresolved point sources.

Though the soft X-ray luminosity from hot gas appears to be subdominant to the HMXB component in nearby galaxies, there are of course uncertainties in how these relations evolve. Furthermore, the bremsstrahlung emission characteristic of hot ISM gas has a much steeper  $\sim v^{-2.5}$  spectrum than inverse Compton ( $\sim v^{-1}$ ) or XRBs ( $\sim v^{-1}$  or  $v^{-1.5}$ ), and thus may heat more efficiently (owing to  $\sigma \propto v^{-3}$  cross section) provided soft X-rays can escape galaxies.

### 2.3.6 Escape of X-rays from Galaxies

Though the mean free paths of X-rays are longer than those of UV photons, they still may not all escape from galaxies into the IGM.

The column density is used to account for absorption by neutral hydrogen in the ISM, which hardens the intrinsic spectrum. Simulations suggest typical values of  $N_{H1} \sim 10^{21} \text{ cm}^{-2}$  [7], which is substantial enough to eliminate emission below  $\sim 0.5 \text{ keV}$ .

Given the many unknowns regarding X-ray emission in the early Universe, 21-cm models often employ a three-parameter approach, i.e., instead of a single value of  $\zeta_X$ , the specific X-ray luminosity is modeled as

$$L_{X,v} = L_{X,0} \left( \frac{hv}{1 \text{ keV}} \right)^{\alpha_X} \exp[-\sigma_v N_{H1}] \quad (2.60)$$

and the normalization,  $L_{X,0}$ , spectral index  $\alpha_X$ , and typical column density,  $N_{H1}$ , are left as free parameters.

It is common to approximate this intrinsic attenuation with a piecewise model for  $L_X$ , i.e.,

$$L_{X,v} = \begin{cases} 0 & hv < E_{\min} \\ L_{X,0} \left( \frac{hv}{1 \text{ keV}} \right)^{\alpha_X} & hv \geq E_{\min} \end{cases} \quad (2.61)$$

Note that  $N_{H1}$  (or  $E_{\min}$ ) can be degenerate with the intrinsic spectrum, e.g., the SED of HMXBs in the high-soft state exhibits a turn-over at energies  $hv < 1 \text{ keV}$ , which could be mistaken for strong intrinsic absorption.

**Translate this to  $\zeta_X$ .**

### 2.3.7 Cosmic Rays from Supernovae

Other sources of high energy radiation have been explored in recent years though are generally found to be sub-dominant. However, surprises may be in store...

## 2.4 Predictions for the 21-cm Background

Over the last four sections we have assembled a simple physical picture of the IGM at high redshift from which we can derive predictions for the 21-cm brightness temperature. Here, we finally describe the generic sequence of events predicted in most models, and the sensitivity of the 21-cm background to various model parameters of interest.

### 2.4.1 Generic Series of Events

Figure XYZ depicts what are now standard predictions for the global 21-cm signal (top) and power spectrum (bottom). Time proceeds from left to right from the Big Bang until the end of reionization. There are four distinct epochs within this time period, labeled A, B, C, and D, which we describe in more detail below.

- A. The Dark Ages:** As the Universe expands after cosmological recombination, Compton scattering between free electrons and photons keep the radiation and matter temperature in equilibrium. The density is high enough the collisional coupling remains effective, and so  $T_S = T_K = T_{CMB}$ . Eventually, Compton scattering becomes inefficient as the CMB cools and the density continues to fall, which allows the gas to cool faster than the CMB (see also earlier figures). Collisional coupling remains effective for a short time longer and so  $T_K$  follows  $T_S$ . This results in the first decoupling of  $T_S$  from  $T_{CMB}$  at  $z \sim 80$ , and thus an absorption signature at  $\nu \sim 15$  MHz, which comes to an end as collisional coupling becomes inefficient, leaving  $T_S$  to reflect  $T_{CMB}$  once again.
- B. First Light:** When the first stars form they flood the IGM with UV photons for the first time. While Lyman continuum photons are trapped near sources, photons with energies  $10.2 < h\nu/\text{eV} < 13.6$  either redshift directly through the Ly- $\alpha$  resonance or cascade via higher Ly- $n$  levels, giving rise to a large-scale Ly- $\alpha$  background capable of triggering Wouthuysen-Field coupling as they scatter through the medium. As a result,  $T_S$  is driven back toward  $T_K$ , which (in most models) still reflects the cold temperatures of an adiabatically-cooling IGM.
- C. X-ray Heating:** The first generations of stars beget the first generations of X-ray sources, whether they be the explosions of the first stars themselves or remnant neutron stars or black holes that subsequently accrete. Though the details change depending on the identity of the first X-ray sources, generally such sources provide photons energetic enough to travel great distances. Upon absorption, they heat and partially ionize the gas, eventually driving  $T_S > T_{CMB}$ . Once  $T_S \gg T_{CMB}$ , the 21-cm signal “saturates,” and subsequently sensitive only to the density and ionization fields. However, it is possible that heating is never “complete” in this sense before the completion of reionization,

name	description	typical values
$\zeta_i$	Ionizing photon production efficiency	40-ish
$\zeta_\alpha$	Ly- $\alpha$ photon production efficiency	40-ish
$\zeta_X$	X-ray photon production efficiency	xxx
$T_{\min}$	Minimum virial temperature of star-forming halos	$10^4$ K

Table 2.1: Parameters in simple 21-cm models.

meaning neutral pockets of IGM gas may remain at temperatures at or below  $T_{\text{CMB}}$  until they are engulfed in the overlap event of large ionized bubbles.

**D. Reionization:** As the global star formation rate density climbs, the growth of ionized regions around groups and clusters of galaxies will continue, eventually culminating in the completion of cosmic reionization. This rise in ionization corresponds to a decline in the amount of neutral hydrogen in the Universe capable of producing or absorbing 21-cm radiation. As a result, the amplitude of the 21-cm signal, both in its mean and fluctuations, falls as reionization progresses.

Draw connection between features in 21-cm signal and evolution of ionization, heating, and  $J_\alpha$  introduced in earlier sections.

The evolution of 21-cm fluctuations is more complicated, though this same series of events imprints on fluctuation patterns as well.

## 2.4.2 Sensitivity to Model Parameters

Use this section to highlight the sensitivity to parameters in more detail.

Things to discuss:

- Sensitivity to  $T_{\min}$  and  $f_*$ .
- Sensitivity to  $\alpha_X$ ,  $E_{\min}$ , and  $f_X$ .
- Sensitivity to  $\zeta$  and  $R_{\text{mfp}}$  (and updates)
- Clumping, feedback
- Shot noise in galaxy counts in voxels.
- PopIII stuff, AGN stuff.
- Exotic physics? Defer to Jonathan's chapter.

### **2.4.3 Modeling Tools**

Predictions from previous section came from a mix of different groups and codes. Discuss some differences here.

- 21CMFAST and DEXM
- Anastasia's code
- simfast21
- ARES
- RT simulations

# Bibliography

[1]

- [2] T. Abel, M. L. Norman, and P. Madau. Photon-conserving Radiative Transfer around Point Sources in Multidimensional Numerical Cosmology. *ApJ*, 523:66–71, September 1999.
- [3] Rennan Barkana and Abraham Loeb. Detecting the Earliest Galaxies through Two New Sources of 21 Centimeter Fluctuations. *ApJ*, 626(1):1–11, Jun 2005.
- [4] Gilles Chabrier. Galactic Stellar and Substellar Initial Mass Function. *PASP*, 115(809):763–795, Jul 2003.
- [5] X. Chen and J. Miralda-Escudé. The Spin-Kinetic Temperature Coupling and the Heating Rate due to Ly $\alpha$  Scattering before Reionization: Predictions for 21 Centimeter Emission and Absorption. *ApJ*, 602:1–11, February 2004.
- [6] Asantha Cooray and Ravi Sheth. Halo models of large scale structure. *Physics Reports*, 372(1):1–129, Dec 2002.
- [7] Arpan Das, Andrei Mesinger, Andrea Pallottini, Andrea Ferrara, and John H. Wise. High-mass X-ray binaries and the cosmic 21-cm signal: impact of host galaxy absorption. *MNRAS*, 469(1):1166–1174, Jul 2017.
- [8] John J. Eldridge and Elizabeth R. Stanway. Spectral population synthesis including massive binaries. *MNRAS*, 400(2):1019–1028, Dec 2009.
- [9] G. Fabbiano. Populations of X-Ray Sources in Galaxies. *ARA&A*, 44(1):323–366, Sep 2006.
- [10] G. B. Field. Excitation of the Hydrogen 21-CM Line. *Proceedings of the IRE*, 46:240–250, January 1958.
- [11] M. Fukugita and M. Kawasaki. Reionization during Hierarchical Clustering in a Universe Dominated by Cold Dark Matter. *MNRAS*, 269:563, August 1994.
- [12] S. R. Furlanetto and J. R. Pritchard. The scattering of Lyman-series photons in the intergalactic medium. *MNRAS*, 372:1093–1103, November 2006.
- [13] Steven Furlanetto, Matias Zaldarriaga, and Lars Hernquist. The Growth of HII Regions During Reionization. *arXiv.org*, March 2004.

- [14] Steven R. Furlanetto. The global 21-centimeter background from high redshifts. *MNRAS*, 371(2):867–878, Sep 2006.
- [15] Steven R Furlanetto and Samuel Johnson Stoever. Secondary ionization and heating by fast electrons. *Monthly Notices of the Royal Astronomical Society*, 404:1869, June 2010.
- [16] M. Gilfanov, H. J. Grimm, and R. Sunyaev.  $L_X$ -SFR relation in star-forming galaxies. *MNRAS*, 347(3):L57–L60, Jan 2004.
- [17] Christopher M Hirata. Wouthuysen-Field coupling strength and application to high-redshift 21-cm radiation. *MNRAS*, 367(1):259–274, March 2006.
- [18] Pavel Kroupa. On the variation of the initial mass function. *MNRAS*, 322(2):231–246, Apr 2001.
- [19] Claus Leitherer, Daniel Schaerer, Jeffrey D. Goldader, Rosa M. González Delgado, Carmelle Robert, Denis Foo Kune, Duilia F. de Mello, Daniel Devost, and Timothy M. Heckman. Starburst99: Synthesis Models for Galaxies with Active Star Formation. *ApJS*, 123(1):3–40, Jul 1999.
- [20] Piero Madau, Avery Meiksin, and Martin J. Rees. 21 Centimeter Tomography of the Intergalactic Medium at High Redshift. *ApJ*, 475(2):429–444, Feb 1997.
- [21] Matthew McQuinn. Constraints on X-ray emissions from the reionization era. *MNRAS*, 426(2):1349–1360, Oct 2012.
- [22] S. Mineo, M. Gilfanov, and R. Sunyaev. X-ray emission from star-forming galaxies - II. Hot interstellar medium. *MNRAS*, 426(3):1870–1883, Nov 2012.
- [23] I. F. Mirabel, M. Dijkstra, P. Laurent, A. Loeb, and J. R. Pritchard. Stellar black holes at the dawn of the universe. *A&A*, 528:A149, Apr 2011.
- [24] Jordan Mirocha, Richard H. Mebane, Steven R. Furlanetto, Krishna Singal, and Donald Trinh. Unique signatures of Population III stars in the global 21-cm signal. *MNRAS*, 478(4):5591–5606, Aug 2018.
- [25] Jordan Mirocha, Stephen Skory, Jack O Burns, and John H Wise. Optimized Multi-frequency Spectra for Applications in Radiative Feedback and Cosmological Reionization. *The Astrophysical Journal*, 756(1):94, September 2012.
- [26] S. Peng Oh. Reionization by Hard Photons. I. X-Rays from the First Star Clusters. *ApJ*, 553(2):499–512, Jun 2001.
- [27] Jonathan R Pritchard and Steven R Furlanetto. Descending from on high: Lyman-series cascades and spin-kinetic temperature coupling in the 21-cm line. *MNRAS*, 367(3):1057–1066, April 2006.
- [28] Ronald A. Remillard and Jeffrey E. McClintock. X-ray properties of black-hole binaries. *Annual Review of Astronomy and Astrophysics*, 44(1):49–92, 2006.

- [29] Edwin E. Salpeter. The Luminosity Function and Stellar Evolution. *ApJ*, 121:161, Jan 1955.
- [30] John Scalo. The IMF Revisited: A Case for Variations. In Gary Gilmore and Debbie Howell, editors, *The Stellar Initial Mass Function (38th Herstmonceux Conference)*, volume 142 of *Astronomical Society of the Pacific Conference Series*, page 201, Jan 1998.
- [31] J M Shull and M E van Steenberg. X-ray secondary heating and ionization in quasar emission-line clouds. *The Astrophysical Journal*, 298:268, November 1985.
- [32] Elizabeth R. Stanway, J. J. Eldridge, and George D. Becker. Stellar population effects on the inferred photon density at reionization. *MNRAS*, 456(1):485–499, Feb 2016.
- [33] Takamitsu L. Tanaka, Ryan M. O’Leary, and Rosalba Perna. The imprint of the cosmic supermassive black hole growth history on the 21 cm background radiation. *MNRAS*, 455(3):2619–2626, Jan 2016.
- [34] Max Tegmark, Joseph Silk, Martin J. Rees, Alain Blanchard, Tom Abel, and Francesco Palla. How Small Were the First Cosmological Objects? *ApJ*, 474:1, Jan 1997.
- [35] Rajat M Thomas and Saleem Zaroubi. Time-evolution of ionization and heating around first stars and miniqsos. *Monthly Notices of the Royal Astronomical Society*, 384(3):1080–1096, March 2008.
- [36] J. Wolcott-Green and Z. Haiman. Feedback from the infrared background in the early Universe. *MNRAS*, 425(1):L51–L55, Sep 2012.
- [37] S. A. Wouthuysen. On the excitation mechanism of the 21-cm (radio-frequency) interstellar hydrogen emission line. *AJ*, 57:31–32, 1952.
- [38] B Zygelman. Hyperfine Transitions in Atomic Hydrogen. *ApJ*, 622:1356–1362, 2005.

# Chapter 3

## Physical cosmology from the 21-cm line

**Jonathan Pritchard**

a discussion of using 21-cm intensity mapping/interferometry to constrain the matter power spectrum and cosmological parameters. The signal can also be used as a signpost for new physics beyond the standard model, such as heating and cooling of the primordial gas through interactions with dark matter. Subtopics could include: redshift space distortions and their likely observability, measuring the matter power spectrum during the cosmic dawn and (eventually) the dark ages, IGM heating through dark matter annihilations, IGM cooling through interactions with exotic dark matter candidates.

This chapter discusses some important things

### 3.1 Physical cosmology through the 21-cm epoch

Summarise the different ways in which cosmology underpins the nature of the 21 cm signal.

#### 3.1.1 Dark matter

Discuss different dark matter models and impact

#### 3.1.2 PMBH

Discuss primordial black holes and other exotic objects

### 3.2 Unique signatures of cosmology

What might be distinctive signatures of cosmology in the 21cm signal?

### 3.2.1 Non-Gaussianity

Impact of clustering on bubbles.

### 3.2.2 IGM Heating

Various ways exotic physics can impact 21 cm signal

## 3.3 Separating cosmology from astrophysics

How might cosmology be separated from astrophysics?

### 3.3.1 Redshift space distortions

As route to separating different elements of signal

### 3.3.2 Time evolution

Looking at the dark ages, or via time evolution, or going to late times to post-EoR.

## 3.4 Summary

*Lorem ipsum dolor sit amet, consectetur adipiscing elit. Duis eu egestas erat. Maecenas tincidunt lacinia tincidunt. Mauris id lectus nec neque feugiat condimentum vitae at diam. In vel orci nunc, non commodo mauris. Vivamus ipsum enim, vulputate quis pharetra non, molestie quis felis. Vivamus porttitor placerat turpis at accumsan. Nunc tortor velit, faucibus a rhoncus nec, blandit non elit. Nam consectetur lectus eu nisi blandit dapibus rhoncus dui tempus. Mauris fermentum dolor vel ipsum vulputate sit amet ultricies tortor lacinia. Donec ut nibh erat. Morbi nec mi ante. Integer nec vestibulum diam. Donec tincidunt pellentesque quam, ut interdum mauris venenatis condimentum. Nam condimentum, augue in aliquet gravida, neque dui elementum eros, id semper eros purus sed felis. Curabitur in justo sit amet sapien ultrices hendrerit at quis nibh. Quisque iaculis pulvinar tincidunt.*

$$\begin{aligned}
 C(12) &= \left[ \vec{\pi} \cdot \vec{\phi}(x+r) \right] \\
 &\approx 1 - \text{const} \frac{r^2}{L^2} \int_r^L \frac{x dx}{x^2} + \dots \\
 &\approx 1 - \text{const} \frac{r^2}{L^2} \ln \frac{x dx}{x^2} + \dots
 \end{aligned} \tag{3.1}$$

*Aenean tellus risus, porta sit amet porta vitae, tincidunt ut felis. Class aptent taciti sociosqu ad litora torquent per conubia nostra, per inceptos himenaeos. Vestibulum ante ipsum primis in faucibus orci luctus et ultrices posuere cubilia Curae; Phasellus pulvinar placerat velit auctor egestas. Vivamus euismod fringilla tincidunt. Sed ut magna felis, id sollicitudin nunc. Quisque a dui eu erat consectetur egestas a quis justo. Aenean euismod congue diam,*



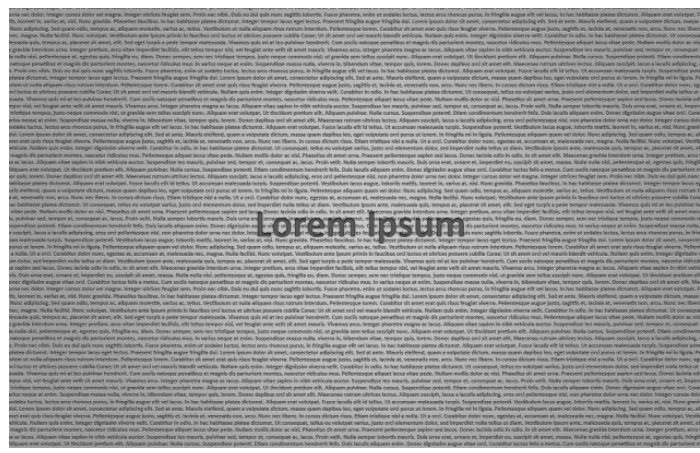


Figure 3.2: This is figure 2 in chapter 1.

# Chapter 4

## Inference from the 21cm signal

Bradley Greig

### Abstract

In the previous chapters we have discussed in-depth the astrophysical and cosmological information that is encoded by the cosmic 21-cm signal. However, once we have a measurement, how do we extract this information from the signal? This chapter focusses on the inference of the interesting astrophysics and cosmology once we obtain a detection of the 21-cm signal.

Essentially, inference of the astrophysics can be broken down into three parts:

1. **Compression of the observed data into a manageable dataset:** The observed 21-cm signal varies spatially as well as along the line-of-sight (frequency or redshift dimension) to provide a full three dimensional movie of the intergalactic medium in the early Universe. However, the signal is faint, requiring either statistical methods to sum the data in order to increase the signal-to-noise or sophisticated approaches to extract the faint signal directly.
2. **An efficient method to model/simulate the 21-cm signal:** In order to interpret the observations and understand the astrophysical processes responsible, we must be able to produce physically motivated models capable of replicating the signal. Further, these must be as computationally efficient as possible in order to be able to realistically investigate the 21-cm signal.
3. **A robust probabilistic framework to extract the physics:** The observed 21-cm signal is dependent on numerous physical processes, which within our models or simulations are described by many unknown parameters. Further, these contain approximations in order to deal with the requisite dynamic range. We must be able to characterise our ignorance in a meaningful way in order to be truly able to infer the astrophysical processes of the epoch of reionisation and cosmic dawn.

In this chapter we will focus on each separately, discussing the current state-of-the-art in inferring the 21cm signal.

## 4.1 What do we actually measure?

The 21-cm signal from the neutral hydrogen in the intergalactic medium is measured by its brightness temperature,  $T_b$ . However, this cannot be measured directly, instead it is expressed as a brightness temperature contrast,  $\delta T_b$ , relative to the Cosmic Microwave Background (CMB) temperature,  $T_{\text{CMB}}$  [9]:

$$\delta T_b(\mathbf{x}, v) \equiv T_b(\mathbf{x}, v) - T_{\text{CMB}, 0}. \quad (4.1)$$

As such, this brightness temperature contrast can be seen either in emission or absorption, dependent on the 21-cm brightness temperature which itself is dependent on the excitation state of the neutral hydrogen (i.e. its spin temperature,  $T_S$ , see [previous chapter](#)). We can re-express Equation 4.1 in terms of  $T_S$  to recover ([should have been introduced in a previous chapter](#)),

$$\delta T_b(\mathbf{x}, v) \equiv \frac{T_S(\mathbf{x}, v) - T_{\text{CMB}}(z)}{1 + z} \left( 1 - e^{-\tau_{v_0}(\mathbf{x}, v)} \right), \quad (4.2)$$

where  $\tau_{v_0}$  is the optical depth of the 21-cm line.  $\delta T_b(\mathbf{x}, v)$  varies spatially due to its two-dimensional angular position on the sky while it varies along the line-of-sight direction owing to the 21-cm line being redshifted by cosmological expansion (i.e. adding a frequency or time dependence to the signal). Thus, measuring  $\delta T_b(\mathbf{x}, v)$  can reveal a full three-dimensional movie of the neutral hydrogen in the early Universe.

Unfortunately,  $\delta T_b(\mathbf{x}, v)$  is faint. Further, in reality it is buried under numerous astrophysical foregrounds all of which are orders of magnitude brighter ([see relevant chapters for more detailed discussions](#)). In order to deal with this faint signal coupled with the astrophysical foregrounds, typically we seek to compress the data to boost the signal-to-noise or specifically tailor methods to extract the faint signal. In this chapter, we will discuss the numerous methods proposed in order to tease out the faint astrophysical signal from the noise.

## 4.2 Optimal methods for characterising the 21-cm signal

The first step in our efforts to be able to infer information about the astrophysical processes responsible for reionisation and the cosmic dawn is to explore optimal methods to characterise the 21-cm signal. In this section, we summarise the wide variety of approaches considered in the literature, highlighting the leverage that each is able to provide with respect to the underlying astrophysical processes. Note that throughout this chapter, all investigations into detecting the 21-cm signal are generated theoretically, either analytically or numerically. Thus, we urge the reader to refer to the citations in order to understand the limiting assumptions.

### 4.2.1 Global signal

The simplest way to deal with such a faint signal is to average it over as large a volume as possible. Since the 21-cm signal is visible across the entire sky, one can produce a complete sky-averaged (global) 21-cm brightness temperature as a function of frequency (redshift).

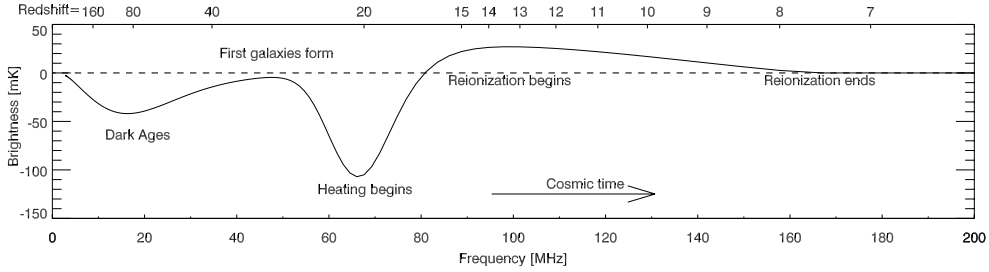


Figure 4.1: A representative example of the all-sky averaged (global) 21-cm brightness temperature signal, demarcating the major cosmological transitions. Taken from [28].

Although the two-dimensional spatial information from the 21-cm signal is lost, the main advantage is that it is relatively cheap to observe, requiring comparatively simple instrumentation (see future chapter on global signal or observations?). A fact that several experiments have used in an attempt to provide a measurement of the 21-cm signal, given that a single radio dipole is capable of seeing essentially the entire sky at any one time. In Figure 4.1, we show a representative model of the global 21-cm signal, highlighting the major cosmological milestones that have been discussed in previous chapters. Thus, in each frequency bin, we measure an all-sky average of the 21-cm brightness temperature.

The global signal has been studied extensively in the literature. Use this hook here to add in citations to works investigating the global signal.

Roughly speaking the global 21-cm signal can be broken up into five major turning points (e.g. [9, 27]) corresponding to: (i) a minimum during the dark ages where collisional coupling becomes ineffective, (ii) a maximum at the transition from the dark ages to the Ly $\alpha$  pumping regime (Ly $\alpha$  pumping from the first sources becomes efficient), (iii) a minimum at the commencement of X-ray heating taking the signal back towards emission, (iv) a maximum once the 21-cm signal becomes saturated during the EoR and finally (v) when reionisation is complete. Importantly, both the amplitude of the 21-cm signal as well as the frequency (redshift) of these transitions is strongly dependent on the underlying astrophysical processes. Thus, measuring both the amplitude and frequency of the turning points can reveal information into the underlying astrophysics.

In [24], these authors connect these transitions more closely to the astrophysics. The second turning point (end of the dark ages) can, under certain simple assumptions, be used to place limits on the spin temperature,  $T_S$ . Details on  $T_S$ , through equation (should be in an earlier chapter) can provide an estimate on the angle-averaged intensity of Ly $\alpha$  photons,  $J_\alpha$ . This provides insight into both the number density of sources and their corresponding emission spectrum (e.g. PopIII stars). The relative depth of the third turning point (heating epoch) can be used to place limits on the co-moving heating rate density, that is, the amount of heating that the IGM has undergone owing to heating sources (e.g. X-rays from HMXBs, the ISM or other more exotic scenarios should be discussed in an earlier chapter). Again, distinguishing the number density and type of sources responsible. Finally, the saturation of the spin temperature,  $T_S$ , during the epoch of reionisation collapses the brightness temperature into an approximate proportionality (cite appropriate equation,  $T_S \propto x_{\text{HI}}(1 + \delta_{\text{nl}})$ ) with the underlying ionisation fraction,  $x_{\text{HI}}$ . Tracking the evolution of the ionised fraction, i.e. the reionisation history, reveals the time-span of reionisation. This reveals insights into the

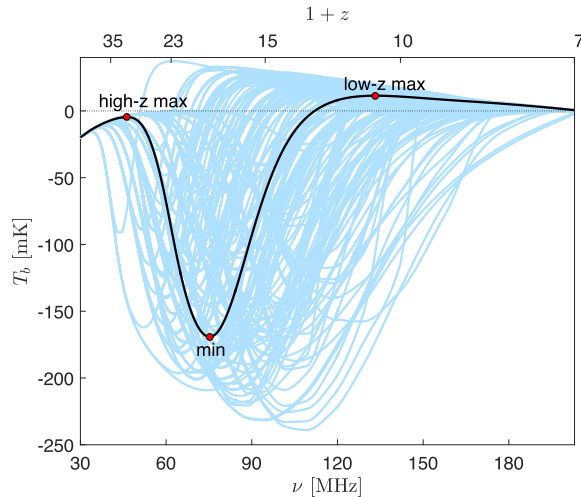


Figure 4.2: The all-sky averaged (global) 21-cm brightness temperature signal obtained when varying the astrophysical parameters in  $\sim 200$  theoretical models from [5].

number density of ionising photons produced, and thus the types of sources responsible for reionising the Universe.

Up until very recently, the first transition was typically ignored, as it was assumed that this transition was well understood theoretically. That is, that the dark matter and baryons decoupled from the CMB temperature at the same time, both cooling adiabatically. It turns out that the dark matter decouples earlier than the baryons, meaning the dark matter is colder than the baryons. As such, the baryons can be cooled by a coupling between the dark matter and baryons (e.g. [33]) altering the amplitude of the 21-cm signal. In addition to this, relative velocity differences between the two fluids (dark matter and baryons) will affect the structure formation on small-scales (e.g. [35]) again impacting on the temperature of the baryons. These will result in observable differences in the location and amplitude of this first turning point in the global signal, enabling dark matter models to be distinguishable (e.g. [25, 7]).

To highlight the expected variation in the global 21-cm signal as a result of the underlying astrophysical processes, in Figure 4.2 we show  $\sim 200$  theoretical models of the global 21-cm signal from [5]. Here, the authors explore the maximal variation in the global 21-cm signal when varying the ionisation and heating properties of the astrophysical sources. Some common features in the signal are, the depth of the absorption trough deepens for lower X-ray luminosities (including some models which never appear in emission as a result of inefficient heating) or the turning points push to later times when the minimum masses of sources increases (i.e. require more massive haloes in which stars can form and produce ionising photons).

### 4.2.2 Power spectrum

After the global signal, the next simplest and most straightforward approach to characterise the 21-cm signal is through the power spectrum. This is the Fourier transform of the 2-point correlation function. Basically, a measure of the excess signal (above random) on all possible

spatial scales. The workhorse statistic for any signal containing structural information, the power spectrum is simply the number of modes (in Fourier space) as a function of physical scale (or size). It produces a distribution of modes characterising the amount of structural information which is contained within the signal. The power spectrum is the natural method for observing the 21-cm signal from a radio interferometer, since these measure differences in the arrival times of the cosmological signal between radio dipoles or dishes of some fixed separation. Thus, a radio interferometer is sensitive to the spatial fluctuations rather than the total amplitude.

To obtain the 21-cm power spectrum, we normalise the 21-cm brightness temperature,  $\delta T_b(\mathbf{x})$  to be a zero-mean quantity,  $\delta_{21}(\mathbf{x}) = (\delta T_b(\mathbf{x}) - \bar{\delta T}_b)/\bar{\delta T}_b$ , which amplifies the fluctuations (spatial information) in the signal. The power spectrum,  $P(\mathbf{k})$  is computed by the angle-averaged sum of the Fourier transform of the 21-cm brightness temperature fluctuations via,

$$\langle \delta_{21}(\mathbf{k}_1) \delta_{21}(\mathbf{k}_2) \rangle = (2\pi)^3 \delta_D(\mathbf{k}_1 + \mathbf{k}_2) P(\mathbf{k}_1), \quad (4.3)$$

where  $\delta_D$  is the Dirac delta function. Typically, the 21-cm power spectrum is converted into a dimensionless quantity through  $\Delta^2(\mathbf{k}) = (k^3/2\pi^2)P(\mathbf{k})$ . Typically, the Fourier modes are then averaged in spherical shells to obtain the spherically averaged power spectrum,  $P(k)$ , which considerably improves the overall signal-to-noise, at the cost of averaging over some spatial information. Alternatively, one can also measure the two-dimensional cylindrically averaged power spectrum,  $P(k_{\parallel}, k_{\perp})$  decomposing it into modes perpendicular to the line-of-sight ( $k_{\perp}$ ; spatially averaging the two dimensional angular modes on the sky in annuli) and along the line-of-sight ( $k_{\parallel}$ ; in frequency) direction. The strength of the two dimensional 21-cm power spectrum is that most of the contamination of the signal by the astrophysical foregrounds can be contained in what is referred to as the EoR ‘wedge’ while the remaining Fourier modes can be clean tracers of the cosmological signal ([cite references and/or subsequent chapter](#)).

The advantage of the power spectrum over the global signal, is that it provides a measure of the spatial fluctuations in the 21-cm signal. However, it does not encode all the available spatial information from the 21-cm signal. The power spectrum is a measure of how Gaussian the fluctuations are. If these fluctuations were truly Gaussian, the power spectrum would contain all the information, and any higher order  $n$ -point correlation functions would contain no additional information. The structural complexity of the large and small scale processes of reionisation and the cosmic dawn results in the signal being highly non-Gaussian. As such, the power spectrum does not reveal all available information, meaning there is further constraining power from the higher order  $n$ -point statistics. In section 4.2.4 we will return to this. Nevertheless, the power spectrum still contains a wealth of information, and observationally is considerably easier to measure.

The sensitivity of the 21-cm power spectrum to the underlying astrophysics can be highlighted when we decompose the 21-cm brightness temperature fluctuations through a perturbative analysis. In doing so, we can recover the following (see e.g. [needs references](#)),

$$\delta_{21} \propto C_b \delta_b + C_x \delta_x + C_{\alpha} \delta_{\alpha} + C_T \delta_T - \delta_{\partial\nu}, \quad (4.4)$$

Simply put, fluctuations in the 21-cm brightness temperature field,  $\delta_{21}$ , are driven by a sum of contributions from the underlying density field,  $\delta_b$ , the ionisation fraction  $\delta_x$ , the Ly $\alpha$

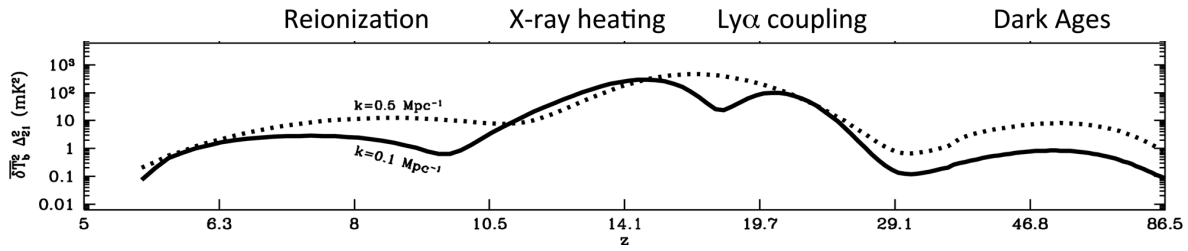


Figure 4.3: The 21-cm power spectrum amplitude for two different Fourier modes,  $k = 0.1 \text{ Mpc}^{-1}$  (solid) and  $k = 0.5 \text{ Mpc}^{-1}$  (dashed). Peaks in the 21-cm power spectrum amplitude correspond to the different cosmic milestones. Taken from [23].

coupling co-efficient,  $\delta_\alpha$ , the temperature of the neutral hydrogen  $\delta_T$  and line-of-sight peculiar velocity gradient,  $\delta_{\partial v}$ . Computing the power spectrum then measures the combined signal from the power spectra of each field as well as the cross-power spectra of each. Thus, if we measure the 21-cm power spectrum across cosmic time, we will be sensitive to both the epochs when each component dominates (similar to the global signal) and also the spatial scales on which the signal is strongest. This, similar to the global signal is depicted in Figure 4.3.

However, rather than using one single Fourier mode, we have a range of spatial scales over which to recover astrophysical information. This provides access to both the small-scale and large-scale physical processes. For example, during the EoR, the 21-cm power spectrum is dominated by the contribution from the ionisation field, which contains particular structural information on the reionisation process due to the characteristic size of the H<sub>II</sub> regions as well as their clustering ([cite references](#)). Similar is true for both the heating or Ly $\alpha$  coupling epochs, whereby the structural information provides insights into the intensity of the radiation, and the number density of sources producing it.

In Figure 4.4 we show the variation in the three dimensional spherically averaged 21-cm power spectrum at a single redshift ( $z = 9$ ) when varying three different astrophysical parameters under the assumption of  $T_S \gg T_{CMB}$  (see e.g. [13]). Inset tables correspond to the parameter being varied and the resultant IGM neutral fraction (stage of reionisation). In the top left panel, we vary the ionising efficiency,  $\zeta$ , a proxy for the number of ionising photons produced by the sources. The shape of the 21-cm power spectrum differs considerably with ionising efficiency. In the early stages, the 21-cm PS matches the density (matter) power spectrum, while in the latter stages its follows the ionisation field [this surely has been discussed in detail already and I don't have to elaborate on it?](#).

Similar behaviour is observed for varying  $T_{\text{vir}}$ , a proxy for the minimum mass of halos hosting star-forming galaxies. Increasing this threshold, results in fewer sources to contribute to reionisation. In the top right panel, the maximum photon horizon,  $R_{\text{mfp}}$ , is varied. Essentially, in this specific work it acts as a maximum allowable bubble size. Note that in this case, the change in  $R_{\text{mfp}}$  does not alter the neutral fraction strongly, thus the changes in the 21-cm power spectrum are purely as a result in changes to the size of the ionised regions. Finally, in the bottom right we highlight astrophysical models with the same IGM neutral fraction (i.e. the same stage of reionisation). Despite being at the same point in reionisation, the amplitude and shape of the 21-cm power spectrum differs considerably, highlighting the

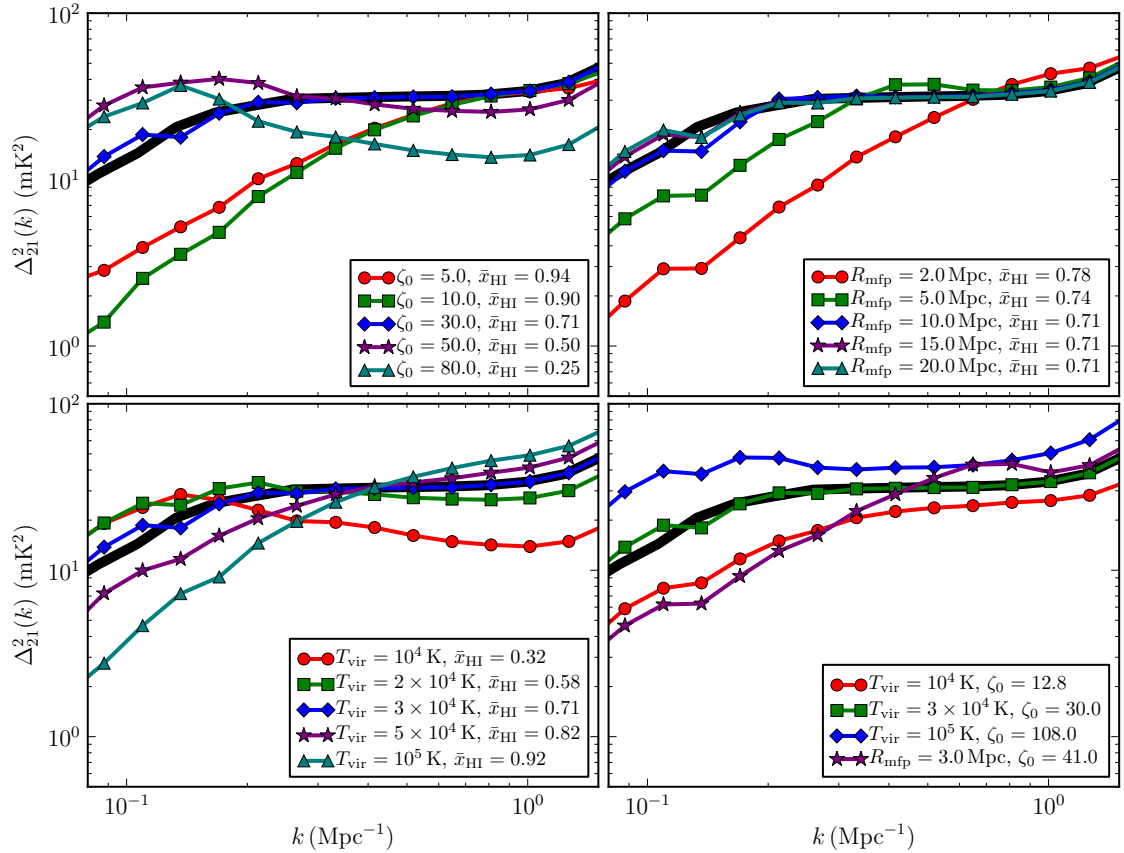


Figure 4.4: The three dimensional spherically averaged 21-cm power spectrum at  $z = 9.0$  when varying astrophysical parameters controlling different astrophysical processes, assuming  $T_S \gg T_{CMB}$  ([13]). Top left: the number of ionising photons produced per baryon (ionising efficiency,  $\zeta$ ), top right: maximum ionising photon horizon (proxy for maximum allowable bubble size,  $R_{\text{mfp}}$ ) and bottom left: minimum mass of halo hosting star-forming galaxy (represented here as  $T_{\text{vir}}$ ). Bottom right: several models at the same ionisation fraction.

sensitivity of the 21-cm power spectrum to the underlying astrophysical parameters.

While this example is only for the epoch of reionisation, the same strong sensitivity of the 21-cm power spectrum to the underlying astrophysics is true for both the heating or Ly $\alpha$  coupling epochs (see e.g. [citations](#)). This highlights the strength and utility of the 21-cm power spectrum for recovering the astrophysical information. As such numerous authors have explored the impact of various astrophysical processes on the 21-cm power spectrum. [refer to a variety of papers here, and potentially highlight the specific process used.](#)

### 4.2.3 Bispectrum

The logical extension beyond the power spectrum, the bispectrum,  $B$ , is simply the Fourier transform of the 3-point correlation function,

$$\langle \delta_{21}(\mathbf{k}_1) \delta_{21}(\mathbf{k}_2) \delta_{21}(\mathbf{k}_3) \rangle = (2\pi)^3 \delta_D(\mathbf{k}_1 + \mathbf{k}_2 + \mathbf{k}_3) B(\mathbf{k}_1, \mathbf{k}_2, \mathbf{k}_3), \quad (4.5)$$

where the  $\delta_D$  enforces that the Fourier modes must form closed triangles. It measures the excess probability of the underlying quantity as a function of three spatial positions in real space. The bispectrum provides a scale-dependent measure of the non-Gaussianity of the 21-cm signal, and as such contains additional astrophysical information beyond that held in the power spectrum. However, it suffers from lower signal-to-noise as there are less modes to average over to boost the signal.

Whereas the power spectrum is relatively trivial to interpret as it is a measure of the power over a single length scale,  $k$ , the bispectrum is the measure of power over all possible triangle configurations that satisfy the closure condition from  $\delta_D$ . Thus in order to simplify the interpretation of the bispectrum, it is common to consider several simplified triangle configurations. These are typically: (i) the equilateral triangle ( $k_1 = k_2 = k_3$ ), (ii) the isosceles triangle ( $k_1 > k_2 = k_3$ ), (iii) folded triangle ( $k_1 = 2k_2 = 2k_3$ ), (iv) elongated triangle ( $k_1 = k_2 + k_3$ ) and (v) the squeezed triangle ( $k_1 \simeq k_2 \gg k_3$ ). Each, corresponds to different physical properties of the real-space field.

While a detailed discussion of the 21-cm bispectrum is beyond the scope of this chapter, it is fruitful to provide a brief explanation and example of the various configurations (see for example [21] and [39] for more detailed discussions). The equilateral configuration is essentially an extension of the power spectrum, in the sense that it is expressed as a single amplitude scale,  $k$ . Generally speaking, it produces the largest amplitude signal and as such is the most commonly studied configuration. It is sensitive to the spherical symmetry of the 21-cm signal such as the scale of the ionised H<sub>II</sub> regions during reionisation or the hot/cold spots due to IGM heating. Typically its amplitude grows during the EoR as the signal becomes more non-Gaussian due to the topology of the ionisation field. Shifting towards isosceles or folded triangles, these become more sensitive to planar or filamentary structures in the underlying 21-cm signal. Thus as the topology of either the ionised or X-ray heated regions deviate away from spherical symmetry (i.e. either multiple contributing sources or overlap of ionised regions) the signal should increase with increasing angle. The squeezed limit correlates the small-scale signal from two modes with a large-scale mode, for example capturing the impact of the large-scale environment (i.e. from X-ray heating) on the small-scale power spectrum (i.e. source clustering).

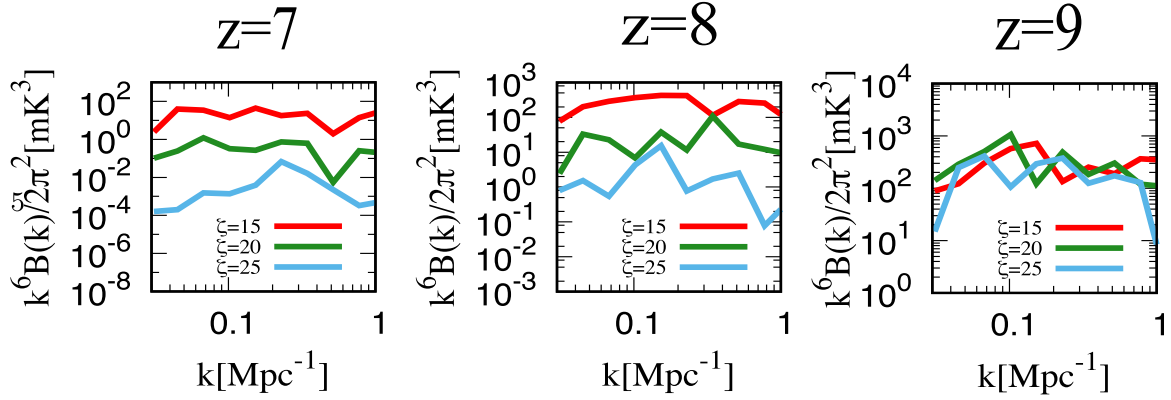


Figure 4.5: Variation in the amplitude of the equilateral bispectrum at  $z = 7, 8$  and  $9$  for different ionising efficiencies,  $\zeta$ , from [32].

In addition to the structural information in the bispectrum amplitude, the relative sign of the bispectrum equally reveals insight into the underlying processes. As discussed in [22], the sign of the bispectrum during reionisation can distinguish between whether the non-Gaussianity is driven by the topology of the ionised regions (where the bispectrum is negative) compared to being driven by the matter and cross-bispectra (where it is positive).

In Figure 4.5, we compare the equilateral bispectrum at  $z = 7, 8$  and  $9$  from [32] for differing ionising efficiency,  $\zeta$ . For decreasing  $\zeta$ , the amplitude of the bispectrum increases due to its amplitude being dependent on the ionisation fraction. Thus, different reionisation models are easily distinguishable by the 21-cm bispectrum.

Note that the bispectrum is not measured independently from the power spectrum, thus both the power spectrum and bispectrum can be combined to considerably improve our understanding of the underlying astrophysics (can refer to the equivalent case for cosmology where the combination of the two improve the constraining power).

In recent times, the 21-cm bispectrum has gained considerable traction in interpreting the astrophysics of reionisation and the cosmic dawn. add in citations here works exploring the bispectrum, and quickly what they are exploring.

Some examples of the exploration of the 21-cm bispectrum. [39, 40, 31]

#### 4.2.4 Trispectrum

I am certain someone looked at the trispectrum...

#### 4.2.5 One-point statistics

Rather than measuring the Fourier transform (e.g. power spectrum) of the 21-cm brightness temperature signal,  $\delta_{21}(\mathbf{x})$ , we can instead measure the one-point statistics (or moments) of the probability distribution function (PDF). In fact, we have already discussed the lowest order one-point statistic, that is, the mean of  $\delta T_b(\mathbf{x})$  given by the global signal (see 4.2.1). These one-point statistics of the PDF essentially measure the deviations away from a fully Gaussian PDF, thus they are by definition sensitive to the non-Gaussian nature of the 21-cm

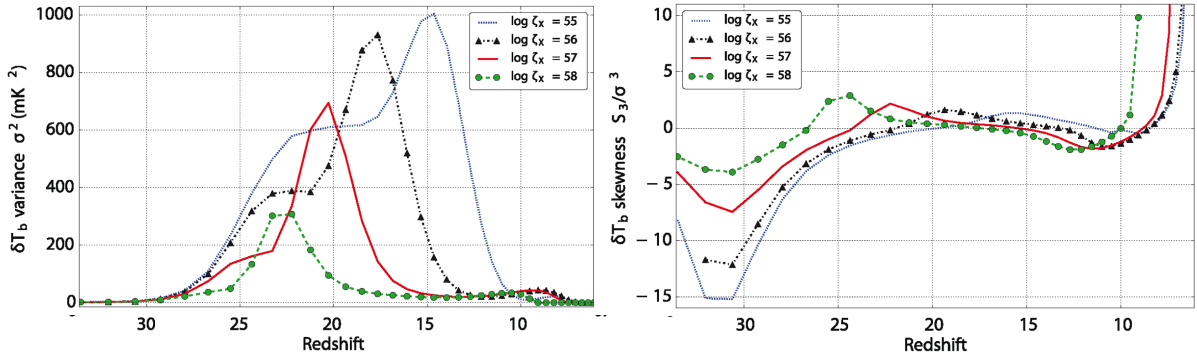


Figure 4.6: The variance (left) and normalised skewness (right) of the 21-cm brightness temperature when varying the efficiency of X-ray heating in the IGM from [38].

signal. Generally speaking, the one-point statistics of  $\delta T_b(\mathbf{x})$  are given by,

$$m_n = \frac{1}{N} \sum_{i=0}^N (\delta T_b(\mathbf{x}_i) - \bar{\delta T}_b)^n, \quad (4.6)$$

where  $m_n$  is the  $n$ -th order moment and  $N$  is the number of pixels over which the signal is measured. For the 21-cm signal, these moments would be generated from the observed two-dimensional tomographic maps of the 21-cm signal.

The next lowest order statistic of the PDF following the mean is the variance,  $\sigma^2$ . The variance is equivalent to the average of the power spectrum over all Fourier modes,  $k$ ,

$$\sigma^2 = (\bar{\delta T}_b)^2 \int \frac{d^3 k}{(2\pi)^3} P(\mathbf{k}). \quad (4.7)$$

As it is the average over all spatial information, the variance itself is less sensitive to the underlying astrophysics than the power spectrum. However, the strength of one-point statistics shines through when using the higher order moments in combination with the variance (or power spectrum). The next two higher order moments are referred to as the skewness and the kurtosis. Equivalent to the variance's relation to the power spectrum, the skewness and kurtosis are the average over all Fourier modes of the bispectrum and trispectrum respectively (the three and four-point correlation functions). As such, whereas the power spectrum only measures the 2-point correlations, the skewness and kurtosis reveals insights from the non-Gaussian properties of the 21-cm signal.

The amplitude of the variance is sensitive to differences in the 21-cm brightness temperature. For example, during the EoR, as the number of ionised regions increases (i.e. the contrast between the 21-cm signal from the neutral regions compared to zero signal from the ionised regions) the variance increases. It subsequently turns over as most of the volume is ionised. The skewness is a measure of the asymmetry of the underlying PDF. A negative skewness corresponds to a longer tail towards a lower amplitude signal and a positive skewness corresponds to a longer tail towards higher amplitude signals. The kurtosis is essentially a measure of the outliers of the distribution, with increasing positive (negative) kurtosis corresponding to larger positive (negative) amplitude outliers.

Figure 4.6 shows an example of both the variance (left) and normalised skewness (right panel) of the 21-cm brightness temperature under different levels of X-ray heating. For increasing X-ray efficiencies (i.e. increase heating) the peak of the variance decreases in amplitude while shifting to earlier times. Increasing the efficiency allows the X-ray heating to occur earlier, reducing the contrast between the  $T_{\text{CMB}}/T_S$  resulting in a lower amplitude peak in the variance. This same behaviour equally results in larger skewness for decreasing X-ray efficiency, owing to a more asymmetric PDF of 21-cm brightness temperatures due to the increasing contrast in  $T_{\text{CMB}}/T_S$ . Clearly from Figure 4.6 it can be seen that these one-point statistics are capable of distinguishing between different astrophysical models.

Some (but not all) references for the one-point statistics. [14, 26, 18, 19, 37, 30, 29]

### 4.2.6 Wavelets

Thus far we have only considered either real-space quantities such as the one-point statistics or the Fourier transform of the  $n$ -point correlation functions (i.e. the power spectrum and bispectrum). The Fourier transform measures the amplitude of the fluctuations of a given spatial scale, and in order to increase the signal-to-noise we must average the signal over all line-of-sight modes within some observed bandwidth. As a result, we average over modes containing different redshift evolutions and thus increase the bias of the signal. This can be minimised somewhat, for the case of the power spectrum, by averaging the signal over relatively narrow observing bandwidths. However, it still results in some loss in fidelity of the signal.

Instead, in [34] the authors explore the potential usage of wavelets, which provide multiple alternatives to the Fourier basis set. Specifically, they explored the application of the Morlet Transform. This provides a family of curves which provide the ability to localise the 21-cm signal both spatially and in frequency. In doing so, the equivalent to the power spectrum, the Morlet power spectrum is capable of providing an unbiased estimator which maximises the three dimensional nature of the 21-cm signal. Preliminary analysis shows that the Morlet power spectrum performs more optimally than the Fourier power spectrum. A physical interpretation of the Morlet power spectrum in the context of the evolution of the 21-cm signal has yet to be explored.

### 4.2.7 Topological measurements of the 21-cm signal

All previous approaches discussed up till this point have characterised the 21-cm signal using some form of statistical analysis, on the basis of maximising the signal-to-noise. However, the most advanced radio interferometers ([do I need to name them or refer to future chapter?](#)) should enable two dimensional images of the 21-cm signal. These images will contain the complicated morphology of the hot/cold patches of the 21-cm brightness temperature throughout the history of reionisation and the cosmic dawn. The relative sizes, shapes and clustering of these hot/cold patches can reveal numerous insights into the underlying astrophysical processes, such as the number density of sources, their contribution to the heating/ionisation of the IGM and the shape of the emitted spectrum of radiation. The study of these geometric shapes in mathematics is referred to as topology.

Topological studies of reionisation and the cosmic dawn are complimentary to the statistical methods described above. For example, reionisation proceeds through three main stages (e.g. [12, 10]): pre-overlap, over-lap and post-overlap. In pre-overlap, the first ionised H II regions (or bubbles) grow completely in isolation roughly until  $x_{\text{HI}} \geq 0.1$ . Over-lap ( $0.9 \geq x_{\text{HI}} \geq 0.1$ ) describes the merging of these ionised bubbles into essentially a single large connected ionised region. Finally, post-overlap  $x_{\text{HI}} \geq 0.9$  corresponds to the breaking down of the last remaining patches of neutral IGM into smaller and smaller islands. Topological studies are capable of breaking down these transitions by describing the ratios of ionised and neutral regions, how the ionised (or neutral) regions are connected together and how they are embedded in the larger structures as they form. This provides unique insights into the reionisation epoch not available from statistical methods.

There are numerous methods to attempt to characterise the topology of the 21-cm signal. Below, we summarise several of the main approaches taken in the literature. Fundamental to topological studies is the definition of how to identify regions of interest. Typically, a threshold value is required, with the quantity above/below this threshold being used to distinguish the two regions.

### Genus or the Euler characteristic

The genus,  $g$ , is a topological property that defines the number of cuts one can make to an object (i.e. H II region) without dividing it into independent disconnected sub-regions. It can simply be expressed as,

$$g = N_{>\text{th}} - N_{<\text{th}} \quad (4.8)$$

where  $N_{>\text{th}}$  and  $N_{<\text{th}}$  are the number of connected (or fully enclosed) regions above and below the threshold value for identification. By gradually increasing the threshold value from some initial starting value, a genus curve is constructed, which is a measure of the connectedness of the quantity as a function of different threshold values (e.g.  $x_{\text{HI}}$ ,  $\delta T_b$ ). Typically, these threshold values are expressed in units of the standard deviation from the mean.

The genus has been explored, both in two and three dimensions, either in the context of the ionised (or neutral) field ([11, 20, 8]) or the 21-cm brightness temperature field ([15, 36]). However, it has yet to be explored in the context of the heating epoch (i.e.  $T_S \gg T_{\text{CMB}}$  is typically assumed). For a purely Gaussian field, the genus curve is symmetric around zero. Thus deviations from symmetry highlight the non-Gaussianity of the 21-cm signal.

Differences in the evolution in the amplitude of the genus as a function of threshold density can distinguish different source biases and ionising efficiencies. For example, reionisation driven by larger, more biased sources exhibits a different topology than one driven by numerous fainter sources. This appears as changes in the amplitude of the genus as a function of threshold. When the ionised regions are isolated, the genus amplitude is higher than when they begin to overlap (as the total number of isolated ionised regions decreases).

### Minkowski functionals

A more generalised description of the geometry or topology of the 21-cm signal can be obtained from what are referred to as Minkowski functionals. These are well known concepts

from the branch of mathematics known as integral geometry. Three dimensional space is completely defined by four Minkowski functionals. Used heavily in cosmology, in particular large-scale structure [need to add citations?](#), recently they have gained favour for describing the topology of reionisation [11, 8, 41, 4].

For a zero mean scalar function,  $u(x)$ , (e.g.  $\delta T_b$ ) within a volume,  $V$ , and standard deviation,  $u$ , we can define an excursion set,  $F_v$ , which contains all points that satisfy the threshold,  $u(x) \geq v\sigma$ , where  $v = u_{\text{th}}/\sigma$  and  $u_{\text{th}}$  is the threshold value. Mathematically, this gives rise to the following Minkowski functionals,

$$V_0(v) = \frac{1}{V} \int_V d^3x \Theta[u(x) - v\sigma] \quad (4.9)$$

$$V_1(v) = \frac{1}{6V} \int_{\partial F_v} ds \quad (4.10)$$

$$V_2(v) = \frac{1}{6\pi V} \int_{\partial F_v} ds [\kappa_1(x) + \kappa_2(x)] \quad (4.11)$$

$$V_3(v) = \frac{1}{4\pi V} \int_{\partial F_v} ds \kappa_1(x) \kappa_2(x). \quad (4.12)$$

Here,  $\Theta$  is the Heaviside step-function,  $\partial F_v$  is the surface of the excursion set,  $ds$  is the surface element and  $\kappa_1(x)$  and  $\kappa_2(x)$  are the principle curvatures (inverse of the principle radii) at  $x$ . The zeroth Minkowski functional,  $V_0$ , corresponds simply to the total volume of the excursion set (i.e. volume above the threshold value),  $V_1$  and  $V_2$  correspond to the total surface and mean curvature of the excursion set while  $V_3$  is the integrated Gaussian curvature over the surface or the Euler characteristic (also  $\chi$ ). The Euler characteristic is related to the genus,  $g$ , via  $V_3 = 2(1 - g)$  thus it effectively describes the shape of the excursion set. Thus, the full set of Minkowski functionals contain additional information beyond that of just the genus.

Generally speaking the following behaviour is expected of the Minkowski functionals throughout reionisation and the cosmic dawn.  $V_0$  describes the volume contained above/below the threshold value. For example, if  $V_0 \sim 0.5$  at  $\delta T_b = 0$  this implies the number of hot/cold patches are roughly equal. The  $V_0$  curve will move from left to right (to increasing  $\delta T_b$ ) as heating occurs.  $V_1$  (reflected in  $V_2$ ) exhibits a similar shift to higher  $\delta T_b$ , however it is initially strongly peaked with a high density tail containing the heated regions. This peak smooths out over a broader range of  $\delta T_b$  as heating continues. During reionisation,  $V_1$ ,  $V_2$  and  $V_3$  will shift toward  $\delta T_b = 0$  as the higher amplitude  $\delta T_b$  regions ionise first. [Is this description even relevant without a figure? Don't want to include too many figures...](#)

In Figure 4.7 we show the four Minkowski functionals for the 21-cm brightness temperature when varying the underlying astrophysical processes from [41] at a fixed neutral fraction ( $x_{H_I} \approx 0.5$ ) and redshift ( $z = 8.6$ ). Here, these authors consider variations in either the ionising efficiency,  $\zeta$ , or the minimum halo mass hosting star-forming galaxies,  $T_{\text{vir}}$ . Clearly, different reionisation histories are distinguishable by the Minkowski functionals.

## Shape-finders

An extension to Minkowski functionals, shape-finders ([need citations to the method](#)) are a way to characterise the shapes of compact surfaces. Applied to reionisation ([2, 1]), these

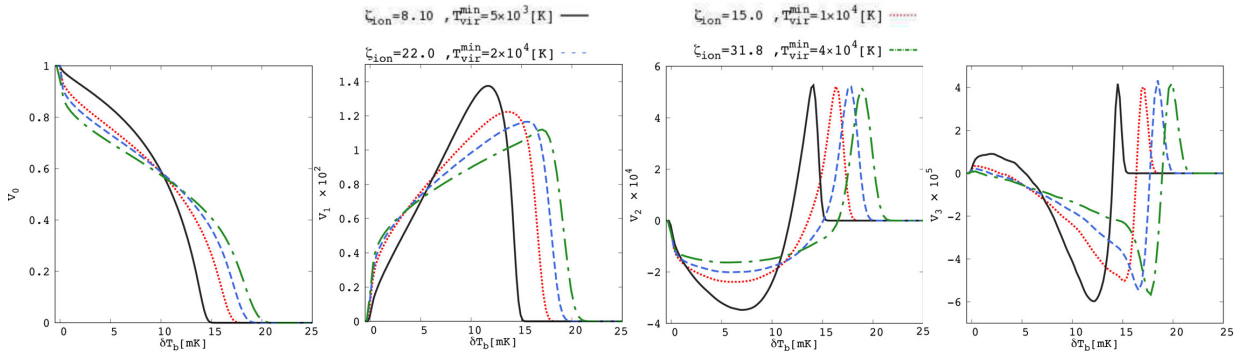


Figure 4.7: The impact of varying the astrophysical parameterisation for a fixed neutral fraction ( $x_{H_I} \approx 0.5$ ) and redshift ( $z = 8.6$ ). Consider the impact of varying either the ionising efficiency  $\zeta$  or the minimum halo mass for star-forming galaxies,  $T_{\text{vir}}$  on the four Minkowski functionals. Figure adapted from [41].

shape-finders can provide a means to characterise how the ionised regions grow. For example, they are useful in being able to distinguish between whether the topology is planar or filamentary. Shapefinders are derived directly from the Minkowski functionals via:

$$\text{Thickness : } T = \frac{3V_0}{V_1} \quad (4.13)$$

$$\text{Breadth : } B = \frac{V_1}{V_2} \quad (4.14)$$

$$\text{Length : } L = \frac{V_3}{4\pi}. \quad (4.15)$$

These shape-finders are interpreted as providing the three principle axes of a physical object. The morphology of the ionised region can then be defined by either the planarity or its filamentarity:

$$\text{Planarity : } P = \frac{B - T}{B + T} \quad (4.16)$$

$$\text{Filamentarity : } F = \frac{L - B}{L + B}, \quad (4.17)$$

where  $P \gg F$  corresponds to planar objects (i.e. sheets) while the opposite  $F \gg P$  corresponds to a filament.

During the reionisation epoch, percolation theory shows that a single infinitely large, multiply connected ionised region will rapidly form (add citations). When describing the largest singly connected ionised region, [2, 1] find that both  $T$  and  $B$  evolve slowly whereas  $L$  increases rapidly. Thus, this large ionised region grows only along its ‘length’ implying a highly filamentary structure.

### Persistent homology theory

Homology characterises the topology of the ionisation bubble network into its fundamental components: ionised regions, tunnels (enclosed neutral filaments) and cavities (patches of

neutral hydrogen). The persistence then quantifies the significance of the feature, for example its lifetime, by computing a birth and death date for an object. Thus far, it has only been applied to the ionisation field ([6]). These ionised regions ( $\beta_0$ ), tunnels ( $\beta_1$ ) and cavities ( $\beta_2$ ) can be described by the so-called Betti numbers, which contain the total number of each. These can be related to the earlier Euler characteristic via,  $\chi = \beta_0 - \beta_1 + \beta_2$ . By breaking the Euler characteristic into the constituent components and tracking their individual growth reveals additional information on the topology, thus it is a more generalised method than either the genus of the Minkowski functionals.

## Fractal dimensions

An alternative to classifying the ionised (neutral) regions embedded in the 21-cm signal is through a fractal dimensions analysis. Applied to reionisation ([3]), this provides a direct means to quantify the deviation away from a homogenous distribution, as well as the degree of clustering and lacunarity (a measure of the size of the ionised regions). The fractal dimension,  $D_q$ , also known as the Minkowski-Bouligand dimension, is a measure of how complicated the topology of the field in question is. A homogeneous distribution in three dimensions has a  $D_q = 3$ . [3] show that the topology of reionisation exhibits a significant multi-fractal behaviour. These authors find that the fractal dimension is relatively insensitive to the minimum halo mass of the star-forming galaxies, however it was sensitive to the mass averaged ionisation fraction. Thus, the correlation dimension can be useful for constraining the global neutral fraction. Additionally, it is a strong discriminant of models of outside-in and inside-out reionisation.

## Contour Minkowski tensor

In [17, 16], these authors introduced the rank-2 contour Minkowski tensor (add citations) in two-dimensions which can probe both the length and time scales of the ionised regions during reionisation. The Minkowski tensors are a generalisation of the scalar Minkowski functionals. The contour Minkowski tensor provides information on both the alignment of structures in two dimensions and their anisotropy. Since the ionised regions are not perfectly spherical, their shape anisotropy can be explored by the ratio of the two eigenvalues of the contour Minkowski tensor while the amplitude of the eigenvalues describes their size.

In this analysis, the number of connected regions and holes (e.g. the Betti numbers) given a specific threshold value are tracked. In addition, a characteristic radius of the structures and their shape anisotropy can be determined. For a description of the evolution of  $\delta T_b$ , we refer the reader to [16], ignoring it here owing to its complexity due to the definition of the connected regions and holes as a function of the threshold value as the 21-cm signal transitions transition from hot/cold regions in the heating epoch to neutral/ionised regions during reionisation (would require several figures and long descriptions. Don't think that's required here (hopefully not)). However, we emphasise that these authors explored varying the minimum mass hosting star-forming haloes and clearly show that different astrophysical parameters can be distinguishable.

### 4.2.8 Bubble size distributions

Throughout reionisation and the cosmic dawn, the morphology of the 21-cm signal is driven by processes that embed a morphological signature on the 21-cm signal. For example the ionised H<sub>II</sub> regions or the hot/cold spots in the 21-cm brightness temperature during the heating epoch. Quite simply, if we could measure the distribution of these ‘bubbles’ and how they evolve over cosmic time we would have a strong discriminant of the populations of sources responsible for the heating and ionisation of the IGM and also the spectrum of their emitted radiation. Effectively, this would behave as a statistical distribution function (number of bubbles given a physical scale) analogous to a halo mass function.

However, the bubbles do not remain isolated, very quickly overlapping into increasingly large and topologically complex structures. Thus, there is no unique way to characterise these bubbles. Nevertheless several methods have been explored in order to be able to construct a probabilistic distribution of the bubble sizes.

The simplest approach is to perform a friends-of-friends approach ([add citations here](#)), which simply connects all cells above (below) a threshold value. However, very rapidly a single large ionised structure exists which fills most of the volume with only a small fraction of isolated regions remaining. The relative volume of this large ionised region and the distribution of the smaller regions can still differentiate reionisation morphologies, however there is less statistical weight.

An alternative approach is to place a sphere on every pixel, averaging out the signal across increasingly larger spheres until a radius is found where the average signal is above the threshold value ([add citations here](#)). While this generates a more statistically meaningful distribution of bubbles, these sizes tend to overestimate the size of the topological feature of interest due to the assumed spherical symmetry.

Recently, more statistically robust methods have been introduced to measure the bubble size distributions. First of these is the mean free path method, which uses a Monte Carlo approach by considering a large number of random positions and determining the distance to the edge of the bubble from different random directions ([add citations here](#)). This results in an unbiased estimator of the bubble size distribution. Next, adapted from the cosmological search for voids, the Watershed ([add citations here](#)) method has been explored. This is a well known two-dimensional image segmentation algorithm creating contours of constant value (i.e.  $\delta T_b$ ) which are treated as levels of a tomographic map. These are then ‘flooded’ to obtain unique locations for the minima (e.g. ionised regions).

Remaining in the image processing regime, ([add citations here](#)) introduced the superpixels method. This uses a region based method to identify regions of complex shapes (i.e. ionised regions) segmenting these regions into smaller segments called superpixels. The bubble size distribution is then obtained by averaging the value of the 21-cm brightness temperature within each segment ([search for specific details on how this becomes a bubble distribution](#)).

### 4.2.9 Individual bubbles

Images will provide a direct tangible link to the process of reionisation. Revealing exactly where ionising bubbles are, and thus where to look for the sources responsible for the bubble creation.

However, bubble identification will become rather problematic, as it is the differential brightness that is observed, not the raw brightness temperature. Need smart/sophisticated approaches to search and characterise the signal.

Look at individual regions of interest, i.e. around a bright QSO or large number of galaxies.

Matched filters etc., are useful for finding/detecting isolated bubbles

### 4.2.10 Stacked images

May be difficult to detect individual objects, instead, one could stack 21cm spectra centred on known galaxies. See Paul Geil's paper.

Border's on potential discussions of synergies. Requires known locations of ionising sources with precise redshifts and positions of the sky. JWST/WFIRST. Is there

### 4.2.11 Other statistics

Are there other statistics that I have overlooked/forgotten. Need to do a search of the literature to ensure I have covered everything.

## 4.3 Efficient methods to model/simulate the 21cm signal

Ideally we want to use the largest, most physically accurate simulations to match the observed 21cm signal. However, this is not practical. Instead, we must come up with methods to compensate accuracy for efficiency.

Originally I envisaged this section to go as follows

- Discuss briefly that numerical simulations are great but too computationally expensive
- Highlight semi-numerical/analytic simulations as fitting the bill by being faster etc.
- Then discuss alternatives (i.e. emulators).

This will need to be re-worked given Jordan's plan to discuss this. I haven't yet thought of a logical plan to motivate this. I guess one way would be to concatenate it into just a simulation section and briefly summarise what was discussed in Jordan's chapter (which is a couple of chapters ago, so might be appropriate to do so). It's less obvious to move into discussing emulators in the absence of motivating the need for them by highlighting the complications of simulations in general.

### 4.3.1 Numerical simulations

Ideally, use large, numerical simulations to make a realisation which matches observation. Want to include as much physics as possible into these simulations. Doing so, comes at a serious cost. Simulating the 21cm signal is complicated! Brief summary on the required dynamic range. Briefly highlight the expensive nature of these simulations, Hydrodynamics, radiative transfer etc. Quickly becomes computationally prohibitive to run more than a couple of realisations. **Jordan's section (Modelling Tools) will likely cover most if not all of this.**

### 4.3.2 Semi-numerical/analytic models of the 21cm signal

Enter semi-numerical approaches, which broadly encapsulate the global average quantities of reionisation and the cosmic dawn and reproduce morphologically similar realisations of the 3D structure. The advantage here is that the computational costs are drastically reduced (orders of magnitude less). **Jordan's section (Modelling Tools) will likely cover most if not all of this.**

### 4.3.3 Intelligent sampling of the parameter space

Running simulations to span all of the allowed parameter space may be too computationally intensive. However, perhaps we can make intelligent assumptions/guesses about how many simulations to run, and on a specific area of physics to focus on. Some of the concepts here may overlap slightly with the Emulator section below. This sampling was discussed in one of Benoit's recent papers.

### 4.3.4 Emulators

An alternative to directly running a simulation to estimate some astrophysical statistic/model, one can instead construct a function which estimates what the statistical signal should be, given some astrophysical or cosmological parameter set. This is what is referred to as an emulator. Using simulations, a generator function is constructed which can approximate the statistics of the signal. Results in multiple orders of magnitude improvement in computational speed as no new simulations are required. However, it can only approximate statistics, it does not generate 3D simulations.

Developing an emulator benefits from efficient parameter space approaches, as it minimises the size of the database required to construct the emulator. There are a variety of approaches to consider when attempting to minimise the sampling of the astrophysical parameter space. For example Latine-Hypercube, Gaussian processes... Can briefly discuss each method, and a few recent papers that explore methods to do this

There are numerous machine learning approaches to construct an emulator.

Discuss Nick Kern's of 21cmFAST and Cohen's global signal one of Anastasia's code.

Highlight and discuss Chardin et al. (2019). Emulation of reionisation simulations (construction of treion maps given source lists). arxiv:1905.06958

### 4.3.5 Characterising our ignorance

We are fully aware that semi-numerical approaches are inaccurate at 10s of per cent level. Additionally, they oversimplify/completely ignore the underlying astrophysical properties. However, if the global quantities (observables such as luminosity functions etc.) can still be reproduced within agreement, we can develop an understanding of how one might map from a semi-numerical simulation, to a more realistic simulation. Basically, tell the large, computationally expensive simulation where exactly to look in the region of parameter space.

Using summary statistics and globally average observables, we can develop a means to calibrate one simulation to mimic the outputs of another. In other words, develop a bias or functional form to smooth out uncertainties from one simulation to mimic the results of a more detailed simulation.

Describe ongoing attempts to quantify this. i.e. use luminosity functions to calibrate simulations, apply redshift corrections to deal with photon non-conservation etc.

These correction factors etc., will be crucial for inferring astrophysics and cosmology from the 21cm signal

## 4.4 Inference methods for 21cm

Having discussed methods to model/simulate the 21cm signal, now need to shift focus to methods to infer information about the astrophysics/cosmology from the 21cm signal.

### 4.4.1 Fisher Matrices

Simplest method, which takes derivatives with respect to model parameters of a functional form (i.e. a 21cm statistical signal) to infer parameter constraints. Effectively, exploits how sensitive the 21cm signal is to specific parameters. Limiting assumption include Gaussianity etc.

Successfully used for cosmology

### 4.4.2 Bayesian MCMC

Significantly more robust method to parameter inference. Outline Bayes' theorem. Highlight that this basically boils down to exploring by random walks, using a likelihood function and priors to accept/penalise regions of parameter space. Very useful for recovering constraints. Again, successfully used in Cosmology etc.

Describe its use in the context of 21cm. Introduce 21CMMC, and a couple of other codes that use MCMC (Sultan's simfast21, Jordan's global signal, Geraint's MCMC, Simon's Mphysa). Highlight that 21CMMC is the only direct MCMC. Emphasise that techniques such as emulators can be coupled with MCMC to improve overall computational efficiency at the cost of some further inaccuracies.

Don't forget the Bernardi and Zwart papers.

### 4.4.3 Nested sampling and model inference

We have a wide variety of simulations, each with their own strength's and weaknesses. In principle, various models/simulations/physical prescriptions can be discriminated against using model selection or inference. Related to MCMC, nested sampling can focus on model selection rather than simply astrophysical recovery. Can refer to Tom Binnie's recent paper.

### 4.4.4 Neural Networks

Instead of using MCMC to recover parameters from statistics, we can use the full 2/3D images of the 21cm signal with neural networks. One can construct a database of simulations and extract the 21cm signal to construct a neural network. This network can then learn a large number of properties, i.e. how changes in the topology are affected by astrophysical parameters etc. Using this technique one can directly convert from an observed 2D image to the underlying astrophysics. Like emulators, the application of the network is extremely quick. Downsides are parameter errors etc. and in some sense physical intuition. It tells you an answer, but not why.

Simulated images of the 21cm signal have already been used to infer astrophysical and cosmological constraints. For example with convolutional networks (e.g Nicolas or Paul La Plante). Discuss other machine learning approaches.

# Bibliography

- [1] Satadru Bag, Rajesh Mondal, Prakash Sarkar, Somnath Bharadwaj, Tirthankar Roy Choudhury, and Varun Sahni. Studying the morphology of H I isodensity surfaces during reionization using Shapefinders and percolation analysis. *Monthly Notices of the Royal Astronomical Society*, 485(2):2235–2251, May 2019.
- [2] Satadru Bag, Rajesh Mondal, Prakash Sarkar, Somnath Bharadwaj, and Varun Sahni. The shape and size distribution of H II regions near the percolation transition. *Monthly Notices of the Royal Astronomical Society*, 477(2):1984–1992, Jun 2018.
- [3] Bidisha Bandyopadhyay, T. Roy Choudhury, and T. R. Seshadri. Studying neutral hydrogen structures during the epoch of reionization using fractal dimensions. *Monthly Notices of the Royal Astronomical Society*, 466(2):2302–2311, Apr 2017.
- [4] Zhaoting Chen, Yidong Xu, Yougang Wang, and Xuelei Chen. Stages of Reionization as revealed by the Minkowski Functionals. *arXiv e-prints*, page arXiv:1812.10333, Dec 2018.
- [5] Aviad Cohen, Anastasia Fialkov, Rennan Barkana, and Matan Lotem. Charting the parameter space of the global 21-cm signal. *Monthly Notices of the Royal Astronomical Society*, 472(2):1915–1931, Dec 2017.
- [6] Willem Elbers and Rien van de Weygaert. Persistent topology of the reionization bubble network - I. Formalism and phenomenology. *Monthly Notices of the Royal Astronomical Society*, 486(2):1523–1538, Jun 2019.
- [7] Anastasia Fialkov, Rennan Barkana, and Aviad Cohen. Constraining Baryon-Dark-Matter Scattering with the Cosmic Dawn 21-cm Signal. *Physical Review Letters*, 121(1):011101, Jul 2018.
- [8] Martina M. Friedrich, Garrelt Mellema, Marcelo A. Alvarez, Paul R. Shapiro, and Illian T. Iliev. Topology and sizes of H II regions during cosmic reionization. *Monthly Notices of the Royal Astronomical Society*, 413(2):1353–1372, May 2011.
- [9] Steven R Furlanetto, Matthew McQuinn, and Lars Hernquist. *Monthly Notices of the Royal Astronomical Society*, 365:115, Jan 2006.
- [10] Steven R. Furlanetto and S. Peng Oh. Reionization through the lens of percolation theory. *Monthly Notices of the Royal Astronomical Society*, 457(2):1813–1827, Apr 2016.

- [11] Liron Gleser, Adi Nusser, Benedetta Ciardi, and Vincent Desjacques. The morphology of cosmological reionization by means of Minkowski functionals. *Monthly Notices of the Royal Astronomical Society*, 370(3):1329–1338, Aug 2006.
- [12] Nickolay Y. Gnedin. Cosmological Reionization by Stellar Sources. *The Astrophysical Journal*, 535(2):530–554, Jun 2000.
- [13] Bradley Greig and Andrei Mesinger. 21CMMC: an MCMC analysis tool enabling astrophysical parameter studies of the cosmic 21 cm signal. *Monthly Notices of the Royal Astronomical Society*, 449(4):4246–4263, Jun 2015.
- [14] Geraint J. A. Harker, Saleem Zaroubi, Rajat M. Thomas, Vibor Jelić, Panagiotis Labropoulos, Garrelt Mellema, Ilian T. Iliev, Gianni Bernardi, Michiel A. Brentjens, and A. G. de Bruyn. Detection and extraction of signals from the epoch of reionization using higher-order one-point statistics. *Monthly Notices of the Royal Astronomical Society*, 393(4):1449–1458, Mar 2009.
- [15] Sungwook E. Hong, Kyungjin Ahn, Changbom Park, Juhan Kim, Ilian T. Iliev, and Garrelt Mellema. 2D Genus Topology of 21-cm Differential Brightness Temperature During Cosmic Reionization. *Journal of Korean Astronomical Society*, 47(2):49–67, Apr 2014.
- [16] Akanksha Kapahtia, Pravabati Chingangbam, and Stephen Appleby. Morphology of 21cm brightness temperature during the Epoch of Reionization using Contour Minkowski Tensor. *arXiv e-prints*, page arXiv:1904.06840, Apr 2019.
- [17] Akanksha Kapahtia, Pravabati Chingangbam, Stephen Appleby, and Changbom Park. A novel probe of ionized bubble shape and size statistics of the epoch of reionization using the contour Minkowski Tensor. *Journal of Cosmology and Astroparticle Physics*, 2018(10):011, Oct 2018.
- [18] Piyanat Kittiwisit, Judd D. Bowman, Daniel C. Jacobs, Nithyanandan Thyagarajan, and Adam P. Beardsley. Impact of Instrument Responses on the Detectability of One-point Statistics from Redshifted 21 cm Observations. *arXiv e-prints*, page arXiv:1610.06100, Oct 2016.
- [19] Kenji Kubota, Shintaro Yoshiura, Hayato Shimabukuro, and Keitaro Takahashi. Expected constraints on models of the epoch of reionization with the variance and skewness in redshifted 21 cm-line fluctuations. *Publications of the Astronomical Society of Japan*, 68(4):61, Aug 2016.
- [20] Khee-Gan Lee, Renyue Cen, III Gott, J. Richard, and Hy Trac. The Topology of Cosmological Reionization. *The Astrophysical Journal*, 675(1):8–15, Mar 2008.
- [21] Antony Lewis. The real shape of non-Gaussianities. *Journal of Cosmology and Astroparticle Physics*, 2011(10):026, Oct 2011.

- [22] Suman Majumdar, Jonathan R. Pritchard, Rajesh Mondal, Catherine A. Watkinson, Somnath Bharadwaj, and Garrett Mellem. Quantifying the non-Gaussianity in the EoR 21-cm signal through bispectrum. *Monthly Notices of the Royal Astronomical Society*, 476(3):4007–4024, May 2018.
- [23] Andrei Mesinger, Bradley Greig, and Emanuele Sobacchi. The Evolution Of 21 cm Structure (EOS): public, large-scale simulations of Cosmic Dawn and reionization. *Monthly Notices of the Royal Astronomical Society*, 459(3):2342–2353, Jul 2016.
- [24] Jordan Mirocha, Geraint J. A. Harker, and Jack O. Burns. Interpreting the Global 21 cm Signal from High Redshifts. I. Model-independent constraints. *The Astrophysical Journal*, 777(2):118, Nov 2013.
- [25] Julian B. Muñoz, Ely D. Kovetz, and Yacine Ali-Haïmoud. Heating of baryons due to scattering with dark matter during the dark ages. *Physical Review D*, 92(8):083528, Oct 2015.
- [26] Ajinkya H. Patil, Saleem Zaroubi, Emma Chapman, Vibor Jelić, Geraint Harker, Filipe B. Abdalla, Khan M. B. Asad, Gianni Bernardi, Michiel A. Brentjens, and A. G. de Bruyn. Constraining the epoch of reionization with the variance statistic: simulations of the LOFAR case. *Monthly Notices of the Royal Astronomical Society*, 443(2):1113–1124, Sep 2014.
- [27] Jonathan R. Pritchard and Abraham Loeb. Constraining the unexplored period between the dark ages and reionization with observations of the global 21 cm signal. *Physical Review D*, 82(2):023006, Jul 2010.
- [28] Jonathan R. Pritchard and Abraham Loeb. 21 cm cosmology in the 21st century. *Reports on Progress in Physics*, 75(8):086901, Aug 2012.
- [29] Hannah E. Ross, Keri L. Dixon, Ilian T. Iliev, and Garrett Mellem. Simulating the impact of X-ray heating during the cosmic dawn. *Monthly Notices of the Royal Astronomical Society*, 468(4):3785–3797, Jul 2017.
- [30] Hayato Shimabukuro, Shintaro Yoshiura, Keitaro Takahashi, Shuichiro Yokoyama, and Kiyotomo Ichiki. Studying 21cm power spectrum with one-point statistics. *Monthly Notices of the Royal Astronomical Society*, 451(1):467–474, Jul 2015.
- [31] Hayato Shimabukuro, Shintaro Yoshiura, Keitaro Takahashi, Shuichiro Yokoyama, and Kiyotomo Ichiki. 21 cm line bispectrum as a method to probe cosmic dawn and epoch of reionization. *Monthly Notices of the Royal Astronomical Society*, 458(3):3003–3011, May 2016.
- [32] Hayato Shimabukuro, Shintaro Yoshiura, Keitaro Takahashi, Shuichiro Yokoyama, and Kiyotomo Ichiki. Constraining the epoch-of-reionization model parameters with the 21-cm bispectrum. *Monthly Notices of the Royal Astronomical Society*, 468(2):1542–1550, Jun 2017.

- [33] Hiroyuki Tashiro, Kenji Kadota, and Joseph Silk. Effects of dark matter-baryon scattering on redshifted 21 cm signals. *Physical Review D*, 90(8):083522, Oct 2014.
- [34] Cathryn M. Trott. Exploring the evolution of reionization using a wavelet transform and the light cone effect. *Monthly Notices of the Royal Astronomical Society*, 461(1):126–135, Sep 2016.
- [35] Dmitriy Tseliakhovich and Christopher Hirata. Relative velocity of dark matter and baryonic fluids and the formation of the first structures. *Physical Review D*, 82(8):083520, Oct 2010.
- [36] Yougang Wang, Changbom Park, Yidong Xu, Xuelei Chen, and Juhan Kim. Two-dimensional Topology of Cosmological Reionization. *The Astrophysical Journal*, 814(1):6, Nov 2015.
- [37] C. A. Watkinson and J. R. Pritchard. Distinguishing models of reionization using future radio observations of 21-cm 1-point statistics. *Monthly Notices of the Royal Astronomical Society*, 443(4):3090–3106, Oct 2014.
- [38] C. A. Watkinson and J. R. Pritchard. The impact of spin-temperature fluctuations on the 21-cm moments. *Monthly Notices of the Royal Astronomical Society*, 454(2):1416–1431, Dec 2015.
- [39] Catherine A. Watkinson, Sambit K. Giri, Hannah E. Ross, Keri L. Dixon, Ilian T. Iliev, Garrelt Mellema, and Jonathan R. Pritchard. The 21-cm bispectrum as a probe of non-Gaussianities due to X-ray heating. *Monthly Notices of the Royal Astronomical Society*, 482(2):2653–2669, Jan 2019.
- [40] Catherine A. Watkinson, Suman Majumdar, Jonathan R. Pritchard, and Rajesh Mondal. A fast estimator for the bispectrum and beyond - a practical method for measuring non-Gaussianity in 21-cm maps. *Monthly Notices of the Royal Astronomical Society*, 472(2):2436–2446, Dec 2017.
- [41] Shintaro Yoshiura, Hayato Shimabukuro, Keitaro Takahashi, and Takahiko Matsubara. Studying topological structure of 21-cm line fluctuations with 3D Minkowski functionals before reionization. *Monthly Notices of the Royal Astronomical Society*, 465(1):394–402, Feb 2017.

# Chapter 5

## Observational strategies: power spectra and images

Gianni Bernardi (INAF-IRA & Rhodes University)

### Abstract

This chapter reviews the basics of radio interferometry (van-Cittert-Zernike theorem, uv-coverage, image formation calibration) and how they are linked to the measurements of the 21-cm power spectrum and its tomography

### 5.1 Interferometry overview

The Van Cittert-Zernike theorem expresses the fundamental relationship between the sky spatial brightness (or brightness distribution)  $I$  and the quantity measured by an interferometer, i.e. the visibility  $V$  (e.g., [57]):

$$V_{ij}(\mathbf{b}, \lambda) = \int_{\Omega} \bar{I}(\hat{\sigma}, \lambda) e^{-2\pi i \mathbf{b} \cdot \hat{\sigma}} d\sigma, \quad (5.1)$$

where  $\mathbf{b}$  is the baseline vector that separates antenna  $i$  and antenna  $j$ , and  $\hat{\sigma}$  is the observing direction (see Figure 5.1) and the integral is taken over the source size  $\Omega$ . The baseline vector is here specified in wavelengths, i.e.  $\mathbf{b} = \frac{\mathbf{b}_m}{\lambda}$ , where  $\mathbf{b}_m$  is the baseline vector expressed in meters and  $\lambda$  is the observing wavelength. It can be seen in Figure 5.1, that the celestial signal travels an extra path between the two antennas, and that length corresponds to a geometrical time delay  $\tau = \mathbf{b} \cdot \hat{\sigma}$ , where the word “geometrical” refers to the fact that the delay depends upon the source position in the sky and the relative separation between the two antennas.

The sky brightness distribution does not enter directly in equation 5.1, but filtered by the antenna primary beam response  $A$  that depends upon the direction in the sky and the wavelength, i.e.  $\bar{I}(\mathbf{b}, \lambda) = A(\mathbf{b}, \lambda) I(\mathbf{b}, \lambda)$ . The response of the primary beam attenuates the sky emission away from the pointing direction, effectively reducing the field of view  $\theta$  of the instrument. Generally speaking, the size of the field of view is essentially given by the

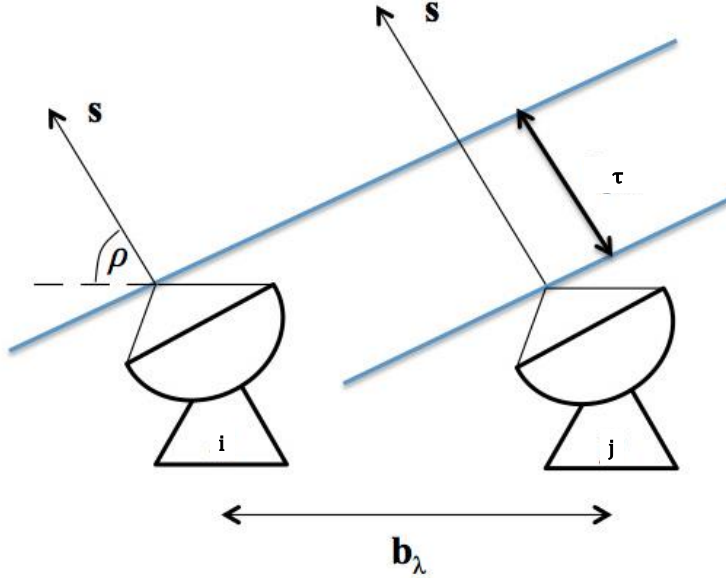


Figure 5.1: A standard schematic of the two element interferometer.

antenna diameter  $D$ :

$$\theta \approx \frac{\lambda}{D}. \quad (5.2)$$

Equation 5.1 is often re-written in a different coordinate system, i.e. using the components of the baseline vector  $(u, v, w)$  and the reciprocal  $(l, m, n)$ , where  $(l, m)$  are the coordinates in the plane on the sky tangent to the observing direction  $n$  (for a detailed discussion of coordinate systems see, for example [57]). Using this coordinate system, equation 5.1 becomes (e.g., [57]):

$$V_{ij}(u, v, w, \lambda) = \int_{\Omega} \bar{I}(l, m, \lambda) e^{-2\pi i(u l + v m + w(n-1))} \frac{dl dm dn}{\sqrt{1 - l^2 - m^2}}, \quad (5.3)$$

Although low frequency radio observations are intrinsically wide-field, for the purpose of studying the 21 cm observables, we can reduce equation 5.3 to a two dimensional Fourier transform:

$$V_{ij}(u, v, \lambda) = \int_{\Omega} \bar{I}(l, m, \lambda) e^{-2\pi i(u l + v m)} dl dm. \quad (5.4)$$

Equation 5.4 indicates that an *interferometer measures the two dimensional Fourier transform of the spatial sky brightness distribution*. If our goal is to reconstruct the sky brightness distribution, equation 5.4 can be inverted into its corresponding Fourier pair:

$$\bar{I}(l, m, \lambda) = \int V_{ij}(u, v, \lambda) e^{2\pi i(u l + v m)} du dv. \quad (5.5)$$

Equation 5.5 is, however, a poor reconstruction of the sky brightness distribution as only one Fourier mode is sampled at a single time instance.

**(GB: ARRIVED HERE)**

Strictly speaking, indeed, all the quantities in equation 5.4 and 5.5 are time variable. In most cases, the time dependence of the primary beam and the sky brightness distribution can be neglected, however, this is not the case for the visibility  $V$  as the projection of the baseline vector with respect to the source direction changes significantly throughout a long (e.g. a few hours) track. In this way, many measurements of the visibility coherence function  $V$  as  $(u, v, \lambda)$  change with time can be made, allowing for a better reconstruction of the  $\bar{I}(l, m, \lambda)$  function. This method is commonly described as *filling the uv plane via Earth rotation synthesis* and was invented by [47]. The other (complementary) way to fill the  $uv$  plane is to deploy more antennas on the ground in order to increase the number of instantaneous measurements of independent Fourier modes. If  $N$  antennas are connected in an interferometric array,  $\frac{N(N-1)}{2}$  instantaneous measurements are made.

The combination of a large number of antennas and the Earth rotation synthesis, defines the sampling function  $S(u, v, \lambda)$  in the  $uv$  plane. In any real case, equation 5.5 can therefore be re-written as:

$$\bar{I}_D(l, m, \lambda) = \int_{-\infty}^{+\infty} S(u, v, \lambda) V(u, v, \lambda) e^{2\pi i(u l + v m)} du dv \quad (5.6)$$

where  $\bar{I}_D$  indicates the sky brightness distribution sampled at a finite number of  $(u, v)$  points (often termed *dirty image*) and I dropped the explicit dependence on the antenna pair as redundant at this point. Using the convolution theorem, equation 5.7 can be re-written as:

$$\bar{I}_D(l, m, \lambda) = \tilde{S} \tilde{V} = \tilde{S} * \tilde{V} = \text{PSF}(l, m, \lambda) * \tilde{V}(l, m, \lambda), \quad (5.7)$$

where the tilde indicates the Fourier transform,  $*$  the convolution operation and PSF is the Point Spread Function, i.e. the response of the interferometric array to a point sources which, in our case, is also the Fourier transform of the  $uv$  coverage.

I will give some examples of sampling functions for different instruments in Section 5.4, however, the sampling function always effectively reduces the integral over a finite (often not contiguous) area of the  $uv$  plane. In particular, the sampled  $uv$  plane is restricted to a minimum  $uv$  distance that cannot be shorter than the antenna size and a maximum  $uv$  distance given by equation 5.2. The result of not sampling all the Fourier modes is that the PSF has got “sidelobes”, i.e. nulls and secondary lobes that can often contaminate fainter true sky emission. The best reconstruction of the sky brightness distribution  $\bar{I}$  requires deconvolution of the dirty image from the PSF.

## 5.2 21 cm observables: power spectra and images

The ultimate goal of 21 cm observations is to image the spatial distribution of the 21 cm signal as a function of redshift, also known as *21 cm tomography*. Given the current theoretical predictions, such observations need to achieve mK sensitivity on a few arcminute angular scales (see Chapter 1 in this book). Most of the current arrays, however, only have the sensitivity to perform a statistical detection of the 21 cm, i.e. to measure its power spectrum. Given an intensity field  $T$  function of the three dimensional spatial coordinate  $\mathbf{x}$ , its power spectrum  $P(k)$  can be defined as:

$$\langle \tilde{T}^*(\mathbf{k}) \tilde{T}(\mathbf{k}') \rangle = (2\pi)^3 P(k) \delta^3(\mathbf{k} - \mathbf{k}') \quad (5.8)$$

where  $\langle \rangle$  indicates the ensamble average,  $\mathbf{k}$  is the Fourier conjugate of  $\mathbf{x}$ , tilde the Fourier transform,  $*$  the complex conjugate operator and  $\delta$  the Dirac delta function. In 21 cm observations, power spectra can be computed directly from interferometric image cubes after deconvolution of  $\tilde{I}_D(l, m, \lambda)$  from the point spread function (e.g., [43], [19], [2], [40]). An alternative way to estimate the 21 cm power spectrum that has driven the design and calibration strategies of some of the arrays. Equation 5.4 already shows that the interferometer is a “natural” spatial power spectrum instrument (e.g., [61]). Visibilities can be further Fourier transformed along the frequency axis (the so-called *delay trasform*, [39]):

$$\tilde{V}_{ij}(u, v, \tau) = \int_B \tilde{I}(l, m, v) e^{-2\pi i v \tau} dv \quad (5.9)$$

where  $B$  is the observing bandwidth and  $\tau$  is the geometrical delay. The delay transform is therefore proportional to the three dimensional power spectrum ([38]):

$$P(k) \propto \tilde{V}_{ij}(|\mathbf{b}|, \tau), \quad (5.10)$$

where the proportionality constant transforms the visibility units into power units ([38]) and the observer units  $(\mathbf{b}, \tau)$  map directly in  $k$  modes parallel and perpendicular to the line of sight (e.g., [34]):

$$k_{\perp} = \frac{2\pi|\mathbf{b}|}{D} = \frac{2\pi\sqrt{u^2 + v^2}}{D}, \quad k_{\parallel} = \frac{2\pi f_{21} H_0 E(z)}{c(1+z)^2} \tau, \quad (5.11)$$

where  $D$  is the transverse comoving distance,  $f_{21} = 1421$  MHz,  $H_0$  is the Hubble constant and  $E(z) = \sqrt{\Omega_m(1+z)^3 + \Omega_k(1+z)^2 + \Omega_{\Lambda}}$ . Due to the dependence of the geometrical delay upon frequency, equation 5.10 is only valid for short baselines, typically shorter than a few hundred meters, for which the geometrical delay is fairly constant across the bandwidht and lines of constant  $k_{\parallel}$  are practically orthogonal to the  $k_{\perp}$  axis ([38]).

Equation 5.9 does not only provide a link between visibilities and three dimensional power spectra, but also introduces the concept of “horizon limit” which is the maximum physical delay allowed  $\tau_{\max} = \frac{|\mathbf{b}|}{c}$ , where  $c$  is the speed of light. The most relevant implication of an horizon limit is the definition of a region in power spectrum space where smooth-spectrum foregrounds are confined leaving the remaining area potentially uncontaminated where to measure the 21 cm signal (“EoR window”, Figure 5.2). Foregrounds can therefore “avoided” with no requirements for subtraction (e.g., [33], [60], [44], [58]; see also Chapter !!!). The choice of a foreground avoidance strategy versus subtraction plays an important role in planning an experiment, its related observing strategy and the array calibration strategy. (GB: add a paragraph on imaging!!!)

## 5.3 Interferometric calibration and 21 cm observations

Celestial signals always experience a corruption due to the non-ideal instrumental response that needs to be corrected for a posteriori, in a process that is known as interferometric calibration. Calibration relies on the definition of a data model where the corruptions are described by antenna based quantities known as Jones matrices. The data model is known as the interferometric measurement equation ([18],[50]) that will be summarized in the following.

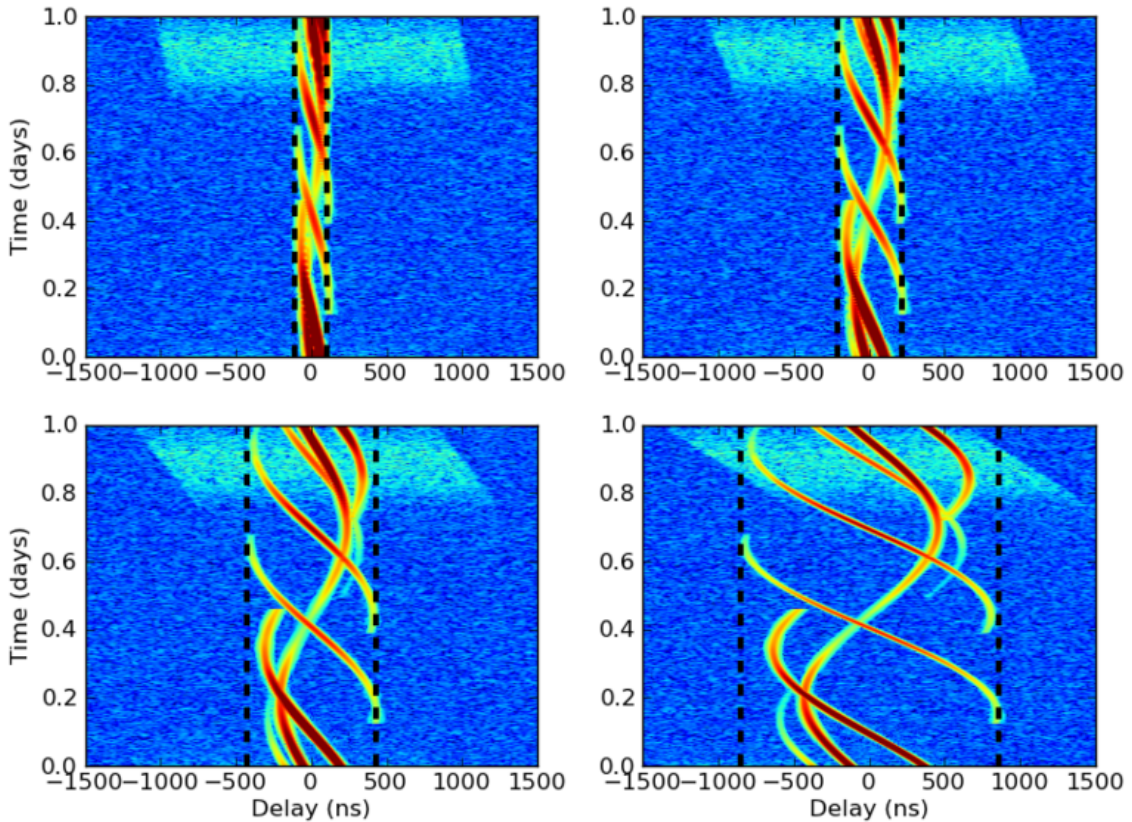


Figure 5.2: Amplitude of delay transformed visibilities as a function of time and delay for a 32 (top left), 64 (top right), 128 (bottom left) and 256 m (bottom right) respectively (from [39]). A number of smooth spectrum point sources are simulated as foregrounds and their tracks are clearly bound within the horizon limit (black dashed line). The cyan emission is a fiducial 21 cm model that has power at high delays regardless of the baseline length.

If antenna 1 and antenna 2 measure two orthogonal, linear polarizations  $x$  and  $y$ , the cross-polarization visibility products can be grouped in a  $2 \times 2$  matrix  $\mathbf{V}$

$$\mathbf{V}_{12}(u, v, \lambda) \equiv \begin{bmatrix} V_{12,xx}(u, v, \lambda) & V_{12,xy}(u, v, \lambda) \\ V_{12,yx}(u, v, \lambda) & V_{12,yy}(u, v, \lambda) \end{bmatrix}. \quad (5.12)$$

The sky brightness distribution  $I$  can also be written as a  $2 \times 2$  matrix  $\mathbf{B}$  using the Stokes parameters as a polarization basis:

$$\mathbf{B}_I(l, m, \lambda) \equiv \begin{bmatrix} I(l, m, \lambda) + Q(l, m, \lambda) & U(l, m, \lambda) + iV(l, m, \lambda) \\ U(l, m, \lambda) - iV(l, m, \lambda) & I(l, m, \lambda) - Q(l, m, \lambda) \end{bmatrix}. \quad (5.13)$$

At this point, equation 5.3 can be written by including the corruptions represented by the Jones matrices  $J$  ([18],[50]):

$$\mathbf{V}_{12}(u, v, \lambda) = \mathbf{J}_1 \left( \int_{\Omega} \mathbf{B}_I(l, m, \lambda) e^{-2\pi i(u l + v m)} dl dm \right) \mathbf{J}_2^H \quad (5.14)$$

Equation 5.14 is known as the measurement equation and is the core of interferometric calibration. For an array with  $N$  antennas, equation 5.14 can be written for each of the  $\frac{N(N-1)}{2}$  visibilities forming an overdetermined system of equations. The development of calibration algorithms is a very active research line ([30], [27], [55], [64], [52]) although beyond the scope of this chapter and we mention it here for completeness. The solution of the system of calibration equations requires some knowledge of the sky brightness distribution  $\mathbf{B}_I$ , or a *sky model*. Traditionally this is achieved by observing a calibration source, i.e. a bright, unresolved point source with known spectral and polarization properties. Calibration solutions are then applied to the observed field that, in turn, is then used to improve the sky model  $\mathbf{B}_I$  which, in turn, leads to more accurate calibration solutions  $J$  in the loop that is traditionally called *self calibration* ([10], [42]). This approach can lead to a highly accurate calibration (e.g., [4], [51]).

The advantage of the measurement equation is that it can factorize different physical terms into different matrices. For example, the frequency response of the electronic filters and its time variations essentially affects only the two polarization response and are modeled with a diagonal Jones matrix  $B$ :

$$\mathbf{B}(t, \lambda) \equiv \begin{bmatrix} b_x(t, \lambda) & 0 \\ 0 & b_y(t, \lambda) \end{bmatrix}, \quad (5.15)$$

whereas the undesired instrumental leakage between the two orthogonal polarized is represented by a  $D$  Jones matrix of the form:

$$\mathbf{D}(t, \lambda) \equiv \begin{bmatrix} 1 & d_x(t, \lambda) \\ -d_y(t, \lambda) & 1 \end{bmatrix}, \quad (5.16)$$

and the measurement equation can be written as:

$$\mathbf{V}_{12}(u, v, \lambda) = \mathbf{B}_1 \mathbf{D}_1 \left( \int_{\Omega} \mathbf{B}_I(l, m, \lambda) e^{-2\pi i(u l + v m)} dl dm \right) \mathbf{D}_2^H \mathbf{B}_2^H. \quad (5.17)$$

We note that, in principle, the primary beam response should appear as an additional  $2 \times 2$  Jones matrix before the  $D$  matrix. For our pedagogical purposes, we assume that it can be incorporated in the  $B$  matrix, although we later illustrate an exception to this assumption.

Retaining only the first order terms, equation 5.17 can be written as ([48]):

$$V_{12,xx}(u, v, \lambda) = b_{1,x} b_{2,x}^* [V_I(u, v, \lambda) - V_Q(u, v, \lambda)] \quad (5.18)$$

$$V_{12,xy}(u, v, \lambda) = b_{1,x} b_{2,y}^* [(d_{1,x} - d_{2,y}^*) V_I(u, v, \lambda) + V_U(u, v, \lambda) + iV_V(u, v, \lambda)] \quad (5.19)$$

$$V_{12,yx}(u, v, \lambda) = b_{1,y} b_{2,x}^* [(d_{2,x} - d_{1,y}^*) V_I(u, v, \lambda) + V_U(u, v, \lambda) - iV_V(u, v, \lambda)] \quad (5.20)$$

$$V_{12,yy}(u, v, \lambda) = b_{1,y} b_{2,y}^* [V_I(u, v, \lambda) - V_Q(u, v, \lambda)], \quad (5.21)$$

where we dropped the explicit dependence on time and wavelength from the Jones matrices for notation clarity and where  $V_{i=I,Q,U,V}$  are the Fourier transforms of the sky brightness matrix  $B$ .

This form of the measurement equation offers an intuitive understanding as to why calibration is so important in 21 cm observations. The observed visibilities are essentially a measurement of foreground emission and, in the ideal case, their amplitudes would vary smoothly with frequency, enabling either their avoidance or subtraction. However, the instrumental response inevitably corrupts this smoothness in several ways: because the telescope primary beam is not sufficiently smooth in frequency, because of the filter response or because of reflection along the signal path. Calibration attempts to restore the intrinsic foreground frequency smoothness, however, calibration errors (i.e., deviations from the true  $B$  solutions) will corrupt the foreground frequency smoothness. In practice, calibration errors result into foreground power leaking out of the horizon limit and jeopardizing (part of) the EoR window. The corruption of the foreground frequency smoothness will limit the accuracy of any subtraction method (see Chapter !!!). *The effectiveness of foreground separation, proven in ideal cases, depends significantly on the accuracy of interferometric calibration.*

There are a few topics of active research in improving the accuracy of interferometric calibration:

- *sky models.* Ideally, the sky brightness model matrix  $\mathbf{B}_I$  (equation 5.17 and 5.21) should include the whole sky emission. This is practically impossible as part of the sky signal is the unknown that we want to discover (the 21 cm signal) and part of the signal has not been observed before or, even if observed, its detailed properties are not known sufficiently well.

Efforts to achieve the most accurate calibration include in the brightness matrix  $B_I$  thousands of compact sources in an area larger than the telescope field of view (e.g., [65]). This sky model may still be insufficient as it does not include sources over the whole sky nor Galactic diffuse emission. Galactic emission contributes to most of the power on angular scales  $\theta > 10 - 20$  arcmin ([3], [9]), therefore a compact sources sky model is not adequate for baselines shorter than a few tens of meters. Excluding short baselines from the calibration solutions would prevent the problem but can bias the solution ([41]) if the system of calibration equation is not properly regularized ([35]).

Another form of sky model incompleteness is related to angular resolution: due to its finite resolution, sources that are not completely unresolved are nevertheless treated

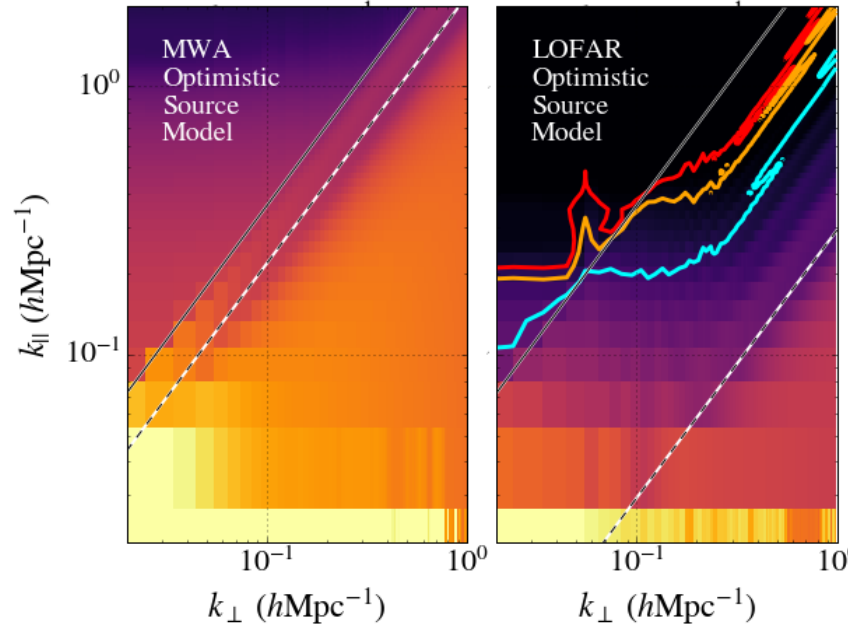


Figure 5.3: Example of power spectrum bias introduced by calibration errors due to incomplete sky models for the Murchison Widefield Array (MWA, left) and the Low Frequency Aray (LOFAR, right) cases respectively (from [14]). Power spectra are shown in their two dimensional ( $k_{\perp}, k_{\parallel}$ ) form in order to show the foreground dominated region below the horizon limit (grey solid line). Cyan, orange and red lines are the lines where a fiducial 21 cm model is one, five and ten times higher than the power spectrum bias level. In an ideal case with perfectly smooth foregrounds and no calibration errors, the 21 cm power sepctrum should be detectable just outside the horizon limit. The errors introduced by an incomplete sky model lead to a foreground power leakage in the EoR window which, in the MWA case, may completely prevent a detection.

as point-like and this too biases the calibration solutions, leading to an excess of foreground contamination in the EoR window ([45]).

[16], [63] and [17] show that effect of sky model incompleteness on calibration eventually leads to artifacts in the form of ghost-like sources in interferometric images, most of the times fainter than the image noise level. They also show that the ghost pattern is stronger for regularly spaced arrays and if the sky model is more incomplete. [14] and [1] formalize the effect of incomplete sky models on calibration as a leakage of foreground power in the EoR window.

Significant effort is currently ongoing in order to improve the all-sky compact-source model via wider and deeper low frequency surveys (e.g., [20], [22], [49]), more accurate low frequency catalogues ([8]) and even improvements of the Galactic diffuse emission observations ([67], [13]). Some of the calibration strategies described in the next sections may, however, mitigate the requirements of extremely accurate sky models;

- *instrument/primary beam models.* A complete knowledge of a sky model may not be, by itself, sufficient for an accurate calibration of 21 cm observations as the brightness matrix  $B_I$  appears in the calibration equation multiplied by the antenna primary beam (equation 5.14 and 5.4) and the measurement of an intrinsic sky model requires the separation from the primary beam effect.

Unlike steerable dishes, most 21 cm interferometers are constituted of dipoles fixed on the ground, in some cases clustered together to form tiles or stations that can digitally pointed in a sky direction via a physical delay (e.g., like the MWA and LOFAR arrays, see Section 5.4). As station beams are formed to track the source on the sky, the station projected area changes with time and the shape of the primary beam changes significantly (Figure 5.4). This effect leads to time variable sky models with variations that are larger away from the pointing direction due to the large variations in the sidelobe pattern. For examples, sky sources that are well within the main lobe of the primary beam in Figure 5.4 will experience relatively negligible variations throughout an observation, the opposite will occur to sources located well outside the main lobe as they enter and exit different sidelobes.

Primary beams are also frequency variable and, at first order, their size scales with wavelength (similar to the angular resolution, equation 5.2), i.e. rather smoothly. However, in the sidelobe region, such variation becomes rather abrupt as the sidelobe pattern changes too, therefore the source can be at the peak of a sidelobe at a certain frequency and in the sidelobe null at another frequency. As a final remark, stations are not perfectly equal to each other, due to manufacturing reasons or mutual coupling between their elements (e.g., [53]), therefore the sky brightness matrix  $B_I$  is potentially different for each baseline as the primary beams are different. The left panel of Figure 5.4 attempt to quantify this effect in a simulated case: variations in the sidelobe region can be as large as  $\sim 30\%$ .

If not accurately modeled and taken into account, the aforementioned effects can bias the calibration solution and, again, corrupt the foreground smoothness. [6], [54] and [56] have developed methods to incorporate time and frequency variable primary

beams in interferometric images, however, the accuracy of the correction is limited by the accuracy of the primary beam model. Increasing effort is therefore being placed in accurate modeling and measuring primary beams (e.g., [46], [12], [23], [11]);

- *polarization leakage calibration.* Equation 5.14 and 5.21 show that, even if the 21 cm signal is unpolarized, care needs to be taken against the contamination from polarized foreground emission. Most point sources are unpolarized below 200 MHz ([5], [28], [59]), therefore the assumption of an unpolarized sky model is well justified. However, errors in the matrix  $B$  different between the  $xx$  and  $yy$  polarizations would lead to polarized emission to leak into total intensity, particularly on short baselines, where polarized foreground emission is brighter ([3], [21], [24], [28]). Polarized foregrounds Faraday rotated by the interstellar medium that leak to total intensity may be a severe contamination of the 21 cm signal (e.g., [25], [31], [37]).

Even if calibration errors are negligible, low frequency antennas have a non negligible polarized response across their wide field of view. If we call the Jones matrix that represents the polarized primary beam response  $E \equiv E(l, m, \lambda)$ , its associate measurement equation can be written as ([37]):

$$\begin{bmatrix} V_{12,I}(u, v, \lambda) \\ V_{12,Q}(u, v, \lambda) \\ V_{12,U}(u, v, \lambda) \\ V_{12,V}(u, v, \lambda) \end{bmatrix} = \int_{\Omega} \mathbf{S}^{-1} [\mathbf{E}_1 \otimes \mathbf{E}_2^H] \mathbf{S} \begin{bmatrix} I(l, m, \lambda) \\ Q(l, m, \lambda) \\ U(l, m, \lambda) \\ V(l, m, \lambda) \end{bmatrix} e^{-2\pi i(ul+vm)} dl dm = \\ = \int_{\Omega} \mathbf{A}(l, m, \lambda) \begin{bmatrix} I(l, m, \lambda) \\ Q(l, m, \lambda) \\ U(l, m, \lambda) \\ V(l, m, \lambda) \end{bmatrix} e^{-2\pi i(ul+vm)} dl dm, \quad (5.22)$$

where  $\mathbf{S}$  is the matrix that relates the intrinsic Stokes parameters to the observer  $-y$  frame,  $\otimes$  is the outer product. The visibilities are written as a four-element vector as this form shows that the outer product of the beam Jones matrices maps the intrinsic Stoke parameters into the observed ones:

$$\begin{pmatrix} I' \leftarrow I & I' \leftarrow Q & I' \leftarrow U & I' \leftarrow V \\ Q' \leftarrow I & Q' \leftarrow Q & Q' \leftarrow U & Q' \leftarrow V \\ U' \leftarrow I & U' \leftarrow Q & U' \leftarrow U & U' \leftarrow V \\ V' \leftarrow I & V' \leftarrow Q & V' \leftarrow U & V' \leftarrow V \end{pmatrix}. \quad (5.23)$$

The first raw of the matrix shows how the four intrinsic Stokes parameters contribute to the observed total intensity and, therefore, how polarized foregrounds leak into the 21 cm signal even in absence of any calibration errors: any polarized signal (Stokes  $Q$  and  $U$ ) will contaminate the observed total intensity signal, and the magnitude of the contamination increases away from the pointing direction. An example of  $\mathbf{A}$  matrix is shown in Figure 5.6.

Calibration of the polarization leakage remains a challenging task. It can be mitigated by extending the sky model to include polarization (e.g. [15]), although modeling the

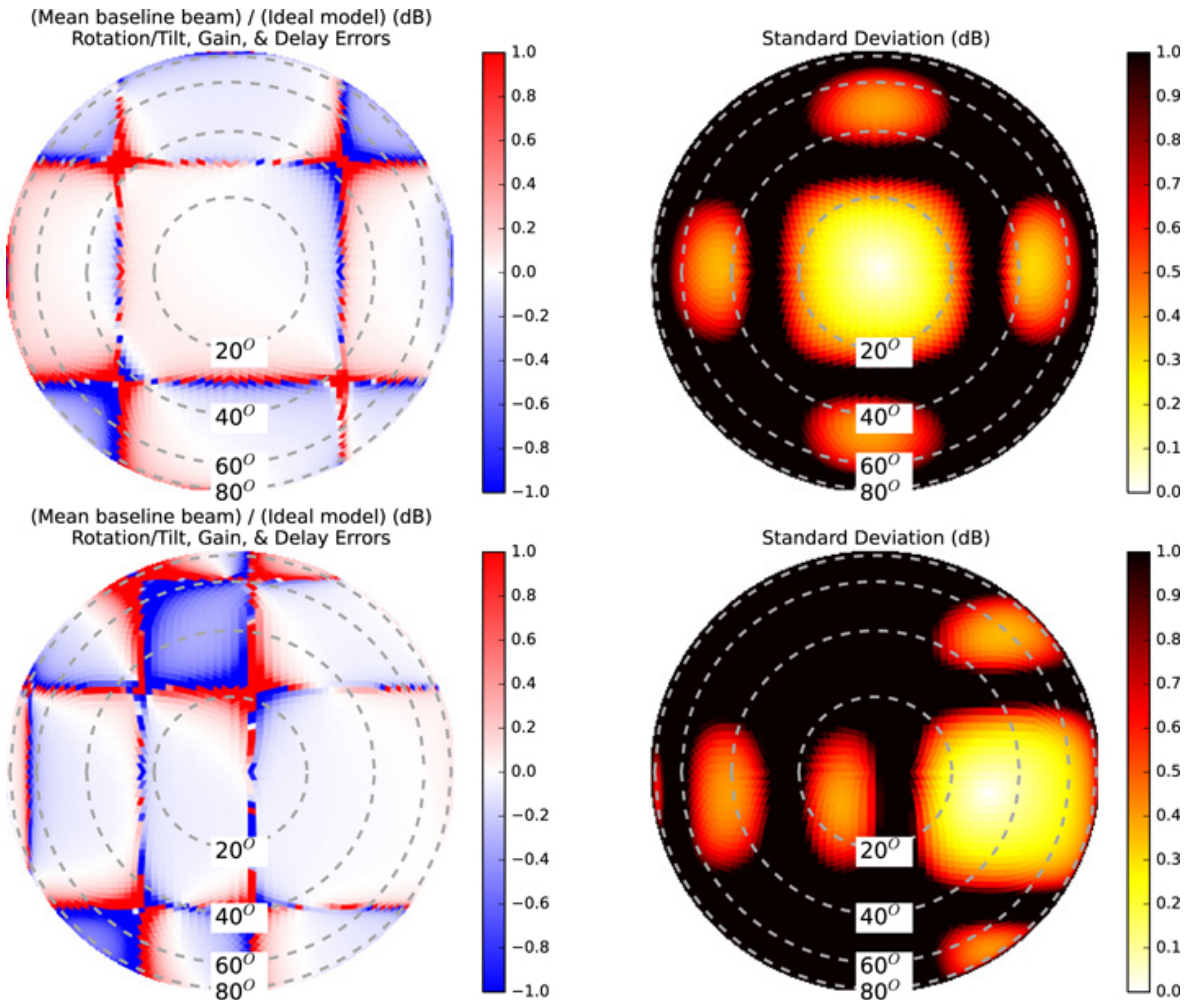


Figure 5.4: Example of primary beam variations as the MWA station points at zenith (top right) and  $\sim 30^\circ$  away from zenith (bottom right) at 150 MHz. The left column shows the fractional variation of individual station beam models, with respect to the nominal primary beam (right column, from [36]). It is visible how different sidelob pattern is when pointing towards two different directions. It should also be noticed that the magnitude of the first lobe is at the  $\sim 10\%$  level and the large null areas around the lobes. The specific pattern is due to the regular shape of the MWA station, where 16 dipoles are arranged in a square  $4 \times 4$  grid.

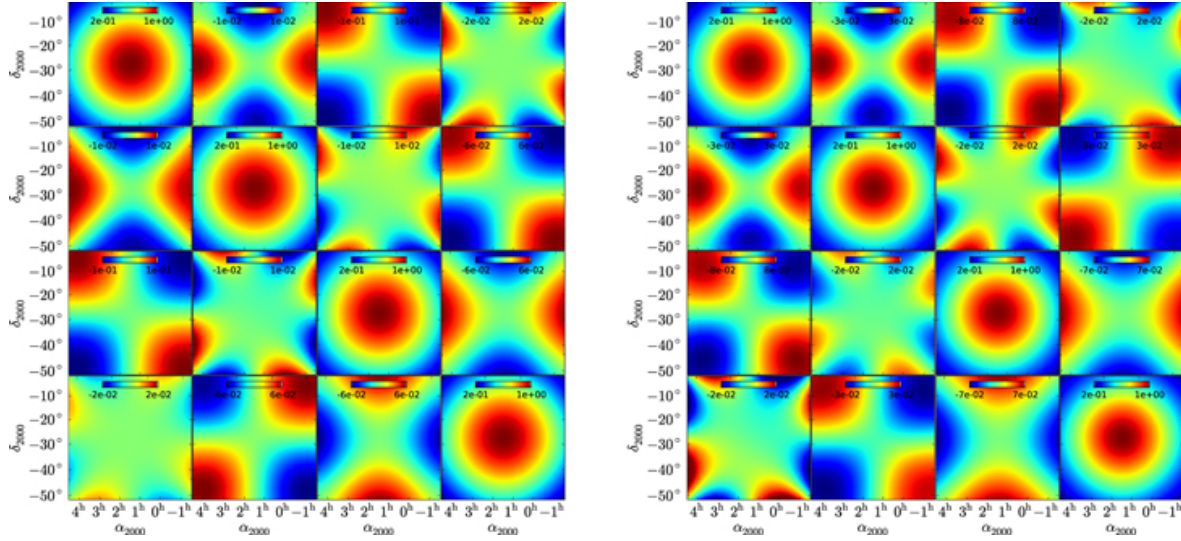


Figure 5.5: Examples of  $\mathbf{A}$  matrices at 130 (left) and 150 MHz respectively (from [37]). The matrix maps the intrinsic Stokes parameters into observed ones: the diagonal terms represent the expected primary beam shapes, whereas the off-diagonal terms represents leakage terms. The second, the third and the fourth element of the first row show how Stokes parameters  $Q$ ,  $U$  and  $V$  respectively contaminate the total intensity signal.

diffuse Galactic foreground - the brightest component - is not straightforward and requires accurate imaging. [37] showed that also polarized foregrounds may be avoided if they are not highly Faraday rotated by the interstellar medium, although a more extensive characterization of polarized foreground properties is needed.

- *ionospheric distortions*

### 5.3.1 Direction dependent calibration

In the previous section I have summarized the calibration equations and the main effects that lead to calibration errors that, in turn, may jeopardize foreground separation. The calibration formalism describe

### 5.3.2 Redundant calibration

An interferometric array where most of the baselines have the same length and orientation is called *redundant* as they measure the same Fourier mode of the sky brightness distribution. Redundant array configurations are often not appealing as they have poor imaging performances as they do not measure sufficient Fourier modes to reconstruct accurate sky images. However, a maximally redundant array where the antennas are laid out in a regularly spaced square grid offers the maximum power spectrum sensitivity on the  $k_{\perp}$  modes corresponding to the most numerous baselines. This criterium has inspired the highly redundant layouts of

the MIT Epoch of Reionization experiment ([66]), the Precision Array to Probe the Epoch of Reionization (PAPER, [38]) and partly driven the updated MWA.

One of the advantages of a redundant array is that it enables a different calibration strategy called *redundant calibration*. In redundant calibration the form of the measurement equation does not change and can be written, for a single polarization, like equation 5.21:

$$V_{12,xx}(u, v, \lambda) = b_{1,x} b_{2,x}^* y_{12,xx}(u, v, \lambda), \quad (5.24)$$

with the difference now that the model visibility  $y$  is not tied to a sky model, but it is solved for, simply assuming that it is the same for each group of redundant baselines [62], [29]). In other words, redundant calibration is independent on the sky model and, therefore, bypasses entirely the biases related to sky model incompleteness described in Section 8.5. However, as redundant calibration is not tied to any physical (i.e. sky-based) spatial or spectral model, its solutions have degeneracies that need to be solved for by using a sky model (e.g., [66], [7]). In particular, spectral calibration, which is critical for foreground separation, cannot currently be obtained using redundant calibration and requires a sky-based calibration. [7] suggest that sky model incompleteness can bias this calibration step, in a way similar to what happens with a traditional calibration scheme.

Redundant calibration is also prone to effects that break the assumption of redundancy, the most common being errors in the antenna positions and different primary beams for different antennas. Even if antenna position errors can be reduced to have a negligible impact on redundant calibration [26], the effect of primary beam variations amongst the different antennas on redundant calibration is still largely unknown. **Comment on the limitations of redundant calibration to treat polarization.**

## 5.4 Array design and observing strategies

I will conclude this chapter by discussing how the various interferometric effects discussed so far impact the choice of array designs and the consequent observing strategies. [32] and [38], for example, investigate how instrumental choices like the array layout, the antenna size and the bandwidth (do not) affect the 21 cm power spectrum spectrum. Here I would rather like to emphasize the interdependence between instrumental choices and calibration and foreground separation strategies. If the total collecting area is kept fixed, there are two main elements that impact calibration and foreground separation:

- *station size*. The choice of station size determines the minimum  $k_\perp$  value accessible and the footprint of each  $uv$  measurement. Indeed each visibility is not a single point in the  $uv$  plane but has a footprint corresponding to the two dimensional Fourier transform of the primary beam. This can be seen using the convolution theorem to re-write equation 5.1:

$$V_{ij}(\mathbf{b}, \lambda) = \tilde{A}(\mathbf{b}, \lambda) * \tilde{I}(\mathbf{b}, \lambda), \quad (5.25)$$

where  $*$  is the convolution operator.

- *array layout* Beyond the obvious sensitivity requirement, decisions need to be taken as to which layout to adopt, which antenna size and these choice are intrinsically related

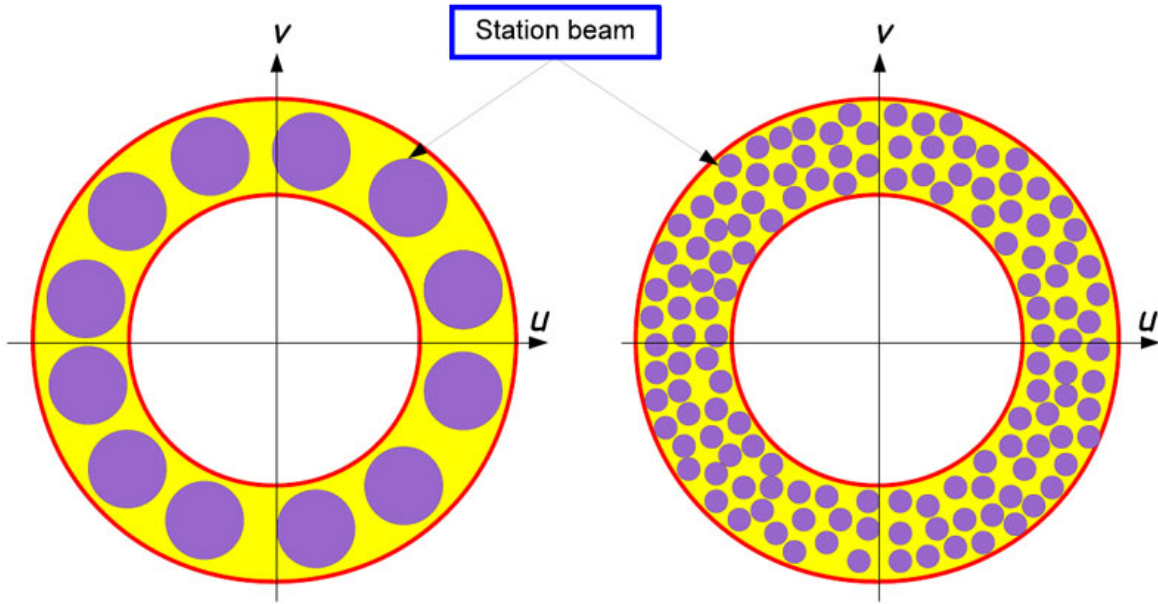


Figure 5.6: Cartoon illustration of the  $uv$  footprint due to the primary beam.

to calibration and foreground separation strategies. For instance a filled  $uv$ -coverage (between the minimum and the maximum station separation) is highly desirable for imaging, modeling and subtracting foregrounds. It is not a stringent requirement for power spectrum measurement and in the avoidance strategy.

As examples, I will use four existing low frequency arrays that, concidentally, span the range of parameters of interest:

- effect of the field of view, calibratability,  $uv$  cell, drift scan versus tracking, suppression of sources outside the main lobe ionosphere
- $uv$  coverage choices power spectra vs images, redundant vs pseud random (reconstructing sky brightness), minimum/maximum  $k$  mode accessible... avoidance (compact) vs subtraction (less compact)
- obviously sensitivity
- *Low Frequency Array (LOFAR)*. LOFAR is an array mainly located in The Netherlands but it include also remote stations acros Europe. Each station
- Murchison Widefield Array (MWA)
- Precision Array to Probe the Epoch of Reionization (PAPER)
- Hydrogen Epoch of Reionization Array (HERA)
- Square Kilometre Array (SKA)

# Bibliography

- [1] N. Barry, B. Hazelton, I. Sullivan, M. F. Morales, and J. C. Pober. Calibration requirements for detecting the 21 cm epoch of reionization power spectrum and implications for the SKA. *MNRAS*, 461:3135–3144, September 2016.
- [2] A. P. Beardsley, B. J. Hazelton, I. S. Sullivan, P. Carroll, N. Barry, M. Rahimi, B. Pindor, C. M. Trott, J. Line, D. C. Jacobs, M. F. Morales, J. C. Pober, G. Bernardi, J. D. Bowman, M. P. Busch, F. Briggs, R. J. Cappallo, B. E. Corey, A. de Oliveira-Costa, J. S. Dillon, D. Emrich, A. Ewall-Wice, L. Feng, B. M. Gaensler, R. Goeke, L. J. Greenhill, J. N. Hewitt, N. Hurley-Walker, M. Johnston-Hollitt, D. L. Kaplan, J. C. Kasper, H. S. Kim, E. Kratzenberg, E. Lenc, A. Loeb, C. J. Lonsdale, M. J. Lynch, B. McKinley, S. R. McWhirter, D. A. Mitchell, E. Morgan, A. R. Neben, N. Thyagarajan, D. Oberoi, A. R. Offringa, S. M. Ord, S. Paul, T. Prabu, P. Procopio, J. Riding, A. E. E. Rogers, A. Roshi, N. Udaya Shankar, S. K. Sethi, K. S. Srivani, R. Subrahmanyan, M. Tegmark, S. J. Tingay, M. Waterson, R. B. Wayth, R. L. Webster, A. R. Whitney, A. Williams, C. L. Williams, C. Wu, and J. S. B. Wyithe. First Season MWA EoR Power spectrum Results at Redshift 7. *ApJ*, 833:102, December 2016.
- [3] G. Bernardi, A. G. de Bruyn, M. A. Brentjens, B. Ciardi, G. Harker, V. Jelić, L. V. E. Koopmans, P. Labropoulos, A. Offringa, V. N. Pandey, J. Schaye, R. M. Thomas, S. Yatawatta, and S. Zaroubi. Foregrounds for observations of the cosmological 21 cm line. I. First Westerbork measurements of Galactic emission at 150 MHz in a low latitude field. *A&A*, 500:965–979, June 2009.
- [4] G. Bernardi, A. G. de Bruyn, G. Harker, M. A. Brentjens, B. Ciardi, V. Jelić, L. V. E. Koopmans, P. Labropoulos, A. Offringa, V. N. Pandey, J. Schaye, R. M. Thomas, S. Yatawatta, and S. Zaroubi. Foregrounds for observations of the cosmological 21 cm line. II. Westerbork observations of the fields around 3C 196 and the North Celestial Pole. *A&A*, 522:A67, November 2010.
- [5] G. Bernardi, L. J. Greenhill, D. A. Mitchell, S. M. Ord, B. J. Hazelton, B. M. Gaensler, A. de Oliveira-Costa, M. F. Morales, N. Udaya Shankar, R. Subrahmanyan, R. B. Wayth, E. Lenc, C. L. Williams, W. Arcus, B. S. Arora, D. G. Barnes, J. D. Bowman, F. H. Briggs, J. D. Bunton, R. J. Cappallo, B. E. Corey, A. Deshpande, L. deSouza, D. Emrich, R. Goeke, D. Herne, J. N. Hewitt, M. Johnston-Hollitt, D. Kaplan, J. C. Kasper, B. B. Kincaid, R. Koenig, E. Kratzenberg, C. J. Lonsdale, M. J. Lynch, S. R. McWhirter, E. Morgan, D. Oberoi, J. Pathikulangara, T. Prabu, R. A. Remillard, A. E. E. Rogers, A. Roshi, J. E. Salah, R. J. Sault, K. S. Srivani, J. Stevens, S. J. Tingay,

- M. Waterson, R. L. Webster, A. R. Whitney, A. Williams, and J. S. B. Wyithe. A 189 MHz, 2400 deg<sup>2</sup> Polarization Survey with the Murchison Widefield Array 32-element Prototype. *ApJ*, 771:105, July 2013.
- [6] S. Bhatnagar, T. J. Cornwell, K. Golap, and J. M. Uson. Correcting direction-dependent gains in the deconvolution of radio interferometric images. *A&A*, 487:419–429, August 2008.
- [7] R. Byrne, M. F. Morales, B. Hazelton, W. Li, N. Barry, A. P. Beardsley, R. Joseph, J. Pober, I. Sullivan, and C. Trott. Fundamental Limitations on the Calibration of Redundant 21 cm Cosmology Instruments and Implications for HERA and the SKA. *ApJ*, 875:70, April 2019.
- [8] P. A. Carroll, J. Line, M. F. Morales, N. Barry, A. P. Beardsley, B. J. Hazelton, D. C. Jacobs, J. C. Pober, I. S. Sullivan, R. L. Webster, G. Bernardi, J. D. Bowman, F. Briggs, R. J. Cappallo, B. E. Corey, A. de Oliveira-Costa, J. S. Dillon, D. Emrich, A. Ewall-Wice, L. Feng, B. M. Gaensler, R. Goeke, L. J. Greenhill, J. N. Hewitt, N. Hurley-Walker, M. Johnston-Hollitt, D. L. Kaplan, J. C. Kasper, H. Kim, E. Kratzenberg, E. Lenc, A. Loeb, C. J. Lonsdale, M. J. Lynch, B. McKinley, S. R. McWhirter, D. A. Mitchell, E. Morgan, A. R. Neben, D. Oberoi, A. R. Offringa, S. M. Ord, S. Paul, B. Pindor, T. Prabu, P. Procopio, J. Riding, A. E. E. Rogers, A. Roshi, N. U. Shankar, S. K. Sethi, K. S. Srivani, R. Subrahmanyam, M. Tegmark, N. Thyagarajan, S. J. Tingay, C. M. Trott, M. Waterson, R. B. Wayth, A. R. Whitney, A. Williams, C. L. Williams, C. Wu, and J. S. B. Wyithe. A high reliability survey of discrete Epoch of Reionization foreground sources in the MWA EoR0 field. *MNRAS*, 461:4151–4175, October 2016.
- [9] S. Choudhuri, S. Bharadwaj, S. S. Ali, N. Roy, H. T. Intema, and A. Ghosh. The angular power spectrum measurement of the Galactic synchrotron emission in two fields of the TGSS survey. *MNRAS*, 470:L11–L15, September 2017.
- [10] T. J. Cornwell and P. N. Wilkinson. A new method for making maps with unstable radio interferometers. *MNRAS*, 196:1067–1086, September 1981.
- [11] E. de Lera Acedo, P. Bolli, F. Paonessa, G. Virone, E. Colin-Beltran, N. Razavi-Ghods, I. Aicardi, A. Lingua, P. Maschio, J. Monari, G. Naldi, M. Piras, and G. Pupillo. SKA aperture array verification system: electromagnetic modeling and beam pattern measurements using a micro UAV. *Experimental Astronomy*, 45:1–20, March 2018.
- [12] E. de Lera Acedo, C. M. Trott, R. B. Wayth, N. Fagnoni, G. Bernardi, B. Wakley, L. V. E. Koopmans, A. J. Faulkner, and J. G. bij de Vaate. Spectral performance of SKA Log-periodic Antennas I: mitigating spectral artefacts in SKA1-LOW 21 cm cosmology experiments. *MNRAS*, 469:2662–2671, August 2017.
- [13] J. Dowell, G. B. Taylor, F. K. Schinzel, N. E. Kassim, and K. Stovall. The LWA1 Low Frequency Sky Survey. *MNRAS*, 469:4537–4550, August 2017.
- [14] A. Ewall-Wice, J. S. Dillon, A. Liu, and J. Hewitt. The impact of modelling errors on interferometer calibration for 21 cm power spectra. *MNRAS*, 470:1849–1870, September 2017.

- [15] P. M. Geil, B. M. Gaensler, and J. S. B. Wyithe. Polarized foreground removal at low radio frequencies using rotation measure synthesis: uncovering the signature of hydrogen reionization. *MNRAS*, 418:516–535, November 2011.
- [16] T. L. Grobler, C. D. Nunhokee, O. M. Smirnov, A. J. van Zyl, and A. G. de Bruyn. Calibration artefacts in radio interferometry - I. Ghost sources in Westerbork Synthesis Radio Telescope data. *MNRAS*, 439:4030–4047, April 2014.
- [17] T. L. Grobler, A. J. Stewart, S. J. Wijnholds, J. S. Kenyon, and O. M. Smirnov. Calibration artefacts in radio interferometry - III. Phase-only calibration and primary beam correction. *MNRAS*, 461:2975–2992, September 2016.
- [18] J. P. Hamaker, J. D. Bregman, and R. J. Sault. Understanding radio polarimetry. I. Mathematical foundations. *A&AS*, 117:137–147, May 1996.
- [19] G. Harker, S. Zaroubi, G. Bernardi, M. A. Brentjens, A. G. de Bruyn, B. Ciardi, V. Jelić, L. V. E. Koopmans, P. Labropoulos, G. Mellem, A. Offringa, V. N. Pandey, A. H. Pawlik, J. Schaye, R. M. Thomas, and S. Yatawatta. Power spectrum extraction for redshifted 21-cm Epoch of Reionization experiments: the LOFAR case. *MNRAS*, 405:2492–2504, July 2010.
- [20] N. Hurley-Walker, J. R. Callingham, P. J. Hancock, T. M. O. Franzen, L. Hindson, A. D. Kapińska, J. Morgan, A. R. Offringa, R. B. Wayth, C. Wu, Q. Zheng, T. Murphy, M. E. Bell, K. S. Dwarakanath, B. For, B. M. Gaensler, M. Johnston-Hollitt, E. Lenc, P. Procopio, L. Staveley-Smith, R. Ekers, J. D. Bowman, F. Briggs, R. J. Cappallo, A. A. Deshpande, L. Greenhill, B. J. Hazelton, D. L. Kaplan, C. J. Lonsdale, S. R. McWhirter, D. A. Mitchell, M. F. Morales, E. Morgan, D. Oberoi, S. M. Ord, T. Prabu, N. U. Shankar, K. S. Srivani, R. Subrahmanyam, S. J. Tingay, R. L. Webster, A. Williams, and C. L. Williams. GaLactic and Extragalactic All-sky Murchison Widefield Array (GLEAM) survey - I. A low-frequency extragalactic catalogue. *MNRAS*, 464:1146–1167, January 2017.
- [21] M. Iacobelli, M. Haverkorn, E. Orrú, R. F. Pizzo, J. Anderson, R. Beck, M. R. Bell, A. Bonafede, K. Chyzy, R.-J. Dettmar, T. A. Enßlin, G. Heald, C. Horellou, A. Horneffer, W. Jurusik, H. Junklewitz, M. Kuniyoshi, D. D. Mulcahy, R. Paladino, W. Reich, A. Scaife, C. Sobey, C. Sotomayor-Beltran, A. Alexov, A. Asgekar, I. M. Avruch, M. E. Bell, I. van Bemmel, M. J. Bentum, G. Bernardi, P. Best, L. Birzan, F. Breitling, J. Broderick, W. N. Brouw, M. Brüggen, H. R. Butcher, B. Ciardi, J. E. Conway, F. de Gasperin, E. de Geus, S. Duscha, J. Eislöffel, D. Engels, H. Falcke, R. A. Fallows, C. Ferrari, W. Frieswijk, M. A. Garrett, J. Grießmeier, A. W. Gunst, J. P. Hamaker, T. E. Hassall, J. W. T. Hessels, M. Hoeft, J. Hörandel, V. Jelic, A. Karastergiou, V. I. Kondratiev, L. V. E. Koopmans, M. Kramer, G. Kuper, J. van Leeuwen, G. Macario, G. Mann, J. P. McKean, H. Munk, M. Pandey-Pommier, A. G. Polatidis, H. Röttgering, D. Schwarz, J. Sluman, O. Smirnov, B. W. Stappers, M. Steinmetz, M. Tagger, Y. Tang, C. Tasse, C. Toribio, R. Vermeulen, C. Vocks, C. Vogt, R. J. van Weeren,

- M. W. Wise, O. Wucknitz, S. Yatawatta, P. Zarka, and A. Zensus. Studying Galactic interstellar turbulence through fluctuations in synchrotron emission. First LOFAR Galactic foreground detection. *A&A*, 558:A72, October 2013.
- [22] H. T. Intema, P. Jagannathan, K. P. Mooley, and D. A. Frail. The GMRT 150 MHz all-sky radio survey. First alternative data release TGSS ADR1. *A&A*, 598:A78, February 2017.
- [23] D. C. Jacobs, J. Burba, J. D. Bowman, A. R. Neben, B. Stinnett, L. Turner, K. Johnson, M. Busch, J. Allison, M. Leatham, V. Serrano Rodriguez, M. Denney, and D. Nelson. First Demonstration of ECHO: an External Calibrator for Hydrogen Observatories. *PASP*, 129(3):035002, March 2017.
- [24] V. Jelić, A. G. de Bruyn, V. N. Pandey, M. Mevius, M. Haverkorn, M. A. Brentjens, L. V. E. Koopmans, S. Zaroubi, F. B. Abdalla, K. M. B. Asad, S. Bus, E. Chapman, B. Ciardi, E. R. Fernandez, A. Ghosh, G. Harker, I. T. Iliev, H. Jensen, S. Kazemi, G. Mellema, A. R. Offringa, A. H. Patil, H. K. Vedantham, and S. Yatawatta. Linear polarization structures in LOFAR observations of the interstellar medium in the 3C 196 field. *A&A*, 583:A137, November 2015.
- [25] V. Jelić, S. Zaroubi, P. Labropoulos, G. Bernardi, A. G. de Bruyn, and L. V. E. Koopmans. Realistic simulations of the Galactic polarized foreground: consequences for 21-cm reionization detection experiments. *MNRAS*, 409:1647–1659, December 2010.
- [26] R. C. Joseph, C. M. Trott, and R. B. Wayth. The Bias and Uncertainty of Redundant and Sky-based Calibration Under Realistic Sky and Telescope Conditions. *AJ*, 156:285, December 2018.
- [27] S. Kazemi, S. Yatawatta, S. Zaroubi, P. Lampropoulos, A. G. de Bruyn, L. V. E. Koopmans, and J. Noordam. Radio interferometric calibration using the SAGE algorithm. *MNRAS*, 414:1656–1666, June 2011.
- [28] E. Lenc, B. M. Gaensler, X. H. Sun, E. M. Sadler, A. G. Willis, N. Barry, A. P. Beardsley, M. E. Bell, G. Bernardi, J. D. Bowman, F. Briggs, J. R. Callingham, R. J. Cappallo, P. Carroll, B. E. Corey, A. de Oliveira-Costa, A. A. Deshpande, J. S. Dillon, K. S. Dwarkanath, D. Emrich, A. Ewall-Wice, L. Feng, B.-Q. For, R. Goeke, L. J. Greenhill, P. Hancock, B. J. Hazelton, J. N. Hewitt, L. Hindson, N. Hurley-Walker, M. Johnston-Hollitt, D. C. Jacobs, A. D. Kapińska, D. L. Kaplan, J. C. Kasper, H.-S. Kim, E. Kratzenberg, J. Line, A. Loeb, C. J. Lonsdale, M. J. Lynch, B. McKinley, S. R. McWhirter, D. A. Mitchell, M. F. Morales, E. Morgan, J. Morgan, T. Murphy, A. R. Neben, D. Oberoi, A. R. Offringa, S. M. Ord, S. Paul, B. Pindor, J. C. Pober, T. Prabu, P. Procopio, J. Riding, A. E. E. Rogers, A. Roshi, N. Udaya Shankar, S. K. Sethi, K. S. Srivani, L. Staveley-Smith, R. Subrahmanyan, I. S. Sullivan, M. Tegmark, N. Thyagarajan, S. J. Tingay, C. Trott, M. Waterson, R. B. Wayth, R. L. Webster, A. R. Whitney, A. Williams, C. L. Williams, C. Wu, J. S. B. Wyithe, and Q. Zheng. Low-frequency Observations of Linearly Polarized Structures in the Interstellar Medium near the South Galactic Pole. *ApJ*, 830:38, October 2016.

- [29] A. Liu, M. Tegmark, S. Morrison, A. Lutomirski, and M. Zaldarriaga. Precision calibration of radio interferometers using redundant baselines. *MNRAS*, 408:1029–1050, October 2010.
- [30] D. A. Mitchell, L. J. Greenhill, R. B. Wayth, R. J. Sault, C. J. Lonsdale, R. J. Cappallo, M. F. Morales, and S. M. Ord. Real-Time Calibration of the Murchison Widefield Array. *IEEE Journal of Selected Topics in Signal Processing*, 2:707–717, November 2008.
- [31] D. F. Moore, J. E. Aguirre, A. R. Parsons, D. C. Jacobs, and J. C. Pober. The Effects of Polarized Foregrounds on 21 cm Epoch of Reionization Power Spectrum Measurements. *ApJ*, 769:154, June 2013.
- [32] M. F. Morales. Power Spectrum Sensitivity and the Design of Epoch of Reionization Observatories. *ApJ*, 619:678–683, February 2005.
- [33] M. F. Morales, B. Hazelton, I. Sullivan, and A. Beardsley. Four Fundamental Foreground Power Spectrum Shapes for 21 cm Cosmology Observations. *ApJ*, 752:137, June 2012.
- [34] M. F. Morales and J. Hewitt. Toward Epoch of Reionization Measurements with Wide-Field Radio Observations. *ApJ*, 615:7–18, November 2004.
- [35] A. Mouri Sardarabadi and L. V. E. Koopmans. Quantifying suppression of the cosmological 21-cm signal due to direction-dependent gain calibration in radio interferometers. *MNRAS*, 483:5480–5490, March 2019.
- [36] A. R. Neben, J. N. Hewitt, R. F. Bradley, J. S. Dillon, G. Bernardi, J. D. Bowman, F. Briggs, R. J. Cappallo, B. E. Corey, A. A. Deshpande, R. Goeke, L. J. Greenhill, B. J. Hazelton, M. Johnston-Hollitt, D. L. Kaplan, C. J. Lonsdale, S. R. McWhirter, D. A. Mitchell, M. F. Morales, E. Morgan, D. Oberoi, S. M. Ord, T. Prabu, N. Udaya Shankar, K. S. Srivani, R. Subrahmanyan, S. J. Tingay, R. B. Wayth, R. L. Webster, A. Williams, and C. L. Williams. Beam-forming Errors in Murchison Widefield Array Phased Array Antennas and their Effects on Epoch of Reionization Science. *ApJ*, 820:44, March 2016.
- [37] C. D. Nunhokee, G. Bernardi, S. A. Kohn, J. E. Aguirre, N. Thyagarajan, J. S. Dillon, G. Foster, T. L. Grobler, J. Z. E. Martinot, and A. R. Parsons. Constraining Polarized Foregrounds for EoR Experiments. II. Polarization Leakage Simulations in the Avoidance Scheme. *ApJ*, 848:47, October 2017.
- [38] A. Parsons, J. Pober, M. McQuinn, D. Jacobs, and J. Aguirre. A Sensitivity and Array-configuration Study for Measuring the Power Spectrum of 21 cm Emission from Reionization. *ApJ*, 753:81, July 2012.
- [39] A. R. Parsons, J. C. Pober, J. E. Aguirre, C. L. Carilli, D. C. Jacobs, and D. F. Moore. A Per-baseline, Delay-spectrum Technique for Accessing the 21 cm Cosmic Reionization Signature. *ApJ*, 756:165, September 2012.

- [40] A. H. Patil, S. Yatawatta, L. V. E. Koopmans, A. G. de Bruyn, M. A. Brentjens, S. Zaroubi, K. M. B. Asad, M. Hatef, V. Jelić, M. Mevius, A. R. Offringa, V. N. Pandey, H. Vedantham, F. B. Abdalla, W. N. Brouw, E. Chapman, B. Ciardi, B. K. Gehlot, A. Ghosh, G. Harker, I. T. Iliev, K. Kakiichi, S. Majumdar, G. Mellema, M. B. Silva, J. Schaye, D. Vrbanec, and S. J. Wijnholds. Upper Limits on the 21 cm Epoch of Reionization Power Spectrum from One Night with LOFAR. *ApJ*, 838:65, March 2017.
- [41] A. H. Patil, S. Yatawatta, S. Zaroubi, L. V. E. Koopmans, A. G. de Bruyn, V. Jelić, B. Ciardi, I. T. Iliev, M. Mevius, V. N. Pandey, and B. K. Gehlot. Systematic biases in low-frequency radio interferometric data due to calibration: the LOFAR-EoR case. *MNRAS*, 463:4317–4330, December 2016.
- [42] T. J. Pearson and A. C. S. Readhead. Image Formation by Self-Calibration in Radio Astronomy. *ARA&A*, 22:97–130, 1984.
- [43] U.-L. Pen, T.-C. Chang, C. M. Hirata, J. B. Peterson, J. Roy, Y. Gupta, J. Odegova, and K. Sigurdson. The GMRT EoR experiment: limits on polarized sky brightness at 150 MHz. *MNRAS*, 399:181–194, October 2009.
- [44] J. C. Pober, A. R. Parsons, J. E. Aguirre, Z. Ali, R. F. Bradley, C. L. Carilli, D. DeBoer, M. Dexter, N. E. Gugliucci, D. C. Jacobs, P. J. Klima, D. MacMahon, J. Manley, D. F. Moore, I. I. Stefan, and W. P. Walbrugh. Opening the 21 cm Epoch of Reionization Window: Measurements of Foreground Isolation with PAPER. *ApJ*, 768:L36, May 2013.
- [45] P. Procopio, R. B. Wayth, J. Line, C. M. Trott, H. T. Intema, D. A. Mitchell, B. Pindor, J. Riding, S. J. Tingay, M. E. Bell, J. R. Callingham, K. S. Dwarakanath, B.-Q. For, B. M. Gaensler, P. J. Hancock, L. Hindson, N. Hurley-Walker, M. Johnston-Hollitt, A. D. Kapińska, E. Lenc, B. McKinley, J. Morgan, A. Offringa, L. Staveley-Smith, C. Wu, and Q. Zheng. A High-Resolution Foreground Model for the MWA EoR1 Field: Model and Implications for EoR Power Spectrum Analysis. *PASA*, 34:e033, August 2017.
- [46] G. Pupillo, G. Naldi, G. Bianchi, A. Mattana, J. Monari, F. Perini, M. Poloni, M. Schiaffino, P. Bolli, A. Lingua, I. Aicardi, H. Bendea, P. Maschio, M. Piras, G. Virone, F. Paonessa, Z. Farooqui, A. Tibaldi, G. Addamo, O. A. Peverini, R. Tascone, and S. J. Wijnholds. Medicina array demonstrator: calibration and radiation pattern characterization using a UAV-mounted radio-frequency source. *Experimental Astronomy*, 39:405–421, June 2015.
- [47] M. Ryle and A. Hewish. The synthesis of large radio telescopes. *MNRAS*, 120:220, 1960.
- [48] R. J. Sault, J. P. Hamaker, and J. D. Bregman. Understanding radio polarimetry. II. Instrumental calibration of an interferometer array. *A&AS*, 117:149–159, May 1996.

- [49] T. W. Shimwell, C. Tasse, M. J. Hardcastle, A. P. Mechev, W. L. Williams, P. N. Best, H. J. A. Röttgering, J. R. Callingham, T. J. Dijkema, F. de Gasperin, D. N. Hoang, B. Hugo, M. Mirmont, J. B. R. Oonk, I. Prandoni, D. Rafferty, J. Sabater, O. Smirnov, R. J. van Weeren, G. J. White, M. Atemkeng, L. Bester, E. Bonnassieux, M. Brüggen, G. Brunetti, K. T. Chyžý, R. Cochrane, J. E. Conway, J. H. Croston, A. Danezi, K. Duncan, M. Haverkorn, G. H. Heald, M. Iacobelli, H. T. Intema, N. Jackson, M. Jamrozy, M. J. Jarvis, R. Lakhoo, M. Mevius, G. K. Miley, L. Morabito, R. Morganti, D. Nisbett, E. Orrú, S. Perkins, R. F. Pizzo, C. Schrijvers, D. J. B. Smith, R. Vermeulen, M. W. Wise, L. Alegre, D. J. Bacon, I. M. van Bemmel, R. J. Beswick, A. Bonafede, A. Botteon, S. Bourke, M. Brienza, G. Calistro Rivera, R. Cassano, A. O. Clarke, C. J. Conselice, R. J. Dettmar, A. Drabent, C. Dumba, K. L. Emig, T. A. Enßlin, C. Ferrari, M. A. Garrett, R. T. Génova-Santos, A. Goyal, G. Gürkan, C. Hale, J. J. Harwood, V. Heesen, M. Hoeft, C. Horellou, C. Jackson, G. Kokotanekov, R. Kon-dapally, M. Kunert-Bajraszewska, V. Mahatma, E. K. Mahony, S. Mandal, J. P. McKean, A. Merloni, B. Mingo, A. Miskolczi, S. Mooney, B. Nikiel-Wroczyński, S. P. O’Sullivan, J. Quinn, W. Reich, C. Roskowiński, A. Rowlinson, F. Savini, A. Saxena, D. J. Schwarz, A. Shulevski, S. S. Sridhar, H. R. Stacey, S. Urquhart, M. H. D. van der Wiel, E. Varenius, B. Webster, and A. Wilber. The LOFAR Two-metre Sky Survey. II. First data release. *A&A*, 622:A1, February 2019.
- [50] O. M. Smirnov. Revisiting the radio interferometer measurement equation. I. A full-sky Jones formalism. *A&A*, 527:A106, March 2011.
- [51] O. M. Smirnov. Revisiting the radio interferometer measurement equation. II. Calibration and direction-dependent effects. *A&A*, 527:A107, March 2011.
- [52] O. M. Smirnov and C. Tasse. Radio interferometric gain calibration as a complex optimization problem. *MNRAS*, 449:2668–2684, May 2015.
- [53] M. Sokolowski, T. Colegate, A. T. Sutinjo, D. Ung, R. Wayth, N. Hurley-Walker, E. Lenc, B. Pindor, J. Morgan, D. L. Kaplan, M. E. Bell, J. R. Callingham, K. S. Dwarakanath, B.-Q. For, B. M. Gaensler, P. J. Hancock, L. Hindson, M. Johnston-Hollitt, A. D. Kapińska, B. McKinley, A. R. Offringa, P. Procopio, L. Staveley-Smith, C. Wu, and Q. Zheng. Calibration and Stokes Imaging with Full Embedded Element Primary Beam Model for the Murchison Widefield Array. *PASA*, 34:e062, November 2017.
- [54] I. S. Sullivan, M. F. Morales, B. J. Hazelton, W. Arcus, D. Barnes, G. Bernardi, F. H. Briggs, J. D. Bowman, J. D. Bunton, R. J. Cappallo, B. E. Corey, A. Deshpande, L. deSouza, D. Emrich, B. M. Gaensler, R. Goeke, L. J. Greenhill, D. Herne, J. N. Hewitt, M. Johnston-Hollitt, D. L. Kaplan, J. C. Kasper, B. B. Kincaid, R. Koenig, E. Kratzenberg, C. J. Lonsdale, M. J. Lynch, S. R. McWhirter, D. A. Mitchell, E. Morgan, D. Oberoi, S. M. Ord, J. Pathikulangara, T. Prabu, R. A. Remillard, A. E. E. Rogers, A. Roshi, J. E. Salah, R. J. Sault, N. Udaya Shankar, K. S. Srivani, J. Stevens, R. Subrahmanyan, S. J. Tingay, R. B. Wayth, M. Waterson, R. L. Webster, A. R. Whitney, A. Williams, C. L. Williams, and J. S. B. Wyithe. Fast Holographic Deconvolution: A New Technique for Precision Radio Interferometry. *ApJ*, 759:17, November 2012.

- [55] C. Tasse. Nonlinear Kalman filters for calibration in radio interferometry. *A&A*, 566:A127, June 2014.
- [56] C. Tasse, S. van der Tol, J. van Zwieten, G. van Diepen, and S. Bhatnagar. Applying full polarization A-Projection to very wide field of view instruments: An imager for LOFAR. *A&A*, 553:A105, May 2013.
- [57] A. Richard Thompson, James M. Moran, and Jr. Swenson, George W. *Interferometry and Synthesis in Radio Astronomy, 3rd Edition*. 2017.
- [58] N. Thyagarajan, N. Udaya Shankar, R. Subrahmanyam, W. Arcus, G. Bernardi, J. D. Bowman, F. Briggs, J. D. Bunton, R. J. Cappallo, B. E. Corey, L. deSouza, D. Emrich, B. M. Gaensler, R. F. Goeke, L. J. Greenhill, B. J. Hazelton, D. Herne, J. N. Hewitt, M. Johnston-Hollitt, D. L. Kaplan, J. C. Kasper, B. B. Kincaid, R. Koenig, E. Kratzenberg, C. J. Lonsdale, M. J. Lynch, S. R. McWhirter, D. A. Mitchell, M. F. Morales, E. H. Morgan, D. Oberoi, S. M. Ord, J. Pathikulangara, R. A. Remillard, A. E. E. Rogers, D. Anish Roshi, J. E. Salah, R. J. Sault, K. S. Srivani, J. B. Stevens, P. Thigaraj, S. J. Tingay, R. B. Wayth, M. Waterson, R. L. Webster, A. R. Whitney, A. J. Williams, C. L. Williams, and J. S. B. Wyithe. A Study of Fundamental Limitations to Statistical Detection of Redshifted H I from the Epoch of Reionization. *ApJ*, 776:6, October 2013.
- [59] C. L. Van Eck, M. Haverkorn, M. I. R. Alves, R. Beck, P. Best, E. Carretti, K. T. Chyžý, J. S. Farnes, K. Ferrière, M. J. Hardcastle, G. Heald, C. Horellou, M. Iacobelli, V. Jelić, D. D. Mulcahy, S. P. O’Sullivan, I. M. Polderman, W. Reich, C. J. Riseley, H. Röttgering, D. H. F. M. Schnitzeler, T. W. Shimwell, V. Vacca, J. Vink, and G. J. White. Polarized point sources in the LOFAR Two-meter Sky Survey: A preliminary catalog. *A&A*, 613:A58, June 2018.
- [60] H. Vedantham, N. Udaya Shankar, and R. Subrahmanyam. Imaging the Epoch of Reionization: Limitations from Foreground Confusion and Imaging Algorithms. *ApJ*, 745:176, February 2012.
- [61] M. White, J. E. Carlstrom, M. Dragovan, and W. L. Holzapfel. Interferometric Observation of Cosmic Microwave Background Anisotropies. *ApJ*, 514:12–24, March 1999.
- [62] M. H. Wieringa. An investigation of the telescope based calibration methods ‘redundancy’ and ‘self-cal’. *Experimental Astronomy*, 2:203–225, 1992.
- [63] S. J. Wijnholds, T. L. Grobler, and O. M. Smirnov. Calibration artefacts in radio interferometry - II. Ghost patterns for irregular arrays. *MNRAS*, 457:2331–2354, April 2016.
- [64] S. Yatawatta. Distributed radio interferometric calibration. *MNRAS*, 449:4506–4514, June 2015.
- [65] S. Yatawatta, A. G. de Bruyn, M. A. Brentjens, P. Labropoulos, V. N. Pandey, S. Kazemi, S. Zaroubi, L. V. E. Koopmans, A. R. Offringa, V. Jelić, O. Martinez

- Rubi, V. Veligatla, S. J. Wijnholds, W. N. Brouw, G. Bernardi, B. Ciardi, S. Daiboo, G. Harker, G. Mellema, J. Schaye, R. Thomas, H. Vedantham, E. Chapman, F. B. Abdalla, A. Alexov, J. Anderson, I. M. Avruch, F. Batejat, M. E. Bell, M. R. Bell, M. Bentum, P. Best, A. Bonafede, J. Bregman, F. Breitling, R. H. van de Brink, J. W. Broderick, M. Brüggen, J. Conway, F. de Gasperin, E. de Geus, S. Duscha, H. Falcke, R. A. Fallows, C. Ferrari, W. Frieswijk, M. A. Garrett, J. M. Griessmeier, A. W. Gunst, T. E. Hassall, J. W. T. Hessels, M. Hoeft, M. Iacobelli, E. Juette, A. Karastergiou, V. I. Kondratiev, M. Kramer, M. Kuniyoshi, G. Kuper, J. van Leeuwen, P. Maat, G. Mann, J. P. McKean, M. Mevius, J. D. Mol, H. Munk, R. Nijboer, J. E. Noordam, M. J. Norden, E. Orru, H. Paas, M. Pandey-Pommier, R. Pizzo, A. G. Polatidis, W. Reich, H. J. A. Röttgering, J. Sluman, O. Smirnov, B. Stappers, M. Steinmetz, M. Tagger, Y. Tang, C. Tasse, S. ter Veen, R. Vermeulen, R. J. van Weeren, M. Wise, O. Wucknitz, and P. Zarka. Initial deep LOFAR observations of epoch of reionization windows. I. The north celestial pole. *A&A*, 550:A136, February 2013.
- [66] H. Zheng, M. Tegmark, V. Buza, J. S. Dillon, H. Gharibyan, J. Hickish, E. Kunz, A. Liu, J. Losh, A. Lutomirski, S. Morrison, S. Narayanan, A. Perko, D. Rosner, N. Sanchez, K. Schutz, S. M. Tribiano, M. Valdez, H. Yang, K. Z. Adami, I. Zelko, K. Zheng, R. P. Armstrong, R. F. Bradley, M. R. Dexter, A. Ewall-Wice, A. Magro, M. Matejek, E. Morgan, A. R. Neben, Q. Pan, R. F. Penna, C. M. Peterson, M. Su, J. Villasenor, C. L. Williams, and Y. Zhu. MITEoR: a scalable interferometer for precision 21 cm cosmology. *MNRAS*, 445:1084–1103, December 2014.
- [67] H. Zheng, M. Tegmark, J. S. Dillon, A. Liu, A. R. Neben, S. M. Tribiano, R. F. Bradley, V. Buza, A. Ewall-Wice, H. Gharibyan, J. Hickish, E. Kunz, J. Losh, A. Lutomirski, E. Morgan, S. Narayanan, A. Perko, D. Rosner, N. Sanchez, K. Schutz, M. Valdez, J. Villasenor, H. Yang, K. Zarb Adami, I. Zelko, and K. Zheng. Brute-force mapmaking with compact interferometers: a MITEoR northern sky map from 128 to 175 MHz. *MNRAS*, 465:2901–2915, March 2017.

# Chapter 6

## Foregrounds

Emma Chapman (Imperial College London), Vibor Jelić, (Ruder Bošković Institute)

### Abstract

This chapter discusses some important things

### 6.1 A Section

Lorem ipsum dolor sit amet, consectetur adipiscing elit. Duis eu egestas erat. Maecenas tincidunt lacinia tincidunt. Mauris id lectus nec neque feugiat condimentum vitae at diam. In vel orci nunc, non commodo mauris. Vivamus ipsum enim, vulputate quis pharetra non, molestie quis felis. Vivamus porttitor placerat turpis at accumsan. Nunc tortor velit, faucibus a rhoncus nec, blandit non elit. Nam consectetur lectus eu nisi blandit dapibus rhoncus dui tempus. Mauris fermentum dolor vel ipsum vulputate sit amet ultricies tortor lacinia. Donec ut nibh erat. Morbi nec mi ante. Integer nec vestibulum diam. Donec tincidunt pellentesque quam, ut interdum mauris venenatis condimentum. Nam condimentum, augue in aliquet gravida, neque dui elementum eros, id semper eros purus sed felis. Curabitur in justo sit amet sapien ultrices hendrerit at quis nibh. Quisque iaculis pulvinar tincidunt.

$$\begin{aligned} C(12) &= \left[ \vec{\pi} \cdot \vec{\phi}(x+r) \right] \\ &\approx 1 - \text{const} \frac{r^2}{L^2} \int_r^L \frac{x \, dx}{x^2} + \dots \\ &\approx 1 - \text{const} \frac{r^2}{L^2} \ln \frac{x \, dx}{x^2} + \dots \end{aligned} \tag{6.1}$$

Aenean tellus risus, porta sit amet porta vitae, tincidunt ut felis. Class aptent taciti sociosqu ad litora torquent per conubia nostra, per inceptos himenaeos. Vestibulum ante ipsum primis in faucibus orci luctus et ultrices posuere cubilia Curae; Phasellus pulvinar placerat velit auctor egestas. Vivamus euismod fringilla tincidunt. Sed ut magna felis, id sollicitudin nunc. Quisque a dui eu erat consectetur egestas a quis justo. Aenean euismod congue diam, vel posuere urna fermentum sit amet. Lorem ipsum dolor sit amet, consectetur adipiscing



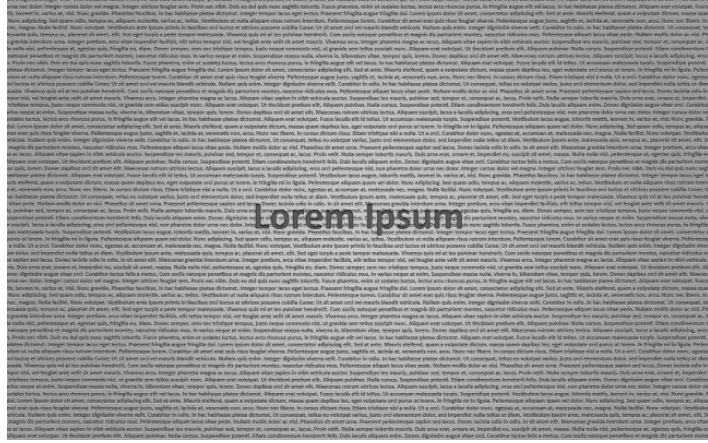


Figure 6.2: This is figure 2 in chapter 1.

Terrestrially, radio frequency interference (RFI) from any human-made sources of radio transmission, such as wind turbines, leads to the necessary excision of frequency channels using a flagging technique (e.g. [65, 52]). The number of channels excised is significant, around 1% of channels of data for MWA and LOFAR [50, 53]. Without careful mitigation in the calibration, imaging and diffuse foreground removal stages, RFI excision can result in an excess power that scales with the number of excised channels and does not integrate down with time, significantly dominating over the cosmological 21-cm signal by 1-2 magnitudes [50]. Extra-terrestrially, there exist a multitude of foregrounds which dominate all frequencies of observation and so more subtle methods than excision are required. This part of the chapter discusses the development and current use of Galactic and extragalactic foreground mitigation methods in Epoch of Reionization 21-cm experiments.

### 6.2.1 Foreground Mitigation in the Data Analysis Pipeline

#### Bright Source Removal

The first stage of foreground removal involves mitigating the effect of the very brightest sources on the sky: the point sources and extended sources. Bright source removal often comes under the umbrella of calibration as opposed to foreground mitigation however we will briefly summarize the process here. For example, the MWA real-time system (RTS) [45] carries out sequential bright source ‘peeling’ on the visibilities, tracking a few hundred of the brightest sources and comparing to a sky model constructed from existing catalogues and MWA observations [15]. The gains are calibrated on the strongest source, before that source is peeled (subtracted) from the data, and the next strongest source is used to refine the calibration, and so on until it is deemed that enough bright sources have been removed, usually a few hundred to a thousand at most. The other MWA calibration pipeline, Fast Holographic Deconvolution (FHD) [69], uses the MWA extragalactic catalogue GLEAM [31] to calibrate gains, modelling all sources out to 1% beam level in the primary lobe, amounting to approximately 50000 sources [4] and then removing a smaller population of them from the data. Similarly, LOFAR has built up a sky model over several years using the

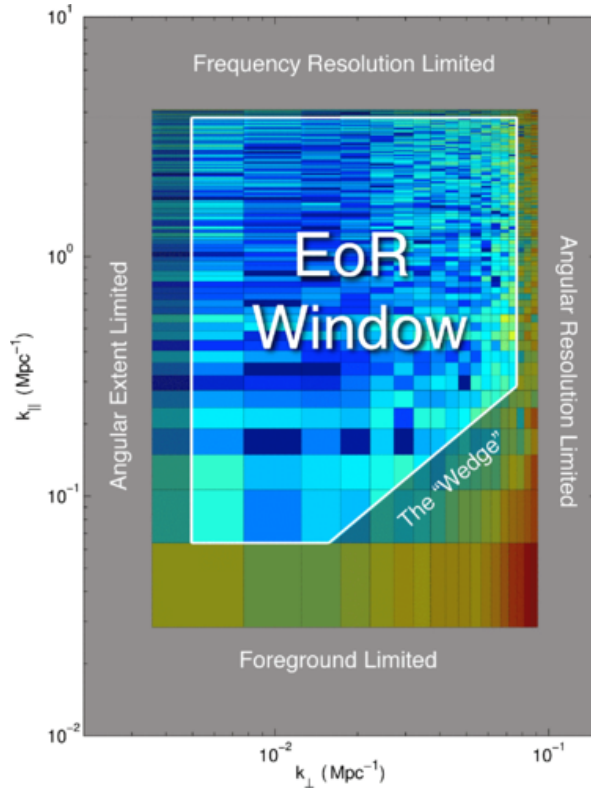


Figure 6.3: A schematic of the ‘EoR Window’ in the cylindrical  $k_{\parallel}, k_{\perp}$  Fourier plane, taken from Fig.1 of [24]. In a perfect observation, with zero instrumental effects, the foregrounds would be entirely contained in the well defined horizontal band. In a realistic observation however, the chromaticity of the instrument results in a leakage of power up into the EoR window, into a region called the ‘wedge’. Aside from these contaminated areas there should be a relatively clean area called the EoR window.

highest resolution LOFAR images and subtracts the sources in visibility space also [81, 80]. As of 2017, the LOFAR EoR sky model contained around 20,800 unpolarized sources.

### The EoR Window

It has previously been traditional when discussing diffuse foreground mitigation to assume that the previous stage of bright source subtraction has already been implemented perfectly. This is no longer seen to be a valid or safe assumption, as the chromaticity of the instrument, calibration errors and incorrect source subtraction lead to significant bias in the EoR signal for all current and planned experiments (e.g. [26, 66, 5, 61, 20, 42]), including redundant arrays [14].

The spectral differences between the EoR signal and the bias introduced by the foregrounds and instrument lend themselves to a neat separation in  $k_{\perp} - k_{\parallel}$  space, Fig. 6.3. In this formalism, spectrally-smooth foregrounds live in a well-defined area of  $k$ -space, at the smallest  $k_{\parallel}$  scales, equivalent to the red stripe at the bottom of Fig. 6.3, excluding the wedge area. The assumption that the foregrounds would remain smooth and confined in a horizontal area

at low  $k_{\parallel}$  even after observation by a radio interferometer drove early foreground removal techniques such as those introduced in Section 6.2.3 but is now known to be an incorrect assumption. The chromaticity of the instrument results in a ‘mode-mixing’ where power is transferred from the angular to the frequency scales, throwing power upwards from the foreground area in the window into the larger  $k_{\parallel}$  scales, with the effect increasing with larger  $k_{\perp}$ . This results in a wedge like structure, a structure that has been now extensively discussed and mathematically defined in the literature (e.g. [35, 24, 40, 39, 29, 72, 64, 47, 76, 74, 59, 20]. Because the point sources reside on the largest  $k_{\perp}$  scales they, or even their residuals when incorrectly calibrated, can overwhelm the EoR power in the frequency scales (e.g. [11] and immediately preceding references).

Now we have defined the problem, namely the overpowering magnitude and potential leakage of foregrounds onto the EoR signal, we can consider how to achieve our aim of making accurate statistical conclusions on the nature of the EoR using the data within this window. To proceed, we can consider two philosophies. The first, **foreground subtraction**, aims to remove foreground contamination on all scales. The benefit of this is that there are more  $k$  scales available for analysis. The drawback of foreground subtraction across all  $k$ -scales is that any failure in the method will potentially result in a foreground fitting bias across all scales of the window, providing another layer of contamination. One could instead avoid the foregrounds and therefore the need to remove them: **foreground avoidance**. This philosophy aims to then quantify the foregrounds and wedge such that any analysis occurs within a well-defined window free of contamination. The benefit of this is, as stated, the avoidance of foreground subtraction bias. The drawback is that any analysis is performed on a significantly reduced set of scales which can for example introduce its own bias into the spherically averaged power spectrum [35]. Additional to both philosophies, we can implement **foreground suppression**, which down-weights scales where the foregrounds or foreground removal residuals are dominant. We will now discuss these approaches in further detail in the context of current EoR experiments.

## 6.2.2 Foreground Avoidance and Suppression

The Murchison Widefield Array (MWA) has two separate pipelines which differ in their application of foreground mitigation techniques and calibration methods, while mostly employing foreground avoidance. They way in which MWA is optimized for making images allows the option to directly subtract known foregrounds but in this case the direct foreground subtraction is primarily applied to get access to a cleaner EoR window, not to get access to within the wedge, as is the motivation of foreground subtraction in LOFAR.

The FHD [69] and  $\epsilon$ psilon [4] pipeline builds a sky model of point sources based on a golden set of data, including all sources above a floor limit within the primary beam of the instrument, and those beyond the primary beam if they are above 1% of the maximum primary beam level. This point source model is used in calibration in a similar way to LOFAR, and contains about 7000 sources as of 2016 [6]. In contrast to the RTS [45] and CHIPS [73] pipeline, the FHD- $\epsilon$ psilon pipeline also generates a diffuse foreground model by subtracting away the point source model from the observed data, and integrating over frequency to create a diffuse foreground model free of spectral information [6]. They then subtract both the point source model and the diffuse model from the data to minimise the leakage from

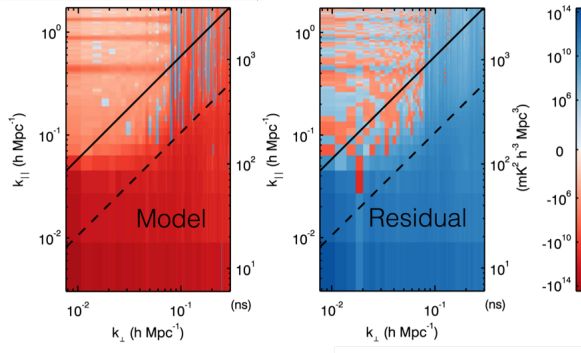


Figure 6.4: Left: MWA foreground model without diffuse foregrounds (i.e. just point sources) and with diffuse foregrounds. Adding diffuse foregrounds into the model produces leakage far up into the EoR window and instrumental contamination can be seen in the horizontal lines throughout the EoR window. Right: the difference between the power spectrum of the residuals when only the point sources have been subtracted as described above, and the power spectrum of the residuals where the diffuse foregrounds have also been subtracted. There is a clear reduction in foreground residuals all along the wedge and the EoR window is noise-like, suggesting a lack of foreground contamination there. There is a 70% reduction in residual power of the foregrounds using this method. Figure taken from [6].

the wedge into the EoR window. In Fig 6.4 we see the effect of this foreground subtraction on the EoR window. The left image is the difference between the power spectrum of the MWA foreground model without diffuse foregrounds (i.e. just point sources) and with diffuse foregrounds. The plot shows that the diffuse foregrounds have power far up into the EoR window, due to non-uniform spectral sampling and the effect of windowing the data along frequency during the Fourier Transform. This figure if no other demonstrates the danger of assuming that the observed foreground signal is smooth and contained only at the smallest  $k_{\parallel}$ . Further instrumental complications can be seen in the horizontal lines throughout the EoR window, which is contamination due to the periodic frequency sampling function used by MWA [51]. The right plot of Fig. 6.4 shows the difference between the power spectrum of the residuals when only the point sources have been subtracted as described above, and the power spectrum of the residuals where the diffuse foregrounds have also been subtracted. There is a clear reduction in foreground residuals all along the wedge and the noise-like characteristic of the EoR window suggests a lack of foreground contamination there. [6] report a 70% reduction in residual power of the foregrounds using this method.

The black lines in Fig. 6.5 show the area of the EoR window used in the FHD- $\epsilon$  pipeline, with the masks ensuring the avoidance of the horizontal contamination lines and the wedge.

The RTS-CHIPS pipeline subtracts significantly fewer sources, a few hundred to a thousand at most, and does so in visibility space. There is no diffuse foreground model in the subtraction stage and instead CHIPS down-weight modes with residual point source power. There is also the option of diffuse foreground weighting based on a simple foreground model where the covariances are known, though in practice this diffuse down-weighting is not cur-

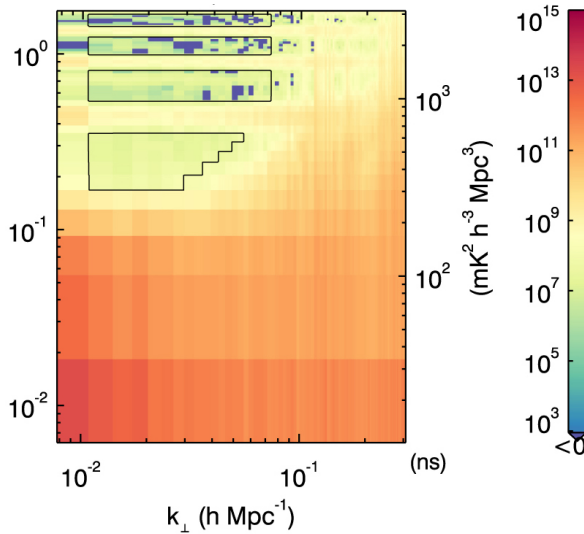


Figure 6.5: An example 2D cylindrical power spectrum of the first season MWA data after foreground mitigation. The data used for the upper limits can be seen bounded by black lines. The amount of data available for a power spectrum analysis has been severely reduced by the presence of foregrounds and instrumental contamination but the data within the bounded regions displays noise-like behaviour indicative of successful foreground mitigation. Figure taken from [6].

rently utilised.

### Delay Space Filtering

Delay space filtering is a method of foreground avoidance primarily adopted by the Donald C. Backer Precision Array for Probing the Epoch of Reionization (PAPER) [58]. As with most foreground mitigation methods it requires the foregrounds to be reasonably smooth, even after instrumental effects. The wedge is the end-result of an instrument where the frequency-dependence of the instrument's sampling is dependent on the length of the baseline measuring the sky. Delay-space filtering exploits this relation by analyzing the data per baseline, circumventing the conspiracy of instrumental effects on the foregrounds and effectively isolating the foregrounds such that they are easily avoided. Fig. 6.6 demonstrates that for a given baseline measurement the visibility sampled changes with frequency, with a steeper change for longer baselines. This results in the mode-mixing seen in the 2D cylindrical power spectrum and the wedge structure, where we see power thrown up into the EoR window increasingly on the largest  $k_{\perp}$  scales, which are the scales sampled by the longest baselines. Delay space filtering aims to mitigate the mode mixing by performing a Fourier transform along the visibility sampled by a given baseline (a solid line in Fig. 6.6), and not along the frequency direction (vertical axis of Fig. 6.6) as is usual.

A delay transform takes a single time sample of a visibility from one baseline, for all observed frequencies (i.e. one of the solid lines on Fig. 6.6), and Fourier transforms it to produce the delay spectrum [59, 56, 57]. The delay transform is:

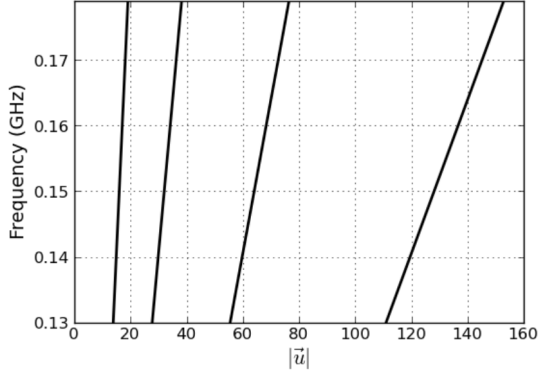


Figure 6.6: This figure, taken from [59], demonstrates the frequency dependence of the wavemode sampled by baselines measuring 16, 32, 64, and 128 wavelengths at 150 MHz. For a given baseline measurement, the visibility sampled changes with frequency, with a steeper change for longer baselines. This results in the mode-mixing seen in the 2D cylindrical power spectrum and particularly "the wedge", where we see power thrown up into the EoR window increasingly on the smallest  $k_{\perp}$  scales, which are the scales sampled by the longest baselines.

$$\tilde{V}_b(\tau) = \int dl dm dv A(l, m, v) I(l, m, v) e^{-2\pi i v (\tau_g - \tau)} \quad (6.2)$$

where  $l, m$  have their usual definition relating to angular coordinates on the sky (e.g. [70]).  $\tau$  is the time-delay between the signal reaching both antennas and the geometric group delay associated with the projection of baseline  $\vec{b} \equiv (b_x, b_y, b_z)$  in the direction  $\hat{s} \equiv (l, m, \sqrt{1 - l^2 - m^2})$  is:

$$\tau_g \equiv \frac{\vec{b} \cdot \hat{s}}{c} \quad (6.3)$$

For comparison, the usual equation where the Fourier transform is simply applied along the frequency axis is:

$$\tilde{V}(u, v, \eta) = \int dl dm dv A(l, m, v) I(l, m, v) e^{-2\pi i (ul + vm + \eta v)} \quad (6.4)$$

where  $\eta$  is the Fourier transform of  $v$ .

The delay transform transforms flat spectra sky emission into delta functions. Because the sky emission is not perfectly smooth, and the instrument adds in its own unsmoothing effects, this delta function is effectively convolved with a kernel, which broadens the delta function in delay space. For the smoother foregrounds, that kernel will be narrow, and confined within the "horizon limits", the geometric limit in delay space beyond which no flat spectra emission can enter the telescope. Spectrally unsmooth sky emission can enter beyond these horizon limits and emission such as the cosmological signal finds itself with a wide convolving kernel, spreading power well beyond the horizon limit where the foregrounds are theoretically confined. In Fig. 6.7 we see the delay transform at 150 MHz for

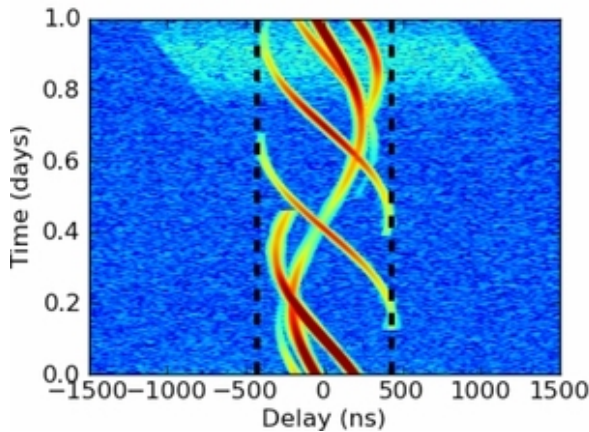


Figure 6.7: The delay spectra of several smooth-spectra sources, which remain largely confined within the geometric horizon limits. The broad 21-cm cosmological signal delay spectra in cyan demonstrates that unsmooth spectral signals have a much wider convolving kernel and produce a much wider delay spectra. If analysis is carried out outside of the horizon limits then the foregrounds can be avoided. Taken from [59].

several spectrally smooth sources and how they remain confined within the horizon limits of the baseline (here 32 metres). In contrast, the delay spectrum of spectrally unsmooth emission, such as the cosmological 21-cm signal, finds itself smeared to high delays. Full mathematical detail can be found in [59, 56] and [57].

By performing this delay space transform, we are effectively moving into the sidelobes of the 21-cm signal in delay space. The cosmological signal is scattered to high delays whereas the foregrounds are not, allowing the data analysis in that large delay space to be free of foregrounds and foreground removal bias. This method also removes the need for imaging in order to remove the foreground directly, making it suitable for a redundant array with little or no ability to image, but a high sensitivity to the 21-cm power spectrum [56].

PAPER is a radio interferometer with a highly redundant antenna layout, with multiple baselines of the same length and orientation. Because these multiple baselines all measure the same sky signal, any differences in the signal received would be due to instrumentation, allowing a quick calibration for multiple calibration parameters - ‘redundant calibration’ (e.g. [36, 37, 25, 84, 79]).

PAPER avoided the use of the delay modes dominated by foregrounds and downweighted residual foregrounds using inverse covariance weighting in order to form an upper limit power spectrum measurement [1]. The latter method of inverse covariance weighting where the covariance is calculated based on the data itself has now been shown to carry the considerable risk of overfitting the EoR data [19]. To be clear, despite the retraction of the PAPER-64 results due to power spectrum estimation errors [2], the delay space filtering technique remains a promising approach to foreground mitigation.

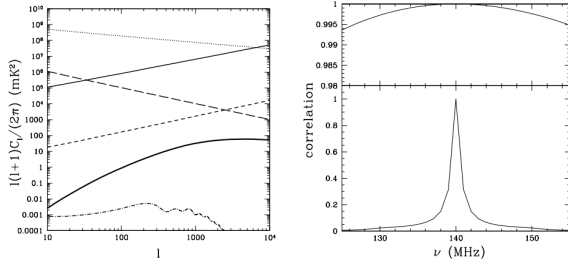


Figure 6.8: Left: The 2D power spectrum at 140MHz for the cosmological signal (thick, solid), point sources (thin, solid), Galactic synchrotron (thin, dotted), extra-Galactic free-free (thin, dash), Galactic free-free (thin, long dash) and the CMB (dot-dash). The cosmological signal is dominated by foregrounds at all scales, such that separation based purely on spatial differences is not feasible. Figure taken from Fig. 5 of [67]. Right: The simulated frequency correlations for the foregrounds (top) and cosmological signal (bottom). This plot shows how the correlation between frequency slices (with the comparison made to a slice at 140 MHz), drops off with increasing frequency separation. The foregrounds are highly frequency coherent, whereas the cosmological signal is significantly less so. Figure taken from Fig. 7 of [67].

### 6.2.3 Foreground Subtraction

Foreground subtraction methods all seek to find a model for the observed foregrounds and remove that model from the observed signal, leaving the cosmological signal, instrumental noise and any foreground fitting errors. Foreground removal is usually applied on all scales, meaning that it potentially allows access into the lowest  $k_{\parallel}$  scales where foregrounds traditionally dominate. A caveat of this is that any foreground fitting bias has the potential to affect all scales in the window: foregrounds may remain within the wedge and cosmological signal may be erroneously fitted out within the previously clean EoR window. As an aside, there has been no method so far that can separate out the cosmological 21-cm signal entirely by itself, separate from instrumental noise. Currently when the foregrounds are subtracted or avoided the cosmological noise and signal are still mixed together in what are often termed the ‘residuals’. The instrumental noise can be obtained from the data for example by the differencing of very fine bandwidth frequency channels, such that both the foregrounds and EoR signal are smooth. The noise power spectrum can then be removed from the residual power spectrum to form the recovered cosmological signal power spectrum. We will now introduce some of the main foreground subtraction techniques.

#### Polynomial Fitting and Global Experiments

As we have seen in the first half of this chapter, the astrophysical foregrounds are 3-5 magnitudes brighter than the cosmological 21-cm signal and so, by magnitude alone, appear to be the most ominous obstacle to the first detection. Despite, or perhaps because of, their overwhelming magnitude they are well constrained, following power laws with known indices and evolution. The sheer magnitude of the foregrounds means that purely spatial separa-

tion, i.e. separation based on only one frequency slice, is not possible: the 21-cm signal and foregrounds are not statistically different enough when only considering spatial scales (see left-hand panel of Fig. 6.8) [67, 21, 54, 22]. While separation based purely on spatial scales is not feasible, the high frequency coherence of the foregrounds compared to both the instrumental noise and cosmological signal provides a way to separate out the two signals (foregrounds and both cosmological signal and noise) (see right-hand panel of Fig. 6.8).

[67] and [82] exploited the large cross-correlation of the foregrounds in slices at different frequencies to model and remove the foregrounds noting that the frequency coherence was also a useful tool for separation. Polynomial fitting went on to exploit the frequency coherence of the foregrounds across the bandwidth, removing the foregrounds along the line of sight without using any spatial correlation information (e.g. [11, 78, 43]). In this method, the foregrounds are modelled by a polynomial function, for example in log-log space such as:

$$\log I = a_3 + a_2 \log v + a_1 (\log v)^2 + \dots \quad (6.5)$$

where  $I$  is the brightness temperature of the data,  $v$  is the frequency of observation and  $a_1, a_2, a_3$  are the coefficients which are to be determined in the fit.

Polynomial fitting is a parametric foreground mitigation method. It uses knowledge from simulated foregrounds to tune the coefficients of the polynomial function (e.g. [34]). There are two areas of concern when using this method. Firstly, the effect of the instrument results in a signal which can differ significantly from the frequency-coherent theoretical foreground model (see Section 6.2.1). By incorporating weighting according to the amount of information in a particular  $uv$  cell, this could possibly be overcome [41, 11]. The second area of concern was that the success of the method relies heavily on having an accurate model for the foreground signal. There are many more instrumental effects than the frequency dependence of the beams, for example polarization leakage (e.g. [49, 3]) and excess instrumental noise [61]. [77] demonstrated that polynomial removal across the EoR frequency band resulted in significant signal loss when using simulations of complex foregrounds, though they also showed that by fitting a polynomial simultaneously in smaller bandwidth segments this signal loss could be mitigated. Polynomial removal is now rarely used within the interferometric experiments with the exception of the upper limit from GMRT [55] which used a similar philosophy to remove their foregrounds, albeit by applying a piecewise linear function, as opposed to a polynomial function.

Aside from interferometric experiments, polynomial fitting does have a prominent place in global EoR experiments (e.g. [68, 12]) which, due to the coherence of the 21-cm global signal over frequency, means that so far all the more sophisticated methods of foreground mitigation have been unworkable on global simulation and data. For example, the very small number of lines of sight observed by a single global experiment mean that there is not enough spatial information for some non-parametric methods to work.

The Experiment to Detect the Global EoR Signature (EDGES) detection [12] used a five term polynomial based on the properties of the foregrounds and ionosphere, incorporating the actions of the instrument into their foreground model. The level of accuracy of this method has since questioned however, with the results showing dependence on the description of the foregrounds [13, 30]. Overall, polynomial fitting correctly exploits the foreground coherence but it is vulnerable to unknown systematics and unexpected foreground signals.

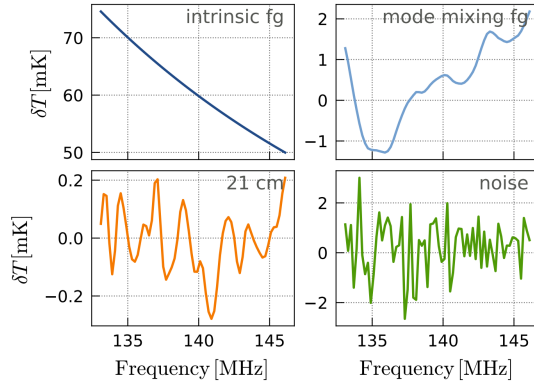


Figure 6.9: Simulated components of the observed signal, demonstrating that the smooth foreground signal is accompanied by an unsMOOTH mode mixing signal. GPR models each of these foreground components separately, making use of prior information about each component in the form of covariance functions. Figure taken from [44].

For global experiments there is currently no other option, but for interferometric experiments the methods in the following section provide an alternative.

### Non-parametric foreground removal

The concern that the instrument might introduce complex spectral structure into the foreground signal has driven research into foreground mitigation methods which rely less on a strongly constrained foreground model. Wp smoothing [28] fits a function along the line of sight whilst penalising the “Wendepunkt”, inflection points, that give the method its name. Unlike polynomial fitting, the function is permitted to be rough but inherently favours the more smooth models. Wp smoothing is applied along each line of sight individually and so spatial correlations of the foregrounds are not utilised in making the foreground fit. The current method employed by the LOFAR EoR pipeline, Gaussian Process Regression (GPR) [44] also relies purely on spectral information. GPR models the foregrounds, mode mixing components, 21-cm cosmological signal and noise by Gaussian Processes, allowing a clear separation and uncertainty estimation (see Fig. 6.9). GPR does not require specification of a functional form for each component but instead allows the data to find its own model, while taking into account the covariance structure priors incorporated by the user. This allows a certain level of control, for example splitting the foreground covariance into a smooth intrinsic foreground model and an unsMOOTH mode mixing component, while still not imposing a strict level of smoothness or a parametric form on the data.

BSS methods have been used in Cosmic Microwave Background experiments ([63, 62]) and their application to EoR data is a natural evolution. BSS methods are used across a wide range of fields in order to separate mixed signals into independent components. The data can be expressed in terms of the mixing model:

$$\mathbf{X} = \mathbf{AS} + \mathbf{N} \quad (6.6)$$

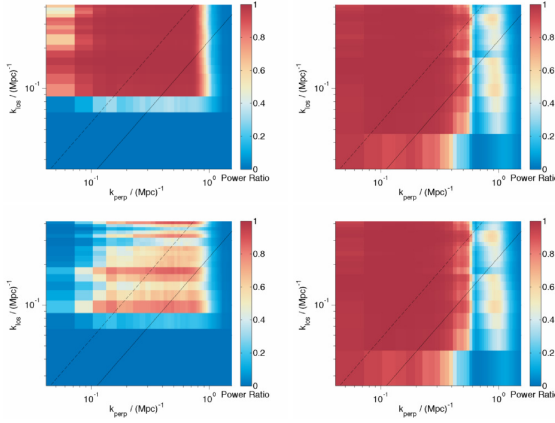


Figure 6.10: The left column shows the ratio of the simulated components, (cosmological signal / (cosmological signal + foregrounds)), demonstrating that the area of the window free from foreground contamination is small when the foregrounds are unsmooth. The top row is where the foreground model has a random wiggle along the line of sight equal in magnitude to 0.1% of the foreground signal. The bottom row shows a 1% wiggle. On the right is the same ratio but with foreground fitting errors after foreground removal by GMCA instead of the simulated foregrounds, demonstrating that the method can open up the EoR window significantly even when the smoothness of the foregrounds is under threat. Figure taken from [18].

where  $\mathbf{X}$  is the observed signal,  $\mathbf{S}$  are the independent components of that signal,  $\mathbf{N}$  is the noise and  $\mathbf{A}$  is a matrix determining how the components are mixed, the ‘mixing matrix’. For an observation of  $m$  frequency channels each constituting  $t$  pixels and a foreground model of  $n$  independent foreground components, the dimensions of these quantities are  $\mathbf{X}[m,t]$ ,  $\mathbf{S}[n,t]$ ,  $\mathbf{N}[m,t]$  and  $\mathbf{A}[m,n]$ .

When this framework is applied to EoR data, the foregrounds are contained within  $\mathbf{S}[n,t]$  while the cosmological signal is contained along with the instrumental noise in  $\mathbf{N}[m,t]$ . The independent components of the foreground model are not directly related to the Galactic synchrotron, Galactic free-free and extragalactic foregrounds, but instead each independent component is potentially a mixture of all these physical foregrounds. This leaves the user without a physically motivated choice for the number of independent components, so that the number must be chosen empirically based on simulated data. Once a foreground model  $\mathbf{AS}$  has been determined this can then be subtracted from the observed signal, leaving the residual data as with the other methods.

The two BSS methods introduced for use on EoR data differ by their definition of independence. FastICA [17, 33, 32] is a long-established independent component analysis technique which uses statistical independence to separate out the foreground components. FastICA constrains the different components by maximizing the negentropy of the signal components, utilising central limit theorem which states that the more independent components a signal contains, the more Gaussian the probability distribution function of that signal will be. In contrast, GMCA [8, 9, 16, 7] is a method developed for use on CMB data that

uses morphological diversity to separate out components. GMCA assumes that the data is represented in a sparse manner which can be achieved by a wavelet decomposition. With the independent components unlikely to have the same few non-zero basis coefficients in wavelet space, the method is able to separate out the components according to the differing sparse basis coefficient values. As with FastICA, we actually care little for the independent components individually, it is the combination of those as a whole which form the foreground model, with the method naturally separating out the decoherent noise and cosmological signal. In simulation both these methods have behaved well, opening up the EoR window into the lowest scales even when subjected to unsmooth foreground simulations, Fig. 6.10. GMCA was used to achieve the current LOFAR upper-limit [60] but since then has not been able to remove the foregrounds down to the same level as, for example, GPR [44]. The reason for this remains unknown and a full comparative analysis is currently underway. [44] also expressed concern that because BSS methods are not based on defining the components in a statistical framework relating to the contributions from foregrounds and mode-mixing, they are not easily assessed for uncertainty and physical meaning. The blind methods are very useful as a separate check on results from what are extremely complex experiments, with many unknown unknowns. There is scope to move these methods towards a more parametric framework, perhaps constraining the mixing matrix columns according to the first-hand knowledge about the instrumental effects and foregrounds we have built up from the pathfinder telescopes. This is a similar philosophy as introduced by [10] in Correlated Component Analysis (CCA). While still based on a mixing matrix framework, CCA is a parametric method which constrains the mixing matrix to represent power law behaviour over frequency, fixing the spectral index for a Galactic free-free contribution explicitly.

While Wp smoothing, GMCA, GPR and FastICA are all labelled non-parametric in the literature, it is important to note than none of them are fully blind or indeed fully non-parametric. Each of them require the selection of parameters to define the fit: whether it is the smoothing parameter in Wp smoothing, or the number of independent components in GMCA and FastICA. So far these parameters have been chosen based on minimizing the foreground fitting error on simulated data, where the foreground model is known. A more robust method is to implement a Bayesian model selection model, as GPR does already. In addition, [27] developed a method based on the Bayesian maximum a posteriori probability (MAP) formalism, assuming priors for the smoothness of the contaminating radiation and for the correlation properties of the cosmological signal and [83] introduced HIEMICA (HI Expectation Maximization Independent Component Analysis), an extension of ICA with a fully Bayesian inference of the foreground power spectra, allowing their separation from the cosmological signal power spectra. Machine learning has also been applied in an effort to seek a foreground model defined by the data itself [38]. There are now a multitude of non-parametric foreground subtraction methods available which have each proved their own principle on simulated, and in the case of GPR and GMCA, observed data. Now we know the constraints of the instrument much better, work on the relative advantages and disadvantages of all these approaches are a logical next step.

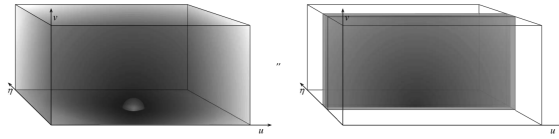


Figure 6.11: The 3D spherical power spectrum of the EoR signal (left), and an example residual foreground signal template (right), where zero is at the centre of the bottom face of the cuboid. The foreground signal displays a separable-axial symmetry while the EoR signal has a symmetric power spectrum. This contrast allows a further separation stage in order to clean the foreground fitting errors which have accumulated from the previous two stages of bright source subtraction and diffuse foreground mitigation. Figure taken from [46].

#### 6.2.4 Residual Error Subtraction

The final stage of foreground mitigation is residual error subtraction [46, 48]. The residual foreground mitigation errors from the previous two stages (bright source subtraction and diffuse foreground mitigation) produce distinct shapes in the spherical power spectrum, Fig. 6.11. One can take the spherical power spectrum of the residual data and apply a multi-parameter fit according to the foreground residual and EoR template power spectrum. This allows a final cleaning of residual foreground contamination. [46] also notes that “because the residual error subtraction relies on the statistical characteristics of the subtraction errors, the foreground removal steps become tightly linked and we must move from focusing on individual subtraction algorithms to the context of a complete foreground removal framework.” This statement leads us neatly to the conclusion of this chapter.

### 6.3 Conclusions

The current EoR experiments are now modelled and constrained to an excellent degree but during that process there has been a blurring of boundaries between the analysis modules. The calibration stage, once assumed to mitigate foreground point sources only, can erroneously suppress diffuse foregrounds [61] and the mode-mixing of the instrument has required more complex modelling as wide-field effects have become apparent [71]. There are a promising number of foreground mitigation techniques now available providing the necessary diversity of pipelines necessary for verifying the first detection. So far, there has not been a wide-reaching comparison of all of these methods or a complete assessment of their strengths and weaknesses for recovery of the different aspects of the EoR signal such as power spectra or images. Foreground subtraction, suppression and avoidance are now used in combination in the experimental pipelines and the further development of the best combination for these methods will provide an exciting area of research in the next decade.

# Bibliography

- [1] Zaki S. Ali, Aaron R. Parsons, Haoxuan Zheng, Jonathan C. Pober, Adrian Liu, James E. Aguirre, Richard F. Bradley, Gianni Bernardi, Chris L. Carilli, and Carina Cheng. PAPER-64 Constraints on Reionization: The 21 cm Power Spectrum at  $z = 8.4$ . *ApJ*, 809(1):61, Aug 2015.
- [2] Zaki S. Ali, Aaron R. Parsons, Haoxuan Zheng, Jonathan C. Pober, Adrian Liu, James E. Aguirre, Richard F. Bradley, Gianni Bernardi, Chris L. Carilli, and Carina Cheng. Erratum: “PAPER-64 Constraints on Reionization: The 21 cm Power Spectrum at  $z = 8.4$ ” (<http://doi.org/10.1088/0004-637x/809/1/61>)<sup>1</sup>, 2015, ApJ, 809, 61(A). *ApJ*, 863(2):201, Aug 2018.
- [3] K. M. B. Asad, L. V. E. Koopmans, V. Jelić, V. N. Pandey, A. Ghosh, F. B. Abdalla, G. Bernardi, M. A. Brentjens, A. G. de Bruyn, and S. Bus. Polarization leakage in epoch of reionization windows - I. Low Frequency Array observations of the 3C196 field. *MNRAS*, 451(4):3709–3727, Aug 2015.
- [4] N. Barry, A. P. Beardsley, R. Byrne, B. Hazelton, M. F. Morales, J. C. Pober, and I. Sullivan. The FHD/\$\{\}\$\$\epsilon\$ Epoch of Reionization Power Spectrum Pipeline. *arXiv e-prints*, page arXiv:1901.02980, Jan 2019.
- [5] N. Barry, B. Hazelton, I. Sullivan, M. F. Morales, and J. C. Pober. Calibration requirements for detecting the 21 cm epoch of reionization power spectrum and implications for the SKA. *MNRAS*, 461:3135–3144, September 2016.
- [6] A. P. Beardsley, B. J. Hazelton, I. S. Sullivan, P. Carroll, N. Barry, M. Rahimi, B. Pindor, C. M. Trott, J. Line, and Daniel C. Jacobs. First Season MWA EoR Power spectrum Results at Redshift 7. *ApJ*, 833(1):102, Dec 2016.
- [7] J. Bobin, Y. Moudden, J. L. Starck, J. Fadili, and N. Aghanim. SZ and CMB reconstruction using generalized morphological component analysis. *Statistical Methodology*, 5(4):307–317, Jul 2008.
- [8] J. Bobin, F. Sureau, and J. L. Starck. Cosmic microwave background reconstruction from WMAP and Planck PR2 data. *A&A*, 591:A50, Jun 2016.
- [9] Jerome Bobin, Jeremy Rapin, Anthony Larue, and Jean-Luc Starck. Sparsity and adaptivity for the blind separation of partially correlated sources. *IEEE Transactions on Signal Processing*, 63(5):1199–1213, 2015.

- [10] Anna Bonaldi and Michael L. Brown. Foreground removal for Square Kilometre Array observations of the epoch of reionization with the correlated component analysis. *MNRAS*, 447(2):1973–1983, Feb 2015.
- [11] Judd D. Bowman, Miguel F. Morales, and Jacqueline N. Hewitt. Foreground Contamination in Interferometric Measurements of the Redshifted 21 cm Power Spectrum. *ApJ*, 695(1):183–199, Apr 2009.
- [12] Judd D. Bowman, Alan E. E. Rogers, Raul A. Monsalve, Thomas J. Mozdzen, and Nivedita Mahesh. An absorption profile centred at 78 megahertz in the sky-averaged spectrum. *Nature*, 555(7694):67–70, Mar 2018.
- [13] Richard F. Bradley, Keith Tauscher, David Rapetti, and Jack O. Burns. A Ground Plane Artifact that Induces an Absorption Profile in Averaged Spectra from Global 21 cm Measurements, with Possible Application to EDGES. *ApJ*, 874(2):153, Apr 2019.
- [14] Ruby Byrne, Miguel F. Morales, Bryna Hazelton, Wenyang Li, Nichole Barry, Adam P. Beardsley, Ronniy Joseph, Jonathan Pober, Ian Sullivan, and Cathryn Trott. Fundamental Limitations on the Calibration of Redundant 21 cm Cosmology Instruments and Implications for HERA and the SKA. *ApJ*, 875(1):70, Apr 2019.
- [15] P. A. Carroll, J. Line, M. F. Morales, N. Barry, A. P. Beardsley, B. J. Hazelton, D. C. Jacobs, J. C. Pober, I. S. Sullivan, and R. L. Webster. A high reliability survey of discrete Epoch of Reionization foreground sources in the MWA EoR0 field. *MNRAS*, 461(4):4151–4175, Oct 2016.
- [16] Emma Chapman, Filipe B. Abdalla, J. Bobin, J. L. Starck, Geraint Harker, Vibor Jelić, Panagiotis Labropoulos, Saleem Zaroubi, Michiel A. Brentjens, and A. G. de Bruyn. The scale of the problem: recovering images of reionization with Generalized Morphological Component Analysis. *MNRAS*, 429(1):165–176, Feb 2013.
- [17] Emma Chapman, Filipe B. Abdalla, Geraint Harker, Vibor Jelić, Panagiotis Labropoulos, Saleem Zaroubi, Michiel A. Brentjens, A. G. de Bruyn, and L. V. E. Koopmans. Foreground removal using FASTICA: a showcase of LOFAR-EoR. *MNRAS*, 423(3):2518–2532, Jul 2012.
- [18] Emma Chapman, Saleem Zaroubi, Filipe B. Abdalla, Fred Dulwich, Vibor Jelić, and Benjamin Mort. The effect of foreground mitigation strategy on EoR window recovery. *MNRAS*, 458(3):2928–2939, May 2016.
- [19] Carina Cheng, Aaron R. Parsons, Matthew Kolopanis, Daniel C. Jacobs, Adrian Liu, Saul A. Kohn, James E. Aguirre, Jonathan C. Pober, Zaki S. Ali, and Gianni Bernardi. Characterizing Signal Loss in the 21 cm Reionization Power Spectrum: A Revised Study of PAPER-64. *ApJ*, 868(1):26, Nov 2018.
- [20] A. Datta, J. D. Bowman, and C. L. Carilli. Bright Source Subtraction Requirements for Redshifted 21 cm Measurements. *ApJ*, 724(1):526–538, Nov 2010.

- [21] Tiziana Di Matteo, Benedetta Ciardi, and Francesco Miniati. The 21-cm emission from the reionization epoch: extended and point source foregrounds. *MNRAS*, 355(4):1053–1065, Dec 2004.
- [22] Tiziana Di Matteo, Rosalba Perna, Tom Abel, and Martin J. Rees. Radio Foregrounds for the 21 Centimeter Tomography of the Neutral Intergalactic Medium at High Redshifts. *ApJ*, 564(2):576–580, Jan 2002.
- [23] KI Diamantaras and SY Kung. *Principal component neural networks: theory and applications*. John Wiley & Sons, Inc. New York, NY, USA, 1996.
- [24] Joshua S. Dillon, Adrian Liu, Christopher L. Williams, Jacqueline N. Hewitt, Max Tegmark, Edward H. Morgan, Alan M. Levine, Miguel F. Morales, Steven J. Tingay, and Gianni Bernardi. Overcoming real-world obstacles in 21 cm power spectrum estimation: A method demonstration and results from early Murchison Widefield Array data. *PRD*, 89(2):023002, Jan 2014.
- [25] Joshua S. Dillon and Aaron R. Parsons. Redundant Array Configurations for 21 cm Cosmology. *ApJ*, 826(2):181, Aug 2016.
- [26] Aaron Ewall-Wice, Joshua S. Dillon, Adrian Liu, and Jacqueline Hewitt. The impact of modelling errors on interferometer calibration for 21 cm power spectra. *MNRAS*, 470(2):1849–1870, Sep 2017.
- [27] Liron Gleser, Adi Nusser, and Andrew J. Benson. Decontamination of cosmological 21-cm maps. *MNRAS*, 391(1):383–398, Nov 2008.
- [28] Geraint Harker, Saleem Zaroubi, Gianni Bernardi, Michiel A. Brentjens, A. G. de Bruyn, Benedetta Ciardi, Vibor Jelić, Leon V. E. Koopmans, Panagiotis Labropoulos, and Garrelt Mellema. Non-parametric foreground subtraction for 21-cm epoch of reionization experiments. *MNRAS*, 397(2):1138–1152, Aug 2009.
- [29] Bryna J. Hazelton, Miguel F. Morales, and Ian S. Sullivan. The Fundamental Multi-baseline Mode-mixing Foreground in 21 cm Epoch of Reionization Observations. *ApJ*, 770(2):156, Jun 2013.
- [30] Richard Hills, Girish Kulkarni, P. Daniel Meerburg, and Ewald Puchwein. Concerns about modelling of the EDGES data. *Nature*, 564(7736):E32–E34, Dec 2018.
- [31] N. Hurley-Walker, J. R. Callingham, P. J. Hancock, T. M. O. Franzen, L. Hindson, A. D. Kapińska, J. Morgan, A. R. Offringa, R. B. Wayth, C. Wu, Q. Zheng, T. Murphy, M. E. Bell, K. S. Dwarakanath, B. For, B. M. Gaensler, M. Johnston-Hollitt, E. Lenc, P. Procopio, L. Staveley-Smith, R. Ekers, J. D. Bowman, F. Briggs, R. J. Cappallo, A. A. Deshpande, L. Greenhill, B. J. Hazelton, D. L. Kaplan, C. J. Lonsdale, S. R. McWhirter, D. A. Mitchell, M. F. Morales, E. Morgan, D. Oberoi, S. M. Ord, T. Prabu, N. Udaya Shankar, K. S. Srivani, R. Subrahmanyan, S. J. Tingay, R. L. Webster, A. Williams, and C. L. Williams. GaLactic and Extragalactic All-sky Murchison Widefield Array (GLEAM) survey - I. A low-frequency extragalactic catalogue. *MNRAS*, 464(1):1146–1167, Jan 2017.

- [32] Aapo Hyvärinen. Fast and robust fixed-point algorithms for independent component analysis. *IEEE transactions on Neural Networks*, 10(3):626–634, 1999.
- [33] Aapo Hyvärinen, Juha Karhunen, and Erkki Oja. *Independent component analysis*, volume 46. John Wiley & Sons, 2004.
- [34] V. Jelić, S. Zaroubi, P. Labropoulos, R. M. Thomas, G. Bernardi, M. A. Brentjens, A. G. de Bruyn, B. Ciardi, G. Harker, L. V. E. Koopmans, V. N. Pandey, J. Schaye, and S. Yatawatta. Foreground simulations for the LOFAR-epoch of reionization experiment. *MNRAS*, 389(3):1319–1335, Sep 2008.
- [35] Hannes Jensen, Suman Majumdar, Garrelt Mellema, Adam Lidz, Ilian T. Iliev, and Keri L. Dixon. The wedge bias in reionization 21-cm power spectrum measurements. *MNRAS*, 456(1):66–70, Feb 2016.
- [36] Ronniy C. Joseph, Cathryn M. Trott, and Randall B. Wayth. The Bias and Uncertainty of Redundant and Sky-based Calibration Under Realistic Sky and Telescope Conditions. *AJ*, 156(6):285, Dec 2018.
- [37] W. Li, J. C. Pober, B. J. Hazelton, N. Barry, M. F. Morales, I. Sullivan, A. R. Parsons, Z. S. Ali, J. S. Dillon, and A. P. Beardsley. Comparing Redundant and Sky-model-based Interferometric Calibration: A First Look with Phase II of the MWA. *ApJ*, 863(2):170, Aug 2018.
- [38] Weitian Li, Haiguang Xu, Zhixian Ma, Ruimin Zhu, Dan Hu, Zhenghao Zhu, Junhua Gu, Chenxi Shan, Jie Zhu, and Xiang-Ping Wu. Separating the EoR signal with a convolutional denoising autoencoder: a deep-learning-based method. *MNRAS*, 485(2):2628–2637, May 2019.
- [39] Adrian Liu, Aaron R. Parsons, and Cathryn M. Trott. Epoch of reionization window. I. Mathematical formalism. *PRD*, 90(2):023018, Jul 2014.
- [40] Adrian Liu, Aaron R. Parsons, and Cathryn M. Trott. Epoch of reionization window. II. Statistical methods for foreground wedge reduction. *PRD*, 90(2):023019, Jul 2014.
- [41] Adrian Liu, Max Tegmark, Judd Bowman, Jacqueline Hewitt, and Matias Zaldarriaga. An improved method for 21-cm foreground removal. *MNRAS*, 398(1):401–406, Sep 2009.
- [42] Adrian Liu, Max Tegmark, and Matias Zaldarriaga. Will point sources spoil 21-cm tomography? *MNRAS*, 394(3):1575–1587, Apr 2009.
- [43] Matthew McQuinn, Oliver Zahn, Matias Zaldarriaga, Lars Hernquist, and Steven R. Furlanetto. Cosmological Parameter Estimation Using 21 cm Radiation from the Epoch of Reionization. *ApJ*, 653(2):815–834, Dec 2006.
- [44] F. G. Mertens, A. Ghosh, and L. V. E. Koopmans. Statistical 21-cm signal separation via Gaussian Process Regression analysis. *MNRAS*, 478(3):3640–3652, Aug 2018.

- [45] D. A. Mitchell, L. J. Greenhill, R. B. Wayth, R. J. Sault, C. J. Lonsdale, R. J. Cappallo, M. F. Morales, and S. M. Ord. Real-Time Calibration of the Murchison Widefield Array. *IEEE Journal of Selected Topics in Signal Processing*, 2:707–717, November 2008.
- [46] Miguel F. Morales, Judd D. Bowman, and Jacqueline N. Hewitt. Improving Foreground Subtraction in Statistical Observations of 21 cm Emission from the Epoch of Reionization. *ApJ*, 648(2):767–773, Sep 2006.
- [47] Miguel F. Morales, Bryna Hazelton, Ian Sullivan, and Adam Beardsley. Four Fundamental Foreground Power Spectrum Shapes for 21 cm Cosmology Observations. *ApJ*, 752(2):137, Jun 2012.
- [48] Miguel F. Morales and Jacqueline Hewitt. Toward Epoch of Reionization Measurements with Wide-Field Radio Observations. *ApJ*, 615(1):7–18, Nov 2004.
- [49] C. D. Nunhokee, G. Bernardi, S. A. Kohn, J. E. Aguirre, N. Thyagarajan, J. S. Dillon, G. Foster, T. L. Grobler, J. Z. E. Martinot, and A. R. Parsons. Constraining Polarized Foregrounds for EoR Experiments. II. Polarization Leakage Simulations in the Avoidance Scheme. *ApJ*, 848(1):47, Oct 2017.
- [50] A. R. Offringa, F. Mertens, and L. V. E. Koopmans. The impact of interference excision on 21-cm epoch of reionization power spectrum analyses. *MNRAS*, 484(2):2866–2875, Apr 2019.
- [51] A. R. Offringa, C. M. Trott, N. Hurley-Walker, M. Johnston-Hollitt, B. McKinley, N. Barry, A. P. Beardsley, J. D. Bowman, F. Briggs, and P. Carroll. Parametrizing Epoch of Reionization foregrounds: a deep survey of low-frequency point-source spectra with the Murchison Widefield Array. *MNRAS*, 458(1):1057–1070, May 2016.
- [52] A. R. Offringa, J. J. van de Gronde, and J. B. T. M. Roerdink. A morphological algorithm for improving radio-frequency interference detection. *A&A*, 539:A95, Mar 2012.
- [53] A. R. Offringa, R. B. Wayth, N. Hurley-Walker, D. L. Kaplan, N. Barry, A. P. Beardsley, M. E. Bell, G. Bernardi, J. D. Bowman, F. Briggs, J. R. Callingham, R. J. Cappallo, P. Carroll, A. A. Deshpande, J. S. Dillon, K. S. Dwarakanath, A. Ewall-Wice, L. Feng, B. Q. For, B. M. Gaensler, L. J. Greenhill, P. Hancock, B. J. Hazelton, J. N. Hewitt, L. Hindson, D. C. Jacobs, M. Johnston-Hollitt, A. D. Kapińska, H. S. Kim, P. Kittiwisit, E. Lenc, J. Line, A. Loeb, C. J. Lonsdale, B. McKinley, S. R. McWhirter, D. A. Mitchell, M. F. Morales, E. Morgan, J. Morgan, A. R. Neben, D. Oberoi, S. M. Ord, S. Paul, B. Pindor, J. C. Pober, T. Prabu, P. Procopio, J. Riding, N. Udaya Shankar, S. Sethi, K. S. Srivani, L. Staveley-Smith, R. Subrahmanyan, I. S. Sullivan, M. Tegmark, N. Thyagarajan, S. J. Tingay, C. M. Trott, R. L. Webster, A. Williams, C. L. Williams, C. Wu, J. S. Wyithe, and Q. Zheng. The Low-Frequency Environment of the Murchison Widefield Array: Radio-Frequency Interference Analysis and Mitigation. *PASA*, 32:e008, Mar 2015.

- [54] S. Peng Oh and Katherine J. Mack. Foregrounds for 21-cm observations of neutral gas at high redshift. *MNRAS*, 346(3):871–877, Dec 2003.
- [55] Gregory Paciga, Tzu-Ching Chang, Yashwant Gupta, Rajaram Nityanada, Julia Odegova, Ue-Li Pen, Jeffrey B. Peterson, Jayanta Roy, and Kris Sigurdson. The GMRT Epoch of Reionization experiment: a new upper limit on the neutral hydrogen power spectrum at  $z \approx 8.6$ . *MNRAS*, 413(2):1174–1183, May 2011.
- [56] Aaron Parsons, Jonathan Pober, Matthew McQuinn, Daniel Jacobs, and James Aguirre. A Sensitivity and Array-configuration Study for Measuring the Power Spectrum of 21 cm Emission from Reionization. *ApJ*, 753(1):81, Jul 2012.
- [57] Aaron R. Parsons and Donald C. Backer. Calibration of Low-Frequency, Wide-Field Radio Interferometers Using Delay/Delay-Rate Filtering. *AJ*, 138(1):219–226, Jul 2009.
- [58] Aaron R. Parsons, Donald C. Backer, Griffin S. Foster, Melvyn C. H. Wright, Richard F. Bradley, Nicole E. Gugliucci, Chaitali R. Parashare, Erin E. Benoit, James E. Aguirre, and Daniel C. Jacobs. The Precision Array for Probing the Epoch of Re-ionization: Eight Station Results. *AJ*, 139(4):1468–1480, Apr 2010.
- [59] Aaron R. Parsons, Jonathan C. Pober, James E. Aguirre, Christopher L. Carilli, Daniel C. Jacobs, and David F. Moore. A Per-baseline, Delay-spectrum Technique for Accessing the 21 cm Cosmic Reionization Signature. *ApJ*, 756(2):165, Sep 2012.
- [60] A. H. Patil, S. Yatawatta, L. V. E. Koopmans, A. G. de Bruyn, M. A. Brentjens, S. Zaroubi, K. M. B. Asad, M. Hatef, V. Jelić, and M. Mevius. Upper Limits on the 21 cm Epoch of Reionization Power Spectrum from One Night with LOFAR. *ApJ*, 838(1):65, Mar 2017.
- [61] Ajinkya H. Patil, Sarod Yatawatta, Saleem Zaroubi, Léon V. E. Koopmans, A. G. de Bruyn, Vibor Jelić, Benedetta Ciardi, Ilian T. Iliev, Maaijke Mevius, and Vishambhar N. Pandey. Systematic biases in low-frequency radio interferometric data due to calibration: the LOFAR-EoR case. *MNRAS*, 463(4):4317–4330, Dec 2016.
- [62] Planck Collaboration. Planck 2018 results. iv. diffuse component separation. *A&A*, 2019.
- [63] Planck Collaboration, Y. Akrami, F. Arroja, M. Ashdown, J. Aumont, C. Baccigalupi, M. Ballardini, A. J. Banday, R. B. Barreiro, and N. Bartolo. Planck 2018 results. I. Overview and the cosmological legacy of Planck. *arXiv e-prints*, page arXiv:1807.06205, Jul 2018.
- [64] Jonathan C. Pober, Aaron R. Parsons, James E. Aguirre, Zaki Ali, Richard F. Bradley, Chris L. Carilli, Dave DeBoer, Matthew Dexter, Nicole E. Gugliucci, and Daniel C. Jacobs. Opening the 21 cm Epoch of Reionization Window: Measurements of Foreground Isolation with PAPER. *ApJ*, 768(2):L36, May 2013.

- [65] Jayanti Prasad and Jayaram Chengalur. FLAGCAL: a flagging and calibration package for radio interferometric data. *Experimental Astronomy*, 33(1):157–171, Mar 2012.
- [66] P. Procopio, R. B. Wayth, J. Line, C. M. Trott, H. T. Intema, D. A. Mitchell, B. Pindor, J. Riding, S. J. Tingay, and M. E. Bell. A High-Resolution Foreground Model for the MWA EoR1 Field: Model and Implications for EoR Power Spectrum Analysis. *PASA*, 34:e033, Aug 2017.
- [67] Mário G. Santos, Asantha Cooray, and Lloyd Knox. Multifrequency Analysis of 21 Centimeter Fluctuations from the Era of Reionization. *ApJ*, 625(2):575–587, Jun 2005.
- [68] Saurabh Singh, Ravi Subrahmanyan, N. Udaya Shankar, Mayuri Sathyanaarayana Rao, Anastasia Fialkov, Aviad Cohen, Rennan Barkana, B. S. Girish, A. Raghunathan, and R. Somashekar. SARAS 2 Constraints on Global 21 cm Signals from the Epoch of Reionization. *ApJ*, 858(1):54, May 2018.
- [69] I. S. Sullivan, M. F. Morales, B. J. Hazelton, W. Arcus, D. Barnes, G. Bernardi, F. H. Briggs, J. D. Bowman, J. D. Bunton, R. J. Cappallo, B. E. Corey, A. Deshpande, L. deSouza, D. Emrich, B. M. Gaensler, R. Goeke, L. J. Greenhill, D. Herne, J. N. Hewitt, M. Johnston-Hollitt, D. L. Kaplan, J. C. Kasper, B. B. Kincaid, R. Koenig, E. Kratzenberg, C. J. Lonsdale, M. J. Lynch, S. R. McWhirter, D. A. Mitchell, E. Morgan, D. Oberoi, S. M. Ord, J. Pathikulangara, T. Prabu, R. A. Remillard, A. E. E. Rogers, A. Roshi, J. E. Salah, R. J. Sault, N. Udaya Shankar, K. S. Srivani, J. Stevens, R. Subrahmanyan, S. J. Tingay, R. B. Wayth, M. Waterson, R. L. Webster, A. R. Whitney, A. Williams, C. L. Williams, and J. S. B. Wyithe. Fast Holographic Deconvolution: A New Technique for Precision Radio Interferometry. *ApJ*, 759:17, November 2012.
- [70] A. Richard Thompson, James M. Moran, and Jr. Swenson, George W. *Interferometry and Synthesis in Radio Astronomy, 2nd Edition*. Wiley-Interscience, 2001.
- [71] Nithyanandan Thyagarajan, Daniel C. Jacobs, Judd D. Bowman, N. Barry, A. P. Beardsley, G. Bernardi, F. Briggs, R. J. Cappallo, P. Carroll, and A. A. Deshpande. Confirmation of Wide-field Signatures in Redshifted 21 cm Power Spectra. *ApJ*, 807(2):L28, Jul 2015.
- [72] Nithyanandan Thyagarajan, N. Udaya Shankar, Ravi Subrahmanyan, Wayne Arcus, Gianni Bernardi, Judd D. Bowman, Frank Briggs, John D. Bunton, Roger J. Cappallo, and Brian E. Corey. A Study of Fundamental Limitations to Statistical Detection of Redshifted H I from the Epoch of Reionization. *ApJ*, 776(1):6, Oct 2013.
- [73] C. M. Trott, B. Pindor, P. Procopio, R. B. Wayth, D. A. Mitchell, B. McKinley, S. J. Tingay, N. Barry, A. P. Beardsley, and G. Bernardi. CHIPS: The Cosmological H I Power Spectrum Estimator. *ApJ*, 818(2):139, Feb 2016.
- [74] Cathryn M. Trott, Randall B. Wayth, and Steven J. Tingay. The Impact of Point-source Subtraction Residuals on 21 cm Epoch of Reionization Estimation. *ApJ*, 757(1):101, Sep 2012.

- [75] D. Tulone and S. Madden. PAQ: Time Series Forecasting for Approximate Query Answering in Sensor Networks. In *Proceedings of the 3rd European Workshop on Wireless Sensor Networks*, pages 21–37. Springer, 2006.
- [76] Harish Vedantham, N. Udaya Shankar, and Ravi Subrahmanyam. Imaging the Epoch of Reionization: Limitations from Foreground Confusion and Imaging Algorithms. *ApJ*, 745(2):176, Feb 2012.
- [77] Jingying Wang, Haiguang Xu, Tao An, Junhua Gu, Xueying Guo, Weitian Li, Yu Wang, Chengze Liu, Olivier Martineau-Huynh, and Xiang-Ping Wu. Exploring the Cosmic Reionization Epoch in Frequency Space: An Improved Approach to Remove the Foreground in 21 cm Tomography. *ApJ*, 763(2):90, Feb 2013.
- [78] Xiaomin Wang, Max Tegmark, Mário G. Santos, and Lloyd Knox. 21 cm Tomography with Foregrounds. *ApJ*, 650(2):529–537, Oct 2006.
- [79] Mark H. Wieringa. An investigation of the telescope based calibration methods ‘redundancy’ and ‘self-cal’. *Experimental Astronomy*, 2(4):203–225, Jul 1992.
- [80] S. Yatawatta, A. G. de Bruyn, M. A. Brentjens, P. Labropoulos, V. N. Pandey, S. Kazemi, S. Zaroubi, L. V. E. Koopmans, A. R. Offringa, and V. Jelić. Initial deep LOFAR observations of epoch of reionization windows. I. The north celestial pole. *A&A*, 550:A136, Feb 2013.
- [81] Sarod Yatawatta. Distributed radio interferometric calibration. *MNRAS*, 449(4):4506–4514, Jun 2015.
- [82] Matias Zaldarriaga, Steven R. Furlanetto, and Lars Hernquist. 21 Centimeter Fluctuations from Cosmic Gas at High Redshifts. *ApJ*, 608(2):622–635, Jun 2004.
- [83] Le Zhang, Emory F. Bunn, Ata Karakci, Andrei Korotkov, P. M. Sutter, Peter T. Timbie, Gregory S. Tucker, and Benjamin D. Wandelt. Bayesian Semi-blind Component Separation for Foreground Removal in Interferometric 21 cm Observations. *ApJS*, 222(1):3, Jan 2016.
- [84] H. Zheng, M. Tegmark, V. Buza, J. S. Dillon, H. Gharibyan, J. Hickish, E. Kunz, A. Liu, J. Losh, and A. Lutomirski. MITEoR: a scalable interferometer for precision 21 cm cosmology. *MNRAS*, 445(2):1084–1103, Dec 2014.

# Chapter 7

## Chapter title

**Author Name**

### Abstract

This chapter discusses some important things

### 7.1 A Section

Lorem ipsum dolor sit amet, consectetur adipiscing elit. Duis eu egestas erat. Maecenas tincidunt lacinia tincidunt. Mauris id lectus nec neque feugiat condimentum vitae at diam. In vel orci nunc, non commodo mauris. Vivamus ipsum enim, vulputate quis pharetra non, molestie quis felis. Vivamus porttitor placerat turpis at accumsan. Nunc tortor velit, faucibus a rhoncus nec, blandit non elit. Nam consectetur lectus eu nisi blandit dapibus rhoncus dui tempus. Mauris fermentum dolor vel ipsum vulputate sit amet ultricies tortor lacinia. Donec ut nibh erat. Morbi nec mi ante. Integer nec vestibulum diam. Donec tincidunt pellentesque quam, ut interdum mauris venenatis condimentum. Nam condimentum, augue in aliquet gravida, neque dui elementum eros, id semper eros purus sed felis. Curabitur in justo sit amet sapien ultrices hendrerit at quis nibh. Quisque iaculis pulvinar tincidunt.

$$\begin{aligned} C(12) &= \left[ \vec{\pi} \cdot \vec{\phi}(x+r) \right] \\ &\approx 1 - \text{const} \frac{r^2}{L^2} \int_r^L \frac{x \, dx}{x^2} + \dots \\ &\approx 1 - \text{const} \frac{r^2}{L^2} \ln \frac{x \, dx}{x^2} + \dots \end{aligned} \tag{7.1}$$

Aenean tellus risus, porta sit amet porta vitae, tincidunt ut felis. Class aptent taciti sociosqu ad litora torquent per conubia nostra, per inceptos himenaeos. Vestibulum ante ipsum primis in faucibus orci luctus et ultrices posuere cubilia Curae; Phasellus pulvinar placerat velit auctor egestas. Vivamus euismod fringilla tincidunt. Sed ut magna felis, id sollicitudin nunc. Quisque a dui eu erat consectetur egestas a quis justo. Aenean euismod congue diam, vel posuere urna fermentum sit amet. Lorem ipsum dolor sit amet, consectetur adipiscing



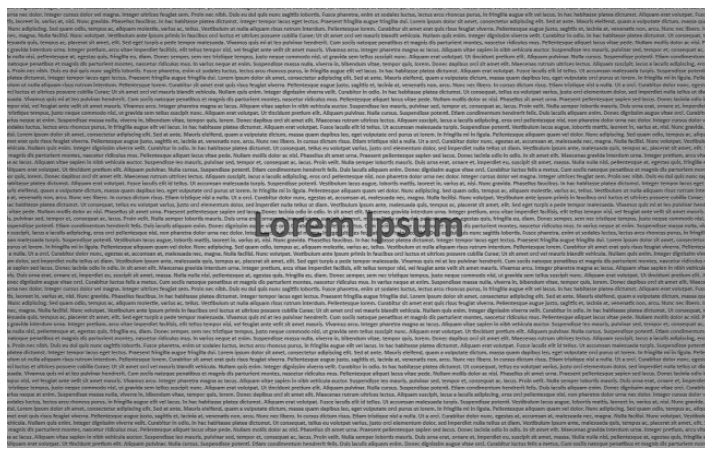


Figure 7.2: This is figure 2 in chapter 1.

# Bibliography

- [1] KI Diamantaras and SY Kung. *Principal component neural networks: theory and applications*. John Wiley & Sons, Inc. New York, NY, USA, 1996.
- [2] D. Tulone and S. Madden. PAQ: Time Series Forecasting for Approximate Query Answering in Sensor Networks. In *Proceedings of the 3rd European Workshop on Wireless Sensor Networks*, pages 21–37. Springer, 2006.

# Chapter 8

## Status of 21 cm interferometric experiments

Cathryn M. Trott (ICRAR-Curtin), Jonathan Pober (Brown University)

### Abstract

Interferometric experiments of the reionization era offer the advantages of measuring power in spatial modes with increased sensitivity afforded by multiple independent sky measurements. Here we review early work to measure this signal, current experiments, and future opportunities, highlighting the lessons learned along the way that have shaped the research field and experimental design. In particular, this chapter discusses the history, progress, challenges and forecasts for detection and exploration of the spatial structure of the 21 cm brightness temperature signal in the Epoch of Reionisation using interferometric experiments. We discuss GMRT, PAPER, LOFAR, MWA, and the future HERA and SKA.

### 8.1 Introduction

Because they provide both rapid mapping speed and good angular resolution, interferometers have become the preferred instrument for experiments looking to measure the expected spatial fluctuations in the 21 cm signal. The current instruments hosting such experiments include the Murchison Widefield Array, MWA<sup>1</sup> [17, 115, 52]; the Precision Array for Probing the Epoch of Reionization, PAPER<sup>2</sup> [94]; the LOw Frequency ARray, LOFAR<sup>3</sup> [124, 100]; and the Long Wavelength Array, LWA<sup>4</sup> [36]. In the future, we expect the Hydrogen Epoch Reionization Array, HERA [31] and the Square Kilometre Array, SKA-Low [65]. Sensitivity predictions for most of the current experiments (e.g. [11, 103]) find that they will not be capable of achieving the necessary signal-to-noise to image the 21 cm signal directly (although

---

<sup>1</sup><http://www.mwatelescope.org>

<sup>2</sup><http://eor.berkeley.edu>

<sup>3</sup><http://www.lofar.org>

<sup>4</sup><http://lwa.unm.edu>

see [134] for a study with LOFAR). As such, most of these experiments are targeting a detection of the 21 cm power spectrum, which can be constrained with higher signal-to-noise compared with an image because the isotropy and homogeneity of the Universe allows the 3D  $k$ -space power spectrum to be averaged over spherical shells of constant  $|k|$ . Even using the power spectrum, typical predictions for the requisite observing time are of order 1,000 hours (see Figure 8.1).

However, beyond the need to achieve the requisite sensitivity, experiments are faced with the daunting task of isolating the 21 cm signal from foregrounds that can be up to five orders of magnitude brighter. While the two can, in principle, be separated by their distinct spectral behavior, the inherently frequency-dependent response of radio interferometers complicates the picture significantly. In this chapter, we review the challenges faced by current interferometric 21 cm experiments as well as the progress to-date in overcoming them. The detailed structure of this chapter is as follows. In §8.2, we present the history of experiments and techniques that led to the design of current 21 cm experiments. In §8.3, we discuss the distinct approaches each experiment has developed to overcome the challenges associated with these observations, and in §8.4 we review the current published upper limits on the 21 cm signal strength from these experiments. In §8.5, we highlight the currently unsolved problems at the forefront of experimental 21 cm cosmology and conclude in §8.6 with a discussion of the potential for both current and future experiments to overcome them.

## 8.2 Early work

The origins of the approaches that current experiments are taking to detect the Epoch of Reionization power spectrum can be traced to the development of radio interferometry observational techniques and Cosmic Microwave Background (CMB) analysis methodology.

Radio interferometers measure the cross-correlation of voltages detected with two antennas, extracting the sky signal in a complex-valued dataset that encodes sky emission location and intensity, and as a function of antenna separation vector and frequency [113]. For small field-of-view instruments (large antenna aperture), the measured signal is well-approximated as the 2D Fourier Transform of the sky brightness, attenuated by the antenna response function (the primary beam).

Motivated by analysis of CMB datasets in the 1990s and 2000s, and the curved nature of full-sky imaging, early discussion of power spectrum estimators used spherical harmonic basis functions to describe the signal and extract optimal estimators [112]. CMB studies suffer from some of the challenges faced also by EoR experiments: wide fields-of-view, low sensitivity, limited angular resolution, and foreground contamination. Unlike EoR, which is an evolving signal in redshift space, CMB studies are single frequency experiments focussed on angular statistics. As such, the foreground mitigation and treatment approaches of CMB studies are of limited use for EoR studies, which attempt to separate foregrounds from the 21 cm signal using the frequency axis. Nonetheless, the fundamental need to extract a weak signal from complex and highly-contaminated data is shared between the two fields, and Tegmark used this experience to apply CMB analysis techniques to early EoR methodology development. Since an interferometer natively measures in Fourier space, there was a transition from the natural basis of curved sky functions (spherical harmonics) to the inter-

ferometer measurement space (Fourier modes) in discussion of optimal estimators for EoR science [73].

This work was supported by groundwork laid out for doing EoR power spectra with radio interferometers, including cosmological and unit conversions [81, 94] and noise considerations for astrophysical parameter estimation with specific future experiments [76]. McQuinn and colleagues discussed a simple foreground model where fitting of a smooth spectral function could remove their effect cleanly, focussing on array sensitivity as the limiting factor for future experiments. However, the lack of any real-world experiments attempting the detection meant they failed to realise the extent of foreground spectral contamination.

More sophisticated approaches to foreground modelling and mitigation appeared in the mid-2000s, with [19] beginning a set of papers that explored the signature of smooth spectrum sources in the EoR power spectrum parameter space. Initially, low-order polynomials were explored to fit and remove these sources. However, lacking a physical motivation for this functional form to robustly separate foregrounds from cosmological signal, polynomials were replaced with more realistic functions. Ultimately, the likelihood of removing not only foregrounds but also cosmological signal when fitting and subtracting models, particularly considering the large difference in magnitude of the two signals, has steered the research field away from this approach to foreground mitigation.

As part of this better appreciation for the impact of foregrounds, particularly with the knowledge that they are used also for data calibration, [29] explored the required accuracy of source models such that foregrounds may be subtracted to a level sufficient to detect the EoR. This work was the first to show the characteristic wedge in power spectrum parameter space, a triangular region in angular and line-of-sight wavenumber space representing the signature of smooth-spectrum sources observed with an interferometer.

### 8.3 Experimental methodologies and current experiments

In this section we introduce the different instruments that have previously taken, or currently are taking and analysing, data for an interferometric EoR experiment. We start by presenting the relevant parameters of the telescopes that these experiments use, highlighting and motivating the different observational and analysis approaches taken by each. Table 8.3 lists the location (including latitude), frequency (redshift) range, number of stations/antennas, station diameters, and maximum baseline, and field-of-view at 150 MHz for the relevant instruments. Italicised telescopes are discussed in this Chapter. We also plot the full uncertainties (including sample variance) for a 1000 hour observation at  $z=8.5$  (10 MHz bandwidth) for each experiment as a function of spatial wavenumber in Figure 8.1. We uniformly assume that the modes within the horizon are inaccessible due to foreground contamination, and note that this is a broad assumption that is not applicable to all experiments. Note also that MWA’s and HERA’s large fields-of-view gives them access to smaller wavenumbers. This figure also includes a nominal signal strength (black, 21cmFAST, [78]), but this level is highly uncertain. The proximity of the curves to this line highlights the difficulty with predicting the real sensitivity of experiments, particularly in light of the large number of observing hours required to reach an expected detection. The parameters shown in the table, and the curves shown in Figure 8.1 motivate and frame the discussion of different experiments in the follow-

Facility	Location (Latitude)	Freq. [MHz] ( $z$ )	$N_{\text{ant}}$	Max. baseline	$\text{FOV}_{150}$
<i>GMRT</i>	India ( $19.1^{\circ}\text{N}$ )	150–300 (3.7–8.5)	30	30 km	$2.5^{\circ}$
<i>MWA</i>	Australia ( $26.5^{\circ}\text{S}$ )	70–90, 135–195 (15–19, 6–10)	128	5 km	$25^{\circ}$
<i>LOFAR</i>	Netherlands ( $52.9^{\circ}\text{N}$ )	30–80, 120–190 (17–46, 6–11)	50–60	50 km	$5^{\circ}$
<i>PAPER</i>	South Africa ( $30.6^{\circ}\text{S}$ )	110–180 (7–12)	32–64	210 m	$60^{\circ}$
<i>LEDA</i> <sup>1</sup>	USA ( $34^{\circ}\text{N}$ )	45–88 (15–30)	256+	<10 km	$70^{\circ}$
21CMA	China ( $42^{\circ}\text{N}$ )	50–200 (6–27)	81	6 km	$10^{\circ}$

Table 8.1: General parameters for the telescopes undertaking interferometric observations of the Cosmic Dawn and EoR. Italicised telescopes are discussed in this Chapter. <sup>1</sup>LEDA is a total power experiment using interferometry for data calibration.

ing sections. Experiments are forced to undertake different approaches to observations and data analysis, because the physical limitations of the systems promote different systematic errors into the forefront for each experiment. There is no silver bullet telescope for undertaking this experiment, however, and after reviewing the main experiments, we discuss the pros and cons of different features.

### 8.3.1 Giant Metrewave Radio Telescope - GMRT

The GMRT [111] is a Y-shaped array of 30 45 m dishes spread over 25 km in western India. Operating between 50 MHz and 1420 MHz, its 153 MHz receiver has been most used for Reionization studies. Motivated by early work in the post-reionization era (325 MHz and 610 MHz receivers) to statistically detect 21 cm fluctuations and understand the foreground contamination to these data, the low frequency receiver opens the door to exploring the Reionization era. The methodology developed has focused on angular power spectra, measured at a range of frequencies, and pioneered much of the early work to use spectral correlation of foregrounds as a way of treating them. With a lack of short baselines and poor instantaneous *uv*-coverage (Figure 8.2), the array is suited to building high resolution foreground models, and computing the foreground angular correlation function ([107]).

GMRT work has largely utilised the visibility correlation function, which cross-correlates visibilities to study the spectral and spatial structure of the sky. Visibility correlation functions were also explored for 21CMA analysis [136]. Unlike other experiments, which have cross-correlated interleaved time samples to remove noise power bias, GMRT has usually opted for cross-correlating visibilities from adjacent frequency channels. This has different systematics, with finer spectral resolution required to minimise visibility decorrelation.

During the 2000s, there was a series of papers developing a formalism for use of this visibility correlation function to measure angular modes. [14] introduced a cross-visibility angular correlation function to measure HI fluctuations post-reionization. [15] then related the cross-visibility correlation function across baselines and frequencies to the power spectrum of brightness temperature fluctuations, presenting the full formalism and expected results in different epochs. They suggest that the cosmological is uncorrelated for frequency channel differences larger than 1 MHz, allowing signal to be ‘easily distinguished from the continuum sources of contamination’. [4] then extended this formalism to model the expected

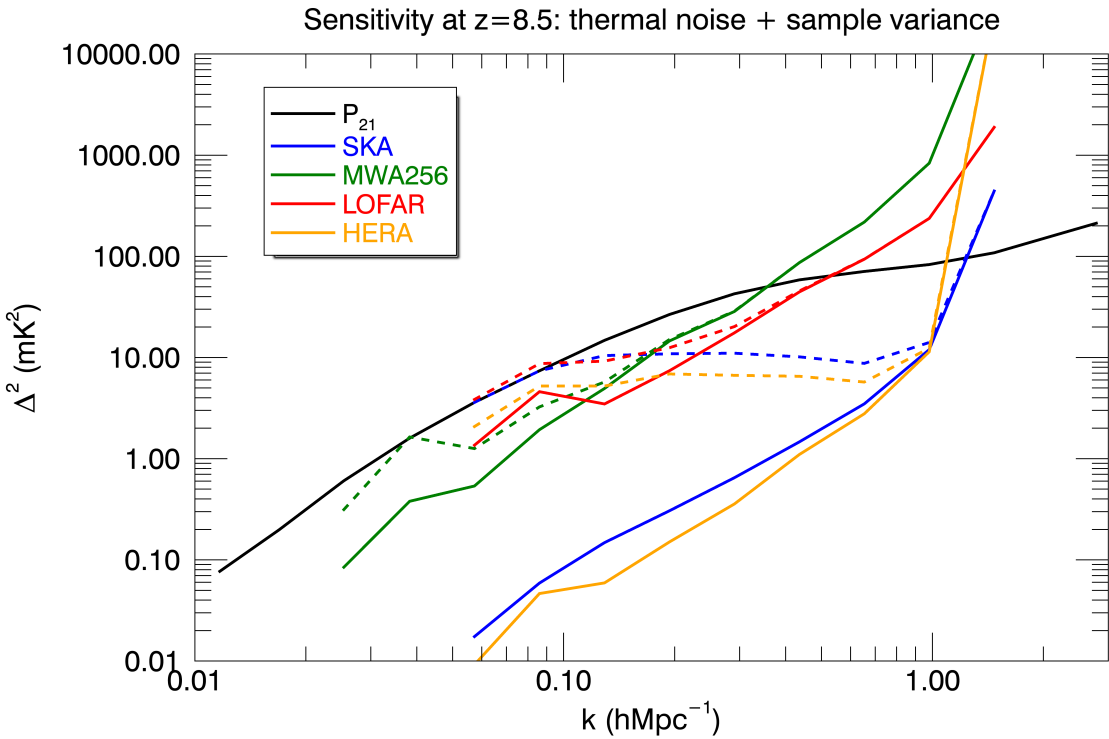


Figure 8.1: Estimated total uncertainty on the dimensionless power spectrum for a 1000 hour observation with several experiments at  $z=8.5$  compared with a model input power spectrum (21cmFAST,[78]), and assuming that modes within the horizon are inaccessible. Solid lines are only thermal noise uncertainty, while dashed lines include sample variance. (Black) Model cosmological signal; (blue) SKA; (green) MWA256; (red) LOFAR; (orange) HERA.

foreground continuum signatures in the cross-correlation visibility space, and compared with GMRT observations. Their results were hindered by calibration errors, which caused decorrelation of the signal over frequency, but presented the first application of this technique to data. [30] provided an extension of the visibility cross-correlation approach to estimating power spectra to a multi-frequency angular power spectrum (MAPS), utilising decorrelation of signals over frequency to extract information about bubble sizes and distributions as a function of redshift while suppressing the effects of foreground contamination.

[41] published the first measurement of post-reionization neutral hydrogen fluctuations with GMRT (HI intensity mapping) at  $z=1.32$  (610 MHz) and using the MAPS formalism. They used a fourth-order polynomial to remove smooth foregrounds, in line with early attempts with many experiments to fit a parametric function without physical motivation. [42] then demonstrated improved foreground removal for 610 MHz observations by tapering the primary beam function and reducing sidelobes; [44] further extended the work to the reionization epoch using 150 MHz observations to characterize the foregrounds with the MAPS formalism.

Using an alternative analysis to the MAPS formalism, [92] analysed 50h of data at

$z=8.6$  with a simple piecewise linear foreground subtraction method and cross-correlation of foreground-subtracted images. The result was a reported upper limit on the 21 cm signal strength of  $(70 \text{ mK})^2$ . However, [91] re-analysed the data with a more sophisticated foreground subtraction technique, including a calculation of signal loss due to foreground fitting. The result was an increase in the upper limit to  $(248 \text{ mK})^2$ , indicative of the degree to which signal loss can affect results.

More recently, [26] published a series of papers introducing and exploring the use of two new optimised power spectrum estimators using visibility correlations: the Tapered Gridded Estimator (TGE) and Bare Estimator (BE). The key concept for the TGE, which has been further discussed in the literature in subsequent papers [27], is to use a Fourier beam gridding kernel that is larger than the physical beam kernel, thereby decorrelating sources at the edge of the field-of-view. Note that this approach is not a silver bullet to removing the effect of horizon sources, because their sidelobes remain in the data even if they have been attenuated. Originally developed as angular power spectra as a function of frequency, the TGE work has recently been expanded to use the line-of-sight spatial information [16]. The BE directly squares adjacent visibilities to provide individual measurements of the power, but this has not been used further, possibly due to the large number of visibilities that are accumulated and stored.

Additionally to power spectra, [108] predicted the amplitude of a bispectrum signal with GMRT using its shortest baselines by modelling non-linear clustering. They predicted the signal strength to be comparable to the power spectrum and detectable in 100 hours but this project has not been explored observationally with this instrument.

### 8.3.2 Murchison Widefield Array - MWA

The Murchison Widefield Array (MWA) is a 256-element interferometer in the Western Australian desert. In Phase I of the array, operating from 2013–2016, it was composed of 128 tiles of 16 dual-polarization dipoles, spread over 3 km [115]. Phase II (2016–) expanded the array to 256 tiles, with longer baselines for improved survey science and sky model building (5 km), and two hexagonal sub-arrays of 36 tiles with short spacings available for redundant calibration and improved EoR sensitivity [126]. It operates in two distinct modes: Extended Array (128 tiles with long baselines), and Compact Array (128 tiles with short baselines including two 36-tile redundant subarrays in a hexagonal configuration). The Compact Array is principally used for EoR science (see Figure 8.3). The MWA is a general science telescope, with multiple science goals [17]. As such, it balances high surface brightness sensitivity on EoR scales, redundant and non-redundant elements, and longer baselines for good imaging capabilities. The instantaneous *uv*-coverage of the MWA is excellent, allowing for science-quality snapshot imaging (2-minute). The MWA is also a wide-field instrument, with a field-of-view of 25 degrees at 150 MHz. This wide field-of-view, combined with the complex frequency-dependent shape of the aperture array primary beam, and analogue electronics, create challenges for data analysis. The two-stage analogue beamformer produces a frequency bandpass that contains 24 coarse channels over a 30.72 MHz bandwidth (chosen from the full bandwidth listed in Table 8.3), with missing regular channels between the coarse bands. This instrumental spectral structure provides a challenge to producing instrumentally-clean output EoR datasets.

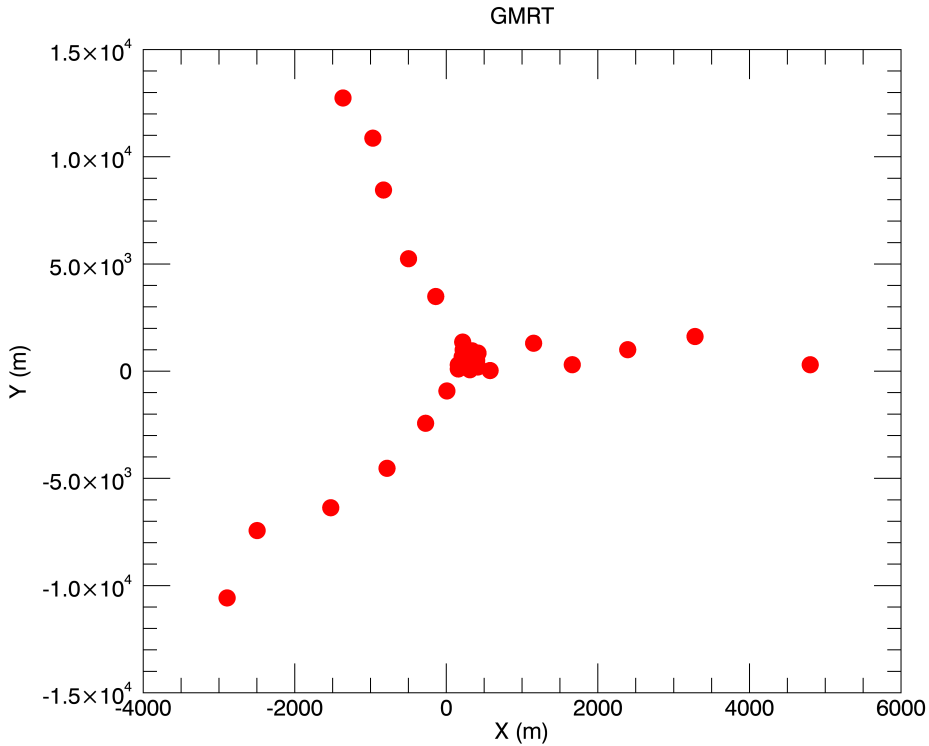


Figure 8.2: Array configuration for the GMRT: thirty 45 m dishes spread over 30 km.

Early deployments of the array, with 32 tiles, were used for preliminary science, and to begin to survey the EoR fields [128]. Upon completion of the 128 tiles, the MWA Commissioning Survey provided the first sky catalogue for use for calibration of EoR data [49]. This work paved the way for the GLEAM survey [125] and catalogue [48], yielding 300,000 sources in the southern sky. GLEAM provides the basis for the current sky model for point sources in EoR observations, augmented by individual models for extended sources.

In line with developments in concurrent experiments, prior to data acquisition the MWA EoR collaboration focused on relatively simplistic foreground fitting and removal methods, but with an increasing understanding of the signature of smooth-spectrum foregrounds in the wavenumber parameter space of an interferometer [19, 29, 118]. There are now two primary EoR data calibration and source subtraction pipelines used by the collaboration: the Real-Time System (RTS, [79]) and Fast Holographic Deconvolution (FHD, [110]). Both use underlying catalogues of sources that have been generated by cross-matching multiple low-frequency sky catalogues. PUMA [72] generates an observation-specific sky model of point sources and double sources [106], and includes shapelet-based and point source-based models for extended sources. The RTS calibrates the data in two steps, both of which rely on a weighted least-squares minimisation: (1) overall direction-independent (flux density and phase) calibration on a full model of 5,000 sources; (2) direction-dependent corrections along the line-of-sight to bright sources. The direction dependent corrections are then ap-

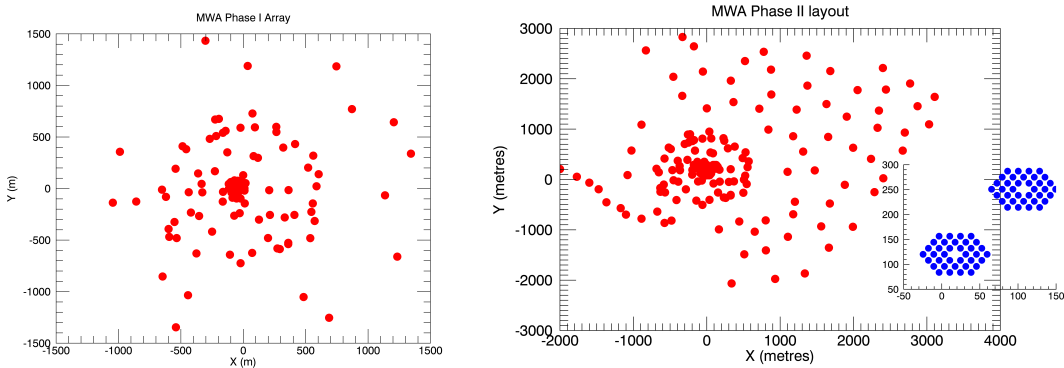


Figure 8.3: Array configurations for the MWA (Phase I, left; Phase II, right, including cutout of hexagonal subarrays (blue)): 128 (256) 4.4 m aperture array tiles spread over 3 (5) km.

plied to sources in the region of the fit, and the 5,000 source sky model is subtracted. FHD calibration [110] computationally optimizes the direction-dependent and wide-field imaging steps by pre-computing the mapping from Fourier to real space. FHD relies on an underlying point source sky model [21], which generates an observation-specific calibration model for  $>10,000$  sources based on the GLEAM catalogue and other cross-matched surveys.

Early developments of power spectrum pipelines stemmed from the inverse covariance quadratic estimator framework pioneered in CMB studies [112], and applied to theoretical EoR datasets by Liu & Tegmark in 2011 [73]. This work was further developed by Dillon in a series of papers that explored how to bridge some of the differences between the ideal estimator and a physical dataset [34, 33]. In particular, Dillon discussed missing data, and large data volumes. An adapted approach was then applied to three hours of MWA data, showing promising results [33].

One key feature of the optimal quadratic estimator formalism is the whitening of data according to the correlated covariance introduced by the uncertainty on residual foregrounds. This is effectively a down-weighting of data that are heavily affected by foregrounds, thereby improving signal-to-error. Subsequent analysis of a higher redshift dataset was used to estimate the principal eigenmodes of the data in spectral space, identifying these with bright foregrounds [34]. The covariances of these modes were then used in the estimator to down-weight and decorrelate data, yielding improved limits at  $z = 6.8$ . However, as with commensurate and subsequent work with PAPER that used this technique, it had the large potential to cause bias in the estimates. Re-use of the same dataset to empirically estimate the data covariance, and then fit for it, causes re-substitution bias, a well-known statistical effect where the performance of an estimator can appear much better than it actually is. In this work, Dillon was careful to estimate covariances empirically while omitting the  $uv$  cells in question, to avoid bias, however there was still limited information available in the remaining cells. Thus, although this work was careful to not try to subtract the foreground bias directly, use of the empirical covariance in the data weighting, and lack of a full end-to-end simulation to demonstrate no signal loss, makes this approach prone to large bias. It has not been used to analyze MWA data since the original analysis in [34].

In a later paper, describing the CHIPS estimator, Trott also developed an inverse co-

variance quadratic estimator formalism using a model foreground covariance [116]. Unlike the empirical approach of earlier work, this does not use the data itself to form the foreground covariance, but a model for the expected spatial and spectral structure of point source foregrounds. However this approach can suffer from similar effects, whereby error in the covariance can propagate into the analysis. Therefore, this inverse foreground covariance has never been applied to data used in publication due to the output’s sensitivity to the choice of foreground model.

A second principal power spectrum estimator for MWA EoR analysis,  $\epsilon$ psilon, was independently developed from CHIPS [9].  $\epsilon$ psilon prioritizes the propagation of thermal noise error from the visibilities (with estimates provided by FHD) through to the power spectrum while also providing a suite of diagnostics for assessing the performance of the estimator in a number of domains.

Both  $\epsilon$ psilon and CHIPS (without the foreground covariance weighting) were used in the EoR limit paper led by Beardsley [12], which processed 32 hours of MWA Phase I high-band data to power spectrum limits. At the time, these results were highly-competitive in the field, but the data were clearly still systematic-dominated. At a similar time, Ewall-Wice published the first measurement of upper limit from the Cosmic Dawn (Epoch of X-ray heating, EoX) from 3-hours of MWA data above  $z = 15$  [37].

One of the clear outcomes of the early upper limit publications from MWA (and other instruments, particularly LOFAR) was that the data were highly systematic-dominated in modes relevant for EoR, and accumulating more data into the power spectrum estimator would offer no advantage. With this realisation, the MWA collaboration embarked on a two year program to prioritize understanding and treating systematics over processing large datasets, despite more than a thousand hours having been collected by the instrument. This work encompassed (1) improving the sky model (point, extended and multiple sources, [106, 123]); (2) understanding the impact of calibration choices on residuals and uncertainties [10, 117, 119, 38, 84]; (3) improving the primary beam modelling [71]; (4) developing data quality metrics for data triaging (RFI, ionospheric activity, [59, 121, 127]), (5) developing and refining redundant and hybrid calibration pipelines for Phase II [70, 60, 20]. A final important step was the development of a full end-to-end simulation to demonstrate that there was no signal loss in the chain from telescope to data product. The results of this work include upcoming EoR limits from re-analysis of Phase I data and new Phase II data, as well as exploration of new techniques for exploring the EoR [122].

A final, key insight from recent work helps to address the current questions in the EoR research field about robustness of any future claimed detection of cosmological signal. Along with confirmation by other telescopes, ability to detect the same signal in independent observing fields, where the foregrounds are different, is crucial. In [120], MWA data from two observing fields was studied with a Kernel Density Estimator to understand the similarities and differences between the statistical structure of data from independent sky areas. This work can lead to a better understanding of robustly discriminating contamination from cosmological signal.

### 8.3.3 Low Frequency Array - LOFAR

LOFAR is a composite aperture array low-frequency radio interferometer. It has two primary station types; the High-Band Antennas (HBA, 120–190 MHz) and Low-Band Antennas (LBA, 30–90 MHz). Both station types have been used for EoR and Cosmic Dawn science. Although LOFAR formally contains baselines of thousands of kilometres to the international stations, it is only the Dutch-based stations that are used for actual EoR measurements. Figure 8.4 shows the central stations (blue cut out) and the nearest remote stations (red).

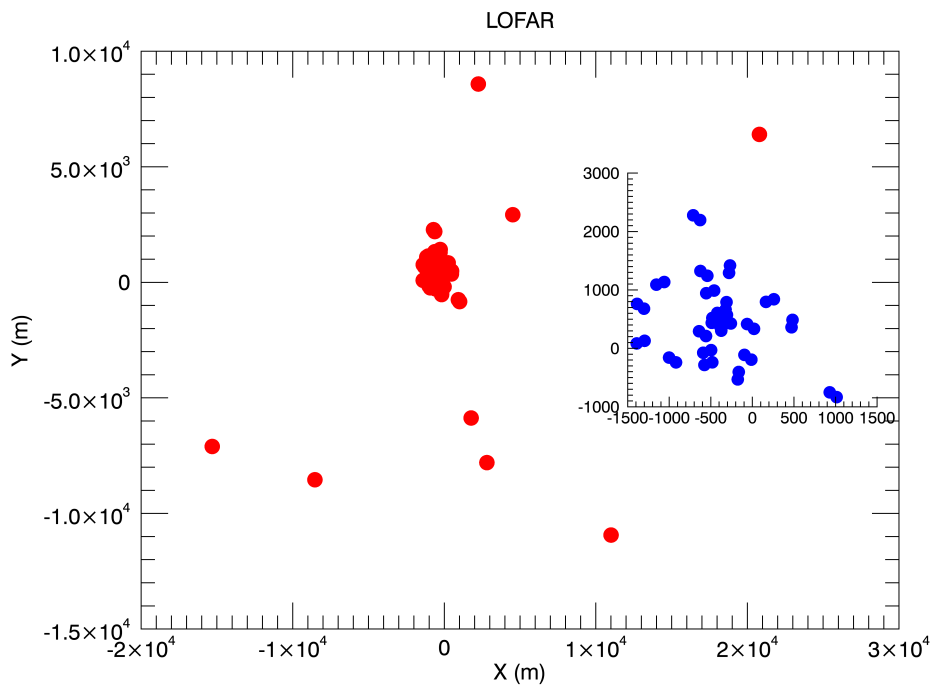


Figure 8.4: Array configuration for the central and inner remote stations of LOFAR (red), and subplot showing the central stations only (blue): 30–40 m aperture array dipole stations spread over tens of kilometres.

The LOFAR latitude allows for circumpolar observations with long winter nights. As such, one of the primary observing fields is the North Celestial Pole, which can be observed for more than 12 hours in the winter months. Early work with the LOFAR EoR Key Science Project focussed on foreground mitigation, choice of observing fields, and data analysis methodology. As with many of the published papers in this early epoch, foregrounds in [57] were modelled to be subtracted with a simple smooth fitting function. This work is notable because it provided realistic models for a range of different foreground components, and included discussion of the treatment of polarized foregrounds.

[58] extended the work from 2008 to focus on simulations of Faraday Rotation from polarized Galactic foregrounds. FR rotates the phase of the intrinsically-smooth foreground component yielding spectral structure that may mimic the EoR signal. In this work, Jelić

shows the effect of inaccurate data calibration on polarized emission, which can imprint total intensity structure if the polarized instrumental response is incorrect.

The SAGE algorithm (Space Alternating Generalized Expectation Maximization) was first introduced in 2011 by [61], and provides the basis for all calibration of LOFAR EoR datasets to the present day. Based on the well-known Expectation Maximization (EM) algorithm, which iteratively fits for calibration parameters (maximizes the likelihood with respect to a set of parameters and then alters the parameters to find a new likelihood) when the underlying system model contains unobserved variables, SAGE extends the traditional least-squares fitting to allow for more model flexibility, and improved convergence and efficiency. Part of the SAGE algorithm performs direction-dependent calibration towards clusters of sources on the sky, thereby allowing for ionospheric distortion of the sky model.

Detailed total intensity and polarized imaging of the LOFAR EoR fields were presented in [130] and [56]. The North Celestial Pole field allows for deep, long winter nighttime observations, and was shown to be able to be calibrated over long integrations. Observations of low Faraday depth structures in the ELAIS-N1 field yielded structures that would be problematic for EoR science if the degree of polarization leakage into total intensity exceeded 1%. This quantification of the accuracy required of instrumental polarization models was the first of a set of papers that explored polarized signal and leakage for EoR science. Thus far, the LOFAR EoR collaboration has undertaken the most extensive work to quantify the impact of polarization leakage, while the MWA collaboration has made some observations of polarized emission in their data ([69], [68], [13]). In [8] and [7], Asad and colleagues first studied the polarized emission in the 3C196 EoR field, finding them to be localized around a small Faraday depth, and quantified the leakage, and then studied the accuracy of the LOFAR polarized beam model to be able to limit leakage into total intensity. Given the level of polarized to total intensity, and a beam model accurate to 10% at the field centre, the leakage and subsequent spectral structure would be acceptable for EoR science. Finally, [6] considered the more problematic impact of wide-field polarization leakage on the EoR power spectrum. Far from the field centre, the primary beam models are less accurate, and sources imprint additional spectral structure due to the chromaticity of an interferometer. In these cases, bias was found to persist in the EoR power spectrum.

In early work on fitting foregrounds, Harker and colleagues [46] discussed the use of Wp smoothing as a non-parametric method for fitting a smooth function, based on limiting the number of inflection points in the fit. Further, they discuss the systematic errors introduced by the fitting routine, methods for estimating these, and for accounting for them in the final uncertainties. This approach is used again in the work of [77] for the Gaussian Process Regression fitting, and also is used generically in the PAPER analysis to try to understand signal loss. There, and elsewhere, use of the same dataset to empirically estimate the bias, and then to correct it, leads to resubstitution bias, underestimate of bias and signal loss.

In a series of papers, Chapman and collaborators explored novel approaches to fitting and removing foreground signal from image-based datacubes. In [24], they introduced the FastICA technique, as a non-parametric method that estimates independent foreground components and their mixing for each image pixel and frequency. The advantage of such methods is that they do not rely on any a priori knowledge of the signal, but instead only assume that the full signal can be represented by a small number of components (sparsity), thereby allowing for good estimation with a given dataset. The disadvantage lies in the sensitivity of

results to the number of components the user chooses that the data should contain, and the potential for signal loss if the projection of the estimated components onto the EoR signal is non-negligible. ICA generically minimizes Gaussianity, thereby enforcing smoothness in the fitted components. Beyond ICA, a generalized method (GMCA; Generalized Morphological Component Analysis) was applied ([23, 22]) to use an underlying blind wavelet decomposition of the components, combined with the sparsity and mixing model methodology of the ICA method. As with other methods when the underlying structure, spatial distribution and amplitude of the cosmological signal and foreground components is unknown, the potential for signal loss is present. The ICA and GMCA methods both assume that the cosmological signal has negligible amplitude and is absorbed in the noise. Structural deviations from this assumption can lead to signal loss.

In a new approach to foreground treatment, Mertens and colleagues discuss use of the well-known Gaussian Process Regression (GPR) technique to fit for foregrounds using only an understanding for the spectral data covariance of different components [77]. Unlike parametric methods that assume an underlying model, GPR (an extended version of kriging, which interpolates data based on their known covariance properties) relies only a statistical separation of foreground and cosmological signal via their spectral correlation lengths. This method also suffers from the potential for cosmological signal loss, but the authors attempt capture the potential bias statistically through increased noise. The ultimate utility of this approach has yet to be demonstrated on a large dataset at the time of the writing.

Along with the power spectrum as a measure of the signal variance as a function of spatial scale, the variance statistic was explored with simulations in [102]. The variance of the brightness temperature, as the wavenumber integral over the power spectrum, quantifies the variability in the cosmological signal on the imaging scale (autocorrelation function). Although it provides limited cosmological information, detection of this variance can be theoretically obtained with fewer observing hours. Bayesian power spectrum extraction techniques were also explored in [43], with a view to allowing for a spatially-smooth component to capture the unmodelled diffuse emission in the NCP field. Like other instruments, the data calibration and foreground models were limited to point and extended sources, with the complex diffuse emission difficult to measure and model. Increasingly, the impact of this incomplete sky model has become apparent.

In a landmark paper published by Patil and colleagues in 2016 [100] the source of ‘excess noise’ and diffuse emission suppression in LOFAR data were studied. Excess noise is the identification of increased noise levels in the data post-calibration compared with expectations of thermal noise and Stokes V measurements. Ultimately, the lack of a diffuse model in the calibration sky model allowed for this signal to be absorbed into the gain calibration solutions, thereby yielding a direction-dependent bias and noise in the residual data. To address this problem, the short baselines containing the majority of the diffuse emission could be excluded, however this leads to increased noise on these scales (due to statistical leverage; effectively this amounts to additional flexibility in the gain solutions on these scales because they are not used in the modelling). This work was undertaken contemporaneously with that of [10] and [117], which both studied the effect of incomplete sky models and spectrally varying bandpass parameters on calibration and residual signal. The combined outcome of these studies is an understanding of the impact of sky model incompleteness, the need to enforce spectral correlation (e.g., regularization as in SAGECal or smooth model fitting) for

calibration parameter fitting, and the approaches to calibration that can mitigate these.

Further exploration of the impact of calibration frameworks and data treatment were then explored in [83] and [88], with a view to having a complete understanding of the end-to-end data processing of LOFAR EoR data on the path to a detection. Unlike in the previous ten years before real observations were undertaken and thermal noise sensitivity was seen to be the major impediment for EoR detection, the field has come to appreciate the crucial roles of unbiased calibration, sky model completeness, and foreground treatment without cosmological signal loss.

The culmination of the lessons learned from statistical leverage and incomplete sky models was applied to two fluctuation upper limit papers published since 2017. In [99], Patil and colleagues presented competitive results from a small set of data ( $\sim 10$  hours) at  $z = [9.6 - 10.6]$ , with the best limit of  $(59.6 \text{ mK})^2$ . This work reported an excess variance, in line with previous discussions, and the use of Stokes V power to remove noise power. At higher redshifts (lower frequencies), Gehlot and colleagues [40] reported upper limits above  $z = 20$ , with use of the Gaussian Process Regression foreground fitting technique introduced by [77] for EoR science.

Beyond the power spectrum, LOFAR has explored other tracers of the neutral hydrogen temperature field, namely the ability to produce low angular resolution images [134] and the 21 cm Forest [28]. LOFAR like other current instruments, does not have the sensitivity to directly image neutral hydrogen bubbles at the instrumental resolution. However, by lowering the resolution of images (thereby improving the radiometric noise), Zaroubi and colleagues argue that the largest of bubbles may be detectable at low signal-to-noise ratio on the largest of scales late in reionization. The ability to detect the 21 cm Forest (absorption of continuum radio emission along the line-of-sight to high redshift AGN due to intervening neutral gas) remains a challenge and aim of many current interferometers. Ciardi and colleagues showed that LOFAR would have the ability to detect an absorption feature under ideal conditions. Unlike the statistical detection of the power spectrum of temperature fluctuations, the absorption signal amplitude is determined by the astrophysical conditions close to the gas, namely gas kinetic temperature. Cold gas is able to absorb light more readily than heated gas. The failure of this method to date is primarily due to the lack of any known high-redshift radio-loud AGN ( $z > 6$ ). Given the sensitivity of current instruments, a source with flux density exceeding 10 mJy and cold neutral gas would be required. It is likely that the arrival of SKA will provide both the sensitivity and the detection (and confirmation) of high-redshift radio-loud AGN to be able to undertake this experiment. Of the current interferometric experiments, only LOFAR has sufficient sensitivity to be able to attempt this experiment at all.

The utility of extracting higher-order statistics of the 21 cm brightness temperature field were explored in a simulation study of foreground-subtracted image cubes by [47]. Again, the ability to smoothly treat and remove foregrounds placed the burden of detection on pure noise considerations.

### 8.3.4 Precision Array for Probing the Epoch of Reionization - PAPER

The PAPER experiment was designed as a testbed for developing novel 21 cm cosmology analysis techniques. PAPER antennas were chosen to be small, single dipoles on elevated

ground-screens to enable reconfiguration of the array, and the system used a flexible digital correlator architecture that could scale as the number of antennas grew [96]. The small antenna sizes was also chosen to limit the frequency evolution of the antenna response over the instrument’s 110 – 180 MHz of usable instantaneous bandwidth. The design and results from an initial 8-station deployment of PAPER in Green Bank, WV, USA were described in [94].

In its earlier stages, PAPER deployed its antennas in configurations designed for imaging, including a single-polarization 16-element 300 m diameter ring in Green Bank used for primary beam measurements in [105]. While the Green Bank array was upgraded to a single-polarization, 32-element array, all subsequent publications came using arrays deployed at the SKA-SA site in the Karoo, South Africa. Highlights of early PAPER studies include the creation of a 145 MHz Southern hemisphere sky-catalog using a single-polarization, 32-element array [53] and a study of the radio galaxy Centaurus A using a single-polarization, 64-element array [109]. In both of these cases, the elements were deployed in a randomized configuration over a circle of 300 m diameter to maximize *uv* coverage.

In 2012, however, members of the PAPER team developed what is now referred to as the “delay spectrum” approach for measuring the 21 cm power spectrum. In the delay spectrum approach, visibility spectra from individual baselines are Fourier transformed and cross-multiplied. [93] demonstrated how these delay spectra can be used as estimates of the 21 cm power spectrum, without ever combining visibilities and making an image. [93] also provided sensitivity estimates for the delay spectrum approach using a 128-element PAPER array. [98] then demonstrated how 21 cm foregrounds isolate into what is now commonly referred to as “the wedge” and included the effects of foreground contamination in the sensitivity study. One consequence of the delay spectrum approach is a higher noise level than alternative approaches: power spectra estimated from individual baselines are averaged together, as opposed to coherently combining all the visibilities and forming a single power spectrum, so noise fluctuations average down more slowly. To make-up for this sensitivity sacrifice, [93] proposed using a “maximum redundancy” configuration, in which antennas are arranged to create multiple copies of the same baseline spacing. These redundant baselines can then be averaged together before squaring, helping the noise level to integrate down faster. Although redundant layouts drastically reduce imaging fidelity, the delay spectrum approach does not requiring imaging and so is, in principle, not affected by this consequence.

The decision was made to reconfigure the PAPER array and test the delay spectrum technique in a maximum redundancy layout. However, a short data set in a single-polarization, 64-element “minimum redundancy” (i.e. random layout) with a 300 m diameter was collected and used to make delay spectra from a range of baseline lengths and orientations in [1]. This analysis demonstrated good isolation of foreground emission to the wedge in 2D cosmological *k*-space, suggesting the promise of the delay spectrum technique.

[95] presented the first deep power spectrum limits from a dual-polarization, 32-element, maximum redundancy array (a grid of 8 columns and 4 rows, with a column spacing of 30 meters and a row spacing of 4 meters). Just over 1000 hours of data were used in the analysis. In addition to the basic delay spectrum formalism, [95] introduced two additional analysis techniques: redundant calibration [2, 74], which was enabled by the redundant layout of the array, and a new technique for removing off-diagonal covariances between redundant baselines. These same techniques were applied to the same data over a range of redshifts in

[55].

The techniques of [95] were then applied to a new, 1000+ hour, dual-polarization, 64-element PAPER data set in [5] (the layout of which is shown in Figure 8.5). This analysis improved upon the redundant calibration technique by using the OMNICAL package [135], replaced the off-diagonal covariance removal technique with an inverse covariance weighting approach using empirically estimated covariance matrices (similar to [34]) and applied a new technique known as “fringe rate filtering” (described in [97]). At the time, the [5] limits on the 21 cm power spectrum were believed to be the most stringent to be published and were followed by two separate publications using their measurement to constrain the temperature of the IGM at  $z = 8.4$  [104, 45].

However, re-analysis of the [5] data by [25] revealed a critical error in the analysis: empirically estimated covariance matrices are correlated with the data, and weighting by them can bias the recovered signal low. (As described in §8.3.1, this bias has frequently been referred to as “signal loss” — the idea that an analysis technique can remove 21 cm signal along with foregrounds.) In practice, the signal loss in the PAPER analysis was very large (nearly four orders of magnitude of potential EoR signal was suppressed) due to the fringe-rate filtering technique that reduced the number of independent samples used to estimate the covariance matrix. Although the analysis in [5] attempted to estimate signal loss using injection of mock EoR signals into the data, their method missed potential loss caused by data-signal cross terms in the covariance matrix and thus concluded that the original analysis was effectively lossless. Incorrect estimates of both the theoretical and observed noise levels in the data also contributed to the belief that the analysis of [5] was sound.

In light of the analysis in [25], all of the PAPER results in [95, 55, 5] are considered to be invalid and do not place meaningful limits on the 21 cm signal.<sup>1</sup> A re-analysis of the full [5] data set using a lossless analysis is forthcoming, but the limits are not expected to be near the same level as [5]. The PAPER experiment also collected two years of data with a dual-polarization, 128-element array, but due to an increased amount of instrument systematics and failures in the aging system, these data are not expected to be published.

The delay spectrum approach does not allow for high accuracy polarization calibration, which needs to be performed in the image domain. Theoretical studies of the effect of Faraday rotated (i.e. frequency-dependent) polarized emission on the delay spectrum technique were presented in [80] and [87] and studies using PAPER data were performed in [3] and [64]. Overall, the effect of polarized emission on the delay spectrum approach can be quite significant, but the overall amplitude is uncertain as there are few constraints on the polarization properties of the 150 MHz sky at the angular scales probed by PAPER. Ionospheric Faraday rotation can also attenuate the polarized signal in data sets averaged over many nights [75].

---

<sup>1</sup>Although [95] did not use the inverse covariance weighting that was the main source of the problem in [5], its covariance removal technique has not been robustly vetted for signal loss and thus the results are considered suspect at best.

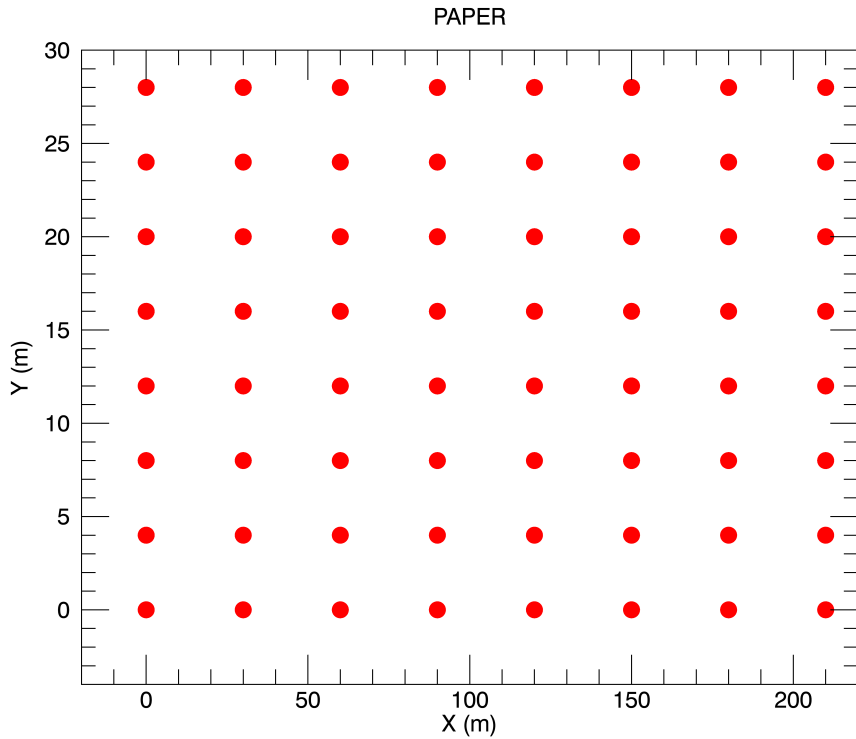


Figure 8.5: Array configuration for the PAPER-64 maximally-redundant array: 64 single dipoles spread over 210 m. Note the distinctly different scales on the  $x$  and  $y$  axes.

## 8.4 Published results

Here we collate the published best limits at each redshift from the current experiments (Table 8.4). PAPER measurements have been omitted. Despite the current published values, there are publications in peer-review now for LOFAR, PAPER, and MWA improving on these results.

## 8.5 Current challenges

21 cm experiments consist of many components, from the analog telescope design through to power spectrum estimation algorithms. One clear lesson from first generation experiments is that no one aspect of the system can provide the necessary 1-part-in- $10^5$  dynamic range required to detect the 21 cm signal; rather, the burden needs to be spread across the components of the experiment, alleviating the demands on each of the other components. In this section, we briefly review what we consider five key areas where 21 cm experiments continue to innovate: (1) analog instrument design; (2) data quality control; (3) calibration; (4) foreground mitigation and the associated potential for signal loss; and (5) end-to-end validation of analysis pipelines.

Facility	$z$	$k (h\text{Mpc}^{-1})$	Upper limit (mK) <sup>2</sup>	Ref.
MWA	12.2	0.18	$2.5 \times 10^7$	[37]
MWA	15.35	0.21	$8.3 \times 10^8$	[37]
MWA	17.05	0.22	$2.7 \times 10^8$	[37]
MWA	7.1	0.23	$2.7 \times 10^4$	[12]
MWA	6.8	0.24	$3.0 \times 10^4$	[12]
MWA	6.5	0.24	$3.2 \times 10^4$	[12]
MWA	9.5	0.05	$6.8 \times 10^4$	[34]
LOFAR	10	0.053	$6.3 \times 10^3$	[100]
LOFAR	9	0.053	$7.5 \times 10^3$	[100]
LOFAR	8	0.053	$1.7 \times 10^4$	[100]
LOFAR	23	0.038	$6.8 \times 10^4$	[40]
GMRT	8.6	0.5	$6.2 \times 10^4$	[91]

Table 8.2: Best two sigma upper limits on the EoR and Cosmic Dawn power spectrum for each experiment. Only the lowest limits have been reproduced.

**1. Analog instrument design.** One of the major challenges for 21 cm cosmology experiments is to remove any spectral structure introduced by the instrument that might otherwise mix smooth spectrum foregrounds into the spectral modes occupied by the cosmological signal. One seemingly straightforward approach is to limit the amount of spectral structure in the instrument response through careful analog design. Initial specifications on the HERA system design were to limit spectral structure to a level that would enable the delay spectrum technique without any additional calibration or analysis requirements; however, further study has shown that the HERA design does not meet this stringent specification and will need data analysis algorithms to also model and remove spectral structure from the instrument [31]. The push to larger bandwidths (e.g. 50 – 250 MHz for HERA and 50 – 350 MHz for the SKA) adds to the challenge of constructing a single instrument with a smooth spectral response over a large range of wavelengths. Analysis with the MWA has also demonstrated how reflections in the analog system can contaminate modes of the EoR power spectrum, suggesting that more stringent specifications on impedance matches and cable lengths are necessary for future instruments [10, 38].

**2. Data Quality Control.** Given the extreme brightness of human-generated radio signals compared to the 21 cm signal, only a very small number of contaminated measurements are enough to significantly affect the analysis of a large data set. The “gold standard” for identifying radio frequency interference, AOFlagger [90], is used by both LOFAR and the MWA. However, additional quality metrics can still catch corrupted data that slips by this first round of flagging, including ultra-faint, broad-band digital TV transmission [127] and effects due to ionospheric weather [121, 59]. As interferometers grow in size, the large data rates may also require computationally faster algorithms for data quality checks [62]. [89] also demonstrate how even flagged RFI can affect power spectrum analysis if care is not taken.

**3. Calibration.** Instrument calibration is often regarded as the greatest challenge for existing and future 21 cm experiments. While both the analog design and the methodology

used for power spectrum estimation can ease calibration requirements [82], experiments still need to control the spectral response of their telescopes over wide bandwidths at a level unprecedented in radio astronomy. Typically, antenna-based gain calibration is performed by forward-modeling visibilities and minimizing the difference with the observed data; however, [10], [100], and [117] demonstrate that without additional constraints, calibration performed with an incomplete sky-model can lead to spurious spectral structure in the calibration solutions that can both overwhelm or remove the EoR signal. Redundancy based calibration has been viewed as a promising alternative because it does not reference a sky-model; however, recent work has shown that a sky model is still required to constrain the degeneracies inherent in redundant calibration, and that the same kind of contamination can affect the power spectrum as in sky-based calibration [20, 70, 60]. Calibration of the primary beam response of the instruments is also a major challenge, and several options have been explored, including sky-based calibration [105], using satellite broadcasts [85, 86, 71], and with drones flying transmitters [54].

**4. Foreground mitigation.** Fundamentally, the real challenges at the heart of 21 cm cosmology come from the intrinsic brightness of the foreground emission. While much of the work to date focuses on removing the instrument response from the foreground spectra, most current experiments use some form of foreground mitigation to help isolate or remove foregrounds. Many distinct approaches have been developed, which can be broadly classified as either “foreground avoidance” and “foreground subtraction.” Foreground avoidance methods attempt to isolate foregrounds into the wedge and minimize bleed into the EoR window; power spectra are then only estimated from within the EoR window. Examples of avoidance techniques includes the wide-band iterative deconvolution filter used in PAPER analyses [63] and the inverse covariance weighting techniques also used by PAPER [25]. Foreground subtraction, on the other hand, attempts to remove specific models of the foregrounds — using either real sky catalogs or parametric models for their spectra — while leaving the 21 cm unaffected. Examples of foreground subtraction including the point-source forward modeling and subtraction performed by FHD [9] and the spectral based fitting methods used by LOFAR [22, 77]. It is worth stressing that while these techniques have historically been developed in the context of specific experiments, they are more generally applicable; see [63] for an example of PAPER-developed techniques applied to MWA data and MWA-developed techniques applied to PAPER data.

One of the greatest risks of foreground removal is the inadvertent removal of 21 cm signal, i.e., signal loss. Although many techniques have been developed using frameworks where signal loss is not expected, due to a presumed orthogonality of the foreground description and 21 cm signal basis, there are subtle challenges that arise when faced with a need to achieve five orders of magnitude of dynamic range. While cross-terms between the foreground and signal might have an expectation value of 0, there are still only a finite number of samples going into the analysis, and these cross terms will not have converged to their expectation value — as was the case in the PAPER analysis of [5].

**5. Validation.** One of the last major challenges for current and future experiments is to rigorously test foreground removal and other analysis algorithms — ideally as part of complete pipeline and not as an independent step — to confirm that 21 cm signal is not being biased or removed. And although foreground removal seems like the step most likely to cause signal loss, it is certainly not the only place that needs further scrutiny. In light of the PAPER

retractions, 21 cm experiments are realizing the importance of simulation-based analysis vetting — ideally with independent, third-party simulations. Many interferometric simulators exist, including CASA, PRISim [114], OSKAR, and pyuvsim [67]. In turn, it has become important to test the simulators against each other, to verify that they achieve the requisite precision for 21 cm cosmology. These validation efforts can be slow and painstaking, but as experiments push closer to a first detection of the 21 cm signal, they have become more vital than ever. The other avenue for verification is with other instruments and other pipelines providing independent analysis. Use of multiple observing fields can also show robustness to foreground treatment [120].

## 8.6 Prospects for the future

### 8.6.1 Current instruments

MWA and LOFAR are both currently pursuing deeper limits. Armed with new calibration and analysis, and critically, a deeper understanding of the effects of different processing approaches, the level of systematics in data are reduced, and more data can be processed to reduce noise. At this stage, it is difficult to predict whether systematics will remain at deeper levels, and if the fundamental limitations of the instrument will preclude a detection. While the reported detection of the Cosmic Dawn global signal from the EDGES experiment [18] suggests that the spatial power spectrum amplitude may be larger than expected, this is highly uncertain, and the flexibility in possible strengths of the signal in the EoR emission part of the spectrum could help or hinder a detection by LOFAR and MWA. Pursuit of the Cosmic Dawn signal from 75–100 MHz observations with the MWA and LOFAR is also underway, but that introduces even greater challenges of large fields-of-view and poor extended source models at those frequencies.

### 8.6.2 Future instruments

The SKA and HERA offer the future vision for EoR and Cosmic Dawn science. Like LOFAR and MWA, SKA is a general science instrument, being able to produce its own sky model and calibration framework, while needing to balance design with the other science aims of the observatory. HERA, like PAPER, is a custom EoR instrument, being able to design with a complete focus on EoR science, likely requiring external information to provide a full end-to-end calibration and source subtraction element.

The low-frequency telescope of the SKA Observatory, SKA-Low, will be centred at the Murchison Radioastronomy Observatory in Western Australia, on the same radio quiet site as MWA, ASKAP, EDGES and BiGHorNS [65, 32]. Despite being designed for 512 38 m stations (256 dual-polarization dipoles in each station) spread over  $>40$  km, the core region will contain  $>200$  stations within the central 1 km, with exceptional surface brightness sensitivity for EoR and CD science. With a frequency range available down to 50 MHz, the CD will be accessible to  $z = 27$ , with sub-stations able to be formed to produce the wider fields-of-view and shorter baselines required for early times. With its exceptional imaging capabilities, SKA-Low aims to pursue power spectrum, direct imaging (tomography) and

21 cm Forest studies. The prices to be paid for this highly-capable instrument are the complexity of the data and instrument, and the large data volumes that will be produced from the telescope, and is therefore faces a more severe version of the challenges currently experienced by multi-purpose dipole arrays such as MWA and LOFAR.

HERA [31] is a smaller instrument (although still significantly larger than any of the existing instruments) being constructed in South Africa. It comprises 350 14 m dipole elements spread over  $<1$  km (331 in a 320 m core) for high EoR sensitivity and moderate imaging and calibration needs (19 outriggers). It will primarily pursue the statistical exploration of the EoR and CD using the delay spectrum technique, with some hope for imaging capability and alternate power spectrum analyses.

### 8.6.3 Future analyses

Although the spatial power spectrum is the primary data product of most current EoR 21 cm experiments, there are other avenues of pursuit to explore this first billion years of the Universe, including an integrated product (the variance statistic, [101]). Direct imaging is beyond the capability of current instruments, demanding a high surface brightness sensitivity and thousands of hours. This will be pursued by the future SKA [65]. However, there are other statistics that can be pursued through the 21 cm line, and also the opportunity for cross-correlating the signal with other tracers of early Universe evolution. The benefit of the latter approach is that the systematic errors may be different between the two tracers, offering an advantage over 21 cm alone.

At early times, the brightness temperature of the 21 cm line, relative to the CMB traces the matter power spectrum, and is highly Gaussian, but at later times the evolution of ionised bubbles dominates the spatial fluctuations and the signal is expected to have non-zero higher order terms [39, 76, 35]. The shape of the temperature distribution function evolves with time and spatial scale, and differs for different underlying models of the evolution of the Universe. As such, probing these non-Gaussian components can provide complementary information to the power spectrum, which, by design, only captures information in the second moment of the distribution [129].

The bispectrum measures the three-point correlation function, and has been shown to encode non-Gaussianity. In early work to study the expected sensitivity of 21 cm experiments to the bispectrum, [133] computed theoretical expectations for a range of instruments, under the assumption of thermal noise only. More sophisticated recent work included the effects of calibration and foregrounds on the ability to detect the signal. In [122], two bispectrum estimators were developed to take a practical approach to estimation with real data, and were applied to 20 hours of data from Phase II of the MWA. This work discussed some of the advantages and challenges of doing such an experiment with real data.

Cross-correlation studies from the early Universe offer the potential for new astrophysical insight and reduced observational biases and errors. In the context of the MWA, [131] used data to explore the cross-correlation of the 21 cm image from the EoR-0 observing field, and the CMB field measured by Planck. An additional tracer that can be used is the population of high-redshift LAEs, which are observable in ionised regions [132, 66, 51]. The SKA's Synergy group is exploring the potential for multi-facility observations, including the exciting prospects available with WFIRST [50].

# Bibliography

[1]

[2]

[3]

- [4] S. S. Ali, S. Bharadwaj, and J. N. Chengalur. Foregrounds for redshifted 21-cm studies of reionization: Giant Meter Wave Radio Telescope 153-MHz observations. *MNRAS*, 385:2166–2174, April 2008.
- [5] Z. S. Ali, A. R. Parsons, H. Zheng, J. C. Pober, A. Liu, J. E. Aguirre, R. F. Bradley, G. Bernardi, C. L. Carilli, C. Cheng, D. R. DeBoer, M. R. Dexter, J. Grobbelaar, J. Horrell, D. C. Jacobs, P. Klima, D. H. E. MacMahon, M. Maree, D. F. Moore, N. Razavi, I. I. Stefan, W. P. Walbrugh, and A. Walker. PAPER-64 Constraints on Reionization: The 21 cm Power Spectrum at  $z = 8.4$ . *ApJ*, 809:61, August 2015.
- [6] K. M. B. Asad, L. V. E. Koopmans, V. Jelić, A. G. de Bruyn, V. N. Pandey, and B. K. Gehlot. Polarization leakage in epoch of reionization windows - III. Wide-field effects of narrow-field arrays. *MNRAS*, 476(3):3051–3062, May 2018.
- [7] K. M. B. Asad, L. V. E. Koopmans, V. Jelić, A. Ghosh, F. B. Abdalla, M. A. Brentjens, A. G. de Bruyn, B. Ciardi, B. K. Gehlot, and I. T. Iliev. Polarization leakage in epoch of reionization windows - II. Primary beam model and direction-dependent calibration. *MNRAS*, 462(4):4482–4494, Nov 2016.
- [8] K. M. B. Asad, L. V. E. Koopmans, V. Jelić, V. N. Pandey, A. Ghosh, F. B. Abdalla, G. Bernardi, M. A. Brentjens, A. G. de Bruyn, and S. Bus. Polarization leakage in epoch of reionization windows - I. Low Frequency Array observations of the 3C196 field. *MNRAS*, 451(4):3709–3727, Aug 2015.
- [9] N. Barry, A. P. Beardsley, R. Byrne, B. Hazelton, M. F. Morales, J. C. Pober, and I. Sullivan. The FHD/epsilon Epoch of Reionization Power Spectrum Pipeline. *arXiv e-prints*, page arXiv:1901.02980, Jan 2019.
- [10] N. Barry, B. Hazelton, I. Sullivan, M. F. Morales, and J. C. Pober. Calibration Requirements for Detecting the 21 cm Epoch of Reionization Power Spectrum and Implications for the SKA. *ArXiv e-prints 1603.00607*, March 2016.

- [11] A. P. Beardsley, B. J. Hazelton, M. F. Morales, W. Arcus, and others. The EoR sensitivity of the Murchison Widefield Array. *MNRAS*, 429:L5–L9, February 2013.
- [12] A. P. Beardsley, B. J. Hazelton, I. S. Sullivan, P. Carroll, N. Barry, M. Rahimi, B. Pindor, C. M. Trott, J. Line, D. C. Jacobs, M. F. Morales, J. C. Pober, G. Bernardi, J. D. Bowman, M. P. Busch, F. Briggs, R. J. Cappallo, B. E. Corey, A. de Oliveira-Costa, J. S. Dillon, D. Emrich, A. Ewall-Wice, L. Feng, B. M. Gaensler, R. Goeke, L. J. Greenhill, J. N. Hewitt, N. Hurley-Walker, M. Johnston-Hollitt, D. L. Kaplan, J. C. Kasper, H. S. Kim, E. Kratzenberg, E. Lenc, A. Loeb, C. J. Lonsdale, M. J. Lynch, B. McKinley, S. R. McWhirter, D. A. Mitchell, E. Morgan, A. R. Neben, N. Thyagarajan, D. Oberoi, A. R. Offringa, S. M. Ord, S. Paul, T. Prabu, P. Procopio, J. Riding, A. E. E. Rogers, A. Roshi, N. Udaya Shankar, S. K. Sethi, K. S. Srivani, R. Subrahmanyan, M. Tegmark, S. J. Tingay, M. Waterson, R. B. Wayth, R. L. Webster, A. R. Whitney, A. Williams, C. L. Williams, C. Wu, and J. S. B. Wyithe. First Season MWA EoR Power Spectrum Results at Redshift 7. *ArXiv e-prints*, August 2016.
- [13] G. Bernardi, L. J. Greenhill, D. A. Mitchell, S. M. Ord, B. J. Hazelton, B. M. Gaensler, A. de Oliveira-Costa, M. F. Morales, N. Udaya Shankar, and R. Subrahmanyan. A 189 MHz, 2400 deg<sup>2</sup> Polarization Survey with the Murchison Widefield Array 32-element Prototype. *ApJ*, 771(2):105, Jul 2013.
- [14] S. Bharadwaj and S. K. Sethi. HI Fluctuations at Large Redshifts: I—Visibility correlation. *Journal of Astrophysics and Astronomy*, 22:293–307, Dec 2001.
- [15] Somnath Bharadwaj and Sk. Saiyad Ali. On using visibility correlations to probe the HI distribution from the dark ages to the present epoch - I. Formalism and the expected signal. *MNRAS*, 356(4):1519–1528, Feb 2005.
- [16] Somnath Bharadwaj, Srijita Pal, Samir Choudhuri, and Prasun Dutta. A Tapered Gridded Estimator (TGE) for the multifrequency angular power spectrum (MAPS) and the cosmological H I 21-cm power spectrum. *MNRAS*, 483(4):5694–5700, Mar 2019.
- [17] J. D. Bowman, I. Cairns, D. L. Kaplan, T. Murphy, D. Oberoi, and others. Science with the Murchison Widefield Array. *PASA*, 30:31, April 2013.
- [18] J. D. Bowman, A. E. E. Rogers, R. A. Monsalve, T. J. Mozdzen, and N. Mahesh. An absorption profile centred at 78 megahertz in the sky-averaged spectrum. *Nature*, 555:67–70, March 2018.
- [19] Judd D. Bowman, Miguel F. Morales, and Jacqueline N. Hewitt. Foreground Contamination in Interferometric Measurements of the Redshifted 21 cm Power Spectrum. *ApJ*, 695(1):183–199, Apr 2009.
- [20] Ruby Byrne, Miguel F. Morales, Bryna Hazelton, Wenyang Li, Nichole Barry, Adam P. Beardsley, Ronniy Joseph, Jonathan Pober, Ian Sullivan, and Cathryn Trott. Fundamental Limitations on the Calibration of Redundant 21 cm Cosmology Instruments and Implications for HERA and the SKA. *ApJ*, 875(1):70, Apr 2019.

- [21] P. A. Carroll, J. Line, M. F. Morales, N. Barry, A. P. Beardsley, B. J. Hazelton, D. C. Jacobs, J. C. Pober, I. S. Sullivan, and R. L. Webster. A high reliability survey of discrete Epoch of Reionization foreground sources in the MWA EoR0 field. *MNRAS*, 461(4):4151–4175, Oct 2016.
- [22] E. Chapman, S. Zaroubi, and F. Abdalla. Foreground Removal vs. Foreground Avoidance: Contamination of the EoR Window. *ArXiv/1408.4695*, August 2014.
- [23] Emma Chapman, Filipe B. Abdalla, J. Bobin, J. L. Starck, Geraint Harker, Vibor Jelić, Panagiotis Labropoulos, Saleem Zaroubi, Michiel A. Brentjens, and A. G. de Bruyn. The scale of the problem: recovering images of reionization with Generalized Morphological Component Analysis. *MNRAS*, 429(1):165–176, Feb 2013.
- [24] Emma Chapman, Filipe B. Abdalla, Geraint Harker, Vibor Jelić, Panagiotis Labropoulos, Saleem Zaroubi, Michiel A. Brentjens, A. G. de Bruyn, and L. V. E. Koopmans. Foreground removal using FASTICA: a showcase of LOFAR-EoR. *MNRAS*, 423(3):2518–2532, Jul 2012.
- [25] Carina Cheng, Aaron R. Parsons, Matthew Kolopanis, Daniel C. Jacobs, Adrian Liu, Saul A. Kohn, James E. Aguirre, Jonathan C. Pober, Zaki S. Ali, Gianni Bernardi, Richard F. Bradley, Chris L. Carilli, David R. DeBoer, Matthew R. Dexter, Joshua S. Dillon, Pat Klima, David H. E. MacMahon, David F. Moore, Chuneeta D. Nunhokee, William P. Walbrugh, and Andre Walker. Characterizing Signal Loss in the 21 cm Reionization Power Spectrum: A Revised Study of PAPER-64. *ArXiv e-prints*, page arXiv:1810.05175, October 2018.
- [26] S. Choudhuri, S. Bharadwaj, A. Ghosh, and S. S. Ali. Visibility-based angular power spectrum estimation in low-frequency radio interferometric observations. *MNRAS*, 445:4351–4365, December 2014.
- [27] Samir Choudhuri, Somnath Bharadwaj, Suman Chatterjee, Sk. Saiyad Ali, Nirupam Roy, and Abhik Ghosh. The visibility-based tapered gridded estimator (TGE) for the redshifted 21-cm power spectrum. *MNRAS*, 463(4):4093–4107, Dec 2016.
- [28] B. Ciardi, P. Labropoulos, A. Maselli, R. Thomas, S. Zaroubi, L. Graziani, J. S. Bolton, G. Bernardi, M. Brentjens, and A. G. de Bruyn. Prospects for detecting the 21 cm forest from the diffuse intergalactic medium with LOFAR. *MNRAS*, 428(2):1755–1765, Jan 2013.
- [29] A. Datta, J. D. Bowman, and C. L. Carilli. Bright Source Subtraction Requirements for Redshifted 21 cm Measurements. *ApJ*, 724:526–538, November 2010.
- [30] Kanan K. Datta, T. Roy Choudhury, and Somnath Bharadwaj. The multifrequency angular power spectrum of the epoch of reionization 21-cm signal. *MNRAS*, 378(1):119–128, Jun 2007.
- [31] D. R. DeBoer, A. R. Parsons, J. E. Aguirre, P. Alexander, Z. S. Ali, A. P. Beardsley, G. Bernardi, J. D. Bowman, R. F. Bradley, C. L. Carilli, C. Cheng, E. de Lera

- Acedo, J. S. Dillon, A. Ewall-Wice, G. Fadana, N. Fagnoni, R. Fritz, S. R. Furlanetto, B. Glendenning, B. Greig, J. Grobbelaar, B. J. Hazelton, J. N. Hewitt, J. Hickish, D. C. Jacobs, A. Julius, M. Kariseb, S. A. Kohn, T. Lekalake, A. Liu, A. Loots, D. MacMahon, L. Malan, C. Malgas, M. Maree, N. Mathison, E. Matsetela, A. Mesinger, M. F. Morales, A. R. Neben, N. Patra, S. Pieterse, J. C. Pober, N. Razavi-Ghods, J. Ringuette, J. Robnett, K. Rosie, R. Sell, C. Smith, A. Syce, M. Tegmark, N. Thyagarajan, P. K. G. Williams, and H. Zheng. Hydrogen Epoch of Reionization Array (HERA). *ArXiv e-prints*, June 2016.
- [32] P. Dewdney, W. Turner, R. Braun, J. Santander-Vela, M. Waterson, and G-H Tan. SKA System Baseline Design v2. *SKA Document Series*, 2016.
- [33] J. S. Dillon, A. Liu, and M. Tegmark. A fast method for power spectrum and foreground analysis for 21 cm cosmology. *PRD*, 87(4):043005, February 2013.
- [34] J. S. Dillon, A. R. Neben, J. N. Hewitt, M. Tegmark, N. Barry, A. P. Beardsley, J. D. Bowman, F. Briggs, P. Carroll, A. de Oliveira-Costa, A. Ewall-Wice, L. Feng, L. J. Greenhill, B. J. Hazelton, L. Hernquist, N. Hurley-Walker, D. C. Jacobs, H. S. Kim, P. Kittiwisit, E. Lenc, J. Line, A. Loeb, B. McKinley, D. A. Mitchell, M. F. Morales, A. R. Offringa, S. Paul, B. Pindor, J. C. Pober, P. Procopio, J. Riding, S. Sethi, N. U. Shankar, R. Subrahmanyan, I. Sullivan, N. Thyagarajan, S. J. Tingay, C. Trott, R. B. Wayth, R. L. Webster, S. Wyithe, G. Bernardi, R. J. Cappallo, A. A. Deshpande, M. Johnston-Hollitt, D. L. Kaplan, C. J. Lonsdale, S. R. McWhirter, E. Morgan, D. Oberoi, S. M. Ord, T. Prabu, K. S. Srivani, A. Williams, and C. L. Williams. Empirical covariance modeling for 21 cm power spectrum estimation: A method demonstration and new limits from early Murchison Widefield Array 128-tile data. *PRD*, 91(12):123011, June 2015.
- [35] D. J. Eisenstein and W. Hu. Power Spectra for Cold Dark Matter and Its Variants. *ApJ*, 511:5–15, January 1999.
- [36] S. W. Ellingson, T. E. Clarke, A. Cohen, J. Craig, N. E. Kassim, Y. Pihlstrom, L. J. Rickard, and G. B. Taylor. The Long Wavelength Array. *IEEE Proceedings*, 97:1421–1430, August 2009.
- [37] A. Ewall-Wice, Joshua S. Dillon, J. N. Hewitt, A. Loeb, A. Mesinger, A. R. Neben, A. R. Offringa, M. Tegmark, N. Barry, and A. P. Beardsley. First limits on the 21 cm power spectrum during the Epoch of X-ray heating. *MNRAS*, 460(4):4320–4347, Aug 2016.
- [38] Aaron Ewall-Wice, Joshua S. Dillon, Adrian Liu, and Jacqueline Hewitt. The impact of modelling errors on interferometer calibration for 21 cm power spectra. *MNRAS*, 470(2):1849–1870, Sep 2017.
- [39] S. R. Furlanetto, S. P. Oh, and F. H. Briggs. Cosmology at low frequencies: The 21 cm transition and the high-redshift Universe. *Phys. Rep.*, 433:181–301, October 2006.

- [40] B. K. Gehlot, F. G. Mertens, L. V. E. Koopmans, M. A. Brentjens, S. Zaroubi, B. Ciardi, A. Ghosh, M. Hatef, I. T. Iliev, and V. Jelić. The first power spectrum limit on the 21-cm signal of neutral hydrogen during the Cosmic Dawn at  $z = 20 - 25$  from LOFAR. *arXiv e-prints*, page arXiv:1809.06661, Sep 2018.
- [41] Abhik Ghosh, Somnath Bharadwaj, Sk. Saiyad Ali, and Jayaram N. Chengalur. GMRT observation towards detecting the post-reionization 21-cm signal. *MNRAS*, 411(4):2426–2438, Mar 2011.
- [42] Abhik Ghosh, Somnath Bharadwaj, Sk. Saiyad Ali, and Jayaram N. Chengalur. Improved foreground removal in GMRT 610 MHz observations towards redshifted 21-cm tomography. *MNRAS*, 418(4):2584–2589, Dec 2011.
- [43] Abhik Ghosh, Léon V. E. Koopmans, E. Chapman, and V. Jelić. A Bayesian analysis of redshifted 21-cm H I signal and foregrounds: simulations for LOFAR. *MNRAS*, 452(2):1587–1600, Sep 2015.
- [44] Abhik Ghosh, Jayanti Prasad, Somnath Bharadwaj, Sk. Saiyad Ali, and Jayaram N. Chengalur. Characterizing foreground for redshifted 21 cm radiation: 150 MHz Giant Metrewave Radio Telescope observations. *MNRAS*, 426(4):3295–3314, Nov 2012.
- [45] Bradley Greig, Andrei Mesinger, and Jonathan C. Pober. Constraints on the temperature of the intergalactic medium at  $z = 8.4$  with 21-cm observations. *MNRAS*, 455(4):4295–4300, Feb 2016.
- [46] Geraint Harker, Saleem Zaroubi, Gianni Bernardi, Michiel A. Brentjens, A. G. de Bruyn, Benedetta Ciardi, Vibor Jelić, Leon V. E. Koopmans, Panagiotis Labropoulos, and Garrelt Mellema. Power spectrum extraction for redshifted 21-cm Epoch of Reionization experiments: the LOFAR case. *MNRAS*, 405(4):2492–2504, Jul 2010.
- [47] Geraint J. A. Harker, Saleem Zaroubi, Rajat M. Thomas, Vibor Jelić, Panagiotis Labropoulos, Garrelt Mellema, Ilian T. Iliev, Gianni Bernardi, Michiel A. Brentjens, and A. G. de Bruyn. Detection and extraction of signals from the epoch of reionization using higher-order one-point statistics. *MNRAS*, 393(4):1449–1458, Mar 2009.
- [48] N. Hurley-Walker, J. R. Callingham, P. J. Hancock, T. M. O. Franzen, L. Hindson, A. D. Kapińska, J. Morgan, A. R. Offringa, R. B. Wayth, C. Wu, Q. Zheng, T. Murphy, M. E. Bell, K. S. Dwarakanath, B. For, B. M. Gaensler, M. Johnston-Hollitt, E. Lenc, P. Procopio, L. Staveley-Smith, R. Ekers, J. D. Bowman, F. Briggs, R. J. Cappallo, A. A. Deshpande, L. Greenhill, B. J. Hazelton, D. L. Kaplan, C. J. Lonsdale, S. R. McWhirter, D. A. Mitchell, M. F. Morales, E. Morgan, D. Oberoi, S. M. Ord, T. Prabu, N. U. Shankar, K. S. Srivani, R. Subrahmanyan, S. J. Tingay, R. L. Webster, A. Williams, and C. L. Williams. GaLactic and Extragalactic All-sky Murchison Widefield Array (GLEAM) survey - I. A low-frequency extragalactic catalogue. *MNRAS*, 464:1146–1167, January 2017.
- [49] Natasha Hurley-Walker, John Morgan, Randall B. Wayth, Paul J. Hancock, Martin E. Bell, Gianni Bernardi, Ramesh Bhat, Frank Briggs, Avinash A. Deshpande,

- and Aaron Ewall-Wice. The Murchison Widefield Array Commissioning Survey: A Low-Frequency Catalogue of 14 110 Compact Radio Sources over 6 100 Square Degrees. *PASA*, 31:e045, Nov 2014.
- [50] Anne Hutter, Pratika Dayal, Sangeeta Malhotra, James Rhoads, Tirthankar Roy Choudhury, Benedetta Ciardi, Christopher J. Conselice, Asantha Cooray, Jean-Gabriel Cuby, and Kanan K. Datta. Astro2020 Science White Paper: A proposal to exploit galaxy-21cm synergies to shed light on the Epoch of Reionization. *arXiv e-prints*, page arXiv:1903.03628, Mar 2019.
- [51] Anne Hutter, Pratika Dayal, Volker Müller, and Cathryn M. Trott. Exploring 21cm-Lyman Alpha Emitter Synergies for SKA. *ApJ*, 836(2):176, Feb 2017.
- [52] D. C. Jacobs, B. J. Hazelton, C. M. Trott, J. S. Dillon, B. Pindor, I. S. Sullivan, J. C. Pober, N. Barry, A. P. Beardsley, G. Bernardi, J. D. Bowman, F. Briggs, R. J. Cappallo, P. Carroll, B. E. Corey, A. de Oliveira-Costa, D. Emrich, A. Ewall-Wice, L. Feng, B. M. Gaensler, R. Goeke, L. J. Greenhill, J. N. Hewitt, N. Hurley-Walker, M. Johnston-Hollitt, D. L. Kaplan, J. C. Kasper, H. Kim, E. Kratzenberg, E. Lenc, J. Line, A. Loeb, C. J. Lonsdale, M. J. Lynch, B. McKinley, S. R. McWhirter, D. A. Mitchell, M. F. Morales, E. Morgan, A. R. Neben, N. Thyagarajan, D. Oberoi, A. R. Offringa, S. M. Ord, S. Paul, T. Prabu, P. Procopio, J. Riding, A. E. E. Rogers, A. Roshi, N. Udaya Shankar, S. K. Sethi, K. S. Srivani, R. Subrahmanyam, M. Tegmark, S. J. Tingay, M. Waterson, R. B. Wayth, R. L. Webster, A. R. Whitney, A. Williams, C. L. Williams, C. Wu, and J. S. B. Wyithe. The Murchison Widefield Array 21 cm Power Spectrum Analysis Methodology. *ApJ*, 825:114, July 2016.
- [53] Daniel C. Jacobs, James E. Aguirre, Aaron R. Parsons, Jonathan C. Pober, Richard F. Bradley, Chris L. Carilli, Nicole E. Gugliucci, Jason R. Manley, Carel van der Merwe, and David F. Moore. New 145 MHz Source Measurements by PAPER in the Southern Sky. *ApJ*, 734(2):L34, Jun 2011.
- [54] Daniel C. Jacobs, Jacob Burba, Judd D. Bowman, Abraham R. Neben, Benjamin Stinnett, Lauren Turner, Kali Johnson, Michael Busch, Jay Allison, and Marc Leatham. First Demonstration of ECHO: an External Calibrator for Hydrogen Observatories. *PASP*, 129(973):035002, Mar 2017.
- [55] Daniel C. Jacobs, Jonathan C. Pober, Aaron R. Parsons, James E. Aguirre, Zaki S. Ali, Judd Bowman, Richard F. Bradley, Chris L. Carilli, David R. DeBoer, and Matthew R. Dexter. Multiredshift Limits on the 21 cm Power Spectrum from PAPER. *ApJ*, 801(1):51, Mar 2015.
- [56] V. Jelić, A. G. de Bruyn, M. Mevius, F. B. Abdalla, K. M. B. Asad, G. Bernardi, M. A. Brentjens, S. Bus, E. Chapman, and B. Ciardi. Initial LOFAR observations of epoch of reionization windows. II. Diffuse polarized emission in the ELAIS-N1 field. *A&A*, 568:A101, Aug 2014.
- [57] V. Jelić, S. Zaroubi, P. Labropoulos, R. M. Thomas, G. Bernardi, M. A. Brentjens, A. G. de Bruyn, B. Ciardi, G. Harker, and L. V. E. Koopmans. Foreground simulations

- for the LOFAR-epoch of reionization experiment. *MNRAS*, 389(3):1319–1335, Sep 2008.
- [58] Vibor Jelić, Saleem Zaroubi, Panagiotis Labropoulos, Gianni Bernardi, A. G. de Bruyn, and Léon V. E. Koopmans. Realistic simulations of the Galactic polarized foreground: consequences for 21-cm reionization detection experiments. *MNRAS*, 409(4):1647–1659, Dec 2010.
- [59] C. H. Jordan, S. Murray, C. M. Trott, R. B. Wayth, D. A. Mitchell, M. Rahimi, B. Pindor, P. Procopio, and J. Morgan. Characterization of the ionosphere above the Murchison Radio Observatory using the Murchison Widefield Array. *MNRAS*, 471:3974–3987, November 2017.
- [60] Ronniy C. Joseph, Cathryn M. Trott, and Randall B. Wayth. The Bias and Uncertainty of Redundant and Sky-based Calibration Under Realistic Sky and Telescope Conditions. *AJ*, 156(6):285, Dec 2018.
- [61] S. Kazemi, S. Yatawatta, S. Zaroubi, P. Lampropoulos, A. G. de Bruyn, L. V. E. Koopmans, and J. Noordam. Radio interferometric calibration using the SAGE algorithm. *MNRAS*, 414(2):1656–1666, Jun 2011.
- [62] Joshua Kerrigan, Paul La Plante, Saul Kohn, Jonathan C. Pober, James Aguirre, Zara Abdurashidova, Paul Alexander, Zaki S. Ali, Yanga Balfour, and Adam P. Beardsley. Optimizing Sparse RFI Prediction using Deep Learning. *arXiv e-prints*, page arXiv:1902.08244, Feb 2019.
- [63] Joshua R. Kerrigan, Jonathan C. Pober, Zaki S. Ali, Carina Cheng, Adam P. Beardsley, Aaron R. Parsons, James E. Aguirre, Nichole Barry, Richard F. Bradley, and Gianni Bernardi. Improved 21 cm Epoch of Reionization Power Spectrum Measurements with a Hybrid Foreground Subtraction and Avoidance Technique. *ApJ*, 864(2):131, Sep 2018.
- [64] S. A. Kohn, J. E. Aguirre, C. D. Nunhokee, G. Bernardi, J. C. Pober, Z. S. Ali, R. F. Bradley, C. L. Carilli, D. R. DeBoer, and N. E. Gugliucci. Constraining Polarized Foregrounds for EoR Experiments I: 2D Power Spectra from the PAPER-32 Imaging Array. *ApJ*, 823(2):88, Jun 2016.
- [65] L. Koopmans, J. Pritchard, G. Mellema, J. Aguirre, K. Ahn, R. Barkana, I. van Beemel, G. Bernardi, A. Bonaldi, F. Briggs, and others. The Cosmic Dawn and Epoch of Reionisation with SKA. *Advancing Astrophysics with the Square Kilometre Array (AASKA14)*, page 1, 2015.
- [66] Kenji Kubota, Shintaro Yoshiura, Keitaro Takahashi, Kenji Hasegawa, Hidenobu Yamada, Masami Ouchi, B. Pindor, and R. L. Webster. Detectability of the 21-cm signal during the epoch of reionization with 21-cm Lyman  $\alpha$  emitter cross-correlation - I. *MNRAS*, 479(2):2754–2766, Sep 2018.

- [67] Adam Lanman, Bryna Hazelton, Daniel Jacobs, Matthew Kolopanis, Jonathan Pober, James Aguirre, and Nithyanandan Thyagarajan. pyuvsim: A comprehensive simulation package for radio interferometers in python. *The Journal of Open Source Software*, 4(37):1234, May 2019.
- [68] E. Lenc, C. S. Anderson, N. Barry, J. D. Bowman, I. H. Cairns, J. S. Farnes, B. M. Gaensler, G. Heald, M. Johnston-Hollitt, and D. L. Kaplan. The Challenges of Low-Frequency Radio Polarimetry: Lessons from the Murchison Widefield Array. *PASA*, 34:e040, Sep 2017.
- [69] E. Lenc, B. M. Gaensler, X. H. Sun, E. M. Sadler, A. G. Willis, N. Barry, A. P. Beardsley, M. E. Bell, G. Bernardi, and J. D. Bowman. Low-frequency Observations of Linearly Polarized Structures in the Interstellar Medium near the South Galactic Pole. *ApJ*, 830(1):38, Oct 2016.
- [70] W. Li, J. C. Pober, B. J. Hazelton, N. Barry, M. F. Morales, I. Sullivan, A. R. Parsons, Z. S. Ali, J. S. Dillon, and A. P. Beardsley. Comparing Redundant and Sky-model-based Interferometric Calibration: A First Look with Phase II of the MWA. *ApJ*, 863(2):170, Aug 2018.
- [71] J. L. B. Line, B. McKinley, J. Rasti, M. Bhardwaj, R. B. Wayth, R. L. Webster, D. Ung, D. Emrich, L. Horsley, and A. Beardsley. In situ measurement of MWA primary beam variation using ORBCOMM. *PASA*, 35:45, Dec 2018.
- [72] J. L. B. Line, R. L. Webster, B. Pindor, D. A. Mitchell, and C. M. Trott. PUMA: The Positional Update and Matching Algorithm. *PASA*, 34:e003, Jan 2017.
- [73] A. Liu and M. Tegmark. A method for 21 cm power spectrum estimation in the presence of foregrounds. *PhRvD*, 83(10):103006–+, May 2011.
- [74] Adrian Liu, Max Tegmark, Scott Morrison, Andrew Lutomirski, and Matias Zaldarriaga. Precision calibration of radio interferometers using redundant baselines. *MNRAS*, 408(2):1029–1050, Oct 2010.
- [75] Zachary E. Martinot, James E. Aguirre, Saul A. Kohn, and Immanuel Q. Washington. Ionospheric Attenuation of Polarized Foregrounds in 21 cm Epoch of Reionization Measurements: A Demonstration for the HERA Experiment. *ApJ*, 869(1):79, Dec 2018.
- [76] M. McQuinn, O. Zahn, M. Zaldarriaga, L. Hernquist, and S. R. Furlanetto. Cosmological Parameter Estimation Using 21 cm Radiation from the Epoch of Reionization. *ApJ*, 653:815–834, December 2006.
- [77] F. G. Mertens, A. Ghosh, and L. V. E. Koopmans. Statistical 21-cm signal separation via Gaussian Process Regression analysis. *MNRAS*, 478(3):3640–3652, Aug 2018.
- [78] A. Mesinger, S. Furlanetto, and R. Cen. 21CMFAST: a fast, seminumerical simulation of the high-redshift 21-cm signal. *MNRAS*, 411:955–972, February 2011.

- [79] D. A. Mitchell, L. J. Greenhill, R. B. Wayth, R. J. Sault, C. J. Lonsdale, R. J. Cappallo, M. F. Morales, and S. M. Ord. Real-Time Calibration of the Murchison Widefield Array. *IEEE Journal of Selected Topics in Signal Processing*, Vol. 2, Issue 5, p.707-717, 2:707–717, November 2008.
- [80] D. F. Moore, J. E. Aguirre, A. R. Parsons, D. C. Jacobs, and J. C. Pober. The Effects of Polarized Foregrounds on 21 cm Epoch of Reionization Power Spectrum Measurements. *ApJ*, 769:154, June 2013.
- [81] M. F. Morales and J. Hewitt. Toward Epoch of Reionization Measurements with Wide-Field Radio Observations. *ApJ*, 615:7–18, November 2004.
- [82] Miguel F. Morales, Adam Beardsley, Jonathan Pober, Nichole Barry, Bryna Hazelton, Daniel Jacobs, and Ian Sullivan. Understanding the diversity of 21 cm cosmology analyses. *MNRAS*, 483(2):2207–2216, Feb 2019.
- [83] A. Mouri Sardarabadi and L. V. E. Koopmans. Quantifying suppression of the cosmological 21-cm signal due to direction-dependent gain calibration in radio interferometers. *MNRAS*, 483(4):5480–5490, Mar 2019.
- [84] S. G. Murray, C. M. Trott, and C. H. Jordan. An Improved Statistical Point-source Foreground Model for the Epoch of Reionization. *ApJ*, 845:7, August 2017.
- [85] A. R. Neben, R. F. Bradley, J. N. Hewitt, G. Bernardi, J. D. Bowman, F. Briggs, R. J. Cappallo, A. A. Deshpande, R. Goeke, and L. J. Greenhill. Measuring phased-array antenna beampatterns with high dynamic range for the Murchison Widefield Array using 137 MHz ORBCOMM satellites. *Radio Science*, 50(7):614–629, Jul 2015.
- [86] Abraham R. Neben, Richard F. Bradley, Jacqueline N. Hewitt, David R. DeBoer, Aaron R. Parsons, James E. Aguirre, Zaki S. Ali, Carina Cheng, Aaron Ewall-Wice, and Nipanjana Patra. The Hydrogen Epoch of Reionization Array Dish. I. Beam Pattern Measurements and Science Implications. *ApJ*, 826(2):199, Aug 2016.
- [87] C. D. Nunhokee, G. Bernardi, S. A. Kohn, J. E. Aguirre, N. Thyagarajan, J. S. Dillon, G. Foster, T. L. Grobler, J. Z. E. Martinot, and A. R. Parsons. Constraining Polarized Foregrounds for EoR Experiments. II. Polarization Leakage Simulations in the Avoidance Scheme. *ApJ*, 848(1):47, Oct 2017.
- [88] A. R. Offringa, F. Mertens, and L. V. E. Koopmans. The impact of interference excision on 21-cm epoch of reionization power spectrum analyses. *MNRAS*, 484(2):2866–2875, Apr 2019.
- [89] A. R. Offringa, F. Mertens, and L. V. E. Koopmans. The impact of interference excision on 21-cm epoch of reionization power spectrum analyses. *MNRAS*, 484(2):2866–2875, Apr 2019.
- [90] A. R. Offringa, J. J. van de Gronde, and J. B. T. M. Roerdink. A morphological algorithm for improved radio-frequency interference detection. *A&A*, 539, March 2012.

- [91] Gregory Paciga, Joshua G. Albert, Kevin Bandura, Tzu-Ching Chang, Yashwant Gupta, Christopher Hirata, Julia Odegova, Ue-Li Pen, Jeffrey B. Peterson, Jayanta Roy, J. Richard Shaw, Kris Sigurdson, and Tabitha Voytek. A simulation-calibrated limit on the H I power spectrum from the GMRT Epoch of Reionization experiment. *MNRAS*, 433(1):639–647, Jul 2013.
- [92] Gregory Paciga, Tzu-Ching Chang, Yashwant Gupta, Rajaram Nityanada, Julia Odegova, Ue-Li Pen, Jeffrey B. Peterson, Jayanta Roy, and Kris Sigurdson. The GMRT Epoch of Reionization experiment: a new upper limit on the neutral hydrogen power spectrum at  $z \approx 8.6$ . *MNRAS*, 413(2):1174–1183, May 2011.
- [93] A. Parsons, J. Pober, M. McQuinn, D. Jacobs, and J. Aguirre. A Sensitivity and Array-configuration Study for Measuring the Power Spectrum of 21 cm Emission from Reionization. *ApJ*, 753:81, July 2012.
- [94] A. R. Parsons, D. C. Backer, G. S. Foster, M. C. H. Wright, R. F. Bradley, N. E. Gugliucci, C. R. Parashare, E. E. Benoit, J. E. Aguirre, D. C. Jacobs, C. L. Carilli, D. Herne, M. J. Lynch, J. R. Manley, and D. J. Werthimer. The Precision Array for Probing the Epoch of Re-ionization: Eight Station Results. *AJ*, 139:1468–1480, April 2010.
- [95] A. R. Parsons, A. Liu, J. E. Aguirre, Z. S. Ali, R. F. Bradley, C. L. Carilli, D. R. DeBoer, M. R. Dexter, N. E. Gugliucci, D. C. Jacobs, P. Klima, D. H. E. MacMahon, J. R. Manley, D. F. Moore, J. C. Pober, I. I. Stefan, and W. P. Walbrugh. New Limits on 21 cm Epoch of Reionization from PAPER-32 Consistent with an X-Ray Heated Intergalactic Medium at  $z = 7.7$ . *ApJ*, 788:106, June 2014.
- [96] Aaron Parsons, Donald Backer, Andrew Siemion, Henry Chen, Dan Werthimer, Pierre Droz, Terry Filiba, Jason Manley, Peter McMahon, and Arash Parsa. A Scalable Correlator Architecture Based on Modular FPGA Hardware, Reuseable Gateware, and Data Packetization. *PASP*, 120(873):1207, Nov 2008.
- [97] Aaron R. Parsons, Adrian Liu, Zaki S. Ali, and Carina Cheng. Optimized Beam Sculpting with Generalized Fringe-rate Filters. *ApJ*, 820(1):51, Mar 2016.
- [98] Aaron R. Parsons, Jonathan C. Pober, James E. Aguirre, Christopher L. Carilli, Daniel C. Jacobs, and David F. Moore. A Per-baseline, Delay-spectrum Technique for Accessing the 21 cm Cosmic Reionization Signature. *ApJ*, 756(2):165, Sep 2012.
- [99] A. H. Patil, S. Yatawatta, L. V. E. Koopmans, A. G. de Bruyn, M. A. Brentjens, S. Zaroubi, K. M. B. Asad, M. Hatef, V. Jelić, and M. Mevius. Upper Limits on the 21 cm Epoch of Reionization Power Spectrum from One Night with LOFAR. *ApJ*, 838(1):65, Mar 2017.
- [100] A. H. Patil, S. Yatawatta, S. Zaroubi, L. V. E. Koopmans, A. G. de Bruyn, V. Jelić, B. Ciardi, I. T. Iliev, M. Mevius, V. N. Pandey, and B. K. Gehlot. Systematic biases in low frequency radio interferometric data due to calibration: the LOFAR EoR case. *MNRAS*, September 2016.

- [101] A. H. Patil, S. Zaroubi, E. Chapman, V. Jelić, G. Harker, F. B. Abdalla, K. M. B. Asad, G. Bernardi, M. A. Brentjens, A. G. de Bruyn, S. Bus, B. Ciardi, S. Daiboo, E. R. Fernandez, A. Ghosh, H. Jensen, S. Kazemi, L. V. E. Koopmans, P. Labropoulos, M. Mevius, O. Martinez, G. Mellema, A. R. Offringa, V. N. Pandey, J. Schaye, R. M. Thomas, H. K. Vedantham, V. Veligatla, S. J. Wijnholds, and S. Yatawatta. Constraining the epoch of reionization with the variance statistic: simulations of the LOFAR case. *MNRAS*, 443:1113–1124, September 2014.
- [102] Ajinkya H. Patil, Saleem Zaroubi, Emma Chapman, Vibor Jelić, Geraint Harker, Filipe B. Abdalla, Khan M. B. Asad, Gianni Bernardi, Michiel A. Brentjens, and A. G. de Bruyn. Constraining the epoch of reionization with the variance statistic: simulations of the LOFAR case. *MNRAS*, 443(2):1113–1124, Sep 2014.
- [103] J. C. Pober, A. Liu, J. S. Dillon, J. E. Aguirre, J. D. Bowman, R. F. Bradley, C. L. Carilli, D. R. DeBoer, J. N. Hewitt, D. C. Jacobs, M. McQuinn, M. F. Morales, A. R. Parsons, M. Tegmark, and D. J. Werthimer. What Next-generation 21 cm Power Spectrum Measurements can Teach us About the Epoch of Reionization. *ApJ*, 782:66, February 2014.
- [104] Jonathan C. Pober, Zaki S. Ali, Aaron R. Parsons, Matthew McQuinn, James E. Aguirre, Gianni Bernardi, Richard F. Bradley, Chris L. Carilli, Carina Cheng, and David R. DeBoer. PAPER-64 Constraints On Reionization. II. The Temperature of the  $z = 8.4$  Intergalactic Medium. *ApJ*, 809(1):62, Aug 2015.
- [105] Jonathan C. Pober, Aaron R. Parsons, Daniel C. Jacobs, James E. Aguirre, Richard F. Bradley, Chris L. Carilli, Nicole E. Gugliucci, David F. Moore, and Chaitali R. Parashare. A Technique for Primary Beam Calibration of Drift-scanning, Wide-field Antenna Elements. *AJ*, 143(2):53, Feb 2012.
- [106] P. Procopio, B. Pindor, D.A.M. Mitchell, and builders. Calibration of MWA data using the MWA Real-Time System. *ApJ*, 2015, in prep.
- [107] Sandeep Rana and Jasjeet S. Bagla. Angular clustering of point sources at 150 MHz in the TGSS survey. *MNRAS*, 485(4):5891–5896, Jun 2019.
- [108] SK. Saiyad Ali, Somnath Bharadwaj, and Sanjay K. Pandey. Probing the bispectrum at high redshifts using 21-cm HI observations. *MNRAS*, 366(1):213–218, Feb 2006.
- [109] Irina I. Stefan, Chris L. Carilli, David A. Green, Zaki Ali, James E. Aguirre, Richard F. Bradley, David DeBoer, Matthew Dexter, Nicole E. Gugliucci, and D. E. Harris. Imaging on PAPER: Centaurus A at 148 MHz. *MNRAS*, 432(2):1285–1293, Jun 2013.
- [110] I. S. Sullivan, M. F. Morales, B. J. Hazelton, W. Arcus, D. Barnes, G. Bernardi, F. H. Briggs, J. D. Bowman, J. D. Bunton, and R. J. Cappallo. Fast Holographic Deconvolution: A New Technique for Precision Radio Interferometry. *ApJ*, 759(1):17, Nov 2012.

- [111] G. Swarup, S. Ananthakrishnan, V. K. Kapahi, A. P. Rao, C. R. Subrahmanya, and V. K. Kulkarni. The Giant Metre-Wave Radio Telescope. *Current Science*, 60:95, Jan 1991.
- [112] M. Tegmark. How to measure CMB power spectra without losing information. *PhRvD*, 55:5895–5907, May 1997.
- [113] A. R. Thompson, J. M. Moran, and G. W. Swenson. *Interferometry and synthesis in radio astronomy*. 1986.
- [114] N. Thyagarajan, D. C. Jacobs, J. D. Bowman, and others. Foregrounds in Wide-field Redshifted 21 cm Power Spectra. *ApJ*, 804:14, May 2015.
- [115] S. J. Tingay, R. Goeke, J. D. Bowman, D. Emrich, and others. The Murchison Wide-field Array: The Square Kilometre Array Precursor at Low Radio Frequencies. *PASA*, 30:7, January 2013.
- [116] C. M. Trott, B. Pindor, P. Procopio, R. B. Wayth, D. A. Mitchell, B. McKinley, S. J. Tingay, N. Barry, A. P. Beardsley, G. Bernardi, J. D. Bowman, F. Briggs, R. J. Cappallo, P. Carroll, A. de Oliveira-Costa, J. S. Dillon, A. Ewall-Wice, L. Feng, L. J. Greenhill, B. J. Hazelton, J. N. Hewitt, N. Hurley-Walker, M. Johnston-Hollitt, D. C. Jacobs, D. L. Kaplan, H. S. Kim, E. Lenc, J. Line, A. Loeb, C. J. Lonsdale, M. F. Morales, E. Morgan, A. R. Neben, N. Thyagarajan, D. Oberoi, A. R. Offringa, S. M. Ord, S. Paul, J. C. Pober, T. Prabu, J. Riding, N. Udaya Shankar, S. K. Sethi, K. S. Srivani, R. Subrahmanyan, I. S. Sullivan, M. Tegmark, R. L. Webster, A. Williams, C. L. Williams, C. Wu, and J. S. B. Wyithe. CHIPS: The Cosmological H i Power Spectrum Estimator. *ApJ*, 818:139, February 2016.
- [117] C. M. Trott and R. B. Wayth. Spectral Calibration Requirements of Radio Interferometers for Epoch of Reionisation Science with the SKA. *PASA*, 33:e019, May 2016.
- [118] C. M. Trott, R. B. Wayth, and S. J. Tingay. The Impact of Point-source Subtraction Residuals on 21 cm Epoch of Reionization Estimation. *ApJ*, 757:101, September 2012.
- [119] Cathryn M. Trott, Eloy de Lera Acedo, Randall B. Wayth, Nicolas Fagnoni, Adrian T. Sutinjo, Brett Wakley, and Chris Ivan B. Punzalan. Spectral performance of Square Kilometre Array Antennas - II. Calibration performance. *MNRAS*, 470(1):455–465, Sep 2017.
- [120] Cathryn M. Trott, Shih Ching Fu, S. G. Murray, C. H. Jordan, J. L. B. Line, N. Barry, R. Byrne, B. J. Hazelton, K. Hasegawa, and R. Joseph. Robust statistics towards detection of the 21 cm signal from the Epoch of Reionization. *MNRAS*, 486(4):5766–5784, Jul 2019.
- [121] Cathryn M. Trott, C. H. Jordan, S. G. Murray, B. Pindor, D. A. Mitchell, R. B. Wayth, J. Line, B. McKinley, A. Beardsley, and J. Bowman. Assessment of Ionospheric Activity Tolerances for Epoch of Reionization Science with the Murchison Widefield Array. *ApJ*, 867(1):15, Nov 2018.

- [122] Cathryn M. Trott, Catherine A. Watkinson, Christopher H. Jordan, Shintaro Yoshiura, Suman Majumdar, N. Barry, R. Byrne, B. J. Hazelton, K. Hasegawa, and R. Joseph. Gridded and direct Epoch of Reionisation bispectrum estimates using the Murchison Widefield Array. *arXiv e-prints*, page arXiv:1905.07161, May 2019.
- [123] Cathryn M. Trott and Randall B. Wayth. Building Models for Extended Radio Sources: Implications for Epoch of Reionisation Science. *PASA*, 34:e061, Nov 2017.
- [124] M. P. van Haarlem, M. W. Wise, A. W. Gunst, G. Heald, J. P. McKean, J. W. T. Hessels, A. G. de Bruyn, R. Nijboer, J. Swinbank, R. Fallows, M. Brentjens, A. Nelles, R. Beck, H. Falcke, R. Fender, J. Hörandel, L. V. E. Koopmans, G. Mann, G. Miley, H. Röttgering, B. W. Stappers, and others. LOFAR: The LOw-Frequency ARray. *A&A*, 556:A2, August 2013.
- [125] R. B. Wayth, E. Lenc, M. E. Bell, J. R. Callingham, K. S. Dwarakanath, T. M. O. Franzen, B.-Q. For, B. Gaensler, P. Hancock, L. Hindson, N. Hurley-Walker, C. A. Jackson, M. Johnston-Hollitt, A. D. Kapińska, B. McKinley, J. Morgan, A. R. Offringa, P. Procopio, L. Staveley-Smith, C. Wu, Q. Zheng, C. M. Trott, G. Bernardi, J. D. Bowman, F. Briggs, R. J. Cappallo, B. E. Corey, A. A. Deshpande, D. Emrich, R. Goeke, L. J. Greenhill, B. J. Hazelton, D. L. Kaplan, J. C. Kasper, E. Kratzenberg, C. J. Lonsdale, M. J. Lynch, S. R. McWhirter, D. A. Mitchell, M. F. Morales, E. Morgan, D. Oberoi, S. M. Ord, T. Prabu, A. E. E. Rogers, A. Roshi, N. U. Shankar, K. S. Srivani, R. Subrahmanyan, S. J. Tingay, M. Waterson, R. L. Webster, A. R. Whitney, A. Williams, and C. L. Williams. GLEAM: The GaLactic and Extragalactic All-Sky MWA Survey. *PASA*, 32:e025, June 2015.
- [126] R. B. Wayth, S. J. Tingay, C. M. Trott, D. Emrich, M. Johnston-Hollitt, B. McKinley, B. M. Gaensler, A. P. Beardsley, T. Booler, B. Crosse, T. M. O. Franzen, L. Horsley, D. L. Kaplan, D. Kenney, M. F. Morales, D. Pallot, G. Sleap, K. Steele, M. Walker, A. Williams, C. Wu, I. H. Cairns, M. D. Filipovic, S. Johnston, T. Murphy, P. Quinn, L. Staveley-Smith, R. Webster, and J. S. B. Wyithe. The Phase II Murchison Widefield Array: Design Overview. *ArXiv e-prints*, September 2018.
- [127] Michael J. Wilensky, Miguel F. Morales, Bryna J. Hazelton, Nichole Barry, Ruby Byrne, and Sumit Roy. Absolving the SSINS of Precision Interferometric Radio Data: A New Technique for Mitigating Ultra-faint Radio Frequency Interference. *arXiv e-prints*, page arXiv:1906.01093, Jun 2019.
- [128] Christopher L. Williams, Jacqueline N. Hewitt, Alan M. Levine, Angelica de Oliveira-Costa, Judd D. Bowman, Frank H. Briggs, B. M. Gaensler, Lars L. Hernquist, Daniel A. Mitchell, and Miguel F. Morales. Low-frequency Imaging of Fields at High Galactic Latitude with the Murchison Widefield Array 32 Element Prototype. *ApJ*, 755(1):47, Aug 2012.
- [129] J. S. B. Wyithe and M. F. Morales. Biased reionization and non-Gaussianity in redshifted 21-cm intensity maps of the reionization epoch. *MNRAS*, 379:1647–1657, August 2007.

- [130] S. Yatawatta, A. G. de Bruyn, M. A. Brentjens, P. Labropoulos, V. N. Pandey, S. Kazemi, S. Zaroubi, L. V. E. Koopmans, A. R. Offringa, and V. Jelić. Initial deep LOFAR observations of epoch of reionization windows. I. The north celestial pole. *A&A*, 550:A136, Feb 2013.
- [131] S. Yoshiura, K. Ichiki, B. Pindor, K. Takahashi, H. Tashiro, and C. M. Trott. Study of systematics effects on the cross power spectrum of 21 cm line and cosmic microwave background using Murchison Widefield Array data. *MNRAS*, 483(2):2697–2711, Feb 2019.
- [132] S. Yoshiura, J. L. B. Line, K. Kubota, K. Hasegawa, and K. Takahashi. Detectability of 21 cm-signal during the Epoch of Reionization with 21 cm-Lyman- $\alpha$  emitter cross-correlation - II. Foreground contamination. *MNRAS*, 479(2):2767–2776, Sep 2018.
- [133] Shintaro Yoshiura, Hayato Shimabukuro, Keitaro Takahashi, Rieko Momose, Hiroyuki Nakanishi, and Hiroshi Imai. Sensitivity for 21 cm bispectrum from Epoch of Reionization. *MNRAS*, 451(1):266–274, Jul 2015.
- [134] S. Zaroubi, A. G. de Bruyn, G. Harker, R. M. Thomas, P. Labropoulos, V. Jelić, L. V. E. Koopmans, M. A. Brentjens, G. Bernardi, and B. Ciardi. Imaging neutral hydrogen on large scales during the Epoch of Reionization with LOFAR. *MNRAS*, 425(4):2964–2973, Oct 2012.
- [135] H. Zheng, M. Tegmark, V. Buza, J. S. Dillon, H. Gharibyan, J. Hickish, E. Kunz, A. Liu, J. Losh, and A. Lutomirski. MITeR: a scalable interferometer for precision 21 cm cosmology. *MNRAS*, 445(2):1084–1103, Dec 2014.
- [136] Qian Zheng, Xiang-Ping Wu, Jun-Hua Gu, Jingying Wang, and Haiguang Xu. A Method to Extract the Angular Power Spectrum of the Epoch of Reionization from Low-frequency Radio Interferometers. *ApJ*, 758(1):L24, Oct 2012.

# Chapter 9

## Future prospects

**Author Name**

### Abstract

This chapter discusses some important things

### 9.1 Forthcoming interferometric ground based instruments and upgrades

#### 9.1.1 The Hydrogen Epoch of Reionization Array

The Hydrogen Epoch of Reionization Array (HERA) is an array currently under construction in the Karoo reserve area in South Africa - following the conclusion of the PAPER experiment. HERA is built following the approach used for PAPER: a highly redundant array to maximize the sensitivity on a number of power spectrum modes measured using the avoidance approach. In order to increase the sensitivity with respect to PAPER, it employs 14 m diameter dishes that, in the final configuration, will be densely packed in a highly redundant hexagonal array configuration of  $\sim 350$  m diameter. HERA is built with the purpose to provide a complete statistical characterization of cosmic reionization: its high brightness sensitivity configuration leads to a significant ( $> 10$ ) power spectrum detection in the  $0.2 < k < 0.4$  Mpc $^{-1}$  range throughout reionization (i.e.,  $6 \leq z \leq 12$ ; Pober et al., 2014; de Boer et al., 2017), fully constraining the evolution of the IGM neutral Hydrogen fraction. As the avoidance approach does not take advantage of foreground modeling, particular attention was paid to prevent the instrumental frequency response from corrupting intrinsically smooth foregrounds (Ewall-Wice et al., 2015; Patra et al., 2017). HERA is currently under construction, with more than 200 dishes deployed and science observations routinely carried out (Carilli et al. 2018, Kohn et al. 2019). New feeds that extend the sensitivity to the 50-250 MHz (i.e. enabling observations of the Cosmic Dawn) are currently deployed for testing. In summary, HERA is planned to deliver a complete characterization of cosmic reionization and to attempt the detection of the Cosmic Dawn. Given its redundant configuration, imaging capabilities remain limited and will be the target of a next generation experiment.

### 9.1.2 The Large aperture Experiment to detect the Dark Ages

The Large aperture Experiment to detect the Dark Ages (LEDA) is located in Owens Valley, California. It operates in the 30-88 MHz frequency range corresponding to  $15 < z < 46$ , therefore seeking to detect the 21 cm signal from the Cosmic Dawn. It is equipped to attempt the measurement of both the global signal via individual dipoles equipped with custom-built calibration sources and 21 cm fluctuations via an array of 256 dipoles. Dipoles are pseudo randomly distributed to achieve an essentially filled array within a 200 m diameter core, providing excellent imaging capabilities to Galactic diffuse emission - the brightest foreground component. The LEDA approach to measure the 21 cm signal can be versatile, allowing to image and subtract foregrounds but also to isolate them in the power spectrum domain without any specific modeling. Current simulations shows that if IGM heating occurs efficiently at  $z = 16$ , LEDA would be able to detect the 21 cm power spectrum at  $k \sim 0.1 \text{ Mpc}^{-1}$  with a 10 signal to noise ratio in 3000 hours. First observations have set a  $108 \text{ (mK)}^2$  upper limits on the 21 cm power spectrum at  $k = 0.1 \text{ Mpc}^{-1}$  at  $z = 18.4$  (Eastwood et al. 2019)

## 9.2 A Section

Lorem ipsum dolor sit amet, consectetur adipiscing elit. Duis eu egestas erat. Maecenas tincidunt lacinia tincidunt. Mauris id lectus nec neque feugiat condimentum vitae at diam. In vel orci nunc, non commodo mauris. Vivamus ipsum enim, vulputate quis pharetra non, molestie quis felis. Vivamus porttitor placerat turpis at accumsan. Nunc tortor velit, faucibus a rhoncus nec, blandit non elit. Nam consectetur lectus eu nisi blandit dapibus rhoncus dui tempus. Mauris fermentum dolor vel ipsum vulputate sit amet ultricies tortor lacinia. Donec ut nibh erat. Morbi nec mi ante. Integer nec vestibulum diam. Donec tincidunt pellentesque quam, ut interdum mauris venenatis condimentum. Nam condimentum, augue in aliquet gravida, neque dui elementum eros, id semper eros purus sed felis. Curabitur in justo sit amet sapien ultrices hendrerit at quis nibh. Quisque iaculis pulvinar tincidunt.

$$\begin{aligned}
C(12) &= \left[ \vec{\pi} \cdot \vec{\phi}(x+r) \right] \\
&\approx 1 - \text{const} \frac{r^2}{L^2} \int_r^L \frac{x dx}{x^2} + \dots \\
&\approx 1 - \text{const} \frac{r^2}{L^2} \ln \frac{x dx}{x^2} + \dots
\end{aligned} \tag{9.1}$$

Aenean tellus risus, porta sit amet porta vitae, tincidunt ut felis. Class aptent taciti sociosqu ad litora torquent per conubia nostra, per inceptos himenaeos. Vestibulum ante ipsum primis in faucibus orci luctus et ultrices posuere cubilia Curae; Phasellus pulvinar placerat velit auctor egestas. Vivamus euismod fringilla tincidunt. Sed ut magna felis, id sollicitudin nunc. Quisque a dui eu erat consectetur egestas a quis justo. Aenean euismod congue diam, vel posuere urna fermentum sit amet. Lorem ipsum dolor sit amet, consectetur adipiscing elit. Mauris faucibus lacus eget est mollis auctor. Donec at nibh ligula, et posuere massa. Phasellus quis leo diam [1]. Donec aliquam blandit risus, eu venenatis ante euismod eu. Curabitur cursus justo id arcu condimentum feugiat. Integer sapien urna, vulputate et adipiscing nec, convallis et justo. Suspendisse in ipsum at felis ornare interdum [2],



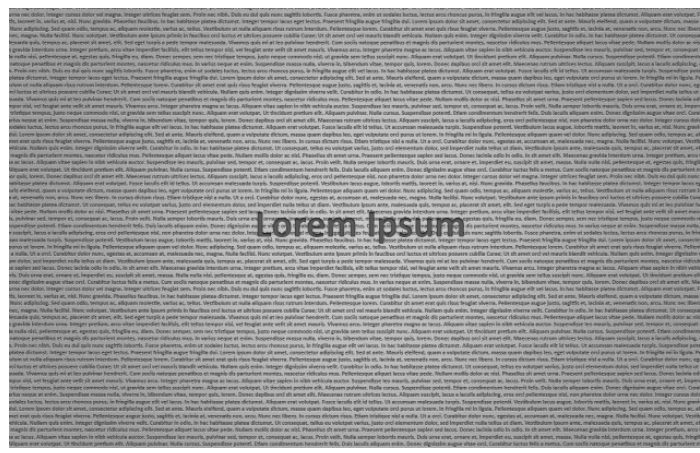


Figure 9.2: This is figure 2 in chapter 1.

# Bibliography

- [1] KI Diamantaras and SY Kung. *Principal component neural networks: theory and applications*. John Wiley & Sons, Inc. New York, NY, USA, 1996.
- [2] D. Tulone and S. Madden. PAQ: Time Series Forecasting for Approximate Query Answering in Sensor Networks. In *Proceedings of the 3rd European Workshop on Wireless Sensor Networks*, pages 21–37. Springer, 2006.